The Dissertation Committee for Xingyu Zhang Certifies that this is the approved version of the following dissertation:

Silicon - Polymer Hybrid Integrated Microwave Photonic Devices for Optical Interconnects and Electromagnetic Wave Detection

Committee:

Ray T. Chen, Supervisor

C. Grant Willson

Andrea Alu

Deji Akinwande

Enrico Poggio

Silicon - Polymer Hybrid Integrated Microwave Photonic Devices for Optical Interconnects and Electromagnetic Wave Detection

by

Xingyu Zhang, B.E.; M.S.E.

Dissertation

Presented to the Faculty of the Graduate School of

The University of Texas at Austin

in Partial Fulfillment

of the Requirements

for the Degree of

Doctor of Philosophy

The University of Texas at Austin

May 2015

Dedicated to my family, teachers and friends

Acknowledgements

I would like to thank my advisor, Prof. Ray T. Chen, for his continuous support and guidance in my doctoral study. Without his guidance and support, I would not be able to finish my research and study in the University of Texas at Austin smoothly. I am also thankful for my committee members, Prof. Grant Willson, Prof. Andrea Alu, Prof. Deji Akinwande, and Dr. Enrico Poggio for serving on my committee and advice on my dissertation.

I appreciate the help from all the former and present members of our Optical Interconnect Group at the University of Texas at Austin, including the research scientists in Omega Optics and the Ph.D students at the Microelectronics Research Center. I also want to acknowledge the contributions of all my collaborators, including Prof. Alex K.-Y. Jen's research group at the University of Washington, Prof. Qiwen Zhan's research group at the University of Dayton, and Prof. Jay Guo's research group at the University of Michigan – Ann Arbor. With their help and important contributions in the whole process of my projects, including the design, modeling, fabrication and testing, we were able to conduct the research work well and achieve the goals of our projects successfully.

Finally, I would like to express my gratitude to all my family members for their love and support throughout my life. Without their love and support, I would not be able to finish my work and be a person who I am now.

Xingyu Zhang

The University of Texas at Austin

Austin, TX

Silicon - Polymer Hybrid Integrated Microwave Photonic Devices for Optical Interconnects and Electromagnetic Wave Detection

Xingyu Zhang, Ph.D

The University of Texas at Austin, 2015

Supervisor: Ray T. Chen

The accelerating increase in information traffic demands the expansion of optical access network systems that require high-performance optical and photonic components. In short-range communication links, optical interconnects have been widely accepted as a viable approach to solve the problems that copper based electrical interconnects have encountered in keeping up with the surge in the data rate demand over the last decades. Low cost, ease of fabrication, and integration capabilities of low optical-loss polymers make them attractive for integrated photonic applications to support futuristic data communication networks. In addition to passive wave-guiding components, electro-optic (EO) polymers consisting of a polymeric matrix doped with organic nonlinear chromophores have enabled wide-RF-bandwidth and low-power active photonic devices. Beside board level passive and active optical components, on-chip micro- or nano-photonic devices have been made possible by the hybrid integration of EO polymers onto the silicon platform.

In recent years, silicon photonics have attracted a significant amount of attentions, because it offers compact device size and the potential of complementary metal–oxide–semiconductor (CMOS) compatible photonic integrated circuits. The combination of

silicon photonics and EO polymers can enable miniaturized and high-performance hybrid integrated photonic devices, such as electro-optic modulators, optical interconnects, and microwave photonic sensors. Silicon photonic crystal waveguides (PCWs) exhibit slow-light effects which are beneficial for device miniaturization. Especially, EO polymer filled silicon slotted PCWs further reduce the device size and enhance the device performance by combining the best of these two systems. The potential applications of these silicon-polymer hybrid integrated devices include not only optical interconnects, but also optical sensing and microwave photonics.

In this dissertation, the design, fabrication, and characterization of several types of silicon-polymer hybrid photonic devices will be presented, including EO polymer filled silicon PCW modulators for on-chip optical interconnects, antenna-coupled optical modulators for electromagnetic wave detections, and low-loss strip-to-slot PCW mode converters. In addition, some polymer-based devices and silicon-based photonic devices will also be presented, such as traveling wave electro-optic polymer modulators based on domain-inversion directional couplers, and silicon thermo-optic switches based on coupled photonic crystal microcavities. Furthermore, some microwave (or RF) components such as integrated broadband bowtie antennas for microwave photonic applications will be covered. Some on-going work or suggested future work will also be introduced, including in-device pyroelectric poling for EO polymer filled silicon slot PCWs, millimeter- or Terahertz-wave sensors based on EO polymer filled plasmonic slot waveguide, low-loss silicon-polymer hybrid slot photonic crystal waveguides fabricated by CMOS foundry, logic devices based on EO polymer microring resonators, and so on.

Table of Contents

List of Tables

List of Figures

Chapter 1: Introduction and Research Goals

1.1 NANOPHOTONICS FOR FUTURE HIGH PERFORMANCE DEVICES AND SYSTEM

With the extension of technology roadmap for semiconductors, the development of next generations of high performance silicon devices and systems is facing quite a few critical challenges. Among them, the performance of interconnects are starting to play more and more indispensable roles. With vastly greater amounts of information communicated at shorter distances in board-level and chip-level, copper-based electrical interconnects become a major bottleneck preventing further improvements due to ringing, crosstalk, increased signal latency, frequency dependent attenuation, and so on. To address these interconnect challenges, various technologies are proposed as potential solutions. Among them, optical interconnects and nanophotonics devices have been demonstrated with unique potentials for constructing high speed and low power on-chip communication links [1, 2].

In addition to long-haul communications which have led to dramatic increases in information traffic in the past decades, optical technology has slowly made its way into board-level and chip-level interconnects, as shown in Fig. 1.1 [3]. Optical interconnects have several benefits such as high bandwidth, negligible frequency dependent loss, low interchannel crosstalk and reduced electromagnetic interference. Optical interconnects are perfect for use at high data speeds, as an optical channel has much lower loss and

lower dispersion than electrical channels composed of copper traces on a PCB or electrical wires and connectors. As recent advances in nanophononics fabrication makes individual devices smaller in footprint and better in performance, optical interconnect is expected to qualify as a feasible interconnect solution. Recently, nanophotonics has been employed in the research and development of on-chip networks and architectures [4] to generate dynamic data traffic routing with high-throughput Time Division Multiplexing and Wavelength Division Multiplexing on-chip nano-photonic links. These works show promising potential for nanophotonics to address inter-core and memory bandwidth limitations. Such nanophotonic devices and optical interconnect systems directly meet the performance requirements of current and future generation of data processors, so they become the key for the development of new applications in data center, high performance computing, cloud systems and big data, etc.

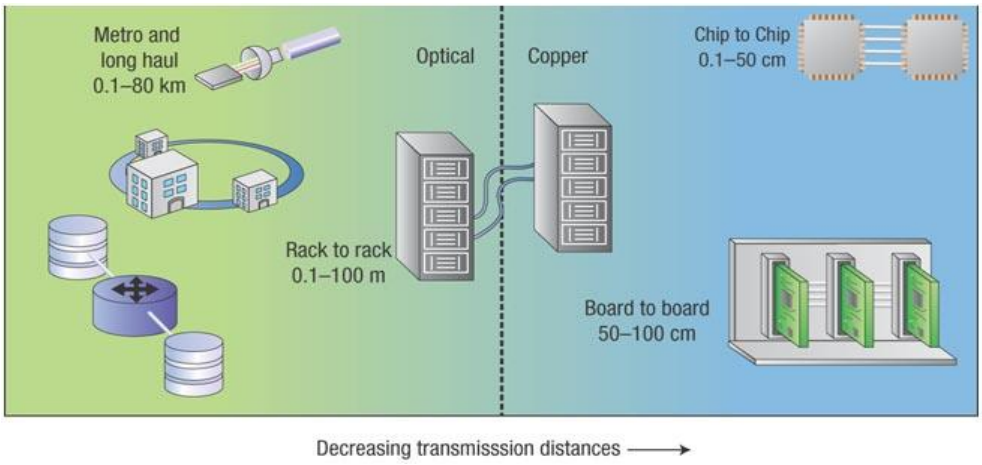

Figure 1.1: Long haul and metro markets are dominated by fiber at present. Although chip-to-chip links still remain electrical for now, this could be replaced by optical links in the foreseeable future. This figure is from Ref. [3].

Silicon photonics technology has enabled highly integrated optical devices for a variety of important applications from telecommunications to interconnects [5]. Various ultra-small silicon waveguide devices, such as lasers, modulators, switches, photodetectors, routers, filters, and grating couplers are quite attractive because these devices can be integrated to functional devices toward the evolution of photonic networks. Large-scale photonic integration is essential for the next generation energy-efficient IT and network equipment capable of handling the large amount of data required by our evolving society. For practical applications of photonic integrated devices, low voltage and compact size are critical because they determine the energy consumption of the photonic devices and their integration density. However, silicon active devices based on plasma-dispersion effects have weak modulation/switching efficiency. This problem can be solved by integrating organic electro-optic (EO) polymers into silicon photonic structures, because EO polymer has very large EO coefficient and thus promises high modulation/switching efficiency. And also, the low cost, ease of fabrication, and integration capabilities of low optical-loss polymers make them attractive. The integration of silicon photonics and high-performance polymers combines the best of these two worlds, paving the way for next generation energy-efficient compact optical interconnect devices. In addition to optical interconnects, these silicon-polymer hybrid nanophotonic devices can be also used for other application areas, such as optical sensing [6] and photonic electromagnetic field detection [7].

In this dissertation, we will talk about several types of silicon and polymer based hybrid integrated nanophotonic devices. By integrating silicon photonics and EO polymers, we combine both of their benefits to develop some high-performance nanophotonic devices. One important application of these devices are on-chip optical interconnects, including wave guiding, electro-optic modulation, and thermo-optic switching. Another main application of these silicon-polymer hybrid integrated devices is microwave photonics, such as photonic electromagnetic wave detection. Although there are various other applications for these nanophotonic devices, we will focus on these two applications in this dissertation. In Chapter 2, we start with a silicon-polymer hybrid passive slot photonic crystal waveguide (PCW) and demonstrate a low-loss strip-to-slot mode converter to efficiently couple light into this slot PCW [8]. Next, we present an EO polymer filled silicon slot photonic crystal waveguide Mach–Zehnder interferometer (MZI) modulator for on-chip optical interconnects in Chapter 3 and 4 [9, 10]. A record-high effective in-device EO coefficient of 1290pm/V is experimentally demonstrated, and this is also the first 50GHz silicon-polymer hybrid PCW MZI modulator [10]. In Chapter 5, we integrate this modulator with a broadband bowtie antenna on the same chip and demonstrate a sensitive photonic electromagnetic wave detector [7], and in Chapter 6 we present a detailed investigation and optimization of the bowtie antennas on glass substrate for this application of microwave photonics [11]. This is the first demonstration of silicon-polymer hybrid PCW devices for the photonic detection of electromagnetic waves [7]. In Chapter 7, a traveling wave directional coupler modulator based on a conventional

polymer waveguide is presented for highly linear broadband analog optical links, and a high dynamic range of 110±3dB/Hz$^{2/3}$ is demonstrated up to 8GHz [12]. In Chapter 8, a thermo-optic switch based on coupled photonic crystal microcavities is demonstrated with compact size, wide spectrum range and low power consumption [13]. In Chapter 8, some future work is suggested, including in-device pyroelectric poling for EO polymer filled silicon slot PCWs, millimeter- or Terahertz-wave sensors based on EO polymer filled plasmonic slot waveguide, low-loss silicon-polymer hybrid slot photonic crystal waveguides fabricated by CMOS foundry, logic devices based on EO polymer microring resonators, and so on.

1.2 SILICON PHOTONICS AND PHOTONIC CRYSTALS

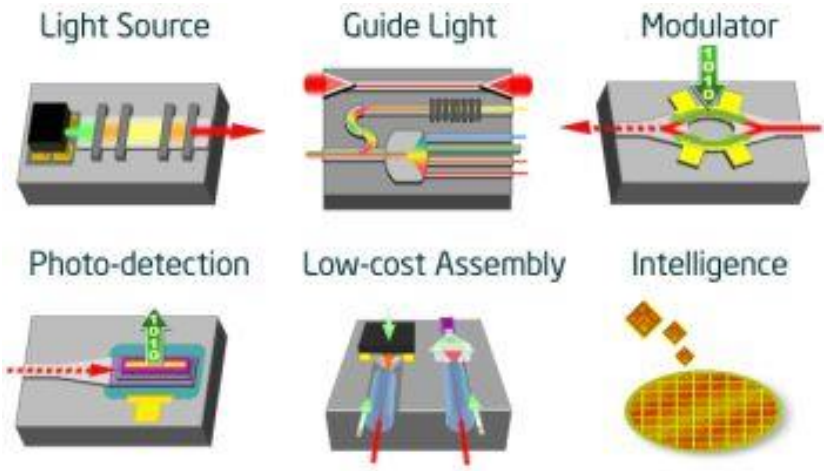

Figure 1.2: Some building blocks in silicon photonics. This figure is from Ref. [20].

In recent years, silicon photonics have attracted a significant amount of attentions, because it offers compact device size and the potential of complementary metal–oxide–semiconductor (CMOS) compatible photonic integrated circuits [5, 14, 15]. Pioneering work in investigating silicon as an optical waveguide material was performed in the late 1980's [16-18]. The development of silicon-on-insulator (SOI) platform for optical device development (few hundred nanometers of single crystal silicon layer on top of a few micron thick buried oxide – BOX layer) has sparked renewed interest in silicon photonics technology, and a number of research groups have actively been involved worldwide since. The large refractive index contrast between silicon (n_{Si}~3.47) and SiO_2 (n_{SiO2}~1.45), and their optical transparency in the 1550nm wavelength window enables ultra-compact device dimensions suitable for large-scale, high density integration on a chip. Additionally, the increasing availability of complementary metal-oxide-semiconductor (CMOS) photonic foundries, development of component libraries, and integration capability with microelectronics promises low-cost development of devices compared to other material technologies [19]. One important application of silicon photonics is optical interconnects. A lot of effects have been made to develop silicon-based passive and active components in optical interconnection systems. Some passive components include fiber-to-chip light couplers, power splitter, polarization splitters, waveguide crossings, and filters. Some active optical devices also play dispensable roles, such as modulators, switches, and photodetectors. Figure 1.2 shows some building blocks in silicon photonics [20].

Among all the silicon photonic structures, photonic crystal waveguides (PCWs) [21] which guide light with lower group velocity are attractive. Photonic crystals are periodic structures where light of certain wavelengths is forbidden to propagate in any direction. This phenomenon is analogous to the energy band gap for electron that exists in semiconductors, so it is called photonic band gap [22, 23]. Photons with an energy that meets the criteria of the allowed states can propagate through the photonic band gap structure, while photons with energy that falls in the disallowed states (photonic band gap) will be reflected. When defects are introduced into a photonic crystal, they induce strong localization of light in the defect area, which can be useful in a number of applications. An example of this line defect waveguide can be formed by etching an array of air holes on a silicon nanomembrane on a silicon-on-insulator (SOI) wafer [24, 25]. For a slab-type PCW, a guided mode is confined by both index guiding in vertical direction and coherent back scattering in horizontal direction. One unique feature in a PCW is that it supports “slow light” at the band edge of the defect induced guided mode [26], due to the combined effect of coherent backscattering and omni-directional reflection from the photonic band gap. With this slow-light effect, PCWs could provide enhanced light-matter interaction, which is beneficial for reducing the required device length and improving the device performance [27].

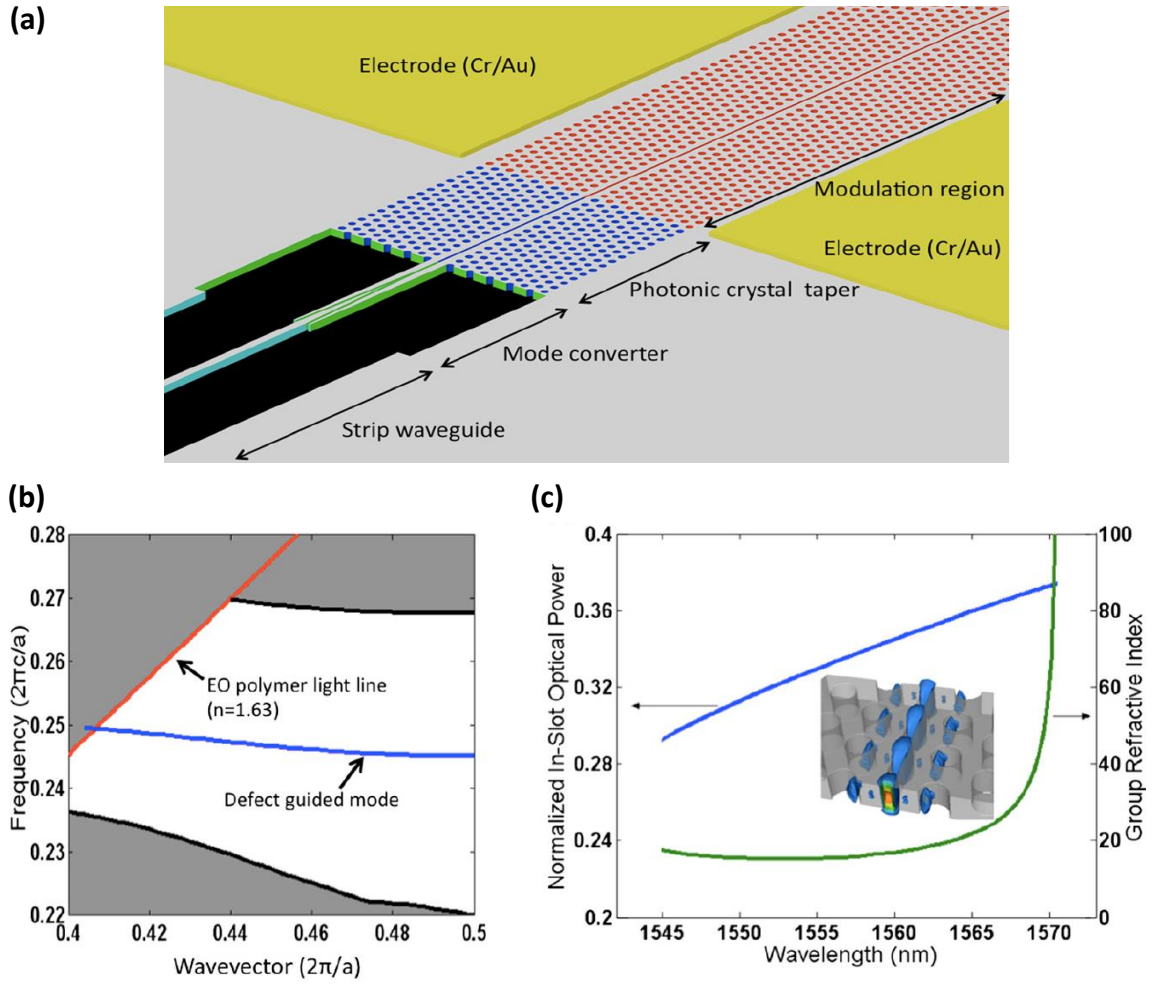

Figure 1.3: Two-dimensional slot photonic crystal waveguide on silicon-on-insulator substrate. Schematics of the input strip waveguide, optical mode converter, PCW group index taper, and active modulation region are shown. Slot width is 75nm. (b) Enlarged portion of the dispersion diagram for the guided mode. (c) Group index and normalized in-slot optical power of the guided mode as a function of the optical wavelength. Optical mode profile at n_g = 100 is shown in inset. The figure is from Ref. [28].

Merging the benefits of PCWs and slot waveguides [29], slot PCWs have been demonstrated to confine and control the propagation of light [30, 31]. In a slot PCW, the

strong optical confinement in the slot filled with a low index material, such as air or organic polymer [32, 33], is combined with the slow-light effect provided by a PCW, which have enabled high-performance active devices [34-36]. Figure 1.3 (a) shows an example of the slot PCW modulator [28], and Fig. 1.3 (b) shows a schematic band diagram of the PCW mode. In Fig. 1.3 (c), the group index as a function of the optical wavelength is overlaid with the normalized in-slot optical power of the guided mode, as well as an optical mode profile. In an electro-optic modulation (switching) device such a Mach–Zehnder interferometer (MZI) modulator, the phase change is proportional to the slow down factor $S=n_g/n_\varphi$, where n_g is the group velocity and n_φ is the phase velocity. As a result, although the index change is limited by the electro-optic effect of the material, the phase difference can be significantly enhanced by the strong dispersion in the slow light region. Figure 1.4 shows a band diagram of an EO polymer filled slot PCW with slot width of 320nm [9], overlaid with that of a conventional strip waveguide for comparison. The slope dispersion curve indicates the group velocity (speed of light/group index). It can be seen from the figure that, in the slow light wavelength (frequency) region close to the band edge where the group index is large, a slight variation of index of silicon or cladding will shift dispersion curve upwards or downwards, leading to a large shift of k vector and thus a large change of phase shift, $\Delta\varphi=\Delta k \cdot L$, where L is the PCW length. Throughout this work, we have successfully demonstrated nanophotonic devices based on slow light silicon photonics, which will be described in the following chapters.

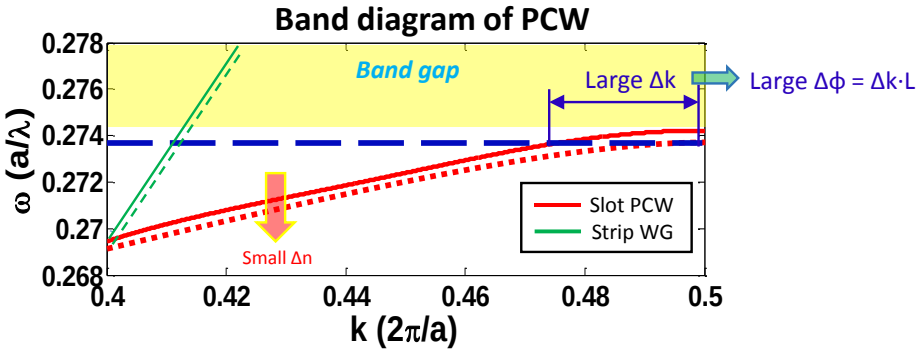

Figure 1.4: A schematic of photonic band diagram of a slot PCW mode, overlaid with that of a conventional strip waveguide. A slight variation of cladding index may induce a shift of dispersion curve upwards or downwards, leading to a large change of optical phase at the photonic band edge (slow light region with large group index). Therefore, the slow-light effects in PCWs can enhance the phase shifts. Slot width is 320nm.

1.3 ELECTRO-OPTIC POLYMER AND POLING

The electro-optic (EO) polymer is a type of organic materials with EO activity. The working mechanism is based on the Pockels effect (also called EO effect), a second-order nonlinear optical effect. When an external electric field is applied across the nonlinear optical materials, the refractive index in the medium is changed linearly proportional to the amplitude of the applied electric field. The Pockels effect is observed only in crystals that lack inversion symmetry such as lithium niobate or gallium arsenide and in non-centrosymmetric media such as EO polymers. When the light propagating in the EO polymer is polarized in the same direction as the applied electric field, the refractive index change in electro-optic polymer is give as

$$\Delta n = -\frac{1}{2} n^3 r_{33} E \tag{1.1}$$

where r_{33} is generally the EO coefficient of interest for EO polymers.

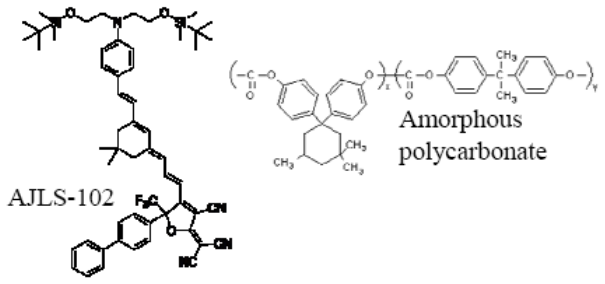

Figure 1.5: One example of the chemical structure of a guest-host EO polymer, including the chromophore (AJLS-102) and host polymer (amorphous polycarbonate).

The materials of interest in this dissertation are the guest-host EO polymers, in which a host polymer is doped with organic molecules called chromophores [37]. An example of the chemical structure of a guest-host EO polymer is shown in Fig. 1.5. Organic chromophores are composed of an electron donating group on one end and an electron accepting group on the other end that are connected by a conjugated π-electron system. Guest-host EO polymers are generally formulated by mixing nonlinear optical chromophores possessing large molecular hyperpolarizability with an amorphous polymer matrix. A variety of guest-host systems can be prepared simply by mixing two components together. Though many organic polymers can be used as

a host matrix, it is necessary to consider the optical transparency of the polymer at the wavelength of interest because this affects the optical absorption loss of the waveguide. Since the two components are dissolved in a common solvent, a thin film can be prepared by casting, dipping, or spin-coating. The guest-host polymer thin films usually need to be dried under vacuum in order to completely remove the residual solvent.

The guest-host EO polymers can offer several advantages. It provides unlimited selection of guest- and host-components, and a wide variety of centrosymmetric nonlinear optical chromophores. It can be easily processed into thin film by spin-coating and to be scaled onto large area of substrates. Its EO coefficient can be as large as 450pm/V in poled thin film [38]. Its ultrafast response time of several femtoseconds can proved polymer based devices with very broad frequency bandwidth. The polymer has low dielectric constant which is beneficial for impedance matching for traveling wave devices. At the same time, the guest-host EO polymer also have some drawbacks and some challenges remains to be addressed in the future, including the decay of the nonlinear optical activity due to orientational relaxation, thermal and environmental instability, limited nonlinear optical activity due to the solubility limit of chromophores in the host matrix, and scattering loss due to the inhomogeneity of chromophores in the host matrix. Some recent efforts shows the improvement of EO polymer performances [39, 40], such as improved thermal stability, lower optical loss and higher power handling abilities.

In this work, the EO polymers were provide by Prof. Alex Jens's research group

in the University of Washington (Soluxra, LLC), such as AJCKL1, SEO300, SEO125, and SEO250. Amorphous polycarbonate (APC) was used as a host matrix. Some basic material properties of these guest-host EO polymer systems are summarized in Table 1.1. Refractive index and material absorption loss are important parameters for polymeric waveguide devices. The glass transition temperature determines the process temperature for the thermally assisted electric-field poling of EO polymers. The r_{33} coefficients of a single layer EO polymer film is a parameter that can be used to evaluate the poling efficiency of the fabricated devices. Since the poling efficiency and the resulting r_{33} coefficient are dependent on the poling process conditions, the poling temperature and the applied poling electric-field are provided as well.

Table 1.1 Material properties of guest-host EO polymers

	AJ-CKL1/APC (25wt%)	SEO125	SEO250
Refractive Index	1.63 @ 1550nm	1.63 @ 1550nm	1.72 @ 1550nm
Absorption Loss	1.8dB/cm	1.5~2.0dB/cm	0.9dB/cm
Tg	135℃	150℃	140℃
Thin film r33 coefficient	~80pm/V (T_p=140℃, E_p=100V/μm)	~120pm/V (T_p=150℃, E_p=100V/μm)	~230pm/V (T_p=140℃, E_p=100V/μm)

(wt%: chromophore loading density, T_g: glass transition temperature, T_p: poling temperature, E_p: poling electric field)

The chromophores are randomly oriented in a thin film of EO polymers and hence the EO polymers are naturally centrosymmetric after the preparation of thin films. In order to induce a macroscopic second-order nonlinearity, thin films must be rendered noncentrosymmetric. This is usually done by a process called thermally assisted electric field poling, and this process is schematically illustrated in Fig. 1.6. First, the EO polymer is heated at or slightly above the glass transition temperature (T_g), and a DC electric field is applied across the polymer. At this elevated temperature, the secondary noncovalent bonds between the polymer chains become weak and the chromophores obtain some freedom to move. Since the chromophores have a permanent dipole moment, they can rotate and align to the applied electric field. Next, the EO polymer is then quickly cooled back to room temperature while maintaining the electric field. Finally, the chromophores are locked and aligned in place.

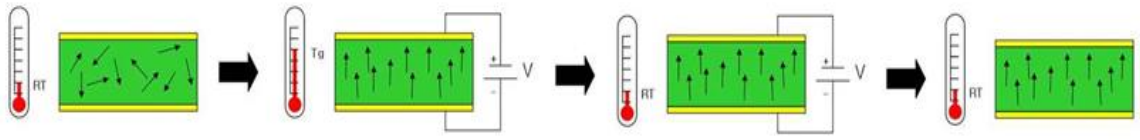

Figure 1.6: A schematic illustration of thermally assisted electric field poling process.

For a stand-alone EO polymer thin film, its EO coefficient after poling can be measured by the optical retardatio method (also called Teng-Man Method) [41]. When measuring the in-device EO coefficient of a modulator, the EO coefficient r_{33} can be

calculated from the half-wave switching voltage (V_π) of the modulator. In a Mach-Zehnder modulator, for example, the half-wave voltage is expressed as

$$V_\pi = \frac{\lambda d}{n^3 r_{33} \sigma L} \tag{1.2}$$

Where λ is the wavelength in free space, d is the electrode separation, n is the waveguide effective refractive index, σ is the overlap integral between the optical mode and electric field, and L is the electrode length. The half-wave voltage is experimentally measured from the over-modulation test and other parameters are obtained from simulations based on the design parameters.

In the past few years, remarkable progress has been made in developing high-performance EO polymer, with increased r_{33} (>200pm/V), better long-term thermal stability, higher optical power handing ability, and lower optical loss (<1dB/cm), and synthetic scalability. Based on recent results from Prof. Alex Jens's research group in the University of Washington (Soluxra, LLC), some EO polymers such as SEO500 can achieve excellent thermal stability up to 100-200^{o}C. And also, the EO polymers can handle optical power up to 100mW [42, 43].

1.4 SILICON-POLYMER HYBRID INTEGRATION

The low cost, ease of fabrication, and integration capabilities of low optical-loss polymers make them attractive for cost reduction of optical and photonic components and high-performance integrated photonic applications. In addition to passive wave-guiding components, electro-optic (EO) polymers consisting of a polymeric matrix doped with

organic nonlinear chromophores have enabled wide-RF-bandwidth and low-power active photonic devices. Beside board level passive and active optical components, on-chip micro- or nano-photonic devices have been made possible by the hybrid integration of EO polymers with other material platforms.

At the same time, silicon photonics have attracted a significant amount of attentions in recent years. It offers small device footprints due to the large index contract between silicon and air, and this promises the complementary metal–oxide–semiconductor (CMOS) compatible photonic integrated circuits. The combination of silicon photonics and EO polymers, called silicon-organic hybrid (SOH) technology [44], can enable miniaturized and high-performance hybrid integrated photonic devices, such as electro-optic modulators [12, 45], optical interconnects [28, 46], and microwave photonic sensors [47]. Silicon photonic crystal waveguides (PCWs) exhibit slow-light effects which are beneficial for enhanced light-mater interaction [23, 48] and device miniaturization [27, 49]. Especially, EO polymer filled silicon slotted PCWs further reduce the device size and enhance the device performance by combining the best of these two systems.

In this dissertation, the design, fabrication, and characterization of several types of silicon-polymer hybrid microwave photonic devices will be presented, including EO polymer filled silicon PCW modulators for on-chip optical interconnects, antenna-coupled optical modulators for electromagnetic wave detections, low-loss strip-to-slot PCW mode converters. Some polymer-based devices and silicon-based photonic devices

will also be presented also, such as traveling wave electro-optic modulators based on polymeric directional coupler, and thermo-optic switches based on coupled silicon photonic crystal microcavities. Some suggested future work will also be introduced.

1.5 REFERENCES

[1] D. A. Miller, "Device requirements for optical interconnects to silicon chips," *Proceedings of the IEEE,* vol. 97, pp. 1166-1185, 2009.

[2] M. Haurylau, G. Chen, H. Chen, J. Zhang, N. A. Nelson, D. H. Albonesi, E. G. Friedman, and P. M. Fauchet, "On-chip optical interconnect roadmap: challenges and critical directions," *Selected Topics in Quantum Electronics, IEEE Journal of,* vol. 12, pp. 1699-1705, 2006.

[3] A. Alduino and M. Paniccia, "Interconnects: Wiring electronics with light," *Nature Photonics,* vol. 1, pp. 153-155, 2007.

[4] A. Shacham, K. Bergman, and L. P. Carloni, "Photonic networks-on-chip for future generations of chip multiprocessors," *Computers, IEEE Transactions on,* vol. 57, pp. 1246-1260, 2008.

[5] R. Soref, "The past, present, and future of silicon photonics," *Selected Topics in Quantum Electronics, IEEE Journal of,* vol. 12, pp. 1678-1687, 2006.

[6] Y. Y. Li, F. Cunin, J. R. Link, T. Gao, R. E. Betts, S. H. Reiver, V. Chin, S. N. Bhatia, and M. J. Sailor, "Polymer replicas of photonic porous silicon for sensing and drug delivery applications," *Science,* vol. 299, pp. 2045-2047, 2003.

[7] X. Zhang, A. Hosseini, H. Subbaraman, S. Wang, Q. Zhan, J. Luo, A. K. Jen, and R. T. Chen, "Integrated Photonic Electromagnetic Field Sensor Based on Broadband Bowtie Antenna Coupled Silicon Organic Hybrid Modulator," *Lightwave Technology, Journal of,* vol. 32, pp. 3774-3784, 2014.

[8] X. Zhang, H. Subbaraman, A. Hosseini, and R. T. Chen, "Highly efficient mode converter for coupling light into wide slot photonic crystal waveguide," *Optics Express,* vol. 22, pp. 20678-20690, 2014.

[9] X. Zhang, A. Hosseini, S. Chakravarty, J. Luo, A. K.-Y. Jen, and R. T. Chen, "Wide optical spectrum range, subvolt, compact modulator based on an electro-optic polymer refilled silicon slot photonic crystal waveguide," *Optics letters,* vol. 38, pp. 4931-4934, 2013.

[10] X. Zhang, A. Hosseini, H. Subbaraman, J. Luo, A. Jen, R. Nelson, and R. T. Chen, "Broadband low-power optical modulator based on electro-optic polymer Infiltrated Silicon Slot Photonic Crystal Waveguide," in *Frontiers in Optics*, 2014, p. FTu1D. 4.

[11] X. Zhang, S. Wang, H. Subbaraman, A. Hosseini, Q. Zhan, R. T. Chen, "Integrated broadband bowtie antenna on transparent substrate," SPIE Photonics West 2015, 9362-23

[12] X. Zhang, B. Lee, C.-y. Lin, A. X. Wang, A. Hosseini, and R. T. Chen, "Highly Linear Broadband Optical Modulator Based on Electro-Optic Polymer," *Photonics Journal, IEEE,* vol. 4, pp. 2214-2228, 2012.

[13] X. Zhang, S. Chakravarty, C. Chung, Z. Pan, H. Yan, and R. T. Chen, "Coupled Photonic Crystal Microcavities for Optical Switching over Wide Spectral Range," IEEE Optical Interconnects Conference, San Diego, CA, April 20-22, 2015, WC6.

[14] B. Jalali and S. Fathpour, "Silicon photonics," *Lightwave Technology, Journal of,* vol. 24, pp. 4600-4615, 2006.

[15] M. Lipson, "Guiding, modulating, and emitting light on silicon-challenges and opportunities," *Journal of Lightwave Technology,* vol. 23, p. 4222, 2005.

[16] R. Soref and J. Lorenzo, "Single-crystal silicon: a new material for 1.3 and 1.6 μm integrated-optical components," *Electronics Letters,* vol. 21, pp. 953-954, 1985.

[17] R. A. Soref and B. R. Bennett, "Electrooptical effects in silicon," *Quantum Electronics, IEEE Journal of,* vol. 23, pp. 123-129, 1987.

[18] R. A. Soref and B. R. Bennett, "Kramers-Kronig analysis of electro-optical switching in silicon," in *Cambridge Symposium-Fiber/LASE'86*, 1987, pp. 32-37.

[19] M. Hochberg and T. Baehr-Jones, "Towards fabless silicon photonics," *Nature Photonics,* vol. 4, pp. 492-494, 2010.

[20] http://www.intel.com/content/www/us/en/research/intel-labs-silicon-photonics-research.html

[21] J. D. Joannopoulos, P. R. Villeneuve, and S. Fan, "Photonic crystals: putting a new twist on light," *Nature,* vol. 386, pp. 143-149, 1997.

[22] T. F. Krauss, "Slow light in photonic crystal waveguides," *Journal of Physics D: Applied Physics,* vol. 40, p. 2666, 2007.

[23] T. Baba, "Slow light in photonic crystals," *Nature Photonics,* vol. 2, pp. 465-473, 2008.

[24] S. G. Johnson, P. R. Villeneuve, S. Fan, and J. Joannopoulos, "Linear waveguides in photonic-crystal slabs," *Physical Review B,* vol. 62, p. 8212, 2000.

[25] M. Notomi, A. Shinya, S. Mitsugi, E. Kuramochi, and H. Ryu, "Waveguides, resonators and their coupled elements in photonic crystal slabs," *Optics Express,* vol. 12, pp. 1551-1561, 2004.

[26] M. Povinelli, S. Johnson, and J. Joannopoulos, "Slow-light, band-edge waveguides for tunable time delays," *Optics Express,* vol. 13, pp. 7145-7159, 2005.

[27] Y. Jiang, W. Jiang, L. Gu, X. Chen, and R. T. Chen, "80-micron interaction length silicon photonic crystal waveguide modulator," *Applied Physics Letters,* vol. 87, p. 221105, 2005.

[28] X. Zhang, A. Hosseini, X. Lin, H. Subbaraman, and R. T. Chen, "Polymer-based Hybrid Integrated Photonic Devices for Silicon On-chip Modulation and Board-

level Optical Interconnects," *IEEE Journal of Selected Topics in Quantum Electronics,* vol. 19, pp. 196-210, 2013.

[29] V. R. Almeida, Q. Xu, C. A. Barrios, and M. Lipson, "Guiding and confining light in void nanostructure," *Optics letters,* vol. 29, pp. 1209-1211, 2004.

[30] A. Di Falco, L. O'Faolain, and T. Krauss, "Photonic crystal slotted slab waveguides," *Photonics and Nanostructures-Fundamentals and Applications,* vol. 6, pp. 38-41, 2008.

[31] X. Chen, W. Jiang, J. Chen, L. Gu, and R. T. Chen, "20 dB-enhanced coupling to slot photonic crystal waveguide using multimode interference coupler," *Applied Physics Letters,* vol. 91, pp. 091111-091111-3, 2007.

[32] Q. Xu, V. R. Almeida, R. R. Panepucci, and M. Lipson, "Experimental demonstration of guiding and confining light in nanometer-size low-refractive-index material," *Optics letters,* vol. 29, pp. 1626-1628, 2004.

[33] C. Koos, P. Vorreau, T. Vallaitis, P. Dumon, W. Bogaerts, R. Baets, B. Esembeson, I. Biaggio, T. Michinobu, and F. Diederich, "All-optical high-speed signal processing with silicon–organic hybrid slot waveguides," *Nature Photonics,* vol. 3, pp. 216-219, 2009.

[34] X. Chen, Y.-S. Chen, Y. Zhao, W. Jiang, and R. T. Chen, "Capacitor-embedded 0.54 pJ/bit silicon-slot photonic crystal waveguide modulator," *Optics letters,* vol. 34, pp. 602-604, 2009.

[35] J.-M. Brosi, C. Koos, L. C. Andreani, M. Waldow, J. Leuthold, and W. Freude, "High-speed low-voltage electro-optic modulator with a polymer-infiltrated silicon photonic crystal waveguide," *Optics Express,* vol. 16, pp. 4177-4191, 2008.

[36] D. M. Beggs, T. P. White, L. O'Faolain, and T. F. Krauss, "Ultracompact and low-power optical switch based on silicon photonic crystals," *Optics letters,* vol. 33, pp. 147-149, 2008.

[37] L. Dalton, A. Harper, A. Ren, F. Wang, G. Todorova, J. Chen, C. Zhang, and M. Lee, "Polymeric electro-optic modulators: from chromophore design to integration with semiconductor very large scale integration electronics and silica fiber optics," *Industrial & engineering chemistry research,* vol. 38, pp. 8-33, 1999.

[38] L. R. Dalton, P. A. Sullivan, and D. H. Bale, "Electric field poled organic electro-optic materials: state of the art and future prospects," *Chemical reviews,* vol. 110, pp. 25-55, 2009.

[39] S. Huang, J. Luo, Z. Jin, X.-H. Zhou, Z. Shi, and A. K.-Y. Jen, "Enhanced temporal stability of a highly efficient guest–host electro-optic polymer through a barrier layer assisted poling process," *Journal of Materials Chemistry,* vol. 22, pp. 20353-20357, 2012.

[40] Z. Shi, J. Luo, S. Huang, B. M. Polishak, X.-H. Zhou, S. Liff, T. R. Younkin, B. A. Block, and A. K.-Y. Jen, "Achieving excellent electro-optic activity and

thermal stability in poled polymers through an expeditious crosslinking process," *Journal of Materials Chemistry,* vol. 22, pp. 951-959, 2012.

[41] C. Teng and H. Man, "Simple reflection technique for measuring the electro‐optic coefficient of poled polymers," *Applied Physics Letters,* vol. 56, pp. 1734-1736, 1990.

[42] J. Luo, S. Huang, Y.-J. Cheng, T.-D. Kim, Z. Shi, X.-H. Zhou, and A. K.-Y. Jen, "Phenyltetraene-based nonlinear optical chromophores with enhanced chemical stability and electrooptic activity," *Organic letters,* vol. 9, pp. 4471-4474, 2007.

[43] S. Takahashi, B. Bhola, A. Yick, W. H. Steier, J. Luo, A. K.-Y. Jen, D. Jin, and R. Dinu, "Photo-Stability Measurement of Electro-Optic Polymer Waveguides With High Intensity at 1550-nm Wavelength," *Journal of Lightwave Technology,* vol. 27, pp. 1045-1050, 2009.

[44] J. Leuthold, W. Freude, J.-M. Brosi, R. Baets, P. Dumon, I. Biaggio, M. L. Scimeca, F. Diederich, B. Frank, and C. Koos, "Silicon organic hybrid technology—A platform for practical nonlinear optics," *Proceedings of the IEEE,* vol. 97, pp. 1304-1316, 2009.

[45] X. Zhang, A. Hosseini, C.-y. Lin, J. Luo, A. K. Jen, and R. T. Chen, "Demonstration of Effective In-device r33 over 1000 pmV in Electro-optic Polymer Refilled Silicon Slot Photonic Crystal Waveguide Modulator," in *CLEO: Science and Innovations*, 2013, p. CTu2F. 6.

[46] F. E. Doany, C. L. Schow, B. G. Lee, R. Budd, C. Baks, R. Dangel, R. John, F. Libsch, J. A. Kash, and B. Chan, "Terabit/sec-class board-level optical interconnects through polymer waveguides using 24-channel bidirectional transceiver modules," in *Electronic Components and Technology Conference (ECTC), 2011 IEEE 61st*, 2011, pp. 790-797.

[47] C.-Y. Lin, A. X. Wang, B. S. Lee, X. Zhang, and R. T. Chen, "High dynamic range electric field sensor for electromagnetic pulse detection," *Optics Express,* vol. 19, pp. 17372-17377, 2011.

[48] Y. A. Vlasov, M. O'Boyle, H. F. Hamann, and S. J. McNab, "Active control of slow light on a chip with photonic crystal waveguides," *Nature,* vol. 438, pp. 65-69, 2005.

[49] X. Zhang, A. Hosseini, J. Luo, A. K.-Y. Jen, and R. T. Chen, "Hybrid silicon-electro-optic-polymer integrated high-performance optical modulator," in *SPIE Photonic West, OPTO*, 2014, pp. 89910O-89910O-6.

Chapter 2: Silicon-polymer hybrid slot photonic crystal waveguides and mode converters *

2.1 INTRODUCTION

Photonic crystal waveguides (PCWs) are a relatively new platform that have generated significant interest over the last decade due to their ability to confine light to ultra-small mode volumes and their slow-light effects which can enhance the light-mater interaction. In slotted PCWs [1], as shown in Fig. 2.1, the strong optical confinement in the slot filled with a low index material, such as air or organic polymers [2-4], is combined with the enhanced light-matter interaction provided by a slow-light structure [5, 6] for improving the device performance and miniaturizing device size. Specifically, silicon slot PCWs infiltrated with electro-optic (EO) active polymers have shown to enable high performance EO modulators [7-9], optical interconnects [4, 10], and photonic sensors [11-13]. For example, We have recently demonstrated an EO polymer infiltrated silicon slot PCW Mach–Zehnder interferometer (MZI) modulator with a switching voltage of 0.94V and an interaction length of 300μm, corresponding to a record-high effective in-device EO coefficient (r_{33}) of 1230pm/V due to the combined effects of large EO polymer r_{33} and slow-light enhancement [14]. In comparison, in Ref

* Citation: X. Zhang, H. Subbaraman, A. Hosseini, and R. T. Chen, "Highly efficient mode converter for coupling light into wide slot photonic crystal waveguide," Optics Express, vol. 22, pp. 20678-20690, 2014.

X. Zhang mainly worked on the simulation, fabrication and characterization, and serves as the first author of the paper. Other coauthors also contributed to the work from simulation, material processing, discussion, or paper preparation.

[15] a non-slow-light/non-resonant MZI modulator based on EO polymer refilled silicon slot waveguide has an large interaction length of 1.5mm, but the measured in-device r_{33} is only 15pm/V.

For these EO polymer based devices, the EO polymer needs to be poled under a DC electric field, so that the Pockels effect can be produced from the non-centrosymmetric alignment of the guest chromophores doped in the host amorphous polymers [16-20]. In this EO polymer poling process, the leakage current due to the charge injection through the silicon/polymer interface is known to be detrimental to the poling efficiency [21], especially for narrow slot widths (S_w) < 200 nm. Widening the slot has been so far the only successful approach to reduce the leakage current and improve the poling efficiency [22, 23]. It has been demonstrated that a slot width (S_w) as large as 320nm can significantly suppress the leakage current in the poling process and achieve an EO coefficient at the same level as that of the poled thin films of EO polymer, which is over two orders of magnitude larger compared to that in the narrow slot (S_w~75nm), while still achieving high optical confinement of the fundamental mode in this wide slot [22, 23]. Based on our simulations [22], the slot width further increases, the slot mode inclines to be decoupled into two separate waveguide modes [22]. Additionally, large slot width is detrimental to EO modulation efficiency because the electrode separation is increased. Therefore, we believe that a 300-350nm slot width with 30% in-slot power is an optimized design for an EO polymer refilled silicon slot PCW modulator.

Here, we choose slot width of 320nm for demonstration. The refractive index of the polymer is assumed to be independent from the slot width.

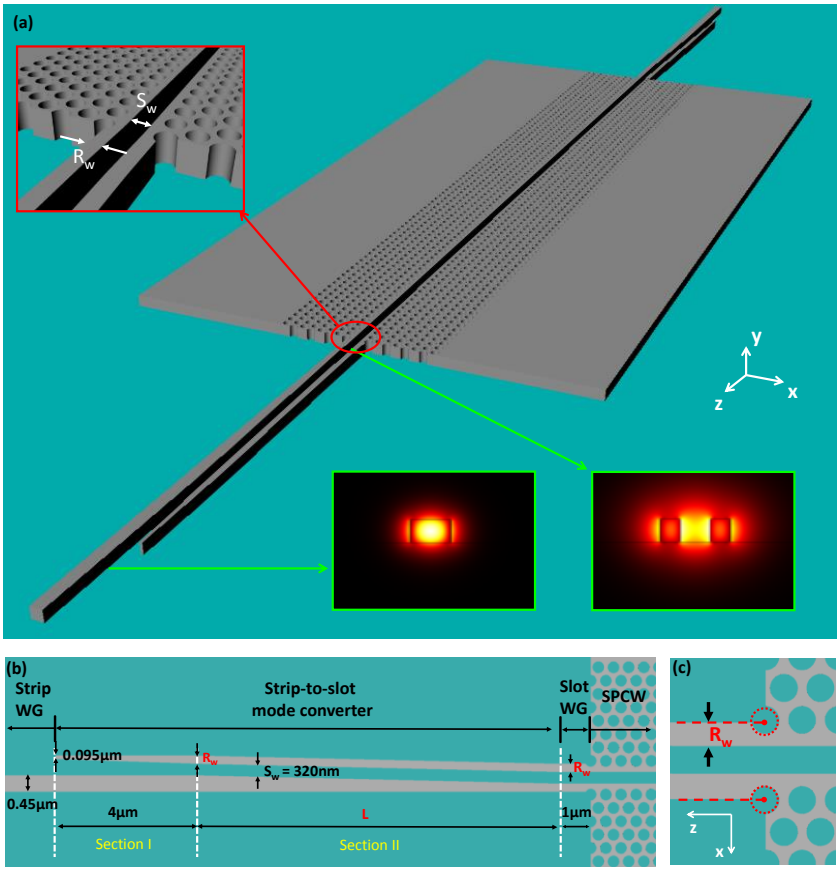

Figure 2.1: (a) Schematic of our mode converter used for coupling light between a strip waveguide and a slot PCW on an SOI substrate. The top inset shows a magnified image of the coupling interface between the slot waveguide and the slot PCW. The bottom insets show the cross-sectional mode profile of the strip waveguide and the slot waveguide, respectively. (b) Top view of the mode converter between the strip waveguide and the slot PCW. Length of Sections I is fixed at 4µm, and the length of Section II is optimized to achieve highest conversion efficiency. (c) Top view of magnified image of the coupling interface between the slot waveguide and the slot PCW. S_w: slot width; R_w: rail width; WG: waveguide; SPCW: slot photonic crystal waveguide; L: length of section II of the mode converter.

In addition to increasing EO polymer poling efficiency for guest-host type EO polymer materials, there are also some other benefits of using large slot width as below. It was demonstrated that the poling-induced optical loss is reduced by the reduction of leakage current through large slot [24]. And also, different from typical slot widths of 100~120nm in conventional slot waveguides [25], widening the slot width to 320nm also reduces the slot capacitance, enabling higher RF bandwidth [26] and lower energy consumption [27]. Additionally, the wider slot provides other benefits such as relaxed fabrication requirement and easier infiltration of cladding material.

Despite the high EO polymer performance in wide slot waveguides, efficient coupling between a strip waveguide and a slot waveguide is challenging due to the large mode mismatch, as shown in the bottom insets of Fig. 2.1 (a) (fundamental TE mode). One common type of strip-to-slot mode converter is a V-shape mode converter [8, 28, 29]. We previously used this V-shape mode converter for coupling light from a strip waveguide into the 320nm slot PCW [22, 23]. However, the non-zero width of the fabricated tip due to lithography limitation leads to a discontinuity at the center of the mode profile, causing the total insertion loss to be as high as 23dB in which each mode converter attributes to a ~1dB insertion loss [22]. To address this problem, in this paper, we explore a new type of adiabatic mode converter to couple light from a single mode strip waveguide into a wide slot PCW, as shown in Figs. 2.1 (a) and (b). The mode converter consists of two linearly tapered sections, and the specific profile and dimensions are given in Fig. 2.1 (b). This type of adiabatic mode converter has been used

for conventional narrow slot waveguides with S_w<130nm [30-32], and insertion losses <0.04dB in a strip-loaded slot waveguide were demonstrated [32]. However, until now, adiabatic mode converters for larger slot widths (e.g. S_w~320nm) have not been reported. It is to be noted that the 320nm slot waveguide here is leaky waveguide, and it needs to be specially designed to minimize the optical power leakage and get the light into/out of the PCW as soon as possible. For this reason, the slot waveguide section is designed to be as short as 1μm as shown in Fig. 2.1 (b), and the rail width (R_w) is optimized to reduce optical loss. Moreover, contrary to conventional design rules, wherein the outer edge of the slot waveguide rails terminate at the center of holes in the first adjacent rows of the slot PCW [1, 22, 23, 29, 33-37], as shown in Fig. 2.1 (c), we find that if the termination is not at the center of the hole, very good coupling efficiency can still be achieved.

In this chapter, we first present the design of the photonic crystal waveguide and group index taper which are used in this work, and then we focus on the design, fabricate and characterize a highly efficient silicon strip-to-slot mode converter for coupling light into a 320nm slot waveguide. The optical loss of the strip-to-slot mode converter is measured to be below 0.08dB. In addition, our adiabatic mode converter and V-shape mode converters are fabricated on the same chip, and the measured loss shows that our adiabatic mode converter has a 0.1dB lower loss compared to V-shape mode converter. Furthermore, we want to emphasize that we not only optimize a strip-to-slot mode converter for slot waveguide with S_w=320nm, but also demonstrate the use of this mode converter for efficiently coupling light into and out of a 300μm-long EO polymer refilled

slot PCW with the same slot width (Figs. 2.1 (a) and (b)). A clear band gap with about 25dB extinction ratio is observed, and an improvement of 3.5dB in coupling efficiency within the slow-light wavelength region compared to the V-shape mode converter is demonstrated. This highly efficient light coupling into wide slot PCWs, combined with the improved poling efficiency of the electro-optic (EO) polymer in wide slot PCWs [22, 23], provides tremendous advantages for several promising applications, including photonic integrated circuits, optical interconnects, EO modulation, and electromagnetic field sensing.

2.2 BAND-ENGINEERED EO POLYMER FILLED SLOT PHOTONIC CRYSTAL WAVEGUIDE AND GROUP INDEX TAPER

The waveguides in this work are designed on a silicon-on-insulator (SOI) substrate with top silicon thickness of 250nm and buried oxide thickness of 3μm. The basic silicon slot PCW structure is schematically shown in Fig. 2.2 (a), with a lattice constant of a=425nm, a hole diameter of d=300nm, and a total photonic crystal length of 314μm (including 300μm-long active length and two 7μm-long PCW tapers). A W1.3 waveguide (the air hole spacing outside the slot is $dW=1.3\sqrt{3}a$) is chosen. A new EO polymer material, SEO125/APC from Soluxra, LLC, consisting of a guest/host system of 25%weight chromophore SEO125 into amorphous polycarbonate (APC) is used in this device. This EO polymer has a refractive index, n=1.63, and EO coefficient, γ_{33}=125pm/V. The optical intensity profiles ($|E|^2$) of the guided mode at the band edge (wave vector of π/a) is numerically calculated to have in-slot power fraction around Γ=0.33.

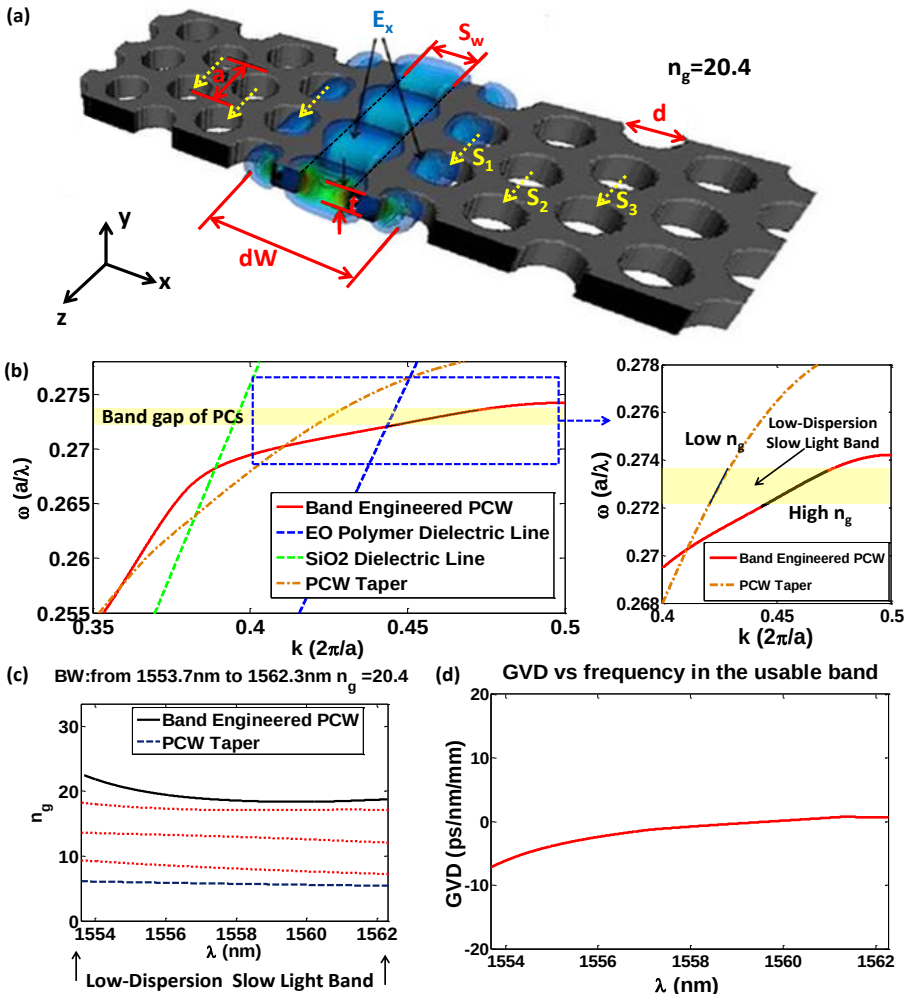

Figure 2.2: (a) A 3D schematic of band-engineered slot PCW, overlaid with the 3D electric field profile of the fundamental guided defect mode. (b) The band structure for 2 PCWs, the band-engineered slot PCW (a=425nm, d=300nm, s_1=0, s_2=-85nm, s_3=85nm, S_w=320nm, dW=1.54($\sqrt{3}$a), and the PCW taper (a=425nm, d=300nm, s_1=0, s_2=0, s_3=0, S_w=320nm, dW=1.45($\sqrt{3}$a). The "flattening" of the mode in the band-engineered slot PCW can be noticed. The black curve highlights the low dispersion slow light section of the mode of the band-engineered slot PCW. The dielectric light lines corresponding to the SiO_2 (n=1.45) and EO polymer (n=1.63) cladding layers are shown. The useful part of the mode falls below the both light lines. (c) Variation of the group index vs. wavelength for the band-engineered slot PCW and the PCW taper. (d) Variation of the group velocity dispersion v.s. wavelength for the band-engineered slot PCW.

In addition, band-engineering technique is used to achieve low-dispersion slow-light (constant group velocity) propagation in this slot PCW for the MZI operation [38, 39]. Specifically, we have chosen the lateral lattice shifting approach [36] for the following advantages. First, all the PCW holes are the same and this increases the fabrication yield and reproducibility compared to techniques that require precise control of multiple hole diameters. Also, it facilitates targeting a desired group velocity over a bandwidth of interest since these two parameters can be tuned relatively independently compared to longitudinal lattice shifting. Finally, it does not change the defect line width and facilitates efficient coupling between the fast-light mode of a silicon slot waveguide (group index, n_g ~3) and the slow-light mode in the slot PCW (n_g >10).

In the lattice-shifted slot PCW is shown in Fig. 2.2 (a). The first three adjacent rows on each side of the defect line are shifted parallel to the line defect to modify the dispersion diagram of the defect mode, as shown by the yellow arrows. Using Rsoft BandSolve module, we simulate the fundamental guided defect mode profile and band structure of this band-engineered slot PCW, as shown in Figs. 2.2 (a) and (b). For lattice constant, a=425nm, it is found that with hole diameter, d=300nm, lattice shifting step s_1=0, s_2=-85nm, s_3=85nm, slot width of S_w=320nm, and dW=1.54($\sqrt{3}$)a, we can achieve an average n_g of 20.4 (±10%) over 8.2nm bandwidth as shown in Fig. 2.2 (c). Note that the second and third rows are shifted in different directions. The absolute value of the group velocity dispersion (GVD) remains below 10ps/nm/mm over the entire bandwidth, as shown in Fig. 2.2 (d).

To couple light form a fast-light slot waveguide to a slow-light slot PCW, a group index taper (also called PCW taper) is used to reduce the group index mismatch [36]. The group index taper consists of eight periods of non-band-engineered PCW (a=425nm, d=300nm, s_1=0, s_2=0, s_3=0, S_w=320nm), for which, the width of the line defect (dW) parabolically increases from dW=1.45($\sqrt{3}$)a to dW=1.54($\sqrt{3}$)a. The slot width (S_w), hole diameter (d), and the period (a) remain constant. The band structure and the group index variation of the PCW taper are shown in Figs. 2.2 (b) and (c), which can be compared with those of the band-engineered slot PCW. An n_g of ~6 of the PCW taper over the optical bandwidth of interest provides an effective interface for coupling between the slow light mode of the slot PCW (n_g=20.4) and the fast light in the silicon slot waveguides (n_g ~3). In other words, the PCW taper gradually increases (slows down) the group index (propagating light) from the interface with the mode converter to the interface with the high n_g slot PCW.

2.3 OPTIMIZATION OF ADIABATIC MODE CONVERTER FOR WIDE SLOT WAVEGUIDE

As shown in Figs. 2.1 (a) and (b), a slot waveguide is designed and used as an input for a designed slot PCW with the same S_w,. The input and output strip waveguides are connected to the slot waveguides using adiabatic strip-to-slot waveguide mode converters. The slot PCW and mode converters are covered with an EO polymer cladding with refractive index of 1.63 at 1550nm wavelength. Subwavelength grating couplers are used for coupling light between the strip waveguides and single mode fibers [40, 41]. As can be seen from Fig. 2.1 (b), a 1μm-long slot waveguide connects the mode converter

and the slot PCW. For both the slot waveguide and the slot PCW, most electric field is confined inside the slot region. Good optical mode confinement in the slot waveguide plays an important role in increasing the coupling efficiency from the slot waveguide to slot PCW; therefore, our work starts with the optimization of this slot waveguide section.

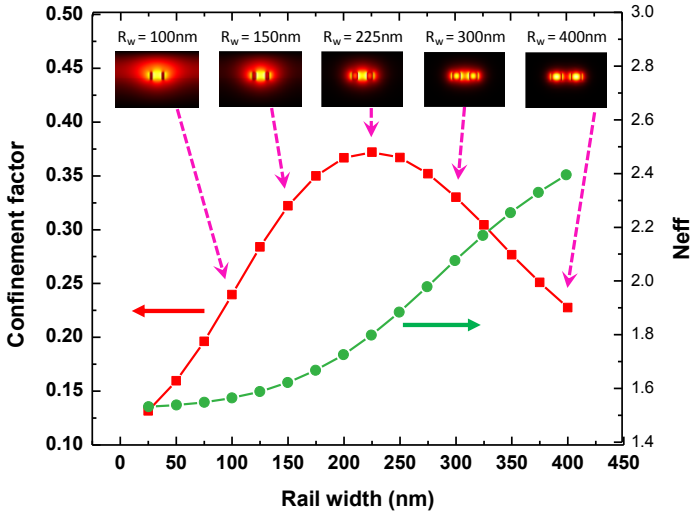

Figure 2.3: Confinement factor within the slot (red curve marked with squares) and n_{eff} (green curve marked with circles) plotted as a function of rail width (R_w), overlaid with the cross-sectional fundamental TE mode profiles for different R_w. The slot width (S_w) is 320nm, and the wavelength is 1550nm.

The S_w is fixed at 320nm [9, 10, 23], and the rail width (R_w), as shown in Figs. 2.1 (a) and (b), of the slot waveguide is optimized for maximum mode confinement. The cross-sectional fundamental TE mode profile and the effective refractive index (n_{eff}) of the slot waveguide at the wavelength of 1550nm are simulated using COMSOL Multiphysics. Correspondingly, the confinement factor, defined as the overlap integral of the optical mode profile with the slot,

whose mathematical expression can be found in Ref [42, 43], is also calculated. Fig. 2.3 shows the calculated confinement factor and n_{eff} plotted as a function of R_w, indicating the largest confinement factor of 38% is achieved at R_w=225nm. In comparison, It can be seen that the conventional design with slot waveguide rails terminating at the center of holes in the slot PCW interface, for example, at R_w=300nm in Fig. 1 (c), has a smaller confinement factor of 33%. In addition, compared to a slot waveguide with narrow S_w=100nm, in which a maximum confinement factor of ~42% can be achieved [42], the wider slot waveguide has a slightly lower confinement factor, but provides other advantages such as better manufacturability, better EO polymer filling, and higher EO polymer poling efficiency, which in turn provides a substantially larger EO coefficient after poling [22].

Utilizing the optimized slot waveguide, we next investigate how the length of the mode converter affects the optical loss. The mode converter consists of two linearly tapered sections, as shown in Fig. 2.1 (b). Section I does not affect the performance of the mode converter significantly because most optical power is still confined in the 450nm-wide strip waveguide [32], so this section is fixed to be 4μm in this work. The length of Section II, L, is critical and is optimized for achieving low enough optical loss. The S_w along section II is constant and fixed to be 320nm. L is tuned from 5μm to 30μm, and the corresponding optical loss is simulated using FIMMWAVE. The results are shown as a blue curve in Fig. 2.4 (c). Next, to verify the simulation, we fabricate mode converter pairs with optimized S_w of 225nm but with L varying from 5μm to 30μm. Test structures with different numbers of mode converters (2, 4 and 8) of varying lengths (L) connected

in series are fabricated using e-beam lithography and reactive ion etching (RIE) on an SOI substrate. The total length of the strip waveguides is kept constant, so that the extracted mode converter loss is not affected by the strip waveguides. Fig. 2.4 (a) shows some SEM images of cascaded pairs of fabricated adiabatic mode converters with L=5μm, 15μm, 20μm, and 30μm, respectively. Then, the fabricated mode converters are covered with EO polymer as claddings using spin coating method [44, 45]. In order to test the devices, TE-polarized light from a tunable laser at 1550nm is coupled into and out of the device utilizing a grating coupler setup [40, 41]. The output optical power is measured using an optical spectrum analyzer (OSA). The measured total insertion loss of the waveguides at 1550nm (including coupling loss on gratings, propagation loss on strip waveguides, and transition loss on mode converters) for different L as a function of the total number of mode converters is plotted in Fig. 2.4 (b). Each measurement data point in the plot is an averaged value from three groups of identical samples. The measured optical loss per mode converter, indicated by the slope of the linear regression lines of the measured data, is extracted and plotted in Fig. 2.4 (c), where error bars indicate variation errors of data in the three groups of measurements. It can be seen that the measured mode converter loss decreases as the mode converter length increases. For L>25μm, the measured mode converter loss is < 0.1dB. It can also be noticed that the variation in the measured losses becomes smaller as the length of the mode converter becomes larger. Therefore, the mode converter length is finally chosen to be 30μm, which is the point of diminishing returns in Fig. 2.4 (c). The measured results match the simulation results

pretty well, as shown in Fig. 2.4 (c). These measured losses are reproducible, and the deviations around the mean value are mainly caused due to fabrication induced errors.

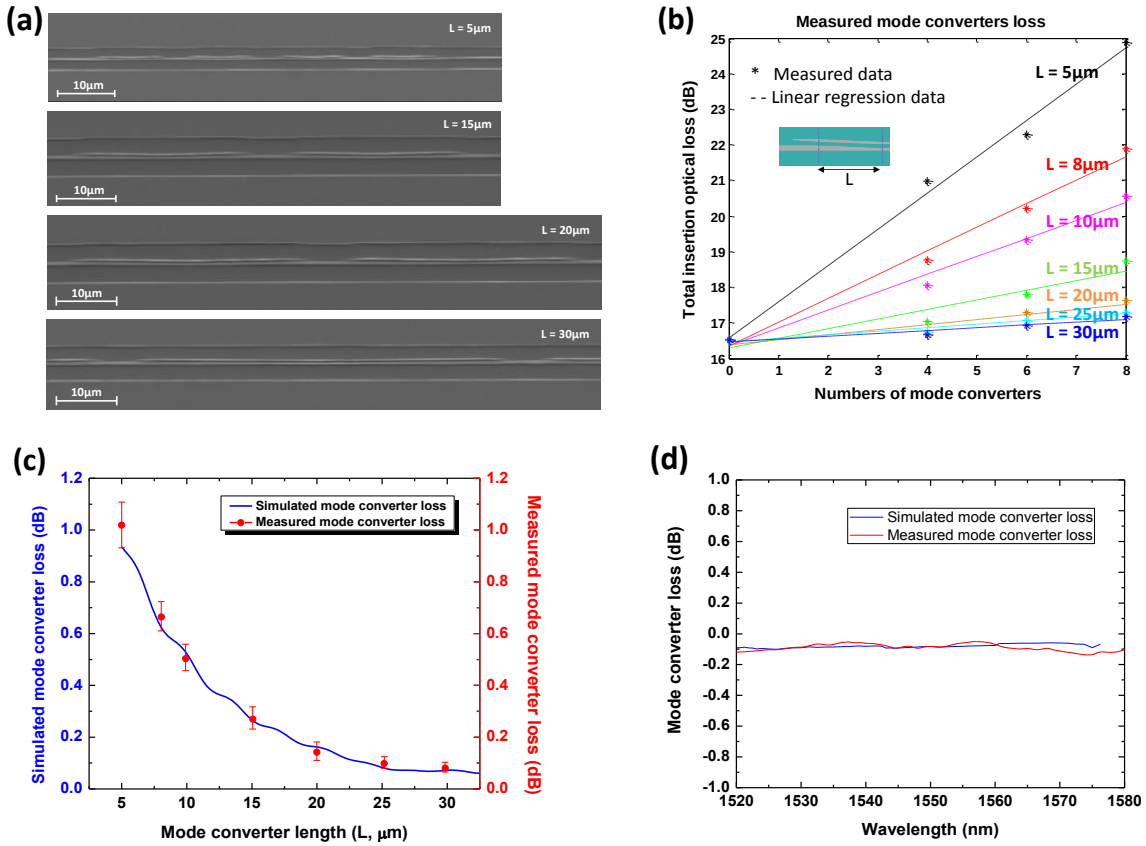

Figure 2.4: (a) SEM images of fabricated test structures consisting of cascaded pairs of mode converters with L=5μm, 15μm, 20μm and 30μm, respectively. (b) Measured insertion loss indicated by dots for three fabricated samples as a function of number of mode converters in the measured arm. The loss is measured at 1550nm. (c) Simulated (blue curve) and measured (red dots) mode converter loss v.s. mode converter length. The error bars indicate the variation range of data in three groups of measurements. (d) Normalized transmission spectrum of one adiabatic mode converter. The simulation results are from FIMMWAVE simulation of a single mode converter, and the testing results are from the measured normalized transmission spectrum of 8 mode converters divided by 8.

Additionally, the optical bandwidth of the mode converter is investigated. The optical loss of a single adiabatic mode converter is simulated by FIMMWAVE over a wavelength range from 1520 to 1580, as shown by the blue curve in Fig. 2.4 (d). The transmission spectrum of 4 pairs of adiabatic mode converters (total number of 8) are measured and normalized. Then the measured loss per mode converter can be obtained by dividing this total loss by 8, as shown by the red curve in Fig. 2.4 (d). It can be seen that the simulation and testing results agree well with each other, indicating that our adiabatic mode converter can provide a wide low-dispersion operation.

2.4 COMPARISON BETWEEN ADIABATIC MODE CONVERTER AND V-SHAPE MODE CONVERTER

Next, we compare the performance of our optimized adiabatic mode converter with the conventional V-shaped mode converter [8, 23, 28, 29]. Both these types of converters have been explored by various groups [8, 23, 28-32]. The single-mode strip waveguide at the input has a width of 450nm, and the slot waveguide has S_w of 320nm and R_w of 225nm. Figs. 2.5 (a) and (b) show the simulated fundamental TE mode profiles (cross-sectional view), n_{eff} transitions, and the propagating mode (top view, normalized real part of E_x calculated by three-dimensional finite-difference time-domain (FDTD) method in RSoft) along the propagation direction for these two types of mode converters, respectively. All the simulations are done at the wavelength of 1550nm. It can be seen that our mode converter results in a smooth transformation of mode profiles and an adiabatic transition of n_{eff} from a strip mode to a slot mode, as shown in Fig. 2.5 (a). In

comparison, the V-shape mode converter has been simulated with a non-zero tip width (~80nm-wide) due to practical lithography limitations. Due to a discontinuity in the mode field distribution at the non-zero tip, an abrupt change of n_{eff} occurs, as shown in Fig. 2.5 (b), resulting in additional optical scattering loss. Note that although an 80nm-wide tip in Section I of our adiabatic mode converter is also included in the simulation, no significant scattering is observed at this non-zero tip based on simulation results. This is because most of the electric field is confined in the 450nm-wide strip waveguide at the cross section where the non-zero tip appears, as shown in Fig. 2.5 (a). In addition, along our strip-to-slot mode converter, a possible second-order slot mode is suppressed due to the asymmetric slot waveguide geometry of the transition region, so the power is more efficiently coupled to the fundamental mode of the slot waveguide [46, 47].

For experimental demonstration, a series of our strip-to-slot mode converters (L=30 μm, S1: R_w=225nm) together with conventional V-shape mode converters (5 μm-long, V1: R_w=225nm, V2: R_w=300nm) are fabricated on the same chip, and the insertion losses at 1550nm of these mode converters are measured and compared. Additionally, another type of mode converter (S2, R_w=225nm) used in Ref [11], with the same length, is also fabricated on the same chip and tested. S2 has a 4 μm-long linearly tapered section I and 10 μm-long section II similar to S1 but both with a narrow slot width of 120nm, and then a 20 μm-long section III with slot width linearly tapered from 120nm to 320nm. SEM images of mode converters S1, S2, V1, and V2 are shown in Figs. 2.6 (a) and (d), respectively. Note that for S2, as shown in Fig. 2.6 (b), the strip waveguide was

converted to a slot waveguide with S_w of 120nm similar to that in Ref [32], and then tapered to slot waveguide with S_w of 320nm and R_w of 225nm. Also note that the only difference between V1 and V2 is that V1 uses an R_w of 225nm (optimized), while V2 uses an R_w of 300nm (un-optimized).

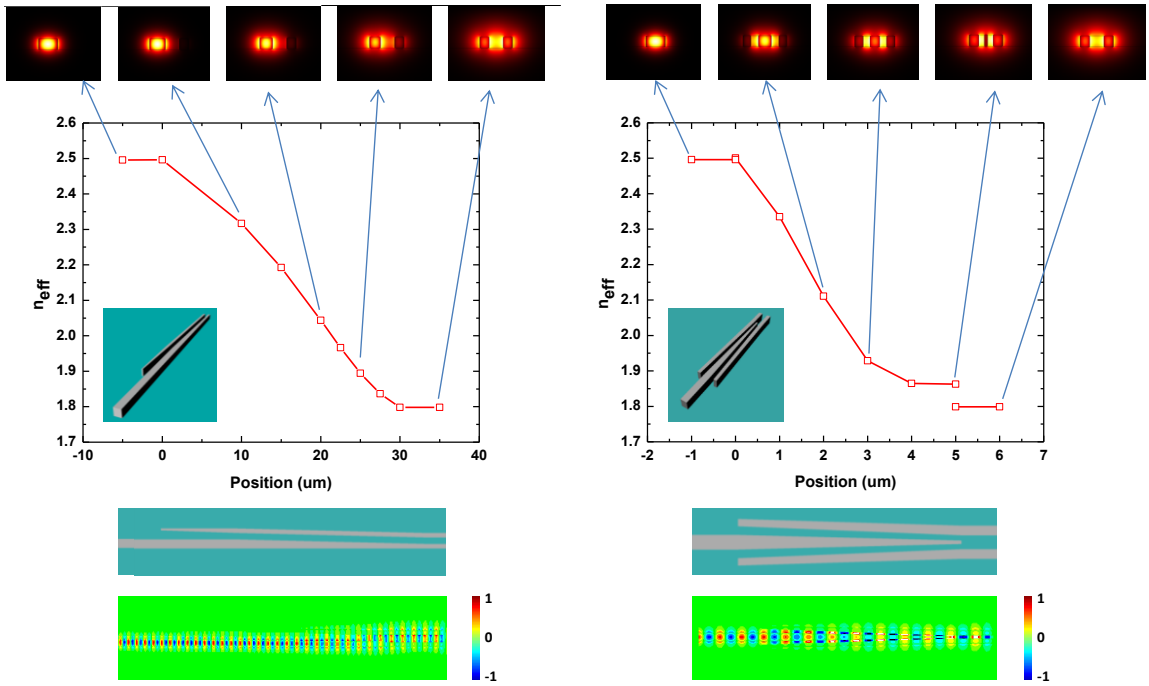

Figure 2.5: The simulated n_{eff} transition along our mode converter (left) and a conventional V-shape mode converter (right), respectively, overlaid with mode profiles transformation (cross-sectional view) and FDTD simulation of mode propagation (top view), at the wavelength of 1550nm. For our adiabatic mode converter, S_w=320nm, R_w=225nm, L=30μm. For V-shape mode converter, S_w=320nm, R_w=225nm, L=5μm.

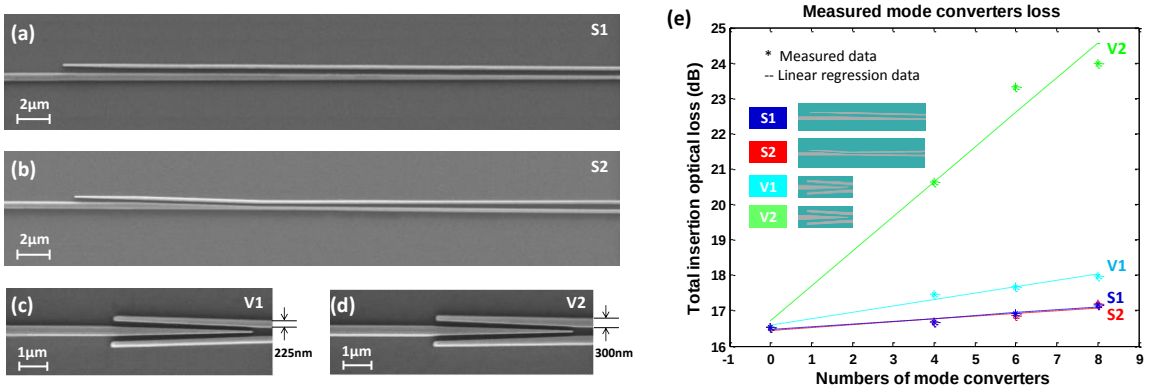

Figure 2.6: (a) our adiabatic mode converter (S1), (b) mode converter (S2) as presented in Ref [11], (c) V-shape mode converter with R_w=225nm (V1), and (d) V-shape mode converter with R_w=300nm (V2). The S_w=320nm for all four mode converters. L=30 μm for S1 and S2, and L=5 μm for V1 and V2. Note: here polymer claddings in (a)-(d) are not shown for better visualization. (e) Comparison of measured loss of our mode converter and conventional V-shape mode converter at 1550nm. S1: loss=0.080dB; S2: loss=0.075dB; V1: loss=0.182 dB; V2: loss=0.981dB.

Fig. 2.6 (e) shows the measured losses for these mode converters. The optical loss per mode converter can be estimated by the slope of the linear regression lines of the measured data. It can be clearly seen that our optimized mode converter (S1) has a loss of 0.080dB, which is at least 0.1dB smaller than those of V-shape mode converters (V1: 0.182dB; V2: 0.981dB). And also, the measured loss of S2 (0.075dB) is quite close to that of S1 (0.080dB) with the same length. Furthermore, from the comparison of the loss of V1 and V2 one can tell that the optimized R_w (225nm) gives smaller loss (0.182dB) than that (0.981dB) of the un-optimized R_w (300nm), and an improvement of about 0.8dB is achieved using the optimized R_w.

Note that the length of V-shape mode converter used here is only 5 μm which is a length commonly used in some works [8, 28, 29], but the loss of the S_w-optimized V-shape mode converter (V2) at 5 μm is not significantly different for loss at 30 μm, since no matter what length of V shape mode converter is used, the sudden discontinuity at the practical tip size still causes a high insertion loss. Therefore, increasing the length of the V shape mode converter does not provide any additional decrease in the insertion loss, as shown by the green curve in Fig. 2.7. The slight increase of loss is due to the increased mismatch at the sudden transition point (non-zero tip); whereas for the adiabatic converter, the longer length provides a greater reduction in the insertion loss. Theoretically, for L > 30 micron, the loss can be even lower as can be seen in Fig. 2.7.

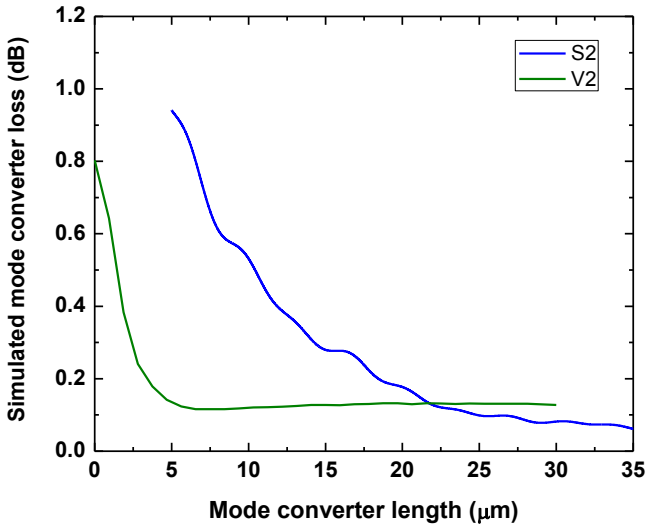

Figure 2.7: Simulated loss of mode converter S2 and V2, as a function of mode converter length at the wavelength of 1550nm.

2.5 COUPLING LIGHT INTO WIDE SLOT PCW USING OPTIMIZED ADIABATIC MODE CONVERTER

Furthermore, we investigate the coupling efficiency into slot PCW at the mode converter/slot-PCW interface. For convenience, researchers previously aligned the outer edge of the rails of the slot waveguide to the center of holes in the first adjacent rows, [1, 22, 23, 29, 33-37] as shown in Fig. 2.1 (c). For example, in Ref [23] the slot PCW has the same structure but an un-optimized R_w of 300nm is used, corresponding to a confinement factor of 33% which can be seen from Fig. 2.3. However, by changing the R_w to 225nm (as in our optimized design) one can achieve the highest optical confinement factor of 38% in the slot, as shown in Fig. 2.3, with similar coupling efficiency to slot PCW.

Finally, in order to demonstrate that our optimized adiabatic mode converter (final slot rail width, R_w=225nm, and Section II length, L=30μm) can enable efficient light coupling between a strip waveguide and a slot PCW, a 300μm-long EO polymer infiltrated slot PCW with S_w=320nm (the same as the one used in Ref [23]) with our mode converter (S1) is fabricated, as shown in Fig. 2.8 (a), and characterized. As a comparison, the same slot PCW with the V-shape mode converter (V1) is also fabricated on the same chip, as shown in Fig. 2.8 (b). PCW tapers [36] are used to connect the fast-light slot waveguide with the slow-light PCW section [group index (n_g) of 20.4], so that the group index is gradually changed from the interface with the slot waveguide to the interface with the high n_g PCW.

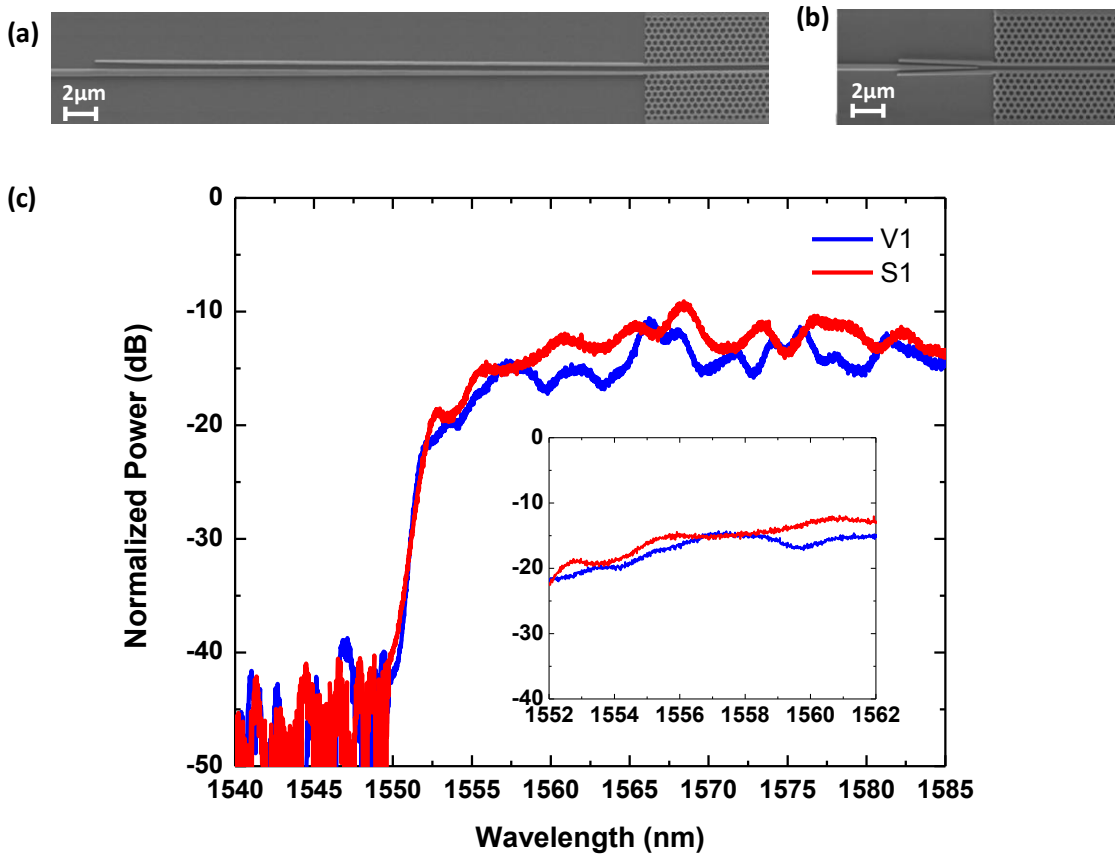

Figure 2.8: (a) An SEM image of our adiabatic mode converter used for a slot PCW. (b) An SEM image of a V-shape mode converter used for a slot PCW. Note: here polymer claddings in (a) and (b) are not shown for better visualization. Only the input ends are shown in (a) and (b), and the output ends are similar but in a reversed direction. (c) Normalized transmission spectrum of the slot PCW using our mode converter (red curve), overlaid with that using V-shape mode converter (blue curve). Inset: magnified portion of the spectrum in the slow-light wavelength region, showing that the total insertion loss in the slow-light wavelength region is lower using our adiabatic mode converter than that using V-shape mode converter.

In order to test the devices, TE polarized light from a broadband amplified spontaneous emission (ASE) source is coupled into and out of the device utilizing grating

coupling setup. The optical transmission spectrum is measured by the OSA and then normalized to that of a reference strip waveguide. As shown in Fig. 2.8 (c), a clear band gap with more than 25dB contrast is observed in the normalized transmission spectrum of the slot PCW with our adiabatic mode converter, indicating that our optimized mode converter enables efficient coupling into the slow-light slot PCW. In comparison, using the V-shape mode converter, the band gap has a ~2dB lower contrast in the normalized transmission spectrum. Note that the Fabry-Perot reflections observed in Fig. 2.8 (c) are due to the PCW structure, instead of the mode converter, because it has been demonstrated in Fig. 2.4 (d) that the mode converter provides a flat spectrum over a wide wavelength range. This statement can also be proved from the observation that this Fabry-Perot reflections appears on both the spectra using our adiabatic mode converter and using V-shape mode converter and that no additional oscillations are introduced comparing the two. The inset of Fig. 2.8 (c) shows a magnified portion of the transmission spectrum in the slow-light wavelength region. The total insertion loss in the slow-light wavelength region is lower using our adiabatic mode converter compared to that using the V-shape mode converter, with a maximum loss difference of up to 3.5dB at 1560nm.

2.6 SUMMARY

In conclusion, we demonstrate a mode converter that achieves highly efficient coupling from a strip waveguide to a 320nm slot waveguide. The rail width (R_w) of the slot waveguide section is optimized to 225nm, yielding an optimized mode converter

length of 30μm. The measured insertion loss of the optimized mode converter is below 0.08dB at 1550nm. The optimized R_w of 225nm provides a loss improvement of about 0.8dB, compared to conventional designs that require R_w to be 300nm. And also, our adiabatic mode converter is demonstrated to provide a wide low-dispersion operation over a wide optical wavelength range. In addition, a comparison between our adiabatic mode converter and a conventional V-shape mode converter is presented, and an improvement of 0.1dB in loss is demonstrated for the adiabatic mode converter. Finally, in addition to coupling light between a strip waveguide and a 320nm-wide slot waveguide, our adiabatic mode converter is also used to couple light into and out of a 320nm-wide EO-polymer refilled slot PCW. We experimentally demonstrate that our mode converter provides up to 3.5dB improvement in coupling efficiency compared to the V-shape mode converter in the slow-light wavelength region of the slot PCW. This adiabatic mode converter has the advantages of low loss, easy manufacturability and large fabrication tolerance. In our future work, the loss of our mode converter can be further improved by replacing linear tapered sections by logarithmic taper profiles [32]. Furthermore, the idea of this work can be generalized and extended to the research on other slot waveguides or slot PCW structures refilled with new high-performance EO active materials, such as binary-chromophore organic glass (BCOG), consisting of shape-engineered spherical dendritic and rod-shaped dipolar chromophores, which has recently been demonstrated with an in-device EO coefficient of 230pm/V [43]. Highly efficient coupling into wide slot waveguides, combined with the improved poling efficiency of the

EO active materials in wide slots, provides tremendous advantages for several promising applications, including photonic integrated circuits [48-51], optical interconnects [52-54], EO modulation [27, 55-62], and electromagnetic field detection [63-66].

2.7 REFERENCES

[1] A. Di Falco, L. O'Faolain, and T. Krauss, "Dispersion control and slow light in slotted photonic crystal waveguides," *Applied Physics Letters,* vol. 92, p. 083501, 2008.

[2] Q. Xu, V. R. Almeida, R. R. Panepucci, and M. Lipson, "Experimental demonstration of guiding and confining light in nanometer-size low-refractive-index material," *Optics letters,* vol. 29, pp. 1626-1628, 2004.

[3] V. R. Almeida, Q. Xu, C. A. Barrios, and M. Lipson, "Guiding and confining light in void nanostructure," *Optics letters,* vol. 29, pp. 1209-1211, 2004.

[4] C. Koos, P. Vorreau, T. Vallaitis, P. Dumon, W. Bogaerts, R. Baets, B. Esembeson, I. Biaggio, T. Michinobu, F. Diederich, W. Freude, and J. Leuthold, "All-optical high-speed signal processing with silicon–organic hybrid slot waveguides," *Nature Photonics,* vol. 3, pp. 216-219, 2009.

[5] Y. A. Vlasov, M. O'Boyle, H. F. Hamann, and S. J. McNab, "Active control of slow light on a chip with photonic crystal waveguides," *Nature,* vol. 438, pp. 65-69, 2005.

[6] Y. Jiang, W. Jiang, L. Gu, X. Chen, and R. T. Chen, "80-micron interaction length silicon photonic crystal waveguide modulator," *Applied Physics Letters,* vol. 87, p. 221105, 2005.

[7] J.-M. Brosi, C. Koos, L. C. Andreani, M. Waldow, J. Leuthold, and W. Freude, "High-speed low-voltage electro-optic modulator with a polymer-infiltrated silicon photonic crystal waveguide," *Optics Express,* vol. 16, pp. 4177-4191, 2008.

[8] J. H. Wülbern, J. Hampe, A. Petrov, M. Eich, J. Luo, A. K.-Y. Jen, A. Di Falco, T. F. Krauss, and J. Bruns, "Electro-optic modulation in slotted resonant photonic crystal heterostructures," *Applied Physics Letters,* vol. 94, p. 241107, 2009.

[9] X. Zhang, A. Hosseini, C.-y. Lin, J. Luo, A. K. Jen, and R. T. Chen, "Demonstration of Effective In-device r33 over 1000 pmV in Electro-optic Polymer Refilled Silicon Slot Photonic Crystal Waveguide Modulator," in *CLEO: Science and Innovations*, 2013, p. CTu2F. 6.

[10] X. Zhang, A. Hosseini, X. Lin, H. Subbaraman, and R. T. Chen, "Polymer-based Hybrid Integrated Photonic Devices for Silicon On-chip Modulation and Board-

level Optical Interconnects," *IEEE Journal of Selected Topics in Quantum Electronics,* vol. 19, pp. 196-210, 2013.

[11] X. Zhang, A. Hosseini, H. Subbaraman, S. Wang, Q. Zhan, J. Luo, A. Jen, and R. Chen, "Integrated Photonic Electromagnetic Field Sensor Based on Broadband Bowtie Antenna Coupled Silicon Organic Hybrid Modulator," *Lightwave Technology, Journal of,* vol. PP, pp. 1-1, 2014.

[12] X. Zhang, A. Hosseini, X. Xu, S. Wang, Q. Zhan, Y. Zou, S. Chakravarty, and R. T. Chen, "Electric field sensor based on electro-optic polymer refilled silicon slot photonic crystal waveguide coupled with bowtie antenna," in *SPIE Photonic West 2013: Terahertz, RF, Millimeter, and Submillimeter-Wave Technology and Applications VI*, 2013, p. 862418.

[13] S. Lin, J. Hu, L. Kimerling, and K. Crozier, "Design of nanoslotted photonic crystal waveguide cavities for single nanoparticle trapping and detection," *Optics letters,* vol. 34, pp. 3451-3453, 2009.

[14] X. Zhang, A. Hosseini, H. Subbaraman, J. Luo, A. K.-Y. Jen, R. L. Nelson, and R. T. Chen, "Ultra-performance Optical Modulator Based on Electro-optic Polymer Infiltrated Silicon Slot Photonic Crystal Waveguide" (Under review)

[15] R. Palmer, A. Luca, D. Korn, P. Schindler, M. Baier, J. Bolten, T. Wahlbrink, M. Waldow, R. Dinu, W. Freude, C. Koos, and J. Leuthold, "Low power mach-zehnder modulator in silicon-organic hybrid technology," *Photonics Technology Letters, IEEE,* vol. 25, 2013.

[16] R. Blum, M. Sprave, J. Sablotny, and M. Eich, "High-electric-field poling of nonlinear optical polymers," *JOSA B,* vol. 15, pp. 318-328, 1998.

[17] X. Zhang, B. Lee, C.-y. Lin, A. X. Wang, A. Hosseini, and R. T. Chen, "Highly Linear Broadband Optical Modulator Based on Electro-Optic Polymer," *Photonics Journal, IEEE,* vol. 4, pp. 2214-2228, 2012.

[18] X. Lin, T. Ling, H. Subbaraman, X. Zhang, K. Byun, L. J. Guo, and R. T. Chen, "Ultraviolet imprinting and aligned ink-jet printing for multilayer patterning of electro-optic polymer modulators," *Optics letters,* vol. 38, pp. 1597-1599, 2013.

[19] C.-Y. Lin, A. X. Wang, X. Zhang, B. S. Lee, and R. T. Chen, "EO-polymer waveguide based high dynamic range EM wave sensors," in *SPIE OPTO*, 2012, pp. 82580Y-82580Y-7.

[20] H. Subbaraman, X. Lin, T. Ling, X. Zhang, L. J. Guo, and R. T. Chen, "Printable EO Polymer Modulators," in *CLEO: Science and Innovations*, 2013, p. CW1O. 2.

[21] S. Huang, T.-D. Kim, J. Luo, S. K. Hau, Z. Shi, X.-H. Zhou, H.-L. Yip, and A. K.-Y. Jen, "Highly efficient electro-optic polymers through improved poling using a thin TiO 2-modified transparent electrode," *Applied Physics Letters,* vol. 96, pp. 243311-243311-3, 2010.

[22] X. Wang, C.-Y. Lin, S. Chakravarty, J. Luo, A. K.-Y. Jen, and R. T. Chen, "Effective in-device r33 of 735 pm/V on electro-optic polymer infiltrated silicon photonic crystal slot waveguides," *Optics letters,* vol. 36, pp. 882-884, 2011.

[23] X. Zhang, A. Hosseini, S. Chakravarty, J. Luo, A. K.-Y. Jen, and R. T. Chen, "Wide optical spectrum range, subvolt, compact modulator based on an electro-optic polymer refilled silicon slot photonic crystal waveguide," *Optics letters,* vol. 38, pp. 4931-4934, 2013.
[24] H. Chen, B. Chen, D. Huang, D. Jin, J. Luo, A.-Y. Jen, and R. Dinu, "Broadband electro-optic polymer modulators with high electro-optic activity and low poling induced optical loss," *Applied Physics Letters,* vol. 93, p. 043507, 2008.
[25] T. Baehr-Jones, B. Penkov, J. Huang, P. Sullivan, J. Davies, J. Takayesu, J. Luo, T.-D. Kim, L. Dalton, and A. Jen, "Nonlinear polymer-clad silicon slot waveguide modulator with a half wave voltage of 0.25 V," *Applied Physics Letters,* vol. 92, p. 163303, 2008.
[26] X. Zhang, A. Hosseini, H. Subbaraman, J. Luo, A. Jen, R. Chen, "Broadband Low-power Optical Modulator Based on Electro-optic Polymer Infiltrated Silicon Slot Photonic Crystal Waveguide," Frontiers in Optics/Laser Science Conference, Optical Society of America, 2014), p. FTu1D.4.
[27] X. Zhang, A. Hosseini, J. Luo, A. Jen, and R. Chen, "Ultralow Power Consumption of 1.5 nW Over Wide Optical Spectrum Range in Silicon Organic Hybrid Modulator," in *CLEO: Science and Innovations*, 2014, p. SM2G. 4.
[28] Z. Wang, N. Zhu, Y. Tang, L. Wosinski, D. Dai, and S. He, "Ultracompact low-loss coupler between strip and slot waveguides," *Optics letters,* vol. 34, pp. 1498-1500, 2009.
[29] C.-Y. Lin, X. Wang, S. Chakravarty, B. S. Lee, W. Lai, J. Luo, A. K.-Y. Jen, and R. T. Chen, "Electro-optic polymer infiltrated silicon photonic crystal slot waveguide modulator with 23 dB slow light enhancement," *Applied Physics Letters,* vol. 97, p. 093304, 2010.
[30] J. Blasco and C. Barrios, "Compact slot-waveguide/channel-waveguide mode-converter," in *Lasers and Electro-Optics Europe, 2005. CLEO/Europe. 2005 Conference on*, 2005, pp. 607-607.
[31] Y. Liu, T. Baehr-Jones, J. Li, A. Pomerene, and M. Hochberg, "Efficient Strip to Strip-Loaded Slot Mode Converter in Silicon-on-Insulator," *Photonics Technology Letters, IEEE,* vol. 23, pp. 1496-1498, 2011.
[32] R. Palmer, A. Luca, D. Korn, W. Heni, P. Schindler, J. Bolten, M. Karl, M. Waldow, T. Wahlbrink, W. Freude, K. C, and L. J, "Low-loss silicon strip-to-slot mode converters," *IEEE Photonics Journal,* 2013.
[33] W.-C. Lai, S. Chakravarty, X. Wang, C. Lin, and R. T. Chen, "On-chip methane sensing by near-IR absorption signatures in a photonic crystal slot waveguide," *Optics letters,* vol. 36, pp. 984-986, 2011.
[34] H. C. Nguyen, Y. Sakai, M. Shinkawa, N. Ishikura, and T. Baba, "10 Gb/s operation of photonic crystal silicon optical modulators," *Optics Express,* vol. 19, pp. 13000-13007, 2011.
[35] C. Caer, X. Le Roux, J. Oden, L. Vivien, N. Dubreuil, and E. Cassan, "Design and fabrication of hollow core slow light slot photonic crystal waveguides for

nonlinear optics," in *Asia Communications and Photonics Conference*, 2013, p. AW4B. 1.

[36] A. Hosseini, X. Xu, D. N. Kwong, H. Subbaraman, W. Jiang, and R. T. Chen, "On the role of evanescent modes and group index tapering in slow light photonic crystal waveguide coupling efficiency," *Applied Physics Letters,* vol. 98, pp. 031107-031107-3, 2011.

[37] A. Hosseini, X. Xu, H. Subbaraman, C.-Y. Lin, S. Rahimi, and R. T. Chen, "Large optical spectral range dispersion engineered silicon-based photonic crystal waveguide modulator," *Opt. Express,* vol. 20, pp. 12318-12325, 2012.

[38] S. Schulz, L. O'Faolain, D. Beggs, T. White, A. Melloni, and T. Krauss, "Dispersion engineered slow light in photonic crystals: a comparison," *Journal of Optics,* vol. 12, p. 104004, 2010.

[39] A. Hosseini, X. Xu, H. Subbaraman, C.-Y. Lin, S. Rahimi, and R. T. Chen, "Large optical spectral range dispersion engineered silicon-based photonic crystal waveguide modulator," *Opt. Express,* vol. 20, pp. 12318-12325, 2012.

[40] H. Subbaraman, X. Xu, J. Covey, and R. T. Chen, "Efficient light coupling into in-plane semiconductor nanomembrane photonic devices utilizing a sub-wavelength grating coupler," *Optics Express,* vol. 20, pp. 20659-20665, 2012.

[41] X. Xu, H. Subbaraman, J. Covey, D. Kwong, A. Hosseini, and R. T. Chen, "Complementary metal–oxide–semiconductor compatible high efficiency subwavelength grating couplers for silicon integrated photonics," *Applied Physics Letters,* vol. 101, pp. 031109-031109-4, 2012.

[42] J. Witzens, T. Baehr-Jones, and M. Hochberg, "Design of transmission line driven slot waveguide Mach-Zehnder interferometers and application to analog optical links," *Optics Express,* vol. 18, pp. 16902-16928, 2010.

[43] R. Palmer, S. Koeber, D. L. Elder, M. Woessner, W. Heni, D. Korn, M. Lauermann, W. Bogaerts, L. Dalton, W. Freude, J. Leuthold, and C. Koos, "High-Speed, Low Drive-Voltage Silicon-Organic Hybrid Modulator Based on a Binary-Chromophore Electro-Optic Material," *Journal of Lightwave Technology,* vol. 32, pp. 2726-2734, 2014.

[44] X. Zhang, A. Hosseini, J. Luo, A. K.-Y. Jen, and R. T. Chen, "Hybrid silicon-electro-optic-polymer integrated high-performance optical modulator," in *SPIE Photonic West, OPTO*, 2014, pp. 89910O-89910O-6.

[45] X. Zhang, A. Hosseini, J. Luo, A. K.-Y. Jen, and R. T. Chen, "Ultraperformance Nanophotonic Modulator Based On Silicon Organic Hybrid Technology," presented at the Optical Interconnects Conference, 2014.

[46] R. Ding, T. Baehr-Jones, W.-J. Kim, B. Boyko, R. Bojko, A. Spott, A. Pomerene, C. Hill, W. Reinhardt, and M. Hochberg, "Low-loss asymmetric strip-loaded slot waveguides in silicon-on-insulator," *Applied Physics Letters,* vol. 98, p. 233303, 2011.

[47] A. Spott, T. Baehr-Jones, R. Ding, Y. Liu, R. Bojko, T. O'Malley, A. Pomerene, C. Hill, W. Reinhardt, and M. Hochberg, "Photolithographically fabricated low-

loss asymmetric silicon slot waveguides," *Optics Express,* vol. 19, pp. 10950-10958, 2011.

[48] F. Kish, "500Gb/s and Beyond PIC-Module Transmitters and Receivers," in *Optical Fiber Communication Conference*, 2014, p. W3I. 1.

[49] D. Dai, J. Bauters, and J. E. Bowers, "Passive technologies for future large-scale photonic integrated circuits on silicon: polarization handling, light non-reciprocity and loss reduction," *Light: Science & Applications,* vol. 1, p. e1, 2012.

[50] Z. Yuan, A. Anopchenko, N. Daldosso, R. Guider, D. Navarro-Urrios, A. Pitanti, R. Spano, and L. Pavesi, "Silicon nanocrystals as an enabling material for silicon photonics," *Proceedings of the IEEE,* vol. 97, pp. 1250-1268, 2009.

[51] B. G. Lee, A. V. Rylyakov, W. M. Green, S. Assefa, C. W. Baks, R. Rimolo-Donadio, D. M. Kuchta, M. H. Khater, T. Barwicz, and C. Reinholm, "Monolithic Silicon Integration of Scaled Photonic Switch Fabrics, CMOS Logic, and Device Driver Circuits," *Journal of Lightwave Technology,* vol. 32, pp. 743-751, 2014.

[52] X. Zheng and A. V. Krishnamoorthy, "Si photonics technology for future optical interconnection," in *SPIE/OSA/IEEE Asia Communications and Photonics*, 2011, pp. 83091V-83091V-11.

[53] A. V. Krishnamoorthy, K. W. Goossen, W. Jan, X. Zheng, R. Ho, G. Li, R. Rozier, F. Liu, D. Patil, and J. Lexau, "Progress in low-power switched optical interconnects," *Selected Topics in Quantum Electronics, IEEE Journal of,* vol. 17, pp. 357-376, 2011.

[54] F. E. Doany, C. L. Schow, C. W. Baks, D. M. Kuchta, P. Pepeljugoski, L. Schares, R. Budd, F. Libsch, R. Dangel, and F. Horst, "160 Gb/s bidirectional polymer-waveguide board-level optical interconnects using CMOS-based transceivers," *Advanced Packaging, IEEE Transactions on,* vol. 32, pp. 345-359, 2009.

[55] C.-H. Chen, C. Li, A. Shafik, M. Fiorentino, P. Chiang, S. Palermo, and R. Beausoleil, "A WDM Silicon Photonic Transmitter Based on Carrier-Injection Microring Modulators," 2014.

[56] R. Ryf, S. Randel, N. K. Fontaine, M. Montoliu, E. Burrows, S. Chandrasekhar, A. H. Gnauck, C. Xie, R.-J. Essiambre, and P. Winzer, "32-bit/s/Hz spectral efficiency WDM transmission over 177-km few-mode fiber," in *Optical Fiber Communication Conference*, 2013, p. PDP5A. 1.

[57] W. M. Green, M. J. Rooks, L. Sekaric, and Y. A. Vlasov, "Ultra-compact, low RF power, 10 Gb/s silicon Mach-Zehnder modulator," *Optics Express,* vol. 15, pp. 17106-17113, 2007.

[58] J. Ding, R. Ji, L. Zhang, and L. Yang, "Electro-optical response analysis of a 40 Gb/s silicon Mach-Zehnder optical modulator," *Journal of Lightwave Technology,* vol. 31, pp. 2434-2440, 2013.

[59] D. M. Gill, J. E. Proesel, C. Xiong, J. Rosenberg, M. Khater, T. Barwicz, S. Assefa, S. M. Shank, C. Reinholm, and E. Kiewra, "Monolithic Travelling-Wave

Mach-Zehnder Transmitter with High-Swing Stacked CMOS Driver," in *CLEO: Science and Innovations*, 2014, p. SM2G. 3.

[60] C. DeRose, "Integrated RF Silicon Photonics from High Power Photodiodes to Linear Modulators," in *Integrated Photonics Research, Silicon and Nanophotonics*, 2014, p. IW2A. 1.

[61] D. Mahgerefteh, "Transmission system comprising a semiconductor laser and a fiber grating discriminator," ed: Google Patents, 2000.

[62] X. Zheng, E. Chang, P. Amberg, I. Shubin, J. Lexau, F. Liu, H. Thacker, S. S. Djordjevic, S. Lin, and Y. Luo, "A high-speed, tunable silicon photonic ring modulator integrated with ultra-efficient active wavelength control," *Optics Express,* vol. 22, pp. 12628-12633, 2014.

[63] C.-Y. Lin, A. X. Wang, B. S. Lee, X. Zhang, and R. T. Chen, "High dynamic range electric field sensor for electromagnetic pulse detection," *Optics Express,* vol. 19, pp. 17372-17377, 2011.

[64] A. B. Matsko, A. A. Savchenkov, V. S. Ilchenko, D. Seidel, and L. Maleki, "On the sensitivity of all-dielectric microwave photonic receivers," *Journal of Lightwave Technology,* vol. 28, pp. 3427-3438, 2010.

[65] R. Chang, V. Lomakin, and E. Michielssen, "Coupling electromagnetics with micromagnetics," in *Antennas and Propagation Society International Symposium (APSURSI), 2012 IEEE*, 2012, pp. 1-2.

[66] X. Zhang, A. Hosseini, H. Subbaraman, S. Wang, Q. Zhan, J. Luo, A. K. Jen, and R. Chen, "Wideband Electromagnetic Wave Sensing Using Electro-optic Polymer Infiltrated Silicon Slot Photonic Crystal Waveguide," in *CLEO: Science and Innovations*, 2014, p. SM2M. 5.

Chapter 3: Low-power low-dispersion silicon-polymer hybrid photonic crystal waveguide modulator *

3.1 INTRODUCTION

Electro-optic (EO) polymer modulators in optical links are promising for low power consumption [1] and broad bandwidth operation [2]. The electro-optic coefficient (r_{33}) of EO polymers can be several times larger than that of lithium niobate. In addition to conventional all-polymer devices [1, 2] , combination of silicon photonics and EO polymer have shown to enable compact and high performance integrated devices [3], such as slot waveguide Mach-Zehnder Interferometer (MZI) modulators [4], slot waveguide ring-resonator modulators [5], and slot Photonic Crystal Waveguide (PCW) modulators [6]. The fabrication process of these devices involves the poling of the EO polymer at an elevated temperature. Unfortunately, the leakage current due to the charge injection through silicon/polymer interface significantly reduces the poling efficiency in narrow slot waveguides (slot width, S_w<200nm). Among the abovementioned structure, the slot PCW can support optical mode for S_w as large as 320nm [7]. Such a wide slot was shown to reduce the leakage current by two orders of magnitude resulting in 5x improvement in the in-device r_{33} compared to a slot PCW with S_w=75nm [7].

---

* Citation: X. Zhang, A. Hosseini, S. Chakravarty, J. Luo, A. K.-Y. Jen, and R. T. Chen, "Wide optical spectrum range, subvolt, compact modulator based on an electro-optic polymer refilled silicon slot photonic crystal waveguide," Optics letters, vol. 38, pp. 4931-4934, 2013.

X. Zhang mainly worked on the simulation, fabrication and characterization, and serves as the first author of the paper. Other coauthors also contributed to the work from simulation discussion, or paper preparation.

One problem remains among slot PCW modulators is their narrow operating optical bandwidth of <1nm [8-10] because of the high group velocity dispersion (GVD) in the slow-light optical spectrum range. To broaden the operating optical bandwidth of PCW modulators, lattice shifted PCWs can be employed, where the spatial shift of certain holes can modify the structure to provide low-dispersion slow light [11-15].

In this chapter, we report a symmetric MZI modulator based on band-engineered slot PCW refilled with EO polymer, SEO125 from Soluxra, LLC. SEO125 exhibits exceptional combination of large EO activity, low optical loss, and good temporal stability. Its r_{33} value of poled thin films is around 125pm/V at the wavelength of 1310 nm, which is measured by the Teng–Man reflection technique. The design and synthesis of SEO125 encompasses recent development of highly efficient nonlinear optical chromophores with a few key molecular and material parameters, including large β values, good near-infrared transparency, excellent chemical- and photo-stability, and improved processability in polymers [16]. Using a band-engineered EO polymer refilled slot PCW with S_w=320nm, we demonstrate a slow-light enhanced effective in-device r_{33} of 1190pm/V over 8nm optical spectrum range. Excluding the slow-light effect, we estimate in-device material' r_{33} of 89pm/V for SEO125 in the slot that show 51% improvement compared to the results (59pm/V) in [7].

3.2 DESIGN OF BAND ENGINEERED EO POLYMER FILLED SLOT PHOTONIC CRYSTAL WAVEGUIDE

A schematic of the device on silicon on insulator (SOI) (Si thickness=250nm, oxide thickness=3μm) is shown in Fig. 3.1 (a). The input and output strip waveguides are connected to the device using a strip-to-slot waveguide mode converter. (Note: a V-shape mode converter used in this chapter, and an adiabatic mode converter described in section 2 will be used in Chapter 4 and 5.) PCW couplers consisting of a fast-light section [17] connect the mode converters to a 300μm-long slow-light PCW section. The slow-light PCW section is band-engineered by lateral shifting of the first three rows on the two sides of the slot [indicated by s_1, s_2, s_3 in Fig. 3.1 (a)] [12] and by varying the center-to-center distance between two rows adjacent to the slot [W in Fig. 3.1 (a)]. Multi-mode interference (MMI) couplers are used for beam splitting/combining [18]. Sub-wavelength grating (SWG) are designed to couple light into and out of the silicon strip [19].

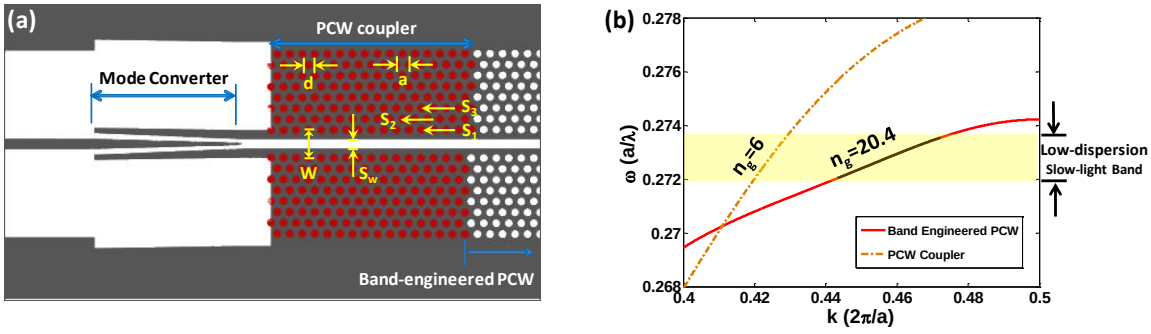

Figure 3.1: (a) Layout of the PCW coupler (mode converter + PCW coupler). The black area corresponds to un-etched silicon. (b) Band diagram of the engineered slow-light PCW and the PCW coupler.

For lattice constant, a=425nm, it is found that with a hole diameter d=300nm, s_1=0, s_2=-85nm, s_3=85nm, S_w=320nm, and W=1.54($\sqrt{3}$)a, we can achieve an average group index ($n_g=c/v_g$) of 20.4 (±10%) over 8.2nm optical bandwidth. The PCW coupler [a=425nm, d=300nm, s_1=0, s_2=0, s_3=0, S_w=320nm, W=1.45($\sqrt{3}$)a] consists of 16 periods and is designed for low n_g=6 over the same wavelength range. The band diagrams of the slow-light and fast-light PCWs are shown in Fig. 3.1 (b).

The required change of effective index of the EO polymer for the optical modulator to achieve a phase shift of π is theoretically calculated as $\Delta n = 1/(2\Gamma)\times(n/L)\times\lambda/n_g = 1/(2\times0.33)\times(1.63/300\,\mu m)\times1550nm/20.4 = 0.000625$. This change of EO polymer index can be realized by applying a half-wave switching voltage of $V_\pi = 2S_w\Delta n/(n^3\gamma_{33}) = 0.853V$, where γ_{33}=100pm/V is the EO coefficient of the polymer. Given the potentially large γ_{33}=125pm/V of EO polymer SEO125 and demonstrated high poling efficiency achievable in wide slots (320nm compared to conventional 100nm) [7], the estimated γ_{33}=100pm/V here is a realistic value. Therefore, from these calculations, the theoretical $V_\pi\times L = 0.853V\times300\,\mu m = 0.256V$ mm. The expected effective in-device γ_{33} is then calculated by (2) to be 1365pm/V, where λ=1560nm, S_w=320nm, n=1.63, L=300μm, Γ=0.33.

In addition, multimode interference (MMI) couplers are used for beam splitting and combining [20], a through-etched subwavelength grating (SWG) with over 50% efficiency are designed to couple light into and out of the silicon strip [19].

3.3 DEVICE FABRICATION

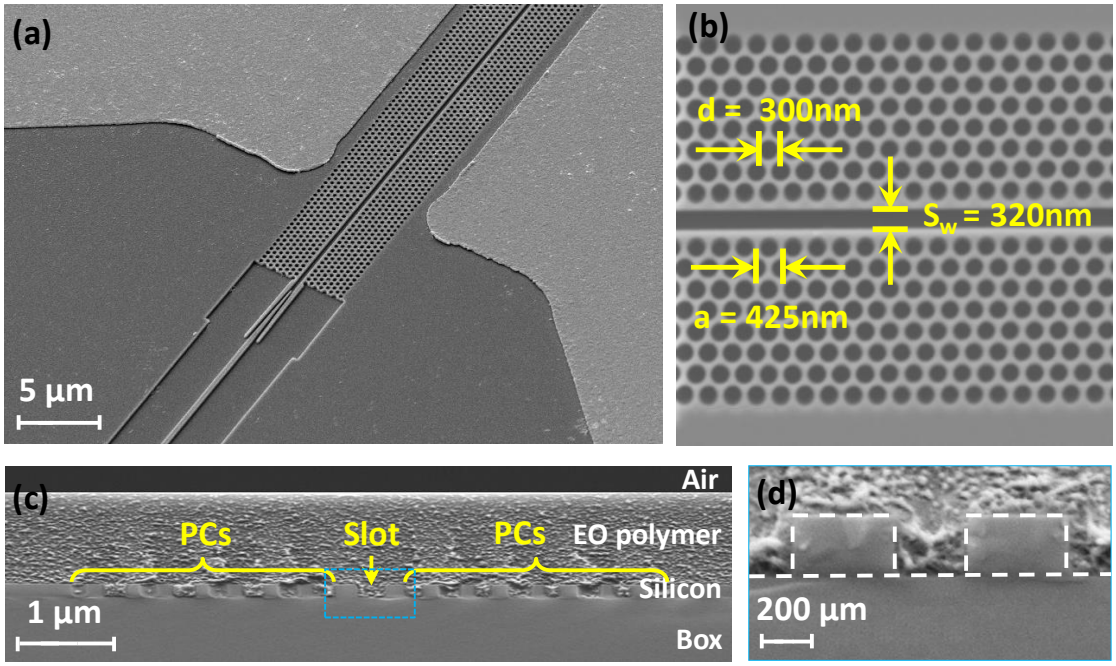

Figure 3.2: SEM images of the fabricated device. (a) Tiled view of a local area of silicon slot PCW modulator. (b) Top view of slot PCW area. (c) Cross-sectional view of the EO polymer refilled silicon slot PCW. PCs: photonic crystals. (d) Zoom-in image of the dashed square area in (c).

The fabrication procedure starts with an SOI wafer with 250nm-thick top silicon. All the photonic circuitries are fabricated using electron-beam lithography and reactive ion etching (RIE) in a single patterning/etching step, while the gold electrodes are patterned by photolithography and lift-off process, as shown in Figs. 3.2 (a) and (b). The EO polymer, SEO125, is infiltrated into the slot PCW by spincoating. The silicon PCW regions including holes and the slot are fully covered by EO polymer, as shown in the

SEM image in Figs. 3.2 (c) and (d). A microscope image of the fabricated MZI is shown in Fig. 3.3 (a).

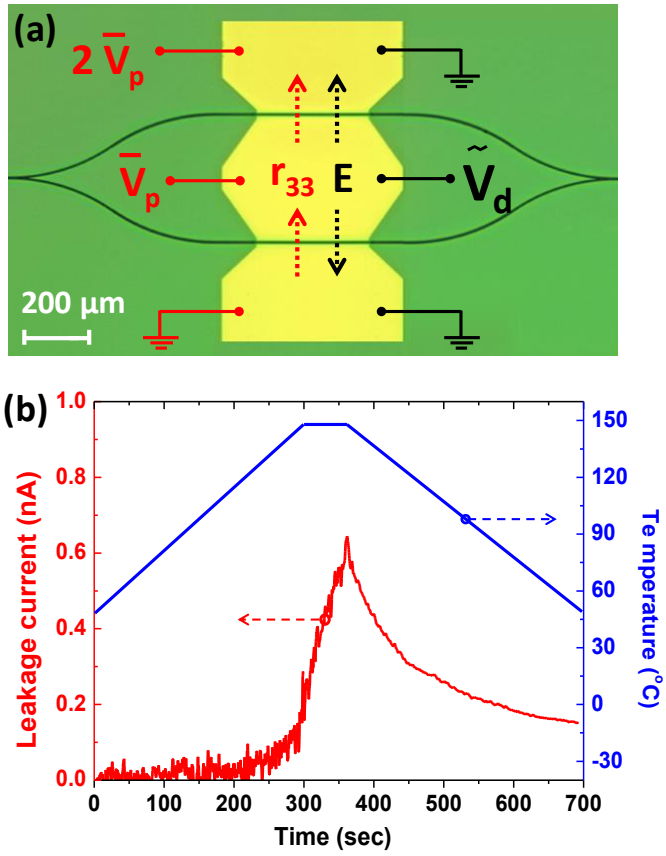

Figure 3.3: (a) Top view of fabricated slot PCW MZI modulator. The red colored circuit connection indicates the push-pull poling configuration and induced r_{33} direction, and the black colored circuit connection indicates the modulation configuration. V_p: poling voltage, V_d: diving voltage. (b) The temperature-dependent leakage current in the EO polymer poling process.

Next, the sample is poled by an electric field of 100V/μm in a push-pull configuration at the glass transition temperature (T_g=145 ℃) of the EO polymer. The

leakage current as well as the hot plate temperature is monitored and shown in Fig. 3.3 (b). It can be seen that the maximum leakage current remains below 0.659nA, corresponding to leakage current density of 8.79A/m^2 [=0.659nA/(300um*250nm)]. For comparison, the typical leakage current density of the EO polymer is 1-10A/m^2 in a thin film configuration. This poling result is repeatable and shows that the 320nm-wide slot dramatically reduces the leakage current that is known to be detrimental to the poling efficiency [21].

3.4 MEASUREMENT OF EFFECTIVE IN-DEVICE ELECTRO-OPTIC COEFFICIENT WITH R_{33} OVER 1000PM/V

For modulation test, TE-polarized light from a tunable laser source (1550nm, 2.5mW) is coupled into and out of the device through grating couplers. The total optical insertion loss is 20dB, including the 6.5dB/facet coupling loss from grating couplers. RF signals are applied to the electrodes as shown in Fig. 3.3 (a). The modulator is biased at the 3dB point and driven by a 100KHz triangular RF wave with a peak-to-peak voltage of 1.4V. The modulated output optical signal is sent to a photodetector and then displayed on a digital oscilloscope. The modulation frequency is within the bandwidth of the photodetector and the oscilloscope. From the output optical waveform measured by the digital oscilloscope, over-modulation is observed [1, 3, 7, 21, 22]. The V_π of the modulator is measured to be 0.973V from the transfer function of the over-modulated optical signal and the input RF signal on the oscilloscope, by finding the difference between the applied voltage at which the optical output is at a maximum and the voltage

at which the optical output is at the following minimum [1, 3, 7, 21, 22]. The effective in-device r_{33} is then calculated to be

$$r_{33-\text{effective}} = \frac{\lambda S_w}{n^3 V_\pi \sigma L} = 1190\text{pm/V} \quad (3.1)$$

where, λ=1.55μm, S_w=320nm, n=1.63, L=300μm, σ=0.33 (confinement factor in the slot) calculated by simulation. This extraordinarily high r_{33} value confirms the combined enhancing effects of slow light and an improved poling efficiency. This band-engineered 320nm slot PCW modulator also achieves very high modulation efficiency with V_π×L=0.973V×300μm=0.292V×mm.

We also estimate the actual in-device r_{33} excluding the slow-light effect using [11]

$$L = \frac{\lambda}{2\sigma n_g}\left(\frac{n}{\Delta n}\right) \quad (3.2)$$

where, $\Delta n = n^3 r_{33} V_\pi / (2S_w)$. The estimated in-device r_{33} is 89pm/V that is significantly larger than our previous work in [7] and is the highest poling efficiency demonstrated in a slot waveguide to the best of our knowledge. Considering the r_{33} dispersion from the two-level model approximation [23], this value also represents nearly 100% poling efficiency that has been obtained in poled thin films of SEO125.

This extraordinarily high γ_{33} value confirms the combined enhancing effects of slow light and an improved poling efficiency. The effective in-device γ_{33} remains over 1000pm/V over 5nm wavelength range. With the designed n_g=20.4, we estimate the in-device γ_{33} to be 74pm/V, significantly more than the 59pm/V in our another work on a non-band-engineered slot PCW [7].

3.5 MEASUREMENT OF SPECTRUM RANGE OF OPERATION

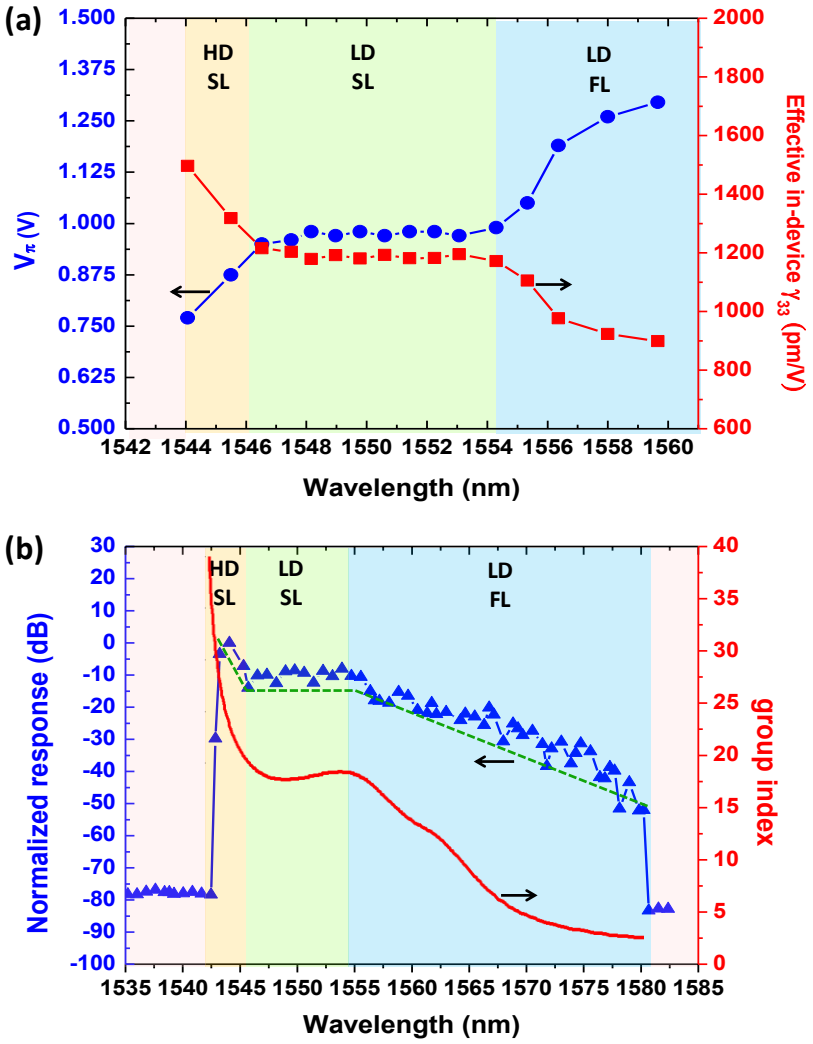

Figure 3.4: (a) Measured V_π and corresponding calculated effective in-device r_{33} v.s. wavelength (at 100KHz). HD SL: high-dispersion slow-light; LD SL: low-dispersion slow-light; LD FL: low-dispersion fast-light. (b) Normalized device response v.s. wavelength (at 100KHz). The green dashed line indicates the trend of the response change over different wavelength. The simulated n_g v.s. wavelength is also overlaid.

To demonstrate the wide optical spectrum range, the optical wavelength is tuned from 1544nm to 1560nm while all other testing conditions are fixed. The V_π measured at different wavelength, as well as the corresponding calculated effective in-device r_{33}, is plotted in Fig. 3.4 (a). It can be seen that the V_π is nearly constant, which is 0.97 ± 0.02V, over optical spectrum range of 8nm (low-dispersion slow-light region: from 1546.5nm to 1554.5nm), corresponding to the effective in-device r_{33} of 1190pm/V and $V_\pi \times L$ of 0.291 ± 0.006V×mm. We note that this $V_\pi \times L$ value is relative to a push-pull configuration. Relative to a single-arm modulator where the effective length of the MZI is the length of both arms together, $V_\pi \times (2L) = 0.582 \pm 0.012$V×mm is still a record low value.

Furthermore, a small signal modulation test is done at $V_{pp}<1$V over a range of wavelength from 1535nm to 1582nm, while all other testing conditions remain the same. The modulated optical signal is converted to electrical signal by a photodetector and then measured by a microwave spectrum analyzer. The wavelength dependence of the normalized modulated optical signal is plotted in Fig. 3.4 (b). It can be seen that the defect-guided mode of slot PCW occurs from 1543nm to 1580nm. The maximum response occurs at the high-dispersion slow-light region (wavelength from 1543nm to 1546.5nm), because of the largest slow-light enhancement (largest n_g) in this region. The response is almost flat in the low-dispersion slow-light region (wavelength from 1546.5nm to 1554.5nm), because the slot PCW is band-engineered to have a nearly constant n_g in this wavelength range. As the optical signal is tuned to longer wavelength (low-dispersion fast-light region: from 1554.5nm to1580nm), the device response

becomes smaller due to decreasing n_g.

3.6 SUMMARY

In summary, we design, fabricate and characterize a band-engineered EO polymer refilled silicon slot PCW MZI modulator. The half-wave switching-voltage is measured to be V_π=0.97±0.02V over optical spectrum range of 8nm, corresponding to the slow-light enhanced effective in-device r_{33} of 1190pm/V and $V_\pi \times L$ of 0.291±0.006V×mm. To the best of our knowledge, this is the best figure of merit that has ever been reported. Table 2.1 shows the comparison of our results with some other group's results in recent years [7, 9, 24-26]. Excluding the slow-light effect, we estimate the EO polymer is poled with a record-high EO activity of 89pm/V in the slot at the wavelength of 1.55μm. In our future work, the optical loss of our modulator can be further reduced, such as by the design of low-loss PCW couplers [27] and improved coupling and packaging method [28]. The photochemical stability, a common issue for polymer based modulators, is expected to be improved by hermetically sealing of EO polymer in a robust packaging [29, 30]. Poled thin films of SEO125 have shown good temporal stability due to its relatively high T_g=145℃, and after the poling its EO coefficients were essentially unchanged under ambient conditions. While SEO125 is a newly developed material and its complete characterization in terms of performance and photo-stability is an ongoing effort, EO polymers with similar compositions have been demonstrated to have potential long-term stability by removing oxygen in the packaging of devices [31].

3.7 REFERENCES

[1] Y. Shi, C. Zhang, H. Zhang, J. H. Bechtel, L. R. Dalton, B. H. Robinson, and W. H. Steier, "Low (sub-1-volt) halfwave voltage polymeric electro-optic modulators achieved by controlling chromophore shape," *Science,* vol. 288, pp. 119-122, 2000.

[2] D. Chen, H. R. Fetterman, A. Chen, W. H. Steier, L. R. Dalton, W. Wang, and Y. Shi, "Demonstration of 110 GHz electro-optic polymer modulators," *Applied Physics Letters,* vol. 70, pp. 3335-3337, 1997.

[3] X. Zhang, A. Hosseini, X. Lin, H. Subbaraman, and R. T. Chen, "Polymer-based Hybrid Integrated Photonic Devices for Silicon On-chip Modulation and Board-level Optical Interconnects," *IEEE Journal of Selected Topics in Quantum Electronics,* vol. 16, pp. 3401115-3401115, 2013.

[4] R. Ding, T. Baehr-Jones, W.-J. Kim, A. Spott, M. Fournier, J.-M. Fedeli, S. Huang, J. Luo, A. K.-Y. Jen, and L. Dalton, "Sub-volt silicon-organic electro-optic modulator with 500 MHz bandwidth," *Journal of Lightwave Technology,* vol. 29, pp. 1112-1117, 2011.

[5] M. Gould, T. Baehr-Jones, R. Ding, S. Huang, J. Luo, A. K.-Y. Jen, J.-M. Fedeli, M. Fournier, and M. Hochberg, "Silicon-polymer hybrid slot waveguide ring-resonator modulator," *Optics Express,* vol. 19, pp. 3952-3961, 2011.

[6] J. H. Wülbern, S. Prorok, J. Hampe, A. Petrov, M. Eich, J. Luo, A. K.-Y. Jen, M. Jenett, and A. Jacob, "40 GHz electro-optic modulation in hybrid silicon–organic slotted photonic crystal waveguides," *Optics letters,* vol. 35, pp. 2753-2755, 2010.

[7] X. Wang, C.-Y. Lin, S. Chakravarty, J. Luo, A. K.-Y. Jen, and R. T. Chen, "Effective in-device r< sub> 33</sub> of 735 pm/V on electro-optic polymer infiltrated silicon photonic crystal slot waveguides," *Optics letters,* vol. 36, pp. 882-884, 2011.

[8] H. C. Nguyen, Y. Sakai, M. Shinkawa, N. Ishikura, and T. Baba, "10 Gb/s operation of photonic crystal silicon optical modulators," *Optics Express,* vol. 19, pp. 13000-13007, 2011.

[9] J. H. Wülbern, J. Hampe, A. Petrov, M. Eich, J. Luo, A. K.-Y. Jen, A. Di Falco, T. F. Krauss, and J. Bruns, "Electro-optic modulation in slotted resonant photonic crystal heterostructures," *Applied Physics Letters,* vol. 94, p. 241107, 2009.

[10] H. C. Nguyen, Y. Sakai, M. Shinkawa, N. Ishikura, and T. Baba, "Photonic crystal silicon optical modulators: carrier-injection and depletion at 10 Gb/s," *Quantum Electronics, IEEE Journal of,* vol. 48, pp. 210-220, 2012.

[11] A. Hosseini, X. Xu, H. Subbaraman, C.-Y. Lin, S. Rahimi, and R. T. Chen, "Large optical spectral range dispersion engineered silicon-based photonic crystal waveguide modulator," *Opt. Express20 (11),* pp. 12318-12325, 2012.

[12] S. Rahimi, A. Hosseini, X. Xu, H. Subbaraman, and R. T. Chen, "Group-index independent coupling to band engineered SOI photonic crystal waveguide with large slow-down factor," *Opt. Express19 (22),* pp. 21832-21841, 2011.

[13] Y. Hamachi, S. Kubo, and T. Baba, "Slow light with low dispersion and nonlinear enhancement in a lattice-shifted photonic crystal waveguide," *Optics letters,* vol. 34, pp. 1072-1074, 2009.

[14] S. Schulz, L. O'Faolain, D. Beggs, T. White, A. Melloni, and T. Krauss, "Dispersion engineered slow light in photonic crystals: a comparison," *Journal of Optics,* vol. 12, p. 104004, 2010.

[15] A. Y. Petrov and M. Eich, "Zero dispersion at small group velocities in photonic crystal waveguides," *Applied Physics Letters,* vol. 85, pp. 4866-4868, 2004.

[16] J. Luo, X.-H. Zhou, and A. K.-Y. Jen, "Rational molecular design and supramolecular assembly of highly efficient organic electro-optic materials," *Journal of Materials Chemistry,* vol. 19, pp. 7410-7424, 2009.

[17] A. Hosseini, X. Xu, D. N. Kwong, H. Subbaraman, W. Jiang, and R. T. Chen, "On the role of evanescent modes and group index tapering in slow light photonic crystal waveguide coupling efficiency," *Applied Physics Letters,* vol. 98, pp. 031107-031107-3, 2011.

[18] A. Hosseini, D. Kwong, C.-Y. Lin, B. S. Lee, and R. T. Chen, "Output Formulation for Symmetrically Excited One-to-< formula formulatype=," *Selected Topics in Quantum Electronics, IEEE Journal of,* vol. 16, pp. 61-69, 2010.

[19] X. Xu, H. Subbaraman, J. Covey, D. Kwong, A. Hosseini, and R. T. Chen, "Complementary metal–oxide–semiconductor compatible high efficiency subwavelength grating couplers for silicon integrated photonics," *Applied Physics Letters,* vol. 101, pp. 031109-031109-4, 2012.

[20] A. Hosseini, D. Kwong, C. Y. Lin, B. S. Lee, and R. T. Chen, "Output Formulation for Symmetrically Excited One-to-< formula formulatype=," *Selected Topics in Quantum Electronics, IEEE Journal of,* vol. 16, pp. 61-69, 2010.

[21] X. Zhang, B. Lee, C.-y. Lin, A. X. Wang, A. Hosseini, and R. T. Chen, "Highly Linear Broadband Optical Modulator Based on Electro-Optic Polymer," *Photonics Journal, IEEE,* vol. 4, pp. 2214-2228, 2012.

[22] C.-Y. Lin, X. Wang, S. Chakravarty, B. S. Lee, W. Lai, J. Luo, A. K.-Y. Jen, and R. T. Chen, "Electro-optic polymer infiltrated silicon photonic crystal slot waveguide modulator with 23 dB slow light enhancement," *Applied Physics Letters,* vol. 97, p. 093304, 2010.

[23] C. Greenlee, A. Guilmo, A. Opadeyi, R. Himmelhuber, R. A. Norwood, M. Fallahi, J. Luo, S. Huang, X.-H. Zhou, and A. K.-Y. Jen, "Mach–Zehnder interferometry method for decoupling electro-optic and piezoelectric effects in poled polymer films," *Applied Physics Letters,* vol. 97, pp. 041109-041109-3, 2010.

[24] T. Baehr-Jones, B. Penkov, J. Huang, P. Sullivan, J. Davies, J. Takayesu, J. Luo, T.-D. Kim, L. Dalton, and A. Jen, "Nonlinear polymer-clad silicon slot waveguide

modulator with a half wave voltage of< equation> 0.25< span style=," *Applied Physics Letters,* vol. 92, pp. 163303-163303-3, 2008.

[25] R. Ding, T. Baehr-Jones, Y. Liu, R. Bojko, J. Witzens, S. Huang, J. Luo, S. Benight, P. Sullivan, and J. Fedeli, "Demonstration of a low V< sub> π</sub> L modulator with GHz bandwidth based on electro-optic polymer-clad silicon slot waveguides," *Optics Express,* vol. 18, pp. 15618-15623, 2010.

[26] C.-Y. Lin, X. Wang, S. Chakravarty, B. S. Lee, W. Lai, J. Luo, A. K.-Y. Jen, and R. T. Chen, "Electro-optic polymer infiltrated silicon photonic crystal slot waveguide modulator with 23 dB slow light enhancement," *Applied Physics Letters,* vol. 97, p. 093304, 2010.

[27] R. Palmer, L. Alloatti, D. Korn, W. Heni, P. C. Schindler, J. Bolten, M. Karl, M. Waldow, T. Wahlbrink, W. Freude, C. Koos, and J. Leuthold, "Low-Loss Silicon Strip-to-Slot Mode Converters," *Ieee Photonics Journal,* vol. 5, Feb 2013.

[28] B. Snyder and P. O'Brien, "Planar fiber packaging method for silicon photonic integrated circuits," in *Optical Fiber Communication Conference and Exposition (OFC/NFOEC), 2012 and the National Fiber Optic Engineers Conference*, 2012, pp. 1-3.

[29] R. Dinu, D. Jin, G. M. Yu, B. Q. Chen, D. Y. Huang, H. Chen, A. Barklund, E. Miller, C. L. Wei, and J. Vemagiri, "Environmental Stress Testing of Electro-Optic Polymer Modulators," *Journal of Lightwave Technology,* vol. 27, pp. 1527-1532, Jun 1 2009.

[30] D. Jin, H. Chen, A. Barklund, J. Mallari, G. Yu, E. Miller, and R. Dinu, "EO polymer modulators reliability study," in *Proceeding of SPIE*, 2010, pp. 75990H-1-75990H-8.

[31] S. Takahashi, B. Bhola, A. Yick, W. H. Steier, J. Luo, A. K.-Y. Jen, D. Jin, and R. Dinu, "Photo-Stability Measurement of Electro-Optic Polymer Waveguides With High Intensity at 1550-nm Wavelength," *Journal of Lightwave Technology,* vol. 27, pp. 1045-1050, 2009.

Chapter 4: High-speed energy-efficient silicon-organic hybrid photonic crystal waveguide modulator [*]

4.1 INTRODUCTION

The combination of silicon photonics and electro-optic (EO) polymers has enabled compact and high-performance hybrid integrated microwave photonic devices [1-3], such as electro-optic modulators [4, 5], optical interconnects [6, 7], and photonic electric-field sensors [8]. The large EO coefficient (r_{33}), ultrafast response time (~1fs), very low dispersion, and spin-coating feature of EO polymers promise low-power consumption, ultra-high speed operation, and ease of fabrication [9-12] . Silicon photonics offers the potential of complementary metal–oxide–semiconductor (CMOS) compatible photonic integrated circuits [13, 14]. Silicon photonic crystal waveguides (PCWs) [15, 16] exhibit slow-light effects, which can be used for device miniaturization [17, 18]. Especially, EO polymer filled silicon slotted PCWs [19] further reduce the device size and enhance the device performance by combining the best of these two platforms.

Our group previously demonstrated an EO polymer filled slot PCW modulator with a slow-light-enhanced effective in-device r_{33} of 735pm/V [20], but the device is

[*] Citation: X. Zhang, C. Chung, A. Hosseini, H. Subbaraman, J. Luo, A. Jen, R. L. Nelson, C. Lee, and Ray T. Chen "High performance Optical Modulator Based on Electro-optic Polymer Infiltrated Silicon Slot Photonic Crystal Waveguide," Journal of Lightwave Technology, 2015. (To Appear)

X. Zhang mainly worked on the simulation, fabrication and characterization, and serves as the first author of the paper. Other coauthors also contributed to the work from modeling, material processing, discussion, or paper preparation.

dispersive over optical wavelength which limits its operational spectrum range. To address this problem, a band-engineered slot PCW modulator was designed using lattice-shifted PCWs, and an effective in-device r_{33} of 1190pm/V over optical spectrum of 8nm was achieved [21]. Since both of these two device were demonstrated at kHz or MHz frequency range, the modulation speed of this type of devices still needs to be improved. A modulator working at GHz frequency regime, while consuming low energy and having large spectrum range, is highly desired for many applications ranging from digital data communications to analog photonic links and networks.

In this chapter, we report the design, fabrication, and characterization results of a high-performance EO polymer filled slot PCW modulator with high-speed, high modulation efficiency, low power consumption, and low optical dispersion. The main motivation of this work is to achieve a high-speed operation of the same device in [21], by doping the silicon PCWs in two levels and thus reducing the RC time constant. With 2-level silicon doping and assisted by a backside gate voltage, the modulation response up to 50GHz is observed, with a 3-dB bandwidth of 15GHz. A small voltage-length product of $V_\pi \times L = 0.282 V \times mm$ is achieved, corresponding to an unprecedented record-high effective in-device EO coefficient (r_{33}) of 1230pm/V at 100KHz. Discounting the slow-light effects, the in-device r_{33} is about 98pm/V. Lattice-shifted PCWs are utilized to engineer the photonic band diagram and thus enable an 8nm-wide low-dispersion spectrum range, which is over an order of magnitude wider than that in modulators based on non-band-engineered PCWs and ring-resonators. This paper is organized as follows.

The design of a band-engineered PCW modulator and the principle of high-speed modulation will be first presented. Then the process of device fabrication will be described. Next, the characterization results of our modulator will be reported, including $V_\pi \times L$, RF bandwidth, power consumption, and optical bandwidth. Finally, a discussion and a summary are presented.

4.2 DESIGN OF HIGH-SPEED MODULATION ELECTRODE

Our optical modulator is a symmetric Mach-Zehnder Interferometer (MZI), with slot photonic crystal waveguides (PCWs) incorporated in both the arms, as shown in Fig. 4.1 (a). We start with a silicon-on-insulator (SOI) substrate with 250nm-thick top silicon and 3μm-thick buried oxide (BOX) layers. The slot and holes of the PCWs are filled with an EO polymer (SEO125 from Soluxra, LLC), which has a refractive index, n=1.63 at 1550nm, and an extraordinary combination of large EO coefficient (r_{33} of ~100pm/V at 1550nm), low optical loss, synthetic scalability, as well as good photochemical stability. Its relatively high glass transition temperature of 150℃ provides good temporal stability, and the EO coefficient of poled SEO125 is essentially unchanged under ambient conditions. The refractive index of the EO polymer can be changed by applying an electric field via the Pockels effect, and is given as $\Delta n = -\frac{1}{2} r_{33} n^3 V / S_w$, where Δn is the change in refractive index of the EO polymer, V is the applied voltage, S_w is the slot width. The slot PCW has a hexagonal lattice of air holes with the lattice constant a=425nm, hole diameter d=300nm, slot width S_w=320nm, and center-to-center distance

between two rows adjacent to the slot W=1.54($\sqrt{3}$)a. The optimum slot width of 320nm supports a confined optical mode, and also tremendously increases the EO polymer poling efficiency by suppressing the leakage current through the silicon/polymer interface during the poling process [22]. We also note that the poling-induced optical loss is reduced by this reduction of leakage current [23]. More importantly, different from typical slot widths of 100~120nm in conventional slot waveguides [19, 24], widening the slot width to 320nm reduces the slot capacitance, enabling the potential of higher RF bandwidth and lower power consumption, and relaxes the fabrication complexities. To address the issue of the narrow operational optical bandwidth of typical PCW modulators (less than 1nm at the group index, n_g>10) [4, 25], lattices of the second and third rows of the PCW are shifted parallel to the slot with relative values of S_2 = -85nm, S_3 = 85nm [indicated by the arrows in Fig. 4.1 (b)]. As a result, a flat group index (n_g) of 20.4 (variations < ±10%) over a wavelength range from 1546nm to 1554nm is achieved, as shown in Fig. 4.1 (c), enabling an optical spectrum range as wide as 8nm for low-dispersion operation. In order to efficiently couple light from a strip waveguide into and out of the slot PCW, an adiabatic strip-to-slot mode converter is designed [26-28]. To make a smooth transition between the group indices from a slot waveguide (n_g~3) to a slot PCW (n_g~20.4), a group index taper consisting of 8 periods of non-lattice-shifted PCW is developed, in which W increases parabolically from W=1.45($\sqrt{3}$)a to W=1.54($\sqrt{3}$)a [29]. Sub-wavelength gratings (SWGs) are used to couple light into and out of the silicon strips [30]. Multi-mode interference (MMI) couplers are used for beam

splitting/combining. The PCW interaction length is chosen to be 300 μm for V_π<1V based on theoretical calculation using $L = \frac{1}{2\sigma} \cdot \frac{n}{\Delta n} \cdot \frac{\lambda}{n_g}$ [31], where σ=0.33 is the confinement factor in the slot [32] calculated by the simulation, λ=1550nm is wavelength, and n_g=20.4.

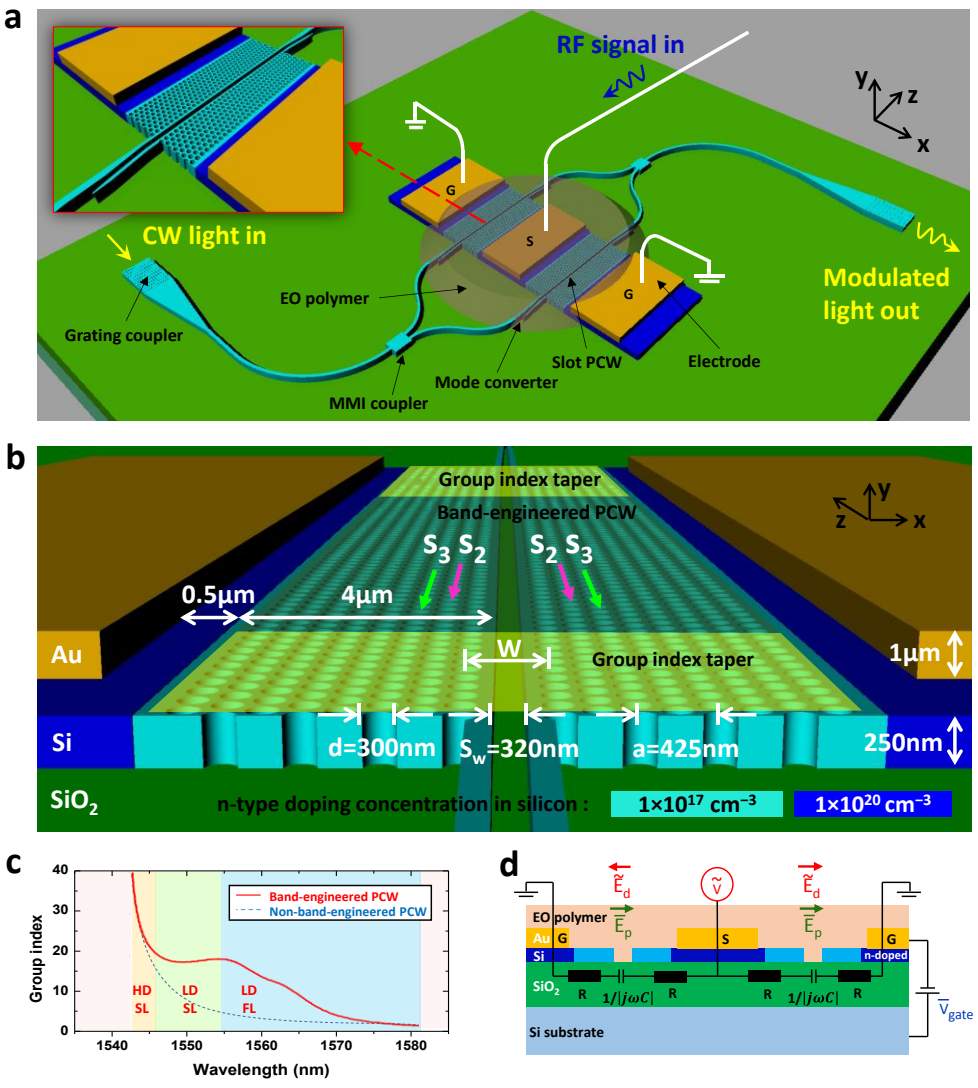

Figure 4.1: continued next page.

Figure 4.1: An EO polymer filled silicon slot PCW MZI modulator designed on an SOI substrate. (a) Three-dimensional schematic of the modulator. The inset shows the magnified image of the silicon slot PCW on one arm of the MZI. PCW: photonic crystal waveguide; MMI: Multi-mode interference; G: ground electrode; S: signal electrode. (b) A tilted view of the slot PCW on one arm of the MZI, showing the cross-sectional device dimension, 2-level doping concentrations, group index taper region, and band-engineered PCW region. Note: the EO polymer is not shown here for better visualization. (c) Simulation result of engineered group index in the slot PCW (red curve) as a function of wavelength, showing 8nm low-dispersion slow-light wavelength region (flat band nature of low-dispersion region highlighted in green). Also overlaid is a blue dashed curve representing the dispersive group index versus wavelength for non-band-engineered PCW for comparison. HD SL: high-dispersion slow-light; LD SL: low-dispersion slow-light; LD FL: low-dispersion fast-light. (d) Equivalent electrical circuit of the MZI modulator in a push-pull configuration, with a constant gate voltage applied on the bottom silicon substrate. E_d: driving field, E_p: poling field, V_{gate}: gate voltage.

Due to the short interaction length (300 μm), the maximum modulation frequency of our modulator is not limited by the group velocity mismatch between RF and optical waves, which is usually the case in conventional modulation devices, necessitating the use of complex traveling wave electrode geometries. Instead, it is mainly limited by the time needed to charge the capacitor formed by the slot through the finite ohmic resistance across the silicon; therefore, our modulator can be driven by lumped electrodes and the RC time delay is the key factor to be engineered for high-speed modulation [3, 5, 33]. The silicon PCW is selectively implanted by n-type dopant (Phosphorus ion, 31P+) with ion concentrations of $1\times10^{20}cm^{-3}$ and $1\times10^{17}cm^{-3}$ [8], as shown in Figs. 4.1 (a) and (b), so that the resistivity of silicon region is reduced to $9\times10^{-6}\Omega\cdot m$ and $9\times10^{-4}\Omega\cdot m$, respectively [34]. The purpose of using relatively lower concentration ($1\times10^{17}cm^{-3}$) in the waveguide region

is to avoid significant impurity-induced optical scattering loss [35, 36]. For reference, the intrinsic doping concentration of the undoped top silicon on our SOI wafer is $1\times10^{14}cm^{-3}$. Based on our previous work [20], in the case of 320nm-wide slots, we use the EO polymer resistivity (ρ_{EO}) value of about $10^{8}\Omega\cdot m$ and RF dielectric constant ($\varepsilon_{RF,EO}$) value of 3.2. The change in the RF dielectric constant of silicon ($\varepsilon_{RF,Si}$) due to the doping is also taken into account [37]. The separation between the gold electrodes is 9.32 μm. Figure 4.1 (d) shows a simplified equivalent circuit of the modulator driven in a push-pull configuration, in which the slot can be represented by a capacitor C and the silicon PCW region by a resistor R. Effective Medium Approximations [8, 38, 39] are used for the calculation of the effective resistance (R) and the effective RF dielectric constant in the region of EO polymer refilled silicon PCW. As the modulation frequency increases, the percentage of electric potential dropped across the slot will decrease due to the reduced slot impedance ($1/|j\omega C|$). The low resistivity of doped silicon can help increase the electric field inside the slot at high frequencies. Simulations by COMSOL Multiphysics show that over 90% of the electric potential is dropped across the slot at 10GHz. Both the optical field and the modulation RF field are concentrated in the 320nm-wide slot, enabling a large field interaction factor, and thus providing efficient modulation at high modulation frequency. Based on simulations performed using Lumerical Device software, the total effective resistance of the 300μm-long silicon PCW is 189 Ohms, and the slot capacitance is as small as 39fF. Thus, the theoretical 3-dB modulation bandwidth of the MZI modulator is estimated to be $1/(2\pi RC)$=22GHz.

It was recently demonstrated that the RF bandwidth of modulators can be further improved by applying a constant gate voltage (V_{gate}) between the bottom silicon substrate and top silicon layer [40, 41] to make the top silicon layer sufficiently conductive. This technique avoids the need for heavy doping, so impurity-scattering optical loss can be minimized [42]. This method was used for conventional silicon slot waveguides to achieve modulation up to 42.7GHz [40] and low energy consumption of 320fJ/bit [41]. Here we adopt a similar technique on our silicon PCW modulator, as shown in Fig. 4.1 (d). By applying a positive voltage on the backside silicon substrate (weakly doped, resistivity of ~15Ω·cm) across the 3μm-thick BOX layer of our device, the energy bands in the n-type top silicon are bent, and thus more electrons accumulate at the interface between the silicon PCW and the BOX layer. Since the resistivity of the silicon region is inversely proportional to the density and mobility of majority free carriers, the resistivity of the silicon PCW region can be reduced, leading to an enhanced RF bandwidth and a reduced power consumption of the modulator.

4.3 DEVICE FABRICATION

The fabrication procedure starts with an SOI wafer. The silicon slot PCW is patterned by electron-beam lithography and reactive ion etching (RIE). Then, the silicon slot PCW is first implanted with 31P+ at energy of 92keV and dose of $1.05\times10^{12}/cm^2$ to reach an ion concentration of $1\times10^{17}cm^{-3}$. Next, the device is patterned by photolithography and selectively implanted with 31P+ at energy of 92keV and dose of $1.05\times10^{15}/cm^2$ to reach an ion concentration of $1\times10^{20}cm^{-3}$ in the region which will

connect the gold electrodes in order to form ohmic contacts. A rapid thermal annealing at 1000ºC for 10min in a flowing nitrogen environment is followed to annihilate the induced defects and activate the implanted ions, which also improves the optical performance of the ion-implanted waveguides. Next, 1μm-thick gold electrodes with 5nm-thick chromium adhesion layers are patterned using photolithography, electron-beam evaporation, and lift-off. Figures 4.2 (a) and (b) show the SEM images of the fabricated device in a tilted view. Figure 4.2 (c) shows a top view of the fabricated slot PCW, with arrows indicating the shifted lattices. Next, the EO polymer is formulated, and then covered over the PCW and dispersed into the holes and slot by spin coating. Figure 4.2 (d) shows the cross section after EO polymer filling.

Finally, to activate the EO effect, a poling process is performed [43-45]. The device is heated up on a hot plate to the EO polymer glass transition temperature of 150℃ in a nitrogen atmosphere, and a constant poling electric field of 110V/μm is applied across the EO polymer inside the slot in a push-pull configuration, as shown in Fig. 4.1 (d). The randomly oriented chromophore dipoles inside the polymer matrix are then free to rotate and align in the direction of poling electric field. Next the temperature is quickly decreased to room temperature while the constant electric field is still applied, and eventually the chromophores are locked in a uniform direction to form a noncentrosymmetric structure. During this poling process, the leakage current is monitored and it remains below 0.53nA, corresponding to a low leakage current density of 5.5A/m^2. This is comparable to the typical leakage current density of 1-10A/m^2

measured in a thin film configuration, indicating a high poling efficiency [21].

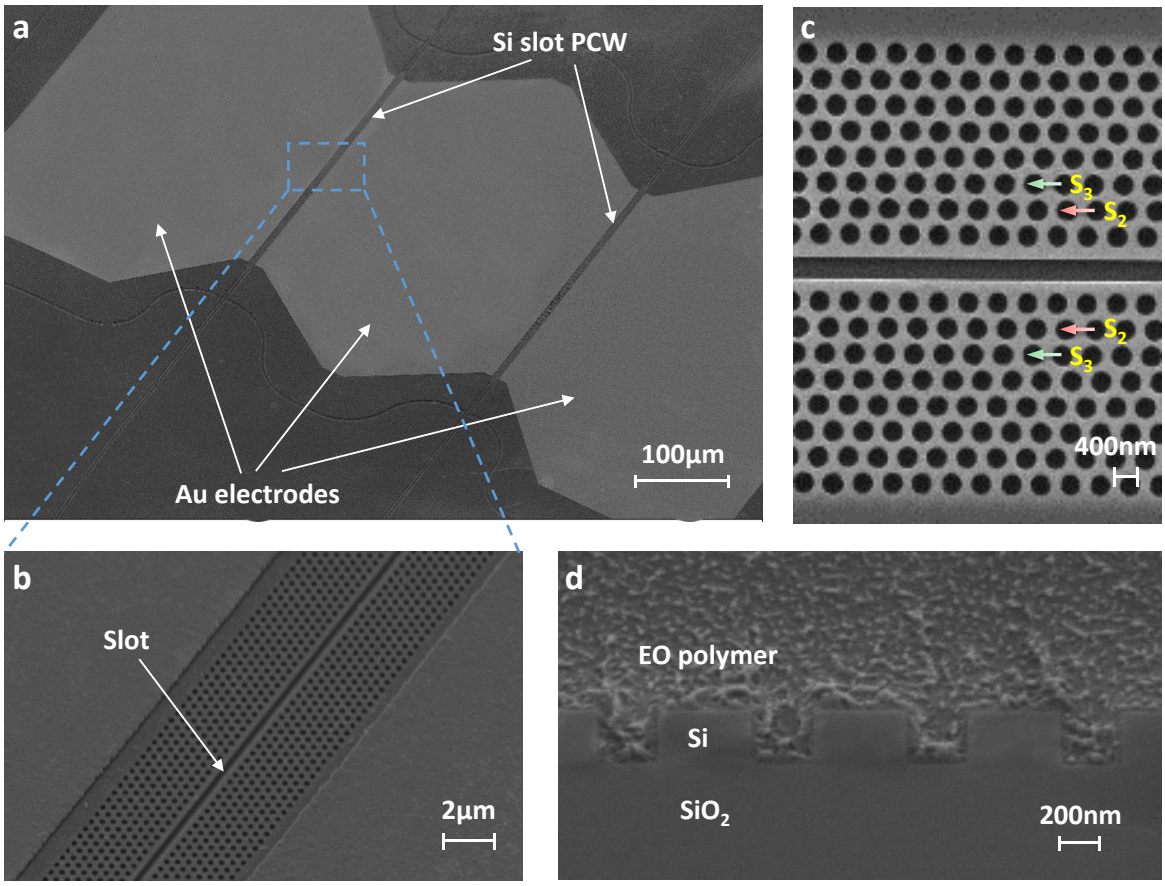

Figure 4.2: SEM images of the fabricated device. (a) A tilted view of the symmetric MZI modulator with silicon slot PCWs in both arms. (b) A magnified image of the silicon slot PCW in one arm inside the gap of electrodes. (c) A top view of the slot PCW, with arrows indicating the shifted lattices on the second and third rows. S_2=-85nm, and S_3=85nm. (d) A cross-sectional view of the photonic crystal structure filled with EO polymer.

4.4 MEASUREMENT OF HIGH MODULATION EFFICIENCY

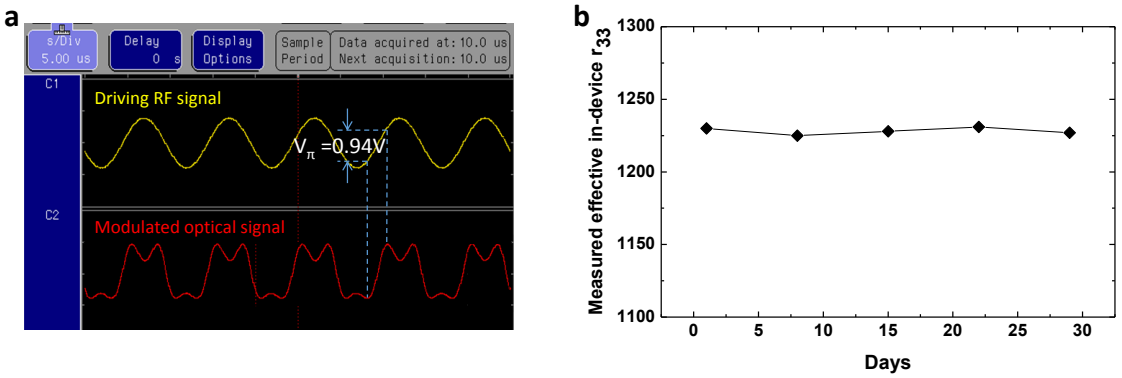

Figure 4.3: Device characterization at low frequency. (a) Transfer function at 100kHz. The V_π is measured to be 0.94V from over-modulation. (b) Measured effective in-device r_{33} as a function of time in days, indicating the long-term stability of the modulator.

A low-frequency modulation test is first performed on the device to measure the voltage-length product, $V_\pi \times L$, which is a figure of merit (FOM) for optical modulators. TE-polarized light from a tunable laser source (1550nm) is coupled into and out of the device utilizing an in-house built grating coupler setup [30]. An RF signal from a function generator is applied onto the electrodes in a push-pull configuration, as shown in Fig. 4.1 (d). The modulator is biased at the 3dB point and driven by a sinusoidal RF wave with a peak-to-peak voltage of V_d=1.5V at 100KHz. The modulated output optical signal is detected using an amplified avalanche photodetector and a digital oscilloscope setup. As shown in Fig. 4.3 (a), over-modulation is observed on the output optical waveform, and the V_π of the modulator is measured to be 0.94V. Thus, the FOM of the modulator achieved is $V_\pi \times L$=0.94V×300μm=0.282V×mm. The effective in-device r_{33} is then calculated to be [8]

$$r_{33,eff} = \frac{\lambda S_w}{n^3 V_\pi \sigma L} = 1230 \text{ pm/V} \quad (4.1)$$

where λ=1550nm, S_w=320nm, n=1.63, L=300μm, and σ=0.33, which is the highest ever in-device r_{33} ever recorded. Such a high r_{33} value originates from the combined effects of a large bulk r_{33} of the EO polymer material, an improved poling efficiency achieved via widening the slot width (320nm), the slow-light enhancement in the silicon PCW, as well as the increased percentage of voltage drop across the slot due to silicon doping. Discounting the slow-light effect, the actual in-device r_{33} is estimated to be as high as 98pm/V [46-48]. In addition, to verify the long-term stability of the device, the same test is repeated in the same conditions over the duration of a month, and the measured effective in-device r_{33} as a function of time in days is shown in Fig. 4.3 (b). It can be seen that no severe degradation of device performance is observed after a month, due to the improved stability of the EO polymer material. Table 4.1 shows the comparison of our results with some other groups' in recent years, from which it can be seen that our group has reported the smallest $V_\pi \times L$ value and the largest effective in-device r_{33} value among silicon-polymer hybrid EO modulators.

Table 4.1 Silicon-polymer hybrid EO modulators reported in recent years

Year	Device Picture	Slot Width	Device Performance	E-O Polymers	Research Group	Publication
2008	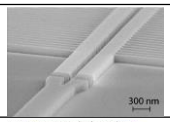	120 nm	$V_\pi L$ = 5 V mm, at 1kHz r_{33} = 30 pm/V at 1550 nm,	YLD124/APC (25wt%)	UW Caltech	T. Jones, et al, Applied Physics Letters
2009	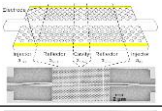	150 nm	r_{33} = 9 pm/V at 1550 nm	AJ-CKL1-25wt%	Technische Universität Berlin	J.H. Wulbern, et al, Applied Physics Letters
2010	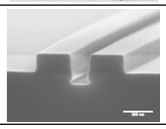	200 nm	$V_\pi L$ = 8 V mm r_{33} = 40 pm/V at 1550 nm	AJSP100 (15wt%), thin film r_{33} of 65 pm/V	UW	R. Ding, et al, Optics Express
2010	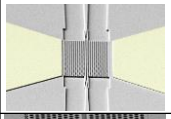	75nm	$V_\pi L$ = 0.56V mm Effective γ_{33} = 132 pm/V	AJ-CKL1-25wt%	UT-Austin OO UW	C.-Y. Lin, et al, Applied Physics Letters
2011	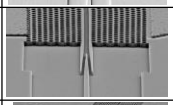	320nm	$V_\pi L$ = 0.44 V mm, at 100kHz Effective γ_{33} = 735 pm/V	AJ-CKL1-25wt%	UT-Austin OO UW	C.-Y. Lin, et al, Optics Letters
2013	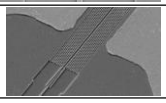	320nm	$V_\pi L$ = 0.291 V mm, at 100kHz Effective γ_{33} = 1190 pm/V	Soluxra's SEO125 25wt%	UT-Austin OO UW	X. Zhang, et al, Optics Letters
2014	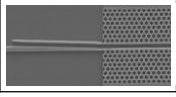	320nm	$V_\pi L$ = 0.282 V mm, at 100kHz Effective γ_{33} = 1230 pm/V	Soluxra's SEO125 25wt%	UT-Austin OO UW	X. Zhang, et al, (Under Review)

4.5 MEASUREMENT OF BROAD RF BANDWIDTH

The RF bandwidth is measured in a small signal modulation test. RF driving signal is provided by a vector network analyzer (VNA) and applied onto the electrodes of the modulator via a ground-signal-ground (GSG) picoprobe. The modulated optical signal is amplified by an erbium doped fiber amplifier (EDFA) and received by a high-speed photodetector, and then the received power is measured using a microwave spectrum analyzer (MSA). The measurement system is calibrated using short-open-load technique. The measured EO response of the device as a function of modulation

frequency is normalized to the response of the photodetector and shown in Fig. 4.4 (a), from which a 3-dB modulation bandwidth of 11GHz is measured. Note that the upper frequency of this measurement is limited by the upper limit of our MSA, which is 26GHz.

Next, in order to overcome this measurement limit and demonstrate the modulation response at frequencies over 26GHz, we perform another measurement using a sideband detection technique [49-52]. The optical output of the modulator is directly connected to the optical spectrum analyzer (OSA), and the transmission spectrum of the modulator is measured. When the modulator is driven by a high frequency RF signal, two sidebands appear in the transmission spectrum, equally spaced around the main peak [49-53]. Figure 4.4 (b) shows overlaid transmission spectra of the optical modulator driven at 10GHz, 20GHz, 30GHz and 40GHz. At higher modulation frequencies, the power of the sidebands becomes lower due to the combined effects of decreased electric potential drop across the slot, reduced output power of the RF source, and increased RF loss on the feeding cable and the probe. Since the power of the main peak and first sideband is proportional to the square of the zero-order and first-order Bessel function of the first kind (J_i, i=0,1) as a function of phase modulation index (η) which represents the achieved phase shift (unit: radians), by measuring the ratio of the main peak power and sideband power ($J_0^2(\eta)/ J_0^2(\eta) \approx (2/\eta)^2$), the phase modulation index (η) can be extracted [40, 51-53]. The obtained modulation index as a function of modulation frequency is plotted as the red curve shown in Fig. 4.4 (c). Sideband signals are observed above the noise floor until the modulation frequency is over 43GHz.

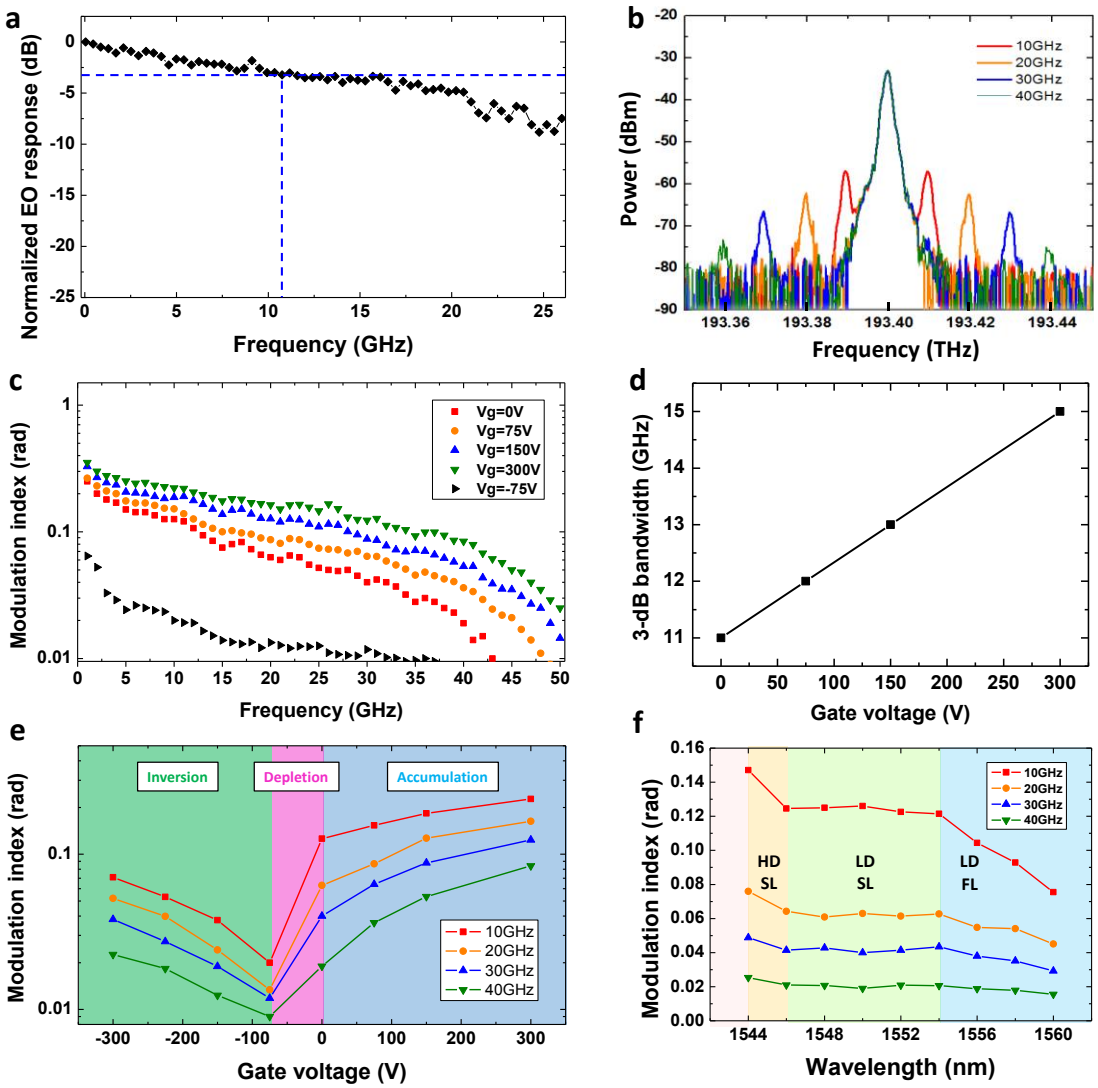

Figure 4.4: Device characterization at high frequency. (a) Measured normalized EO response of the modulator as a function of modulation frequency in a small-signal modulation test. The 3-dB bandwidth is measured to be 11GHz. (b) Measured optical transmission spectra of the modulator operating at 10GHz, 20GHz, 30GHz and 40GHz. (c) Measured modulation index as a function of frequency, under different backside gate voltages. (d) Increased 3-dB RF bandwidth as the positive gate voltage increases. (e) Measured modulation index as a function of V_{gate} at different modulation frequencies, overlaid with the states of accumulation, depletion and inversion. (f) Measured modulation index over a range of optical wavelengths. The modulation index is nearly constant over a low-dispersion slow-light region of 8nm.

4.6 MEASUREMENT OF GATE-ASSISTED IMPROVEMENT OF BANDWIDTH AND ENERGY CONSUMPTION

Next, to further increase the RF bandwidth of the modulator, a positive gate voltage (V_{gate}) from a high-voltage supply is applied to the bottom silicon substrate across the BOX layer of our device [40, 41], as shown in Fig. 4.1 (d). The positive V_{gate} is varied and the corresponding modulation index is measured. As shown in Fig. 4.4 (c), as the positive V_{gate} increases, the measured modulation index at each frequency increases and the whole curve becomes flatter, due to the increased electron accumulation at the interface of the silicon PCW and the BOX [40, 41]. When the V_{gate} is increased over 150V, the sideband power starts to appear above the noise level in the transmission spectrum at 50GHz, and the corresponding modulation index is plotted the blue curve shown in Fig. 5 (c). Further increasing the positive gate voltage, e.g. up to 300V, helps improving the modulation index at the same frequency, or extending the RF frequency with the same modulation index, as shown by the green curve in Fig. 5 (c). 4.4 (d) shows the 3-dB bandwidth of the modulator as a function of positive V_{gate}, and it can be seen that under the V_{gate} of 300V, the 3-dB bandwidth is increased to 15GHz. Note the breakdown electric field of the silicon dioxide is about 0.5GV/m [54], corresponding to a voltage of 1500V that the 3 μm-thick BOX layer can withstand.

In order to further investigate the device performance under V_{gate}, a negative V_{gate} is applied, and the modulation index is measured and plotted in Fig. 4.4 (e). It can be seen that with the magnitude of negative voltage slightly increased, the measured modulation index decreases due to the depletion of electrons. At a V_{gate} of around -75V, the free

electrons are almost completely depleted, so the modulation index becomes the smallest, which is also shown by the black curve in Fig. 4.4 (c). When the magnitude of the negative voltage further increases, modulation index starts to increase because "inversion" state occurs in which holes are accumulated in the top silicon PCW layer. This interesting phenomenon is quite similar to the well-known Metal-Oxide-Semiconductor (MOS) capacitor structure [55].

What is more, a small switching voltage is achieved under a high positive V_{gate}, suggesting a low power consumption. For example, the measured modulation index is η=0.23 at 10GHz under V_{gate}=300V, and correspondingly, the required switching voltage is then $V_\pi = \pi/\eta \times V_d$ =2.2V at 10GHz, where V_d= 0.16V is the RF driving voltage calculated from the output power of RF source. Since our modulator is a lumped device without termination, the power consumption is then dominated by the capacitive load of the slot. The RF power consumption for 100% modulation depth is $2\pi f \times (\frac{1}{2} C V_\pi^2) \times 2$ =24mW at modulation frequency of f=10GHz, where C=39fF is the slot capacitance obtained from simulation and verified experimentally, V_π=2.2V is used as the driving voltage to achieve a maximum extinction ratio, and a factor of 2 is added due to the push-pull configuration. In addition, we make an estimation of energy consumption per bit for our device [56]. If our modulator is driven by PRBS signals with the same power level, we estimate the energy consumption per bit for our modulator at the bit rate of 10Gbit/s as $W_{bit} = \frac{1}{4} C V_\pi^2 \times 2$ = 94.4fJ/bit [3, 41, 52, 56, 57]. Note that, in actual high-speed

digital modulations, the driving voltage can be smaller than V_π, in which case a decently clear eye diagram, a high enough extinction ratio and acceptable bit error rate (BER) can be still achieved using lower energy [18, 25, 41, 58, 59]. Though, we still use V_π as driving voltage (i.e.100% modulation depth) in our estimation, because this can compensate the actual voltage drop caused by experimental imperfections such as reflections, drift, RF loss, etc., and allows for a reasonable estimated value of energy consumption. This very low estimated energy consumption is due to both a significantly reduced V_π and the very small capacitance achieved by widening the slot. Note that, although the applied V_{gate} is high, the power consumption on the backside gate is negligible (<30pW) due to the highly insulating BOX layer.

4.7 MEASUREMENT OF LOW-DISPERSION OPTICAL BANDWIDTH

Finally, to demonstrate the wide optical bandwidth of this PCW modulator, the wavelength of the laser input is tuned from 1544nm to 1560nm, while V_{gate} is set to be zero and all other testing conditions are kept the same. Over this spectrum range, the modulation index is measured at 10GHz, 20GHz, 30GHz, and 40GHz, and the results are plotted in Fig. 4.4 (f). It can be seen that at each modulation frequency, the curve of the measured modulation index looks flat from 1546nm to 1554nm, with a small variation of ±3.5%. This is because the modulation index is proportional to the n_g ($\eta \sim 1/V_\pi$ and $V_\pi \sim B \times \lambda/n_g$, where B is a constant) [60], and n_g has been engineered to be almost constant in this low-dispersion slow-light wavelength region, which agrees well with the simulated low-dispersion spectrum range in Fig. 4.1 (c). This 8nm-wide low-dispersion spectrum

range is useful for some applications such as wavelength division multiplexing (WDM), and also makes our modulator insensitive to variations of wavelength and temperature, which is much better than non-band-engineered PCWs [4, 25] and ring resonators [61-64]. In Fig. 4.4 (f), the largest modulation index is achieved in the high-dispersion slow-light region (from 1543.5nm to 1546 nm), because of the largest n_g in this region. As the wavelength increases over 1554nm, the measured modulation index decreases due to the decreasing value of ng.

4.8 DISCUSSION

In recent years, some groups have reported their work on analog/digital optical modulators based on similar structures such as silicon PCW MZI [18] and EO polymer filled silicon slot waveguide MZI [41], while our EO polymer filled silicon slot PCW MZI modulator combines the benefits from both the slow-light PCW [18] and the silicon-organic hybrid (SOH) structure [41]. In Reference [18], Nguyen, et al, demonstrated a silicon Mach-Zehnder modulators with 90μm-long lattice-shifted photonic crystal waveguides with n_g=20~30. By utilizing the plasma dispersion effect on p-n diode, digital modulation at a data rate of 40Gbit/s, optical bandwidth of 12.5nm, and insertion loss of 14.8dB were experimentally demonstrated. Since only a peak-to-peak driving voltage, V_{pp}=5.3V (instead of V_π), is reported in this reference, we theoretically estimate the V_π of the modulator [31, 60, 65] to be $V_\pi = \pi \Big/ (\frac{2\pi}{\lambda} \Delta n_{eff} n_g L) = \pi \Big/ (\frac{2\pi}{1550nm} \cdot 1.6\times10^{-5} \cdot 30 \cdot 90\mu m)$ =18V for apples-to-apples comparison. This large V_π value leads to a large $V_\pi \times$L product

of 1.62V×mm at 10Gbit/s. In reference [41], Palmer, et al, reported a MZI modulator in which EO polymer is filled into a 1.5mm-long slot waveguide with slot width of 80nm. This modulator was demonstrated with in-device r_{33} of 15pm/V, energy consumption of 320fJ/bit at 10Gbit/s digital modulation, total insertion loss of 21dB, and V_π=2.5V which corresponds to a $V_\pi \times L$=3.75V×mm. In a recent article published by the same group [66], Alloatti, et al, demonstrated a MZI modulator with 500μm-long 120nm-wide-slot waveguide filled with EO polymer, in which they reported a 3dB bandwidth of 100GHz, but a relatively higher $V_\pi \times L$=11V×mm, as well as optical loss of 21±2dB. In addition, recently, a rather specialized SOH modulator based on plasmonic waveguide has been demonstrated by Melikyan, et al, with bit rate of 40Gbit/s, energy consumption of 60fJ/bit, optical bandwidth of 120nm, and insertion loss of 12dB [52]. Considering the reported $V_\pi \times L$=1.3Vmm and device length of 29um, its value of V_π is as large as 45V, which may be prohibitive for some applications.

Besides, the fiber-to-fiber total optical insertion loss is estimated to be 15dB, including the ~3.5dB loss per grating coupler, ~0.4dB loss per MMI coupler, ~0.1dB loss per mode converter, ~0.5dB loss per group index taper, and ~6dB insertion loss on EO polymer filled slot PCW, based on CMOS foundry fabrication conditions [67]. In our measurements, we observed a higher insertion loss, and the additional losses can be mainly dominated by the imperfect fabrication quality (e.g. sidewall roughness) from our university fabrication tools. This abovementioned value is provided instead of the actual measured insertion loss in order to avoid misleading information about the true

performance behavior of the device. The optical loss can be further reduced by the design of a low-loss slot PCW and passive components, improved fabrication quality, and improved coupling and packaging methods [68]. By using a mature commercial CMOS foundry to fabricate our PCW devices [67], the optical loss and fabrication yield can be improved.

4.9 SUMMARY

In summary, we demonstrate a broadband, low-power, low-dispersion and compact optical modulator based on a silicon slot PCW filled with EO polymer. Benefiting from the combined enhancement provided by the slow-light effect and high-r_{33} polymer, the voltage-length product of the modulator is measured to be as small as $V_\pi \times L = 0.282 V \times mm$, corresponding to a record-high effective in-device r_{33} of 1230pm/V ever demonstrated. The silicon PCW is selectively doped to reduce the RC time delay and to achieve high-speed modulation. A backside gate technique is applied to our silicon PCW device to enhance device performance. Assisted by the backside gate voltage of 300V, the 3-dB bandwidth of the modulator is demonstrated to be 15GHz. In addition, the power consumption of the modulator is measured to be 24mW at 10GHz, and the estimated value of energy consumption per bit for a potential digital modulation is approximately 94.4fJ/bit at 10Gbit/s based on measured V_π at 10GHz [3, 41, 52, 56, 57]. By using the band-engineered PCWs, the modulator is demonstrated to have a low-dispersion optical spectrum range as wide as 8nm, which is a factor of ~10X better than other modulators based on non-band-engineered PCWs [4, 25] and ring resonators [61]

which have narrow operating optical bandwidth of <1 nm.

In our future work, the optical loss can be further reduced by the design of a low-loss slot PCW and passive components, improved fabrication quality, and improved coupling and packaging methods [68]. By using a mature commercial CMOS foundry to fabricate our PCW devices [67], the optical loss and fabrication yield can be improved. The $V_{\pi}\times L$ product can be further reduced by using more efficient organic EO materials, such as supramolecular organic EO glasses and binary EO polymers exhibiting intrinsic Pockels coefficients greater than 300 pm/V [69]. Recently, a figure of merit of n^3r_{33}=2601pm/V is achieved in tethered binary nonlinear optical chromophores with enhanced poling efficiency [70]. A transmission line can be designed to drive the modulator as a traveling wave device, in order to achieve modulation frequency over 100GHz [66, 71]. Recently, the SOH slot waveguide structures have been developed for digital modulations more advanced modulation formats such as QPSK and 16QAM with >1Tb/s [72, 73], thus, our future work will also include driving our modulator using high-speed digital signals [18, 25, 59] and also using this modulator for advanced modulation formats and coherent modulation scheme [72, 73]. To further investigate the high-speed behavior limited by the RC constant, detailed information of the actual values of the resistance and capacitance in the equivalent circuit model can be extracted by measuring the complex frequency-dependent amplitude reflection factor S11 at the device input using a vector network analyzer and then curve-fitting the measured S11 data [63, 74, 75]. In addition, potential stability of the modulator, a common issue for almost all

polymer based devices, can be further improved by developing new EO polymers with higher glass transition temperatures and crosslinking chemistry, and by hermetically sealing the EO polymer and removing oxygen in the device packaging [76]. More detailed studies of EO polymer thermal stability indicate that operation up to 150℃ results in a change of EO coefficients < 10% [77, 78].

4.10 REFERENCES

[1] V. R. Almeida, Q. Xu, C. A. Barrios, and M. Lipson, "Guiding and confining light in void nanostructure," *Optics letters,* vol. 29, pp. 1209-1211, 2004.

[2] C. Koos, P. Vorreau, T. Vallaitis, P. Dumon, W. Bogaerts, R. Baets, B. Esembeson, I. Biaggio, T. Michinobu, F. Diederich, W. Freude, and J. Leuthold, "All-optical high-speed signal processing with silicon–organic hybrid slot waveguides," *Nature Photonics,* vol. 3, pp. 216-219, 2009.

[3] J. Leuthold, C. Koos, W. Freude, L. Alloatti, R. Palmer, D. Korn, J. Pfeifle, M. Lauermann, R. Dinu, S. Wehrli, M. Jazbinsek, P. Gunter, M. Waldow, T. Wahlbrink, J. Bolten, H. Kurz, M. Fournier, J.-M. Fedeli, H. Yu, and W. Bogaerts, "Silicon-organic hybrid electro-optical devices," *Selected Topics in Quantum Electronics, IEEE Journal of,* vol. 19, pp. 3401413-3401413, 2013.

[4] J. H. Wülbern, J. Hampe, A. Petrov, M. Eich, J. Luo, A. K.-Y. Jen, A. Di Falco, T. F. Krauss, and J. Bruns, "Electro-optic modulation in slotted resonant photonic crystal heterostructures," *Applied Physics Letters,* vol. 94, p. 241107, 2009.

[5] J.-M. Brosi, C. Koos, L. C. Andreani, M. Waldow, J. Leuthold, and W. Freude, "High-speed low-voltage electro-optic modulator with a polymer-infiltrated silicon photonic crystal waveguide," *Optics Express,* vol. 16, pp. 4177-4191, 2008.

[6] J. Takayesu, M. Hochberg, T. Baehr-Jones, E. Chan, G. Wang, P. Sullivan, Y. Liao, J. Davies, L. Dalton, A. Scherer, and W. Krug, "A Hybrid Electrooptic Microring Resonator-Based 1×4×1 ROADM for Wafer Scale Optical Interconnects," *Journal of Lightwave Technology,* vol. 27, pp. 440-448, 2009.

[7] X. Zhang, A. Hosseini, X. Lin, H. Subbaraman, and R. T. Chen, "Polymer-based Hybrid Integrated Photonic Devices for Silicon On-chip Modulation and Board-level Optical Interconnects," *IEEE Journal of Selected Topics in Quantum Electronics,* vol. 19, pp. 196-210, 2013.

[8] X. Zhang, A. Hosseini, H. Subbaraman, S. Wang, Q. Zhan, J. Luo, A. K. Jen, and R. T. Chen, "Integrated Photonic Electromagnetic Field Sensor Based on Broadband Bowtie Antenna Coupled Silicon Organic Hybrid Modulator," *Lightwave Technology, Journal of,* vol. 32, pp. 3774-3784, 2014.

[9] D. Chen, H. R. Fetterman, A. Chen, W. H. Steier, L. R. Dalton, W. Wang, and Y. Shi, "Demonstration of 110 GHz electro-optic polymer modulators," *Applied Physics Letters,* vol. 70, pp. 3335-3337, 1997.

[10] Y. Shi, C. Zhang, H. Zhang, J. H. Bechtel, L. R. Dalton, B. H. Robinson, and W. H. Steier, "Low (sub-1-volt) halfwave voltage polymeric electro-optic modulators achieved by controlling chromophore shape," *Science,* vol. 288, pp. 119-122, 2000.

[11] R. T. Chen, L. Lin, C. Choi, Y. J. Liu, B. Bihari, L. Wu, S. Tang, R. Wickman, B. Picor, M. Hibb-Brenner, J. Bristow, and Y. S. Liu, "Fully embedded board-level guided-wave optoelectronic interconnects," *Proceedings of the IEEE,* vol. 88, pp. 780-793, 2000.

[12] X. Lin, T. Ling, H. Subbaraman, X. Zhang, K. Byun, L. J. Guo, and R. T. Chen, "Ultraviolet imprinting and aligned ink-jet printing for multilayer patterning of electro-optic polymer modulators," *Optics letters,* vol. 38, pp. 1597-1599, 2013.

[13] G. T. Reed, G. Mashanovich, F. Gardes, and D. Thomson, "Silicon optical modulators," *Nature Photonics,* vol. 4, pp. 518-526, 2010.

[14] R. Soref, "The past, present, and future of silicon photonics," *Selected Topics in Quantum Electronics, IEEE Journal of,* vol. 12, pp. 1678-1687, 2006.

[15] T. Baba, "Slow light in photonic crystals," *Nature Photonics,* vol. 2, pp. 465-473, 2008.

[16] Y. A. Vlasov, M. O'Boyle, H. F. Hamann, and S. J. McNab, "Active control of slow light on a chip with photonic crystal waveguides," *Nature,* vol. 438, pp. 65-69, 2005.

[17] Y. Jiang, W. Jiang, L. Gu, X. Chen, and R. T. Chen, "80-micron interaction length silicon photonic crystal waveguide modulator," *Applied Physics Letters,* vol. 87, p. 221105, 2005.

[18] H. C. Nguyen, S. Hashimoto, M. Shinkawa, and T. Baba, "Compact and fast photonic crystal silicon optical modulators," *Optics Express,* vol. 20, pp. 22465-22474, 2012.

[19] C.-Y. Lin, X. Wang, S. Chakravarty, B. S. Lee, W. Lai, J. Luo, A. K.-Y. Jen, and R. T. Chen, "Electro-optic polymer infiltrated silicon photonic crystal slot waveguide modulator with 23 dB slow light enhancement," *Applied Physics Letters,* vol. 97, p. 093304, 2010.

[20] X. Wang, C.-Y. Lin, S. Chakravarty, J. Luo, A. K.-Y. Jen, and R. T. Chen, "Effective in-device r33 of 735 pm/V on electro-optic polymer infiltrated silicon photonic crystal slot waveguides," *Optics letters,* vol. 36, pp. 882-884, 2011.

[21] X. Zhang, A. Hosseini, S. Chakravarty, J. Luo, A. K.-Y. Jen, and R. T. Chen, "Wide optical spectrum range, subvolt, compact modulator based on an electro-

optic polymer refilled silicon slot photonic crystal waveguide," *Optics letters,* vol. 38, pp. 4931-4934, 2013.

[22] S. Huang, T.-D. Kim, J. Luo, S. K. Hau, Z. Shi, X.-H. Zhou, H.-L. Yip, and A. K.-Y. Jen, "Highly efficient electro-optic polymers through improved poling using a thin TiO 2-modified transparent electrode," *Applied Physics Letters,* vol. 96, pp. 243311-243311-3, 2010.

[23] H. Chen, B. Chen, D. Huang, D. Jin, J. Luo, A.-Y. Jen, and R. Dinu, "Broadband electro-optic polymer modulators with high electro-optic activity and low poling induced optical loss," *Applied Physics Letters,* vol. 93, p. 043507, 2008.

[24] T. Baehr-Jones, B. Penkov, J. Huang, P. Sullivan, J. Davies, J. Takayesu, J. Luo, T.-D. Kim, L. Dalton, and A. Jen, "Nonlinear polymer-clad silicon slot waveguide modulator with a half wave voltage of 0.25 V," *Applied Physics Letters,* vol. 92, p. 163303, 2008.

[25] H. C. Nguyen, Y. Sakai, M. Shinkawa, N. Ishikura, and T. Baba, "10 Gb/s operation of photonic crystal silicon optical modulators," *Optics Express,* vol. 19, pp. 13000-13007, 2011.

[26] J. Blasco and C. Barrios, "Compact slot-waveguide/channel-waveguide mode-converter," in *Lasers and Electro-Optics Europe, 2005. CLEO/Europe. 2005 Conference on*, 2005, pp. 607-607.

[27] R. Palmer, A. Luca, D. Korn, W. Heni, P. Schindler, J. Bolten, M. Karl, M. Waldow, T. Wahlbrink, W. Freude, K. C, and L. J, "Low-loss silicon strip-to-slot mode converters," *IEEE Photonics Journal,* 2013.

[28] X. Zhang, H. Subbaraman, A. Hosseini, and R. T. Chen, "Highly efficient mode converter for coupling light into wide slot photonic crystal waveguide," *Optics Express,* vol. 22, pp. 20678-20690, 2014.

[29] A. Hosseini, X. Xu, D. N. Kwong, H. Subbaraman, W. Jiang, and R. T. Chen, "On the role of evanescent modes and group index tapering in slow light photonic crystal waveguide coupling efficiency," *Applied Physics Letters,* vol. 98, pp. 031107-031107-3, 2011.

[30] X. Xu, H. Subbaraman, J. Covey, D. Kwong, A. Hosseini, and R. T. Chen, "Complementary metal–oxide–semiconductor compatible high efficiency subwavelength grating couplers for silicon integrated photonics," *Applied Physics Letters,* vol. 101, pp. 031109-031109-4, 2012.

[31] M. Soljačić, S. G. Johnson, S. Fan, M. Ibanescu, E. Ippen, and J. Joannopoulos, "Photonic-crystal slow-light enhancement of nonlinear phase sensitivity," *JOSA B,* vol. 19, pp. 2052-2059, 2002.

[32] J. Witzens, T. Baehr-Jones, and M. Hochberg, "Design of transmission line driven slot waveguide Mach-Zehnder interferometers and application to analog optical links," *Optics Express,* vol. 18, pp. 16902-16928, 2010.

[33] J. H. WŘlbern, A. Petrov, and M. Eich, "Electro-optical modulator in a polymerinfiltrated silicon slotted photonic crystal waveguide heterostructure resonator," *Optics Express,* vol. 17, pp. 304-313, 2009.

[34] S. K. Ghandhi, *VLSI fabrication principles: silicon and gallium arsenide*: John Wiley & Sons, 2008.
[35] J. Doylend, P. Jessop, and A. Knights, "Optical attenuation in ion-implanted silicon waveguide racetrack resonators," *Opt. Express19 (16),* pp. 14913-14918, 2011.
[36] A. Chen, H. Sun, A. Szep, S. Shi, D. Prather, Z. Lin, R. S. Kim, and D. Abeysinghe, "Achieving higher modulation efficiency in electrooptic polymer modulator with slotted silicon waveguide," *Lightwave Technology, Journal of,* vol. 29, pp. 3310-3318, 2011.
[37] S. Ristić, A. Prijić, and Z. Prijić, "Dependence of static dielectric constant of silicon on resistivity at room temperature," *Serbian Journal of Electrical Engineering,* vol. 1, pp. 237-247, 2004.
[38] W. Perrins, D. McKenzie, and R. McPhedran, "Transport properties of regular arrays of cylinders," *Proceedings of the Royal Society of London. A. Mathematical and Physical Sciences,* vol. 369, pp. 207-225, 1979.
[39] T. C. Choy, *Effective medium theory: principles and applications*: Oxford University Press, 1999.
[40] L. Alloatti, D. Korn, R. Palmer, D. Hillerkuss, J. Li, A. Barklund, R. Dinu, J. Wieland, M. Fournier, J. Fedeli, H. Yu, W. Bogaerts, P. Dumon, R. Baets, C. Koos, W. Freude, and J. Leuthold, "42.7 Gbit/s electro-optic modulator in silicon technology," *Optics Express,* vol. 19, pp. 11841-11851, 2011.
[41] R. Palmer, A. Luca, D. Korn, P. Schindler, M. Baier, J. Bolten, T. Wahlbrink, M. Waldow, R. Dinu, W. Freude, C. Koos, and J. Leuthold, "Low power mach-zehnder modulator in silicon-organic hybrid technology," *Photonics Technology Letters, IEEE,* vol. 25, 2013.
[42] L. Alloatti, M. Lauermann, C. Sürgers, C. Koos, W. Freude, and J. Leuthold, "Optical absorption in silicon layers in the presence of charge inversion/accumulation or ion implantation," *Applied Physics Letters,* vol. 103, p. 051104 2013.
[43] C.-Y. Lin, A. X. Wang, B. S. Lee, X. Zhang, and R. T. Chen, "High dynamic range electric field sensor for electromagnetic pulse detection," *Optics Express,* vol. 19, pp. 17372-17377, 2011.
[44] X. Zhang, B. Lee, C.-y. Lin, A. X. Wang, A. Hosseini, and R. T. Chen, "Highly Linear Broadband Optical Modulator Based on Electro-Optic Polymer," *Photonics Journal, IEEE,* vol. 4, pp. 2214-2228, 2012.
[45] X. Zhang, A. Hosseini, J. Luo, A. K.-Y. Jen, and R. T. Chen, "Hybrid silicon-electro-optic-polymer integrated high-performance optical modulator," in *SPIE Photonic West, OPTO*, 2014, pp. 89910O-89910O-6.
[46] A. Hosseini, X. Xu, H. Subbaraman, C.-Y. Lin, S. Rahimi, and R. T. Chen, "Large optical spectral range dispersion engineered silicon-based photonic crystal waveguide modulator," *Opt. Express20 (11),* pp. 12318-12325, 2012.

[47] T. F. Krauss, "Slow light in photonic crystal waveguides," *Journal of Physics D: Applied Physics,* vol. 40, p. 2666, 2007.
[48] S.-i. Inoue and A. Otomo, "Electro-optic polymer/silicon hybrid slow light modulator based on one-dimensional photonic crystal waveguides," *Applied Physics Letters,* vol. 103, p. 171101, 2013.
[49] J. H. Wülbern, S. Prorok, J. Hampe, A. Petrov, M. Eich, J. Luo, A. K.-Y. Jen, M. Jenett, and A. Jacob, "40 GHz electro-optic modulation in hybrid silicon–organic slotted photonic crystal waveguides," *Optics letters,* vol. 35, pp. 2753-2755, 2010.
[50] L. D. Tzuang, M. Soltani, Y. H. D. Lee, and M. Lipson, "High RF carrier frequency modulation in silicon resonators by coupling adjacent free-spectral-range modes," *Optics letters,* vol. 39, pp. 1799-1802, 2014.
[51] Y. N. Wijayanto, H. Murata, and Y. Okamura, "Electro-optic microwave-lightwave converters utilizing patch antennas with orthogonal gaps," *Journal of Nonlinear Optical Physics & Materials,* vol. 21, 2012.
[52] A. Melikyan, L. Alloatti, A. Muslija, D. Hillerkuss, P. Schindler, J. Li, R. Palmer, D. Korn, S. Muehlbrandt, D. Van Thourhout, B. Chen, R. Dinu, M. Sommer, C. Koos, M. Kohl, W. Freude, and J. Leuthold, "High-speed plasmonic phase modulators," *Nature Photonics,* vol. 8, pp. 229-233, 2014.
[53] O. Herrera, K. Kim, R. Voorakaranam, R. Himmelhuber, S. Wang, Q. Zhan, L. Li, R. Norwood, R. Neilson, and J. Luo, "Silica/Electro-optic Polymer Optical Modulator with Integrated Antenna for Microwave Receiving."
[54] H. Bartzsch, D. Glöß, P. Frach, M. Gittner, E. Schultheiß, W. Brode, and J. Hartung, "Electrical insulation properties of sputter‐deposited SiO2, Si3N4 and Al2O3 films at room temperature and 400° C," *Physica Status Solidi (A),* vol. 206, pp. 514-519, 2009.
[55] S. M. Sze and K. K. Ng, *Physics of semiconductor devices*: John Wiley & Sons, 2006.
[56] D. A. Miller, "Energy consumption in optical modulators for interconnects," *Optics Express,* vol. 20, pp. A293-A308, 2012.
[57] J. Leuthold, C. Koos, W. Freude, L. Alloatti, R. Palmer, D. Korn, J. Pfeifle, M. Lauermann, R. Dinu, S. Wehrli, M. Jazbinsek, P. Gunter, M. Waldow, T. Wahlbrink, J. Bolten, M. Fournier, J. M. Fedeli, W. Bogaerts, and H. Yu, "High-speed, low-power optical modulators in silicon," in *Transparent Optical Networks (ICTON), 2013 15th International Conference on*, 2013, pp. 1-4.
[58] R. Palmer, S. Koeber, W. Heni, D. Elder, D. Korn, H. Yu, L. Alloatti, S. Koenig, P. Schindler, W. Bogaerts, L. Dalton, W. Freude, J. Leuthold, and C. Koos, "High-speed silicon-organic hybrid (SOH) modulator with 1, 6 fJ/bit and 180 pm/V in-device nonlinearity," in *39th European Conference and Exhibition on Optical Communication (ECOC-2013)*, 2013.
[59] H. C. Nguyen, Y. Sakai, M. Shinkawa, N. Ishikura, and T. Baba, "Photonic crystal silicon optical modulators: carrier-injection and depletion at 10 Gb/s," *Quantum Electronics, IEEE Journal of,* vol. 48, pp. 210-220, 2012.

[60] A. Hosseini, X. Xu, H. Subbaraman, C.-Y. Lin, S. Rahimi, and R. T. Chen, "Large optical spectral range dispersion engineered silicon-based photonic crystal waveguide modulator," *Opt. Express,* vol. 20, pp. 12318-12325, 2012.

[61] M. Gould, T. Baehr-Jones, R. Ding, S. Huang, J. Luo, A. K.-Y. Jen, J.-M. Fedeli, M. Fournier, and M. Hochberg, "Silicon-polymer hybrid slot waveguide ring-resonator modulator," *Optics Express,* vol. 19, pp. 3952-3961, 2011.

[62] C. Zhang, T. Ling, S.-L. Chen, and L. J. Guo, "Ultrabroad Bandwidth and Highly Sensitive Optical Ultrasonic Detector for Photoacoustic Imaging," *ACS Photonics,* 2014.

[63] L. Chen, Q. Xu, M. G. Wood, and R. M. Reano, "Hybrid silicon and lithium niobate electro-optical ring modulator," *Optica,* vol. 1, pp. 112-118, 2014.

[64] C. Xiong, W. H. Pernice, J. H. Ngai, J. W. Reiner, D. Kumah, F. J. Walker, C. H. Ahn, and H. X. Tang, "Active silicon integrated nanophotonics: ferroelectric BaTiO3 devices," *Nano letters,* vol. 14, pp. 1419-1425, 2014.

[65] Y. Terada and T. Baba, "Low-Voltage 25 Gbps Modulators Based On Si Photonic Crystal Slow Light Waveguides," in *CLEO: Science and Innovations*, 2014, p. SM2G. 2.

[66] L. Alloatti, R. Palmer, S. Diebold, K. P. Pahl, B. Q. Chen, R. Dinu, M. Fournier, J. M. Fedeli, T. Zwick, W. Freude, C. Koos, and J. Leuthold, "100 GHz silicon-organic hybrid modulator," *Light-Science & Applications,* vol. 3, May 2014.

[67] E. Schelew, G. W. Rieger, and J. F. Young, "Characterization of integrated planar photonic crystal circuits fabricated by a CMOS foundry," *Lightwave Technology, Journal of,* vol. 31, pp. 239-248, 2013.

[68] B. Snyder and P. O'Brien, "Planar fiber packaging method for silicon photonic integrated circuits," in *Optical Fiber Communication Conference and Exposition (OFC/NFOEC) 2012*, 2012, pp. 1-3.

[69] R. Palmer, S. Koeber, D. L. Elder, M. Woessner, W. Heni, D. Korn, M. Lauermann, W. Bogaerts, L. Dalton, W. Freude, J. Leuthold, and C. Koos, "High-Speed, Low Drive-Voltage Silicon-Organic Hybrid Modulator Based on a Binary-Chromophore Electro-Optic Material," *Journal of Lightwave Technology,* vol. 32, pp. 2726-2734, 2014.

[70] M. Li, S. Huang, X.-H. Zhou, Y. Zang, J. Wu, Z. Cui, J. Luo, and A. K. Jen, "Poling Efficiency Enhancement of Tethered Binary Nonlinear Optical Chromophores for Achieving Ultrahigh n3r33 Figure-of-Merit of 2601 pm/V," *Journal of Materials Chemistry C,* 2015.

[71] D. Korn, R. Palmer, H. Yu, P. C. Schindler, L. Alloatti, M. Baier, R. Schmogrow, W. Bogaerts, S. K. Selvaraja, G. Lepage, M. Pantouvaki, J. Wouters, P. Verheyen, J. V. Campenhout, B. Chen, R. Baets, P. Absil, R. Dinu, C. Koos, W. Freude, and J. Leuthold, "Silicon-organic hybrid (SOH) IQ modulator using the linear electro-optic effect for transmitting 16QAM at 112 Gbit/s," *Optics Express,* vol. 21, pp. 13219-13227, 2013.

[72] C. Weimann, P. Schindler, R. Palmer, S. Wolf, D. Bekele, D. Korn, J. Pfeifle, S. Koeber, R. Schmogrow, L. Alloatti, D. Elder, H. Yu, W. Bogaerts, L. R. Dalton, W. Freude, J. Leuthold, and C. Koos, "Silicon-organic hybrid (SOH) frequency comb sources for terabit/s data transmission," *Optics Express,* vol. 22, pp. 3629-3637, 2014.

[73] M. Lauermann, R. Palmer, S. Koeber, P. C. Schindler, D. Korn, T. Wahlbrink, J. Bolten, M. Waldow, D. L. Elder, L. R. Dalton, J. Leuthold, W. Freude, and C. Koos, "Low-power silicon-organic hybrid (SOH) modulators for advanced modulation formats," *Optics Express,* vol. 22, pp. 29927-29936, 2014/12/01 2014.

[74] G. Li, X. Zheng, J. Yao, H. Thacker, I. Shubin, Y. Luo, K. Raj, J. E. Cunningham, and A. V. Krishnamoorthy, "25Gb/s 1V-driving CMOS ring modulator with integrated thermal tuning," *Optics Express,* vol. 19, pp. 20435-20443, 2011.

[75] S. Koeber, R. Palmer, M. Lauermann, W. Heni, D. L. Elder, D. Korn, M. Woessner, L. Alloatti, S. Koenig, and P. C. Schindler, "Femtojoule electro-optic modulation using a silicon-organic hybrid device," *Light Sci. Appl.(to be published),* 2014.

[76] S. Takahashi, B. Bhola, A. Yick, W. Steier, J. Luo, A. Y. Jen, D. Jin, and R. Dinu, "Photo-Stability Measurement of Electro-Optic Polymer Waveguides With High Intensity at 1550-nm Wavelength," *Journal of Lightwave Technology,* vol. 27, pp. 1045-1050, 2009/04/15 2009.

[77] S. Huang, J. Luo, Z. Jin, X.-H. Zhou, Z. Shi, and A. K.-Y. Jen, "Enhanced temporal stability of a highly efficient guest–host electro-optic polymer through a barrier layer assisted poling process," *Journal of Materials Chemistry,* vol. 22, pp. 20353-20357, 2012.

[78] Z. Shi, J. Luo, S. Huang, B. M. Polishak, X.-H. Zhou, S. Liff, T. R. Younkin, B. A. Block, and A. K.-Y. Jen, "Achieving excellent electro-optic activity and thermal stability in poled polymers through an expeditious crosslinking process," *Journal of Materials Chemistry,* vol. 22, pp. 951-959, 2012.

Chapter 5: Integrated photonic electromagnetic wave sensor based on antenna-coupled modulator on silicon-on-insulator substrate *

5.1 INTRODUCTION

The detection, measurement and evaluation of electromagnetic fields have attracted a significant amount of attention in recent years [1-3]. Electromagnetic field sensors have shown promising applications in high power microwave (HPM) and electromagnetic pulse (EMP) detection, environmental electromagnetic interference (EMI) analysis, electromagnetic compatibility (EMC) measurements, radio frequency (RF) integrated circuit testing, process monitoring and control, as well as in the research of electromagnetic radiation effects on human health. Traditional electronic-based electromagnetic field sensors [4, 5] normally have large active conductive probes which perturb the field to be measured and also make the device bulky. In order to address these problems, integrated photonic sensing of electromagnetic field has been developed, in which the optical signal is modulated by an RF signal collected by an antenna [6-11]. The antennas used here can potentially be designed to be small enough or all-dielectric [12] to minimize the perturbation of high-frequency electric field under measurement. The key element of such devices is an efficient electro-optic (EO) modulator. One common

* Citation: X. Zhang, A. Hosseini, H. Subbaraman, S. Wang, Q. Zhan, J. Luo, A. K. Jen, and R. T. Chen, "Integrated Photonic Electromagnetic Field Sensor Based on Broadband Bowtie Antenna Coupled Silicon Organic Hybrid Modulator," Lightwave Technology, Journal of, vol. 32, pp. 3774-3784, 2014.

X. Zhang mainly worked on the simulation, fabrication and characterization, and serves as the first author of the paper. Other coauthors also contributed to the work from simulation, material processing, discussion, or paper preparation.

structure of EO modulators is a Mach-Zehnder interferometer (MZI), in which an electric-field-induced optical phase modulation is converted into an optical intensity variation [13, 14]. These integrated photonic electromagnetic field sensors have a few inherent advantages over conventional electronic sensors, such as compact size, high sensitivity, broad bandwidth, good galvanic insulation and noise immunity [15].

Recently, silicon-organic hybrid (SOH) technology [16] has shown to enable high performance integrated photonic devices such as compact and low-power EO modulators [17, 18], high-speed optical interconnects [19, 20], and sensitive photonic sensors [21]. Benefiting from the large EO coefficient (r_{33}) of active organic polymers [22, 23] as well as the strong optical mode confinement made possible by the large index of silicon [24, 25], SOH integrated photonic electromagnetic field sensors are promising for achieving high sensitivity, compact size, and broad bandwidth.

It has been demonstrated in [15] that low half-wave voltage (V_π), high input driving voltage (electric field), and large input optical power of EO modulators can improve the sensitivity of the photonic electromagnetic field sensors. To enhance the sensitivity through V_π reduction, silicon slot photonic crystal waveguides (PCWs) refilled with large EO coefficient (r_{33}) EO polymer can be employed due to the slow-light enhanced light-matter interaction [26, 27]. The enhanced light-matter interaction also enables a compact device size [28, 29]. The silicon in the SOH slot PCW modulator can also be doped to achieve high speed operation [30, 31]. For example, modulation speeds up to 40GHz or over 40Gbit/s have been demonstrated in [32, 33]. Furthermore, the

antenna can be designed for broadband resonant electric field enhancement [34] [35], which is equivalent to increasing the input driving voltage of the modulator, thereby increasing the sensitivity of the sensor. The geometrical dimensions of the antenna are much smaller than the wavelength of the electromagnetic field to be measured. This antenna can be combined with the SOH slot PCW modulator to achieve even higher sensitivity over wide frequency bandwidth. Such a combination of integrated RF photonics [36] and SOH technology [16] offers a viable platform for high frequency electromagnetic field sensing.

In this chapter, we present the design, fabrication and characterization of a compact and highly sensitive integrated photonic electromagnetic field sensor based on a silicon-organic hybrid modulator driven by a bowtie antenna. Slow-light effects in the electro-optic (EO) polymer refilled silicon slot photonic crystal waveguide (PCW), together with broadband electric field enhancement provided by the bowtie antenna, are utilized to enhance the interaction of microwaves and optical waves, enabling an ultra large effective in-device EO coefficient over 1000pm/V and thus a high sensitivity. The EO polymer refilled slot PCW is designed for low-dispersion slow-light propagation, high poling efficiency, and high optical mode confinement inside the slot. The bowtie antenna acts not only as a receiving antenna, but also as poling electrodes during the fabrication process. A bowtie antenna integrated on doped silicon slot PCW is demonstrated to have a broad operational bandwidth, with a maximum resonance at the frequency of 10GHz. The strongly enhanced broadband electric field is used to directly

modulate the phase of the optical waves propagating through the slot PCW embedded inside the feed gap of the bowtie antenna. The phase modulation is then converted to intensity modulation using an external reference arm to form a Mach-Zehnder interferometer in our experimental setup. The sensing of electromagnetic field at 8.4GHz is experimentally demonstrated, with a minimum detectable electromagnetic power density of 8.4mW/m^2, corresponding to a minimum detectable electric field of 2.5V/m.

5.2 DEVICE OVERVIEW

The key parts of our photonic electromagnetic field sensor consisting of an EO polymer refilled silicon slot PCW phase modulator coupled with a gold bowtie-shaped antenna are shown schematically in Figs. 5.1 (a)-(e). An EO polymer, SEO125 from Soluxra, LLC, with a large r_{33}, low optical loss, and good temporal stability, is used to refill the silicon slot PCW. This EO polymer refilled silicon slot PCW with a slot width (S_w) of 320nm is band-engineered to achieve low-dispersion slow-light propagation over a broad wavelength range of 8nm [37], as well as high optical mode confinement inside the EO polymer refilled slot. The slow-light enhanced effective in-device r_{33} of this SOH modulator can be over 1000pm/V [18, 37], which is beneficial for high-sensitivity sensing. The slot PCW is embedded in the feed gap of the bowtie antenna, and the silicon layer is selectively implanted with different ion concentrations for high frequency operation [38]. The bowtie antenna is used as a receiving antenna, driving electrodes, and poling electrodes. Here the bowtie antenna with capacitive extension bars has a simple design, and a broadband characteristic. With the two bowtie arms as receivers, a confined

resonant electric field with strong enhancement factor can be generated in the gap between them [34].

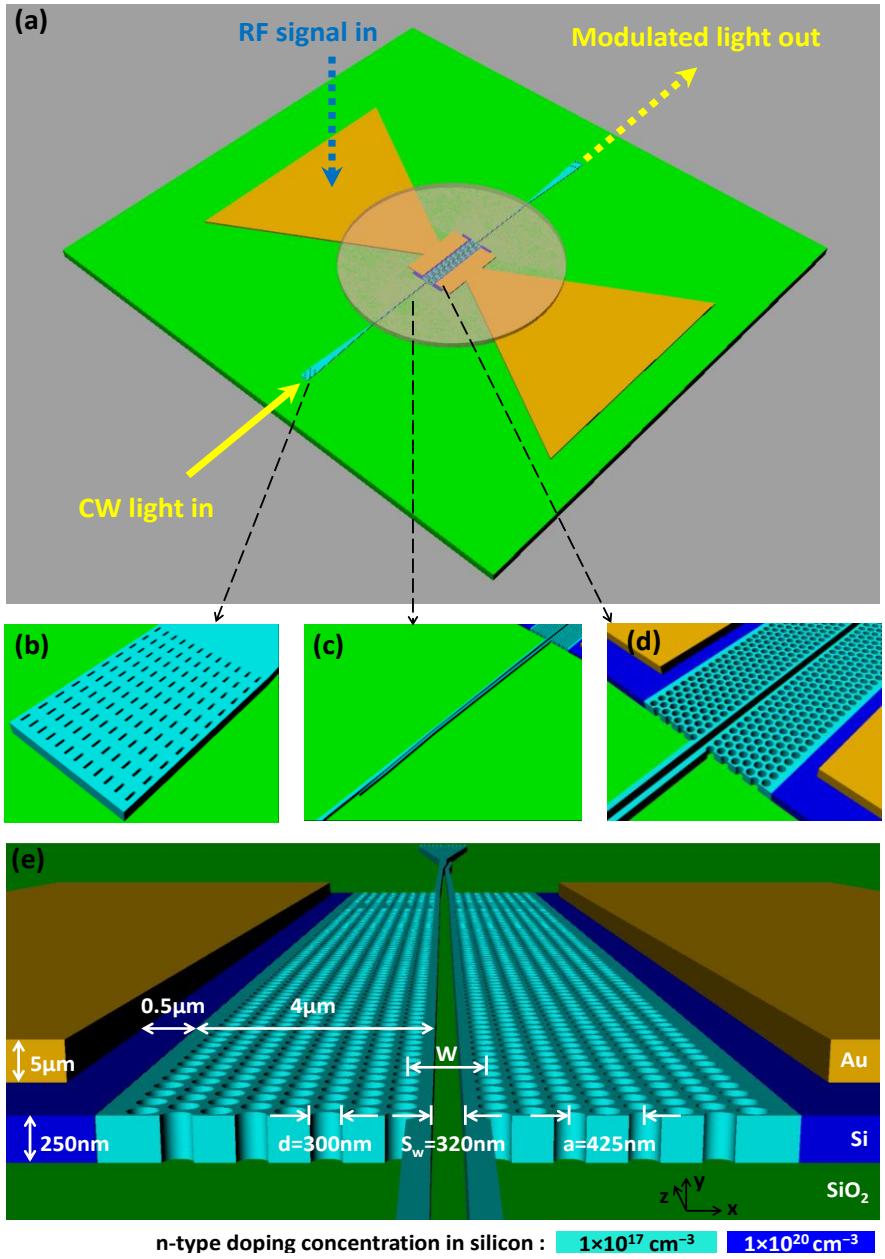

Figure 5.1: continued next page.

Figure 5.1: (a) A schematic view of the key part of the electromagnetic field sensor consisting of an EO polymer refilled silicon slot PCW phase modulator and a bowtie antenna. An external arm combined with this phase modulator forms an MZI structure, converting phase modulation to intensity modulation. (b) Subwavelength grating coupler. (c) Strip-to-slot mode converter (d) Slot PCW. (e) Tilted view showing the cross section of the antenna-coupled slot PCW, with dimension parameters and two levels of n-type silicon doping concentrations. Note: the EO polymer layer covered on top of the device is not shown in (b)-(e) for better visualization.

The working principle of this integrated photonic electromagnetic field sensor is discussed as follows. A continuous wave (CW) laser input is coupled into and out of the device. The bowtie antenna harvests incident electromagnetic waves, transforms it into high-power-density time-varying electric field within the feed gap, which directly interacts with the light propagating along the EO polymer refilled slot PCW embedded within the feed gap (i.e. interaction region). The refractive index of the EO polymer is controlled by the applied electric field via the EO effect, which modulates the phase of the optical wave within the low-dispersion wavelength regime of the slot PCW. For measurement, we convert this phase modulation to an intensity modulation using an external arm enabled MZI structure. Finally, by measuring the modulated optical intensity at the output end of the MZI, an incident electromagnetic field from free space can be detected through optical means. This integrated photonic electromagnetic field sensor can reduce the impact of perturbing fields, since it is based on an optical modulation technique.

5.3 DESIGN OF SILICON-ORGANIC HYBRID SLOT PHOTONIC CRYSTAL WAVEGUIDE MODULATOR

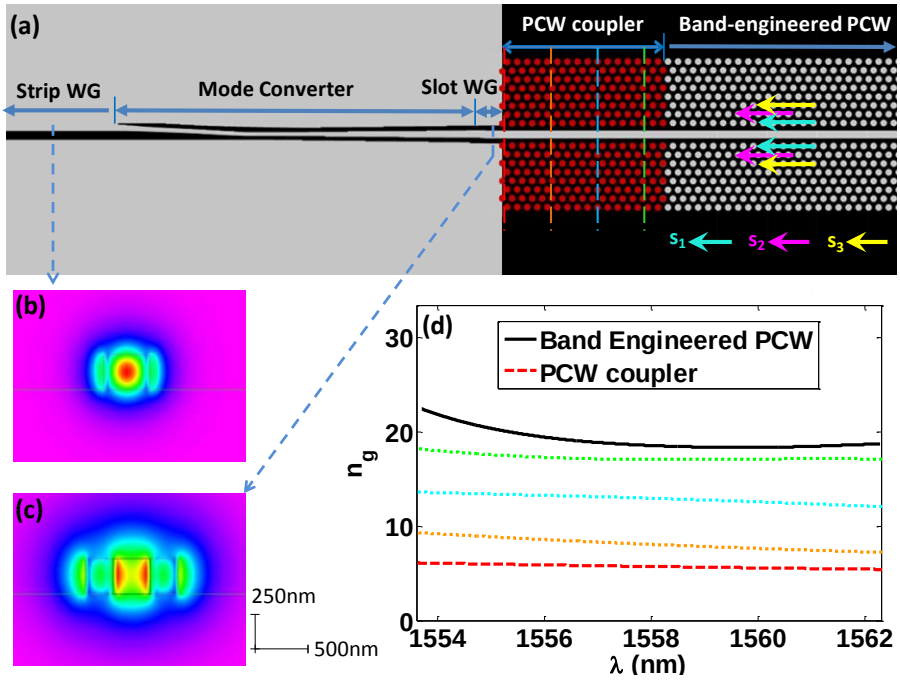

Figure 5.2: (a) Layout of the strip-to-slot mode converter, PCW coupler and band-engineered PCW. The black area corresponds to un-etched silicon, and the gray area corresponds to the etched silicon. The red-color holes indicate the PCW taper section. The s_1, s_2, and s_3 indicate the lattice shift direction in band-engineered PCW section. WG: waveguide. (b) Cross-sectional view of strip waveguide mode profile. (c) Cross-sectional view of slot waveguide mode profile. (d) The small variations of n_g over about 8nm wavelength range, for the band-engineered slow-light PCW and PCW coupler. The lines of different colors represent the n_g at different positions along the PCW coupler as indicated by the dashed lines of corresponding colors in (a). This indicates a smooth transition of n_g from the beginning of the PCW taper to the band-engineered PCW.

The layout of the slot PCW is shown in Fig. 5.2 (a). This slot PCW is designed on a silicon-on-insulator (SOI) substrate with 250nm-thick top silicon and 3μm-thick buried

oxide layers. The PCW holes and slot are assumed to be filled with EO polymer, SEO125, which has a refractive index of 1.63 at 1550nm. SEO125 exhibits an exceptional combination of large EO coefficient, good near-infrared transparency, excellent chemical- and photo-stability, and improved processability [37]. Additionally, a lattice-shifted slot PCW is used to achieve low-dispersion slow light [39], where optimized values of the lattice constant (a=425nm), hole diameter (d=300nm), slot width (S_w=320nm), center-to-center distance between two rows adjacent to the slot (W=1.54($\sqrt{3}$)a), relative lateral shift of the first three rows (s_1=0, s_2=-85nm, s_3=85nm [indicated by the arrows in Fig. 5.2 (a)]) are utilized. A group index (n_g) of 20.4 (±10%) over about 8nm optical wavelength is achieved [37], as shown by Rsoft BandSolve simulations in Fig. 5.2 (d), thereby enabling a relatively large operational optical bandwidth of sensor device compared to non-band-engineered PCW designs with typically narrow optical bandwidth of <1nm at n_g>10 [40]. Note that the large slot width of S_w=320nm in the PCW not only supports a confined optical mode, but also helps in increasing the poling efficiency by suppressing the leakage current in EO polymer poling process [37, 41]. In order to efficiently couple light between the slow-light mode of the slot PCW (n_g~20.4) and the fast-light mode in the slot waveguide at the mode converter end (n_g~3), a PCW taper consisting of non-band-engineered PCW (a=425nm, d=300nm, s_1=0, s_2=0, s_3=0, S_w=320nm) is designed and inserted between the two device components, as indicated in Fig. 5.2 (a), in which W increases parabolically from W=1.45(√3)a to W=1.54(√3)a from the beginning to the end of the PCW taper. Figure.

5.2 (d) shows the n_g variation of the PCW taper over about 8nm wavelength range for the engineered slow-light PCW and the PCW coupler. The colored dashed lines show the gradual increase in the group index from the interface with the mode converter to the interface with the high n_g band-engineered PCW. What is more, a new type of strip-to-slot mode converter [42] is used to couple light between the strip waveguide and the 320nm-wide-slot PCW waveguide more efficiently compared to conventional V-shape mode converters [43]. In addition, subwavelength grating (SWG) couplers [44, 45], as shown in Fig. 5.1 (b), are used to couple light into and out of the device using single mode fibers.

The basic sensing principle is based on the EO modulation inside the EO polymer refilled silicon slot PCWs. The required PCW interaction length for achieving a π phase shift is given as $L=1/(2\sigma)\times(n/\Delta n)\times\lambda/n_g=255.9\mu m$, where $\sigma=0.33$ is the fraction of the energy in the slot calculated using BandSolve simulations, $n=1.63$ is the index of the EO polymer, $\Delta n=0.0007$ is the change in the index of the EO polymer when voltage $V=1V$ is applied, and $\lambda=1550nm$ is the free-space wavelength and $n_g=20.4$ is the group index. The change in the EO polymer index is calculated using $\Delta n=-n^3 r_{33} V/(2S_w)$, where the estimated $r_{33}=100pm/V$ at 1550nm is consistent with the large r_{33} value of 125pm/V of SEO125 thin films at 1.3μm after considering the dispersion factor and the nearly 100% poling efficiency demonstrated in 320nm-wide slots [37]. Therefore, from these calculations, the figure of merit of the modulator is $V_\pi \times L=1V\times 255.9\mu m=0.0256V\times cm$. Such a small $V_\pi \times L$ promises a compact and efficient EO modulator, and thus a highly

sensitive integrated photonic electromagnetic field sensor. The expected effective in-device r_{33} is then calculated as [46]

$$r_{33,effective} = \frac{\lambda S_w}{n^3 V_\pi \sigma L} = \quad 1356\text{pm/V} \tag{5.1}$$

Our another recent work has experimentally demonstrated the $V_\pi \times L$ and effective in-device r_{33} on the same order [37]. Conservatively, the length of the active section of the PCW used in our work is chosen to be 300μm.

5.4 DESIGN OF HIGH-SPEED PHOTONIC CRYSTAL WAVEGUIDE MODULATOR

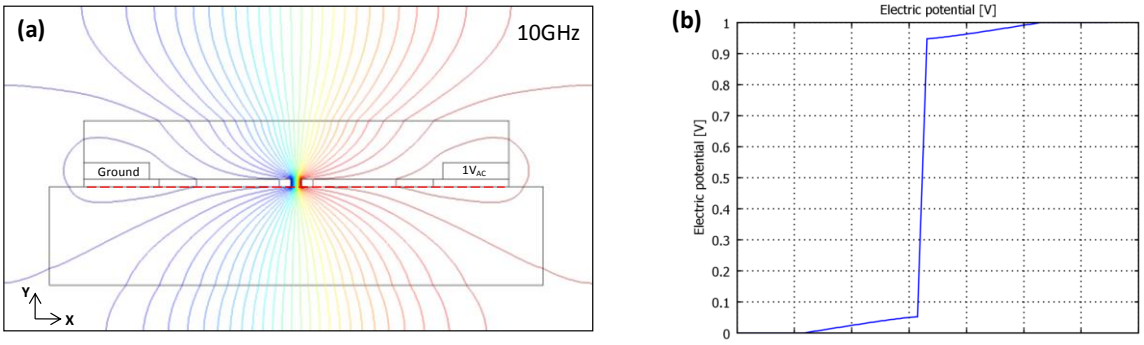

Figure 5.3: (a) Cross-sectional view of RF (10GHz) electric potential distribution across the doped silicon slot PCW filled with EO polymer. (b) Electric potential along the red dashed line in (a), indicating that a large percent of voltage is dropped across the slot filled with EO polymer.

To achieve modulation (or sensing) in GHz frequency regime, both the silicon PCW layer and the bowtie antenna need to be specially designed and carefully optimized.

It is known that the RC time delay of a device is one key factor limiting its operational bandwidth. In order for our sensor to operate at a high frequency, the top silicon layer is doped to reduce the electrical resistivity of the PCW, while maximizing the electric field inside the slot. The designed two-level doping condition in the silicon slot PCW is shown in Fig. 5.1 (e). The resistivity values of the highly-doped silicon (donor, $1\times10^{20}cm^{-3}$) and low-doped (donor, $1\times10^{17}cm^{-3}$) are $9\times10^{-6}\Omega\cdot m$ and $9\times10^{-4}\Omega\cdot m$, respectively [47]. For reference, the intrinsic doping concentration of the undoped top silicon on our SOI wafer is $1\times10^{14}cm^{-3}$. Note that an ion doping concentration of $1\times10^{17}cm^{-3}$ in the waveguide region close to optical mode does not cause significant impurity-induced scattering optical loss [48]. Based on our previous work [17, 41, 49, 50], in the case of 320nm-wide slots, we use the EO polymer resistivity (ρ_{EO}) value of about $10^{8}\Omega\cdot m$ and RF dielectric constant ($\varepsilon_{RF,EO}$) value of 3.2. The change in the RF dielectric constant of silicon ($\varepsilon_{RF,Si}$) due to the doping is also taken into account [51]. Then, effective medium approximations [52] are used for the calculation of both the effective RF dielectric constant ($\varepsilon_{RF,eff}$) and the effective resistivity (ρ_{eff}) in the region of EO polymer refilled silicon PCW shown in Fig. 5.1 (e) [hexagonal lattice, filling factor (volume fraction): f=0.444]. The effective RF dielectric constant (electric field in x-direction) in this region is given as [53].

$$\varepsilon_{RF,eff} = \varepsilon_{RF,Si}\left[\frac{\varepsilon_{RF,EO}(1+f)+\varepsilon_{RF,Si}(1-f)}{\varepsilon_{RF,EO}(1-f)+\varepsilon_{RF,Si}(1+f)}\right] \tag{5.2}$$

The effective resistivity in this region is estimated as [54]

$$\rho_{eff} = \rho_{Si}\left(\frac{1+f}{1-f}\right) \tag{5.3}$$

where, ρ_{si} is the resistivity of un-patterned silicon.

Figure. 5.3 (a) shows the cross-sectional view of the RF electric potential distribution ($1V_{AC}$, 10GHz) across the doped silicon slot PCW, simulated by COMSOL MULTIPHYSICS, with the antenna replaced by perfect conductors. Figure. 5.3 (b) shows that the voltage drop (>90%) mostly occurs inside the slot. As the RF frequency (f_{RF}) increases, the impedance of the slot ($1/(C\omega)$), where C is slot capacitance and $\omega=2\pi f_{RF}$) decreases, and the fraction of the voltage dropped across the slot is reduced due to the finite resistance of the silicon PCW. For this two-level doping condition, a simulation using LUMERICAL DEVICE software shows that the total resistance of our 300 m-long silicon PCW is 189 Ohms and the slot capacitance is 38.6fF, so the limiting RF frequency bandwidth of the device can be estimated to be $1/(2\pi RC)$=22GHz.

5.5 DESIGN OF BROADBAND BOWTIE ANTENNA

As shown in Figs. 5.4 (a) and (b), the antenna is a conventional bowtie antenna with capacitive extension bars attached to the apex points of the bowtie, in order to obtain an extended area with a strong uniform electric field enhancement. The extension bars have a length of 300μm, which is the same as the length of EO polymer refilled slot PCW. The narrow feed gap width between the two capacitive bars is 8.4μm, for the generation of highly enhanced local electric field under RF illumination. The thickness of the gold film is chosen to be 5μm, which is far beyond the skin depth of gold at the RF frequency of operation. This gold antenna is designed with bow arms on silicon dioxide to avoid the impact of conductive silicon region. In the actual device fabricated on an SOI substrate, the top silicon region

everywhere apart from the PCW region is entirely etched away, as shown in Fig. 5.6 (b), letting the buried oxide layer be directly underneath the bow arms to fit this design. The silicon handle underneath the buried oxide layer is taken into account in the simulation.

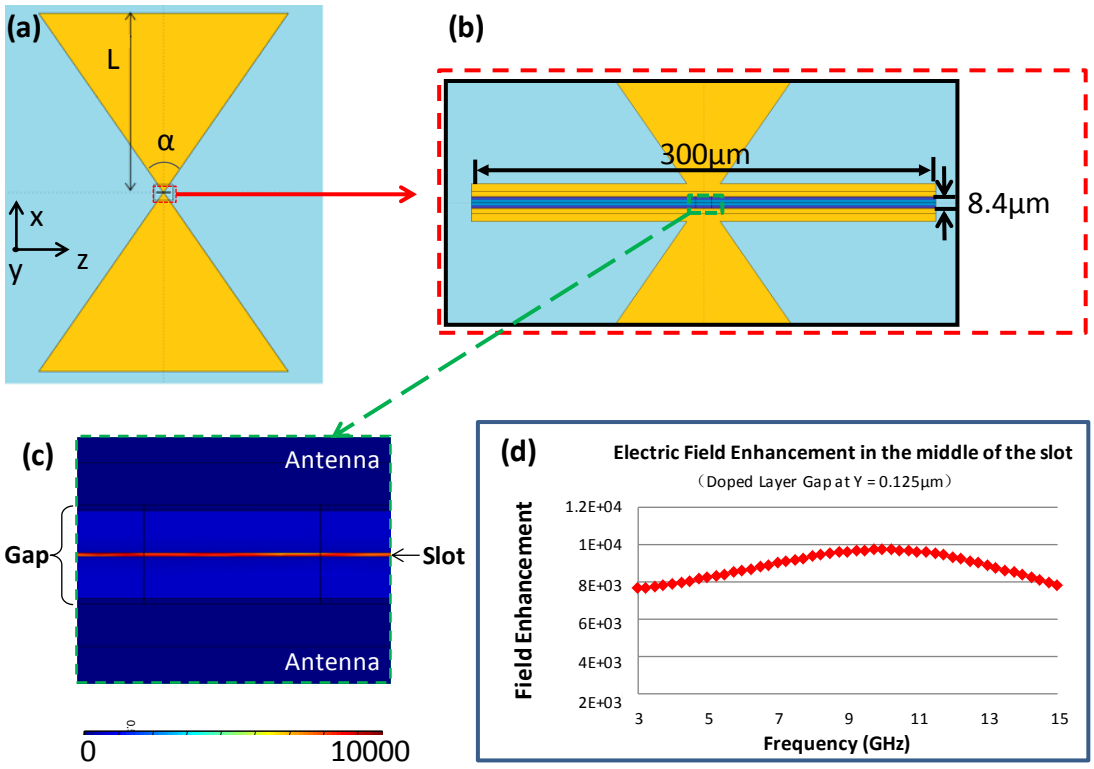

Figure 5.4: (a) Schematic top view of the designed bowtie antenna. Arm length, L=3mm, and flare angle, α=60o. (b) Magnified image of the feed gap region in (a). (c) Top view of electric field enhancement distribution inside the feed gap of the antenna. The electric field enhancement distribution is shown inside the EO polymer refilled slot at y=0.125µm, where y=0 corresponds to the horizontal interface between tsilicon layer and the buried oxide layer. (d) Field enhancement factor inside the slot versus incident RF frequency.

Generally, the antenna system can be considered as a typical LC circuit, which is mainly composed of the inductive bowtie metallic arms and capacitive bars filled with EO polymer, giving rise to an LC resonance determined by antenna geometry [55]. In this work, this resonance effect is characterized by field enhancement (FE) factor, defined as the resonant electric field amplitude (inside the slot) divided by the incident electric field amplitude at the specific observation point. With the feed gap width and capacitive bars fixed, the resonant frequency of a bowtie antenna is mainly determined by the length of each bow arm and the flare angle [L and α in Fig. 5.4 (a)] [56]. This bowtie antenna structure together with the effective-medium approximated silicon RF dielectric constant and conductivity values is used for COMSOL MULTIPHYSICS simulation. With bow arm length L=3mm and flare angle α =60^{o}, the bowtie antenna is optimized with a central resonant frequency at around 10GHz, and a uniform electric field enhancement over the entire feed gap is created. Figures 5.4 (b) and (c) show the top view of the local resonant electric field amplitude inside the antenna feed gap at 10GHz. The electric field is mainly confined in the feed gap region, which is similar to the performance of a typical dipole antenna [57]. Additionally, as explained above, the electric field is actually concentrated inside the slot of the silcon PCW, and this increases the FE even further. Figure 5.4 (d) shows the FE spectrum from simulations, indicating that the electric field radiation compressed inside the slot of the silicon PCW is enhanced by a maximum factor of ~10,000 at 10GHz, with a 1-dB RF bandwidth over 9GHz. This strongly enhanced RF field directly modulates the optical wave propagating along the EO polymer refilled doped silicon slot PCW which is embedded inside the feed gap. No extra connection

lines between the antenna and EO modulator and no external electrical power supply are required [11].

5.6 DEVICE FABRICATION

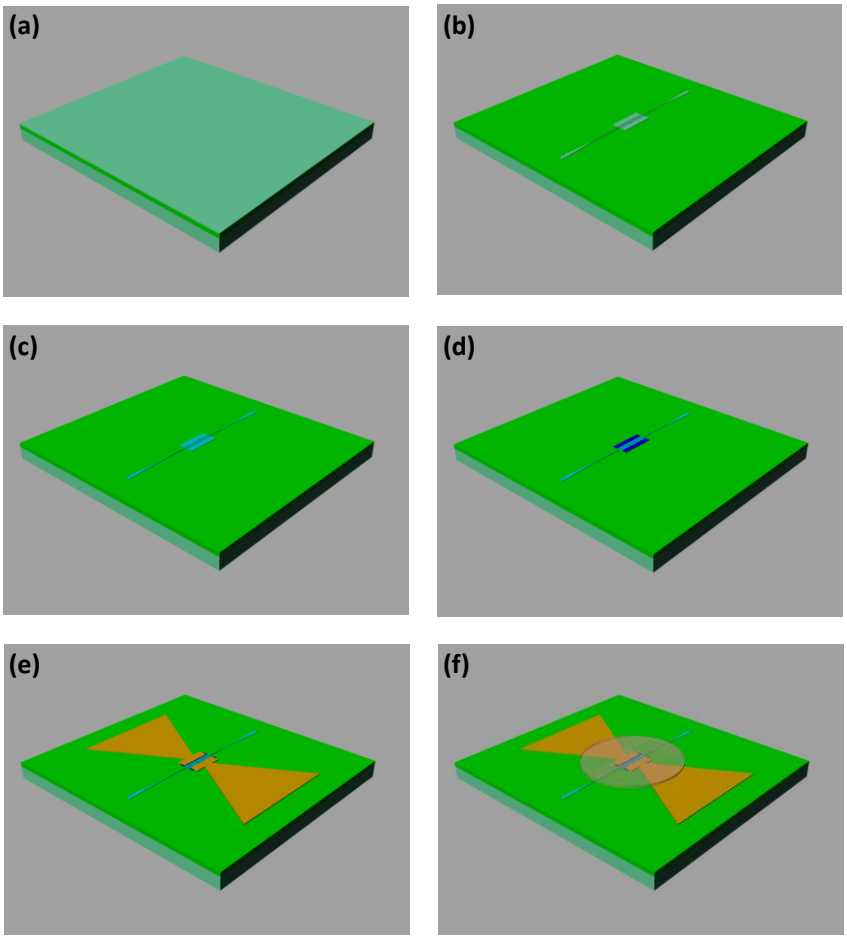

Figure 5.5: Fabrication flow. (a) SOI wafer, (b) Silicon photonic waveguide, patterned by electron-beam lithography, RIE, photolithography, and RIE again, (c) 1st ion implantation, (d) 2nd ion implantation, followed by rapid thermal annealing (e) Gold bowtie antenna, patterned by seed layer deposition, photolithography, electroplating, and seed layer removal, (f) Spincoating of EO polymer (indicated by the circle area), followed by vacuum oven baking and EO polymer poling.

The fabrication flow is briefly illustrated in Fig. 5.5. The fabrication starts with an SOI wafer with a 250nm-thick top silicon and a 3μm-thick buried oxide layer, as shown in Fig. 5.5 (a). The silicon slot PCW is fabricated using electron-beam lithography and reactive ion etching (RIE). Next, all of the top silicon region, except the area with the slot PCW, is completely removed by photolithography and RIE, as shown in Fig. 5.5 (b). Then, the silicon slot PCW is first implanted with P+ at an energy of 92keV and a dose of $1.05\times10^{12}cm^{-2}$ to reach an ion concentration of $1\times10^{17}cm^{-3}$ [Fig. 5.5 (c)]. Next, the device is patterned by photolithography and implanted with P+ at an energy of 92keV and a dose of $1.05\times10^{15}cm^{-2}$ to reach an ion concentration of $1\times10^{20}cm^{-3}$ at the outer sides of the silicon rails which will be connected to the bowtie antenna in order to form Ohmic contacts [Fig. 5.5 (d)]. A rapid thermal annealing at 1000°C for 10min in a nitrogen environment is then performed to annihilate the induced defects and to activate the implanted ions, which also improves the optical performance of the ion-implanted waveguides [58]. Next, a 50nm-thick gold seed layer with a 5nm-thick chromium adhesion buffer is deposited by electron-beam evaporation, and a buffer mask for the bowtie antenna is patterned on a 10μm-thick AZ9260 photoresist using photolithography. Then, a 5μm-thick gold film is electroplated using Techni-Gold 25ES electrolyte under a constant current of 8mA. The AZ9260 buffer mask and gold seed layer are finally removed by lift-off and wet etching, as shown in Fig. 5.5 (e). SEM images of the fabricated device are shown in Figs. 5.6 (a)-(c). The inner sides of the extension bars of

the bowtie antenna are connected to the outer sides of silicon rails which are heavily doped for Ohmic contact between the antenna and the PCW, as shown in Fig. 5.6 (b).

Next, the EO polymer, SEO125, is formulated and filtered. Then a small amount of EO polymer is spincoated onto the device and infiltrated into the holes and the slot of the silicon PCW region, as shown in Fig. 5.5 (f), followed by baking at 80℃ in vacuum oven for 12hrs. Figures. 5.6 (d) and (e) show the SEM images of the cross-sectional view of the slot PCW filled with EO polymer. Figures 5.6 (f) and (g) show the pictures of the real device prior to and after EO polymer spin coating. To align the polymer chromophore noncentrosymmetrically, the EO polymer is poled at a constant electric field of 110V/μm at the EO polymer glass transition temperature of 145℃, in which the bowtie antenna serves as poling electrodes. During this poling process, the monitored leakage current density remains below 8.8 A/m^2 which is comparable to that measured in a thin film configuration (1-10 A/m^2) [37], indicating that the 320nm-wide slot dramatically reduces the leakage current through the silicon/polymer interface compared to sub-100nm slot designs [37, 41].

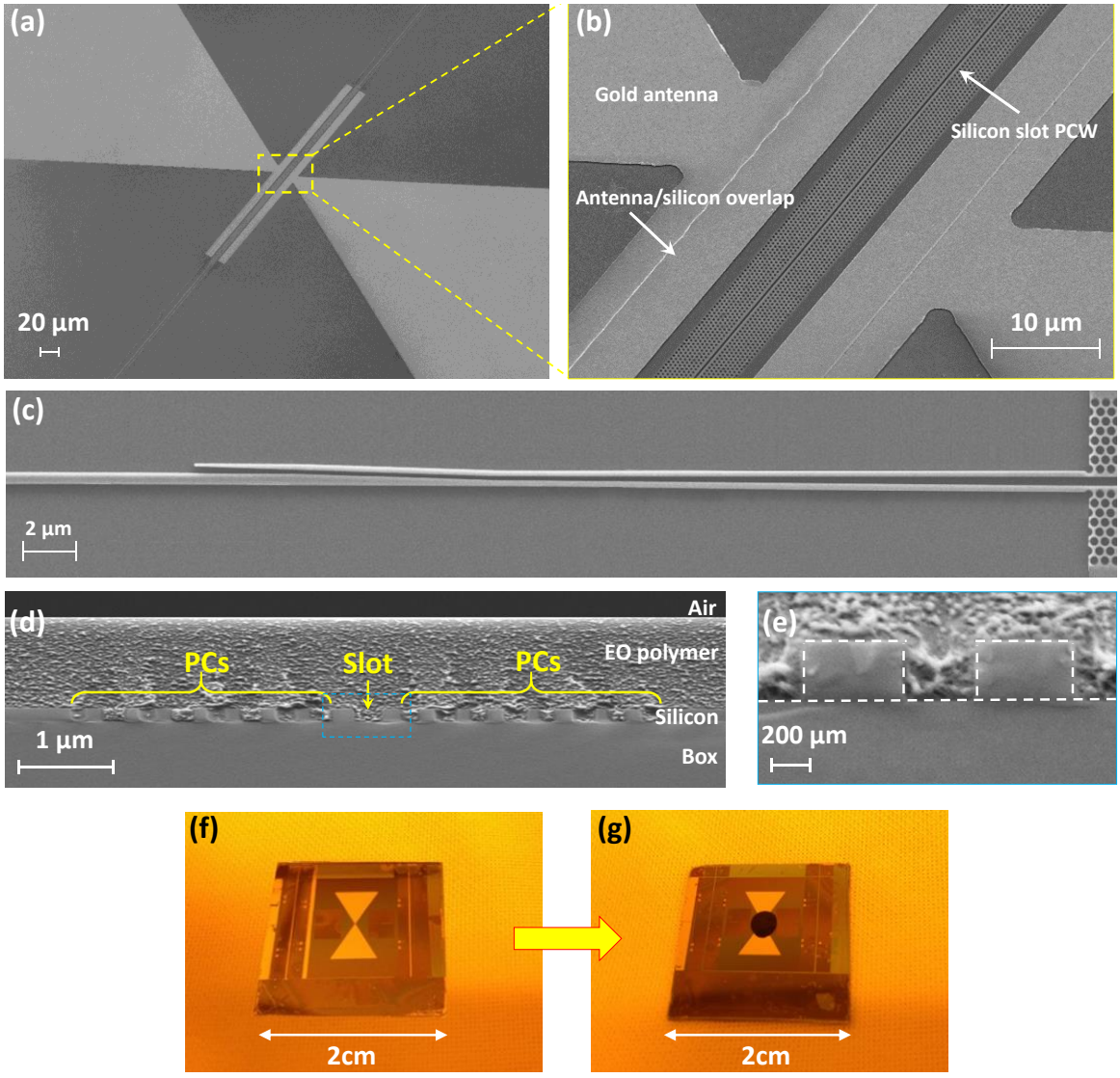

Figure 5.6: (a) SEM image of the fabricated device. (b) Magnified SEM image of the yellow rectangular region in (a) showing the slot PCW region and bowtie antenna overlay. (c) SEM image of the strip-to-slot mode converter for efficient coupling between strip waveguide and the 320nm slot PCW. Note: in (a)-(c) the device is not covered by EO polymer, just for better visualization. (d) SEM image of the cross section of the EO polymer refilled silicon slot PCW. PCs: photonic crystals. (e) Magnified SEM image of the blue rectangular area in (d). (f) Fabricated device prior to EO polymer spincoating. (g) Fabricated device after EO polymer spincoating

5.7 ELECTRO-OPTIC MODULATION TEST

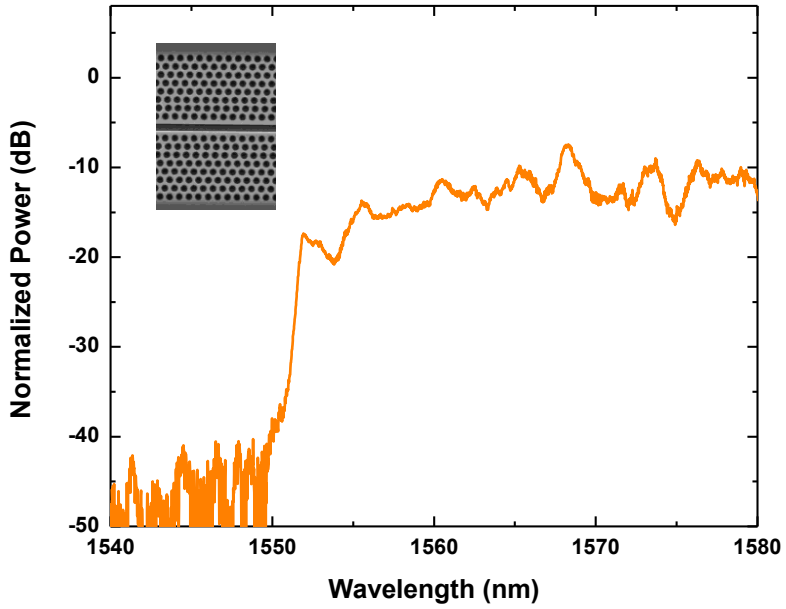

Figure 5.7: Normalized transmission spectrum of the EO polymer refilled silicon slot PCW. The inset shows an SEM image of the fabricated silicon slot PCW.

In order to test the EO polymer refilled silicon slot PCW, light from a broadband amplified spontaneous emission (ASE) source (Thorlabs ASE730) is coupled into and out of the device utilizing an in-house built grating coupler setup [44, 45]. The optical output signal is observed on an optical spectrum analyzer (OSA, Ando AQ6317B). Figure 5.7 shows the measured normalized transmission spectrum of the EO polymer refilled silicon slot PCW. A clear band gap with more than 25dB contrast is observed, indicating efficient coupling into the slot PCW.

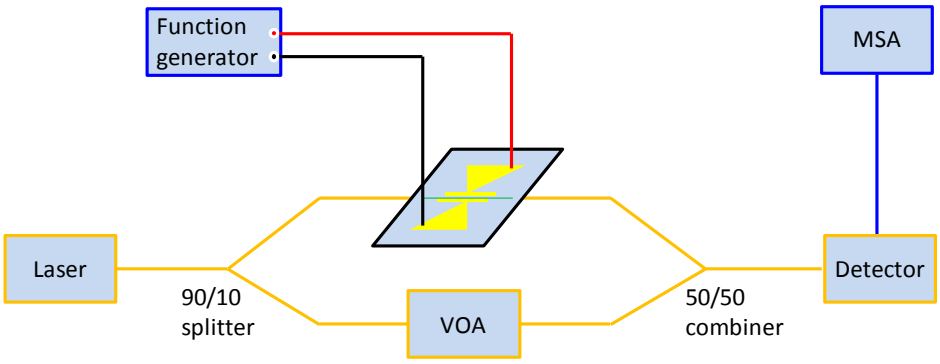

Figure 5.8: The schematic of the system for EO modulation experiment. VOA: variable optical attenuator. MSA: microwave spectrum analyzer.

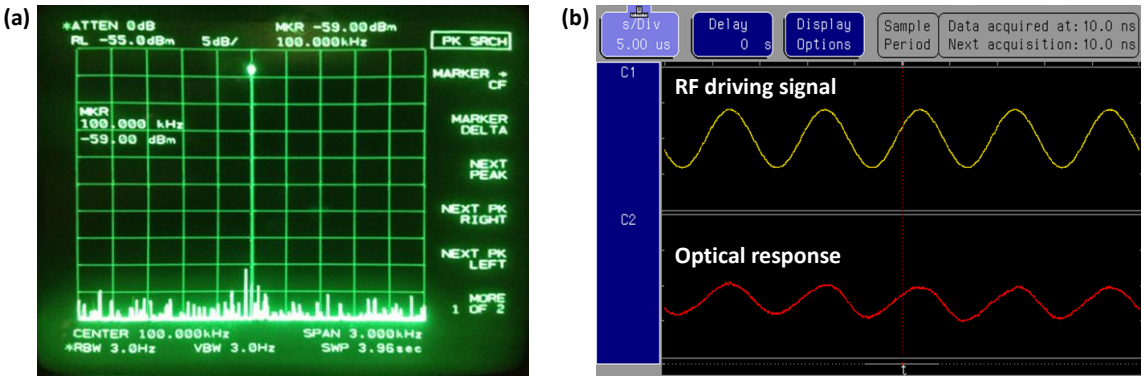

Figure 5.9: (a) The EO modulation response signal as measured on the MSA. (b) EO modulation transfer function.

Next, an EO modulation experiment is performed. An MZI system is formed, using a 90/10 polarization maintaining fiber splitter (Thorlabs L130354603), a 50/50 polarization maintaining fiber combiner (Thorlabs L110313487) and a variable optical attenuator (VOA, Thorlabs VOA50PM-FC), as shown in Fig. 5.8. A low-frequency

modulation test is performed here to verify the functionality of this MZI system.

A tunable laser source (Santec ECL200) is used to provide TE-polarized optical input. The optical wavelength is tuned to 1556nm which is within the low-dispersion region of the band-engineered PCW. The laser input is split by a 90/10 splitter, in which 90% of the optical power is coupled into and out of the sensor device through subwavelength grating (SWG) couplers and 10% goes to the external arm with the VOA. Next, the VOA is adjusted until the optical power at the output of the external arm is equal to that coming out of the sensor device. A 50/50 combiner is then used to combine the optical waves from the two arms, so that the phase modulation can be converted into intensity modulation at the output of this MZI system. A sinusoidal RF signal with a peak-to-peak voltage (V_{pp}) of 1V at a frequency of 100KHz is generated using a function generator (Agilent 33120A) and directly applied across the two arms of the bowtie antenna. In this case, the two arms work as lumped-element driving electrodes and directly modulate the optical waves propagating in the slot PCW embedded in the feed gap of the bowtie antenna. The modulated output optical signal is converted back to an electrical signal using an amplified photodetector (Thorlabs PDA10CS), whose power is measured on a microwave spectrum analyzer (MSA, HP 8563E), as shown in Fig. 5.9 (a). The measured response signal in Fig. 5.9 (a) indicates that the optical signal is modulated at the same frequency as the input RF signal. When the laser is switched off, this response signal on the MSA disappears, confirming that the signal measured by the MSA originates from real EO modulation instead of RF cross talk. This EO modulation

experiment also verfies the successful poling of the EO polymer and the functionality of the MZI system, which is then used in the sensing experiment in Section IV (D).

Another small signal modulation test further demonstrates the validity of the EO modulation, in which an integrated MZI modulator device is fabricated on a chip, with the same EO polymer refilled PCW on both arms [37]. The modulator is driven by a sinusoidal RF signal with V_{pp} <1V at 100KHz. The modulation transfer function is measured by a logic analyzer (HP 1660ES) and shown in Fig. 5.9 (b). In addition, high-frequency modulation was demonstrated in section 4.5 in Chapter 4.

5.8 WIDE BAND ELECTROMAGNETIC WAVE SENSING TEST WITH ULTRA-SENSITIVITY

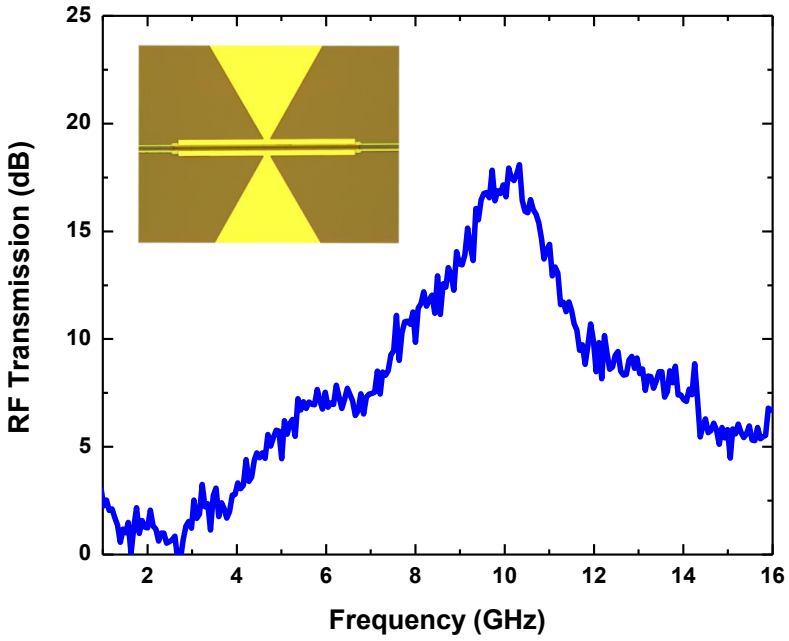

Figure 5.10: Measured transmission signal of the broadband bowtie antenna. The inset shows a top-view microscope image of the fabricated device.

In order to demonstrate the broadband characteristics of the fabricated bowtie antenna, a network analyzer (HP 8510C) is used to measure the S_{11} parameter (reflection coefficient) of the bowtie antenna. A ground-signal (GS) microprobe (Cascade Microtech ACP40GS500) is used to couple RF power from the network analyzer into the bowtie antenna, and the S_{11} parameter over a broad frequency range from 1-16GHz is recorded. Assuming negligible loss, the transmission factor can be inferred from the S_{11} measurements, as shown in Fig. 5.10, from which a broadband response can be clearly seen. The maximum response occurs at 10GHz, which agrees well with the simulated maximum field enhancement at 10GHz in Fig. 5.4 (d). Considering the reciprocity of the bowtie antenna, this result indicates that our sensor can be used to receive the electromagnetic field over a broad frequency bandwidth in the GHz regime.

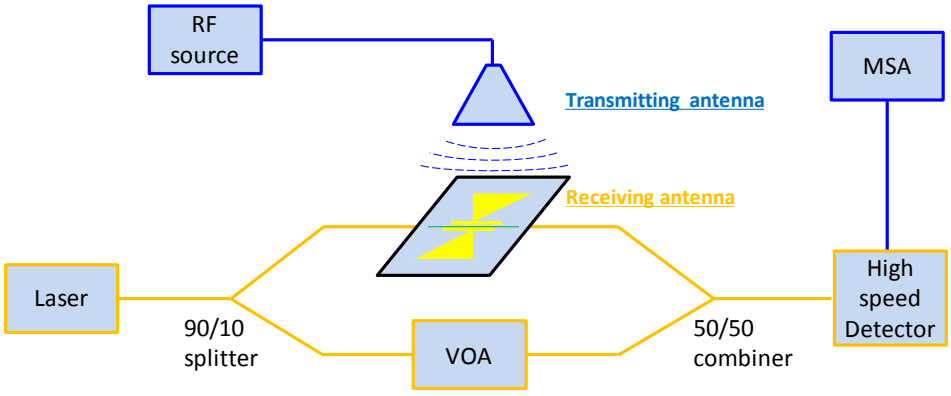

Figure 5.11: The schematic of the system setup for electromagnetic field sensing experiment. VOA: variable optical attenuator. MSA: microwave spectrum analyzer.

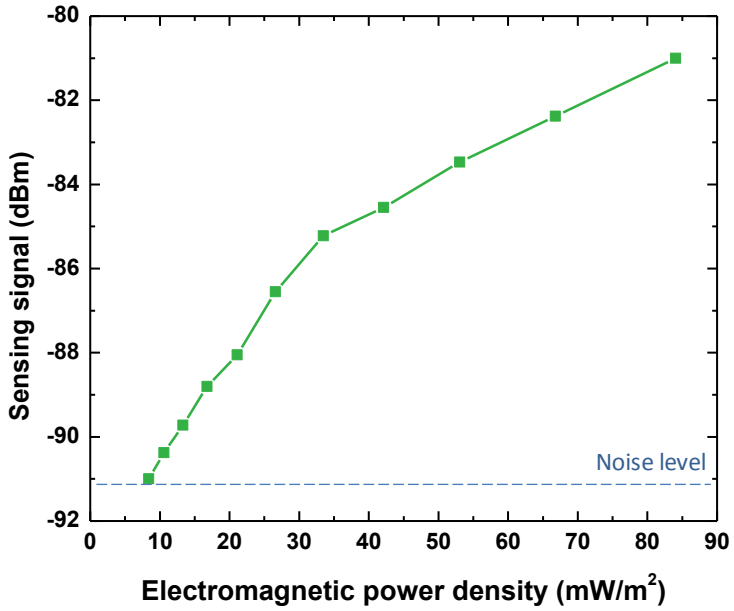

Figure 5.12: The measured sensing signal at 8.4GHz as a function of the electromagnetic power density at the position of sensor device.

The schematic of the experimental system setup for the electromagnetic field sensing is shown in Fig. 5.11. A sweep oscillator (8620C HP, 2-8.4GHz) is used as a high-frequency RF source to provide an RF signal at a frequency of 8.4GHz. This RF signal is applied to an X-band horn antenna with a gain of 6dB. In this case, the horn antenna works as a transmitting antenna to generate electromagnetic field in free space, and the bowtie antenna in our device works as a receiving antenna to detect the electromagnetic field impinging upon it. The horn antenna is placed at a distance of 30cm vertically over the sensor device, which is beyond the far-field distance of the horn antenna so that the electromagnetic waves radiating on the sensor can be treated as plane waves in the following experimental data analysis. To detect the modulated optical signal

at high frequency, a high-speed photodetector (Discovery Semiconductors, DSC40S) is used, and the sensing signal is measured on the MSA.

To characterize the sensitivity of this sensor in terms of electromagnetic power density (or electric field magnitude), the RF power applied on the horn antenna is varied. The corresponding variation in the electromagnetic power density radiating to the position of sensor device is calculated based on Eq. 5.4 [59].

$$S_{avg} = \frac{G_t P_t}{4\pi R^2} \tag{5.4}$$

where S_{avg} is the average Poynting vector (electromagnetic power density, unit: mW/m^2), G_t=6dB is the gain of the transmitting horn antenna, P_t is the input RF power applied on the horn antenna, R=30cm is the distance between the horn antenna and the sensor device. The measured sensing signal as a function of electromagnetic power density is plotted in Fig. 5.12. It can be seen that the sensing signal decreases as the electromagnetic power density decreases. When the electromagnetic power density decreases to $8.4mW/m^2$ (equivalent to the input RF power of 2dBm applied on the horn antenna) at 8.4GHz, the sensing signal is below the noise level. Based on Eq. 5.5, this minimum detectable electromagnetic power density ($8.4mW/m^2$) is used to estimate the minimum detectable electric field amplitude ($|E|$) as 2.5V/m at 8.4GHz, considering the electromagnetic field has a predominantly plane-wave character within the far-field region of the horn antenna [60].

$$|E| = \sqrt{\frac{2S_{avg}}{\varepsilon_0 \varepsilon_r c}} = 2.5\text{V/m} \tag{5.5}$$

where $\varepsilon_0=8.85\times10^{-12}$F/m is the vacuum dielectric constant, $\varepsilon_r\approx1$ is the dielectric constant of air, $c=3\times10^8$m/s is the speed of light. Given the FE, for this incident field, the electric field inside the slot is about 2.5×10^4V/m. In addition, the measurement of the maximum detectable electric field is limited by the upper limit of the output power of the RF source. In practice, the maximum detectable electric field is expected to be very high and is determined by the breakdown electric field of the EO polymer material ($>1\times10^8$V/m). Using the sensitivity defined in Refs. [61, 62], our electromagnetic field sensor has an ultra-high sensitivity of 0.000027V/m $Hz^{-1/2}$ ever demonstrated. As a comparison, other photonic electromagnetic field sensors have lower sensitivity such as 0.61V/m $Hz^{-1/2}$ in Ref. [61] and 7mV/m $Hz^{-1/2}$ in Ref. [62]. The ultra-high sensitivity of our device is attributed to (1) slow-light enhancement by the silicon PCW, (2) large EO coefficient of polymer, and (3) broadband electric field enhancement provided by the bowtie antenna.

As for the electromagnetic field frequency, our sensor has the potential to detect the electromagnetic field over a broad bandwidth, because the bowtie antenna has been demonstrated for broadband operation in GHz frequency regime in section IV (A). Our sensor is also promising for low-frequency electromagnetic field sensing, because an EO activity with ultrahigh r_{33} of 1190pm/V at a modulation frequency of 100kHz has been demonstrated using the same EO polymer refilled slot PCW in our another recent work [37].

5.9 SUMMARY

We design, fabricate and experimentally demonstrate a compact and sensitive integrated photonic electromagnetic field sensor based on EO polymer refilled silicon slot PCW coupled with a miniaturized bowtie antenna. The bowtie antenna is used as receiving antenna, poling electrodes and driving electrodes. The bowtie antenna with doped silicon slot PCW embedded inside its feed gap is demonstrated to have broadband characteristics with a maximum response at 10GHz. Slow-light effects in the PCW, large EO coefficient polymer, as well as broadband electric field enhancement provided by the bowtie antenna, are utilized to enhance the EO modulation efficiency, leading to a very high sensitivity. The minimum detectable electromagnetic power density is demonstrated to be 8.4mW/m2 at 8.4GHz, corresponding to the minimum electric field amplitude of 2.5V/m.

5.10 REFERENCES

[1] P. Drexler and P. Fiala, "Methods for high-power EM pulse measurement," *Sensors Journal, IEEE,* vol. 7, pp. 1006-1011, 2007.

[2] Q. Wu and X. C. Zhang, "Ultrafast electro‐optic field sensors," *Applied Physics Letters,* vol. 68, pp. 1604-1606, 1996.

[3] H. Bassen and G. Smith, "Electric field probes--A review," *Antennas and Propagation, IEEE Transactions on,* vol. 31, pp. 710-718, 1983.

[4] A. Pedersen, C. Cattell, C.-G. Fälthammar, V. Formisano, P.-A. Lindqvist, F. Mozer, and R. Torbert, "Quasistatic electric field measurements with spherical double probes on the GEOS and ISEE satellites," *Space science reviews,* vol. 37, pp. 269-312, 1984.

[5] G. Gustafsson, R. Boström, B. Holback, G. Holmgren, A. Lundgren, K. Stasiewicz, L. Åhlén, F. Mozer, D. Pankow, and P. Harvey, "The electric field and wave experiment for the Cluster mission," in *The Cluster and Phoenix Missions*, ed: Springer, 1997, pp. 137-156.

[6] H. Bassen, C. Bulmer, and W. Burns, "An RF Field Strength Measurement System Using unintegrated Optical Linear Modulator," in *Microwave symposium Digest, 1980 IEEE MTT-S International*, 1980, pp. 317-318.

[7] N. A. Jaeger and L. Young, "High-voltage sensor employing an integrated optics Mach-Zehnder interferometer in conjunction with a capacitive divider," *Lightwave Technology, Journal of,* vol. 7, pp. 229-235, 1989.

[8] W. B. Bridges, F. T. Sheehy, and J. H. Schaffner, "Wave-coupled LiNbO/sub 3/electrooptic modulator for microwave and millimeter-wave modulation," *Photonics Technology Letters, IEEE,* vol. 3, pp. 133-135, 1991.

[9] F. T. Sheehy, W. B. Bridges, and J. H. Schaffner, "60 GHz and 94 GHz antenna-coupled LiNbO3 electrooptic modulators," *IEEE photonics technology letters,* vol. 5, pp. 307-310, 1993.

[10] Y. Wijayanto, H. Murata, and Y. Okamura, "Electro-optic wireless millimeter-wave-lightwave signal converters using planar Yagi-Uda array antennas coupled to resonant electrodes," in *Opto-Electronics and Communications Conference (OECC), 2012 17th*, 2012, pp. 543-544.

[11] Y. N. Wijayanto, H. Murata, and Y. Okamura, "Electrooptic Millimeter-Wave–Lightwave Signal Converters Suspended to Gap-Embedded Patch Antennas on Low-Dielectric Materials," *Selected Topics in Quantum Electronics, IEEE Journal of,* vol. 19, pp. 3400709-3400709, 2013.

[12] A. B. Matsko, A. A. Savchenkov, V. S. Ilchenko, D. Seidel, and L. Maleki, "On the sensitivity of all-dielectric microwave photonic receivers," *Journal of Lightwave Technology,* vol. 28, pp. 3427-3438, 2010.

[13] N. Kuwabara, K. Tajima, R. Kobayashi, and F. Amemiya, "Development and analysis of electric field sensor using LiNbO< sub> 3</sub> optical modulator," *Electromagnetic Compatibility, IEEE Transactions on,* vol. 34, pp. 391-396, 1992.

[14] K. Tajima, R. Kobayashi, N. Kuwabara, and M. Tokuda, "Development of optical isotropic E-field sensor operating more than 10 GHz using mach-zehnder interferometers," *IEICE Transactions on Electronics,* vol. 85 pp. 961-968, 2002.

[15] V. Passaro, F. Dell'Olio, and F. De Leonardis, "Electromagnetic field photonic sensors," *Progress in quantum electronics,* vol. 30, pp. 45-73, 2006.

[16] J. Leuthold, W. Freude, J.-M. Brosi, R. Baets, P. Dumon, I. Biaggio, M. L. Scimeca, F. Diederich, B. Frank, and C. Koos, "Silicon organic hybrid technology—A platform for practical nonlinear optics," *Proceedings of the IEEE,* vol. 97, pp. 1304-1316, 2009.

[17] X. Zhang, B. Lee, C.-y. Lin, A. X. Wang, A. Hosseini, and R. T. Chen, "Highly Linear Broadband Optical Modulator Based on Electro-Optic Polymer," *Photonics Journal, IEEE,* vol. 4, pp. 2214-2228, 2012.

[18] X. Zhang, A. Hosseini, C.-y. Lin, J. Luo, A. K. Jen, and R. T. Chen, "Demonstration of Effective In-device r33 over 1000 pmV in Electro-optic

Polymer Refilled Silicon Slot Photonic Crystal Waveguide Modulator," in *CLEO: Science and Innovations*, 2013, p. CTu2F. 6.

[19] F. E. Doany, C. L. Schow, B. G. Lee, R. Budd, C. Baks, R. Dangel, R. John, F. Libsch, J. A. Kash, and B. Chan, "Terabit/sec-class board-level optical interconnects through polymer waveguides using 24-channel bidirectional transceiver modules," in *Electronic Components and Technology Conference (ECTC), 2011 IEEE 61st*, 2011, pp. 790-797.

[20] X. Zhang, A. Hosseini, X. Lin, H. Subbaraman, and R. T. Chen, "Polymer-based Hybrid Integrated Photonic Devices for Silicon On-chip Modulation and Board-level Optical Interconnects," *IEEE Journal of Selected Topics in Quantum Electronics,* vol. 19, pp. 196-210, 2013.

[21] C.-Y. Lin, A. X. Wang, B. S. Lee, X. Zhang, and R. T. Chen, "High dynamic range electric field sensor for electromagnetic pulse detection," *Optics Express,* vol. 19, pp. 17372-17377, 2011.

[22] L. Jingdong and A. K. Y. Jen, "Highly Efficient Organic Electrooptic Materials and Their Hybrid Systems for Advanced Photonic Devices," *Selected Topics in Quantum Electronics, IEEE Journal of,* vol. 19, pp. 42-53, 2013.

[23] T.-D. Kim, J. Luo, Y.-J. Cheng, Z. Shi, S. Hau, S.-H. Jang, X.-H. Zhou, Y. Tian, B. Polishak, S. Huang, Ma.Hong, L. R. Dalton, and A. K.-Y. Jen, "Binary Chromophore Systems in Nonlinear Optical Dendrimers and Polymers for Large Electrooptic Activities†," *The Journal of Physical Chemistry C,* vol. 112, pp. 8091-8098, 2008.

[24] R. Soref, "The past, present, and future of silicon photonics," *Selected Topics in Quantum Electronics, IEEE Journal of,* vol. 12, pp. 1678-1687, 2006.

[25] B. Jalali and S. Fathpour, "Silicon photonics," *Lightwave Technology, Journal of,* vol. 24, pp. 4600-4615, 2006.

[26] T. Baba, "Slow light in photonic crystals," *Nature Photonics,* vol. 2, pp. 465-473, 2008.

[27] Y. A. Vlasov, M. O'Boyle, H. F. Hamann, and S. J. McNab, "Active control of slow light on a chip with photonic crystal waveguides," *Nature,* vol. 438, pp. 65-69, 2005.

[28] X. Zhang, A. Hosseini, J. Luo, A. K.-Y. Jen, and R. T. Chen, "Hybrid silicon-electro-optic-polymer integrated high-performance optical modulator," in *SPIE Photonic West, OPTO*, 2014, pp. 89910O-89910O-6.

[29] Y. Jiang, W. Jiang, L. Gu, X. Chen, and R. T. Chen, "80-micron interaction length silicon photonic crystal waveguide modulator," *Applied Physics Letters,* vol. 87, p. 221105, 2005.

[30] X. Zhang, A. Hosseini, H. Subbaraman, S. Wang, Q. Zhan, J. Luo, A. K. Jen, and R. Chen, "Wideband electromagnetic wave sensing using electro-optic polymer infiltrated silicon slot photonic crystal waveguide," in *CLEO: Science and Innovations*, 2014, p. SM2M. 5.

[31] X. Zhang, A. Hosseini, H. Subbaraman, J. Luo, A. Jen, R. Nelson, and R. T. Chen, "Broadband low-power optical modulator based on electro-optic polymer Infiltrated Silicon Slot Photonic Crystal Waveguide," in *Frontiers in Optics*, 2014, p. FTu1D. 4.

[32] J. H. Wülbern, S. Prorok, J. Hampe, A. Petrov, M. Eich, J. Luo, A. K.-Y. Jen, M. Jenett, and A. Jacob, "40 GHz electro-optic modulation in hybrid silicon–organic slotted photonic crystal waveguides," *Optics letters,* vol. 35, pp. 2753-2755, 2010.

[33] L. Alloatti, D. Korn, R. Palmer, D. Hillerkuss, J. Li, A. Barklund, R. Dinu, J. Wieland, M. Fournier, J. Fedeli, H. Yu, W. Bogaerts, P. Dumon, R. Baets, C. Koos, W. Freude, and J. Leuthold, "42.7 Gbit/s electro-optic modulator in silicon technology," *Optics Express,* vol. 19, pp. 11841-11851, 2011.

[34] S. Wang and Q. Zhan, "Modified bow-tie antenna with strong broadband field enhancement for RF photonic applications," in *SPIE NanoScience+ Engineering*, 2013, pp. 88061V-88061V-6.

[35] X. Zhang, S. Wang, H. Subbaraman, Q. Zhan, Z. Pan, C.-j. Chung, H. Yan, and R. T. Chen, "Integrated broadband bowtie antenna on transparent substrate," in *SPIE OPTO*, 2015, pp. 93620P-93620P-8.

[36] D. Marpaung, C. Roeloffzen, R. Heideman, A. Leinse, S. Sales, and J. Capmany, "Integrated microwave photonics," *Laser & Photonics Reviews,* vol. 7, pp. 506-538, 2013.

[37] X. Zhang, A. Hosseini, S. Chakravarty, J. Luo, A. K. Y. Jen, and R. T. Chen, "Wide optical spectrum range, subvolt, compact modulator based on an electro-optic polymer refilled silicon slot photonic crystal waveguide," *Optics letters,* vol. 38, pp. 4931-4934, 2013.

[38] X. Zhang, A. Hosseini, X. Xu, S. Wang, Q. Zhan, Y. Zou, S. Chakravarty, and R. T. Chen, "Electric field sensor based on electro-optic polymer refilled silicon slot photonic crystal waveguide coupled with bowtie antenna," in *SPIE Photonic West 2013: Terahertz, RF, Millimeter, and Submillimeter-Wave Technology and Applications VI*, 2013, p. 862418.

[39] A. Hosseini, X. Xu, H. Subbaraman, C.-Y. Lin, S. Rahimi, and R. T. Chen, "Large optical spectral range dispersion engineered silicon-based photonic crystal waveguide modulator," *Opt. Express,* vol. 20, pp. 12318-12325, 2012.

[40] H. C. Nguyen, Y. Sakai, M. Shinkawa, N. Ishikura, and T. Baba, "10 Gb/s operation of photonic crystal silicon optical modulators," *Optics Express,* vol. 19, pp. 13000-13007, 2011/07/04 2011.

[41] X. Wang, C.-Y. Lin, S. Chakravarty, J. Luo, A. K.-Y. Jen, and R. T. Chen, "Effective in-device r33 of 735 pm/V on electro-optic polymer infiltrated silicon photonic crystal slot waveguides," *Optics letters,* vol. 36, pp. 882-884, 2011.

[42] X. Zhang, H. Subbaraman, A. Hosseini, and R. T. Chen, "Highly efficient mode converter for coupling light into wide slot photonic crystal waveguide," *Optics Express,* vol. 22, pp. 20678-20690, 2014.

[43] Z. Wang, N. Zhu, Y. Tang, L. Wosinski, D. Dai, and S. He, "Ultracompact low-loss coupler between strip and slot waveguides," *Optics letters,* vol. 34, pp. 1498-1500, 2009.
[44] X. Xu, H. Subbaraman, J. Covey, D. Kwong, A. Hosseini, and R. T. Chen, "Complementary metal–oxide–semiconductor compatible high efficiency subwavelength grating couplers for silicon integrated photonics," *Applied Physics Letters,* vol. 101, pp. 031109-031109-4, 2012.
[45] H. Subbaraman, X. Xu, J. Covey, and R. T. Chen, "Efficient light coupling into in-plane semiconductor nanomembrane photonic devices utilizing a sub-wavelength grating coupler," *Optics Express,* vol. 20, pp. 20659-20665, 2012.
[46] A. Yariv and P. Yeh, *Optical waves in crystal propagation and control of laser radiation*: Wiley-Interscience, 1983.
[47] S. K. Ghandhi, *VLSI fabrication principles: silicon and gallium arsenide*: John Wiley & Sons, 2008.
[48] J. Doylend, P. Jessop, and A. Knights, "Optical attenuation in ion-implanted silicon waveguide racetrack resonators," *Opt. Express19 (16),* pp. 14913-14918, 2011.
[49] X. Lin, T. Ling, H. Subbaraman, X. Zhang, K. Byun, L. J. Guo, and R. T. Chen, "Ultraviolet imprinting and aligned ink-jet printing for multilayer patterning of electro-optic polymer modulators," *Optics letters,* vol. 38, pp. 1597-1599, 2013.
[50] H. Subbaraman, X. Lin, T. Ling, X. Zhang, L. J. Guo, and R. T. Chen, "Printable EO Polymer Modulators," in *CLEO: Science and Innovations*, 2013, p. CW1O. 2.
[51] S. Ristić, A. Prijić, and Z. Prijić, "Dependence of static dielectric constant of silicon on resistivity at room temperature," *Serbian Journal of Electrical Engineering,* vol. 1, pp. 237-247, 2004.
[52] T. C. Choy, *Effective medium theory: principles and applications*: Oxford University Press, 1999.
[53] D. Gao and Z. Zhou, "Nonlinear equation method for band structure calculations of photonic crystal slabs," *Applied Physics Letters,* vol. 88, p. 163105, 2006.
[54] W. Perrins, D. McKenzie, and R. McPhedran, "Transport properties of regular arrays of cylinders," *Proceedings of the Royal Society of London. A. Mathematical and Physical Sciences,* vol. 369, pp. 207-225, 1979.
[55] C. A. Balanis, *Antenna theory: analysis and design*: John Wiley & Sons, 2012.
[56] J. D. Kraus and R. J. Marhefka, *Antenna for all applications*, 3rd ed.: McGraw-Hill 2002.
[57] H. Duan, A. I. Fernández-Domínguez, M. Bosman, S. A. Maier, and J. K. Yang, "Nanoplasmonics: classical down to the nanometer scale," *Nano letters,* vol. 12, pp. 1683-1689, 2012.
[58] O. Peña-Rodríguez, J. Olivares, M. Carrascosa, Á. García-Cabañes, A. Rivera, and F. Agulló-López, "Optical Waveguides Fabricated by Ion Implantation/Irradiation: A Review," *Ion Implantation, Prof. Mark Goorsky (Ed.), ISBN,* pp. 978-953, 2012.

[59] D. M. Pozar, *Microwave engineering*, 4th ed.: Wiley, 2011.
[60] A. Chen and E. J. Murphy, *Broadband optical modulators: science, technology, and applications*: CRC Press, 2011.
[61] D. Perry, S. Chadderdon, R. Gibson, B. Shreeve, R. H. Selfridge, S. M. Schultz, W. C. Wang, R. Forber, and J. Luo, "Electro-optic polymer electric field sensor," in *SPIE Smart Structures and Materials+ Nondestructive Evaluation and Health Monitoring*, 2011, pp. 79820Q-79820Q-8.
[62] W. C. Wang, H. Lotem, R. Forber, and K. Bui, "Optical electric-field sensors," *Optical Engineering,* vol. 45, pp. 124402-124402-8, 2006.

Chapter 6: Integrated broadband bowtie antenna on transparent silica substrate

6.1 INTRODUCTION

In recent years, bowtie antennas have been a hot topic for intense theoretical and experimental investigation, impelled by its unique features and advantages, including simple planar structure, stable broadband performance, strong near-field enhancement [1-13]. One simple configuration used to achieve broadband characteristics is a biconical antenna formed by two cones, and the bowtie antenna is a simplified two-dimensional structure using two triangular shapes separated with a small gap that resembles the shape of a bowtie [14, 15]. The bowtie antenna concentrates the energy and provides a good localization of electric field inside the feed gap, providing a strong near-field enhancement [16, 17], which is useful for several applications, including optical sensing and energy harvesting [2, 18-20]. In addition, the resonant frequency of a bowtie antenna can be designed and tuned by appropriately modifying and scaling the bowtie geometry, such as the arm length, the flare angle, and the feed gap width. This enables the bowtie antenna to have various applications over a wide frequency range, including extreme-ultraviolet light generation [1], local optical absorption [2], Terahertz-wave near-field imaging [3], mid-infrared plasmonic antennas [4], microwave radar [5], wireless communications [6], and flexible RF devices [7].

A modified gold bowtie antenna on lithium niobate (LiNbO3) substrate has been theoretically studied previously for microwave photonic applications [21]. The structure of this antenna is a conventional bowtie shape with extension bars attached to its apex points. Under RF illumination, an extended near-field area with a uniformly enhanced local electric field is obtained in its feed gap. Recently, such an optimized bowtie antenna has been integrated with an electro-optic modulator in its feed gap to form a very sensitive electromagnetic wave sensor [22, 23]. For the detection of electromagnetic waves, the interaction of the waves and the substrate materials needs to be considered. In this case, a low-k dielectric substrate, such as a silica substrate (dielectric constant is about ε_r=3.9), is desired to provide better microwave coupling, because the size of the antenna is proportional to $1/\sqrt{\varepsilon_{eff}}$ [21] and thus a low-k substrate would allow for a larger antenna and higher received power [23]. In addition, some electromagnetic wave detectors previously demonstrated on silicon-on-insulator (SOI) substrates [22, 24] suffer from unwanted reflection and scattering from backside silicon handle [25], while, in comparison, a silica substrate can avoid this issue and improve the detection sensitivity [26]. Furthermore, nowadays there is an emerging science and technology field focusing on integrated electronic and photonic devices on transparent substrates and even transparent devices, which not only produces 'invisible' circuitry but also provides improved device performance [27] such as improved near-field enhancement of a bowtie antennas on a silica substrate. These transparent devices have also been widely used in many different areas such as thin-film transistors [28], memories [29], displays [30], solar

cells [31], light emitting diodes [32], sensors [33], and so on. Therefore, a cost-effective transparent low-k silica substrate is used in this work.

In order to provide a guide for further development and better optimization of this type of bowtie antenna on silica substrate, more detailed theoretical and experimental investigations on this type of bowtie antennas with different geometrical parameters are required. Especially, experiments need to be performed to verify the theoretical analysis. In this paper, we design, fabricate and experimentally characterize a modified gold bowtie antenna on transparent silica substrate working for X-band. We targeted around an operating frequency of 10.5GHz which is close to the center of X-band, and this optimized antenna will be used for the electromagnetic wave sensors in Ref. [22]. The designed bowtie antenna is miniaturized with an area smaller than $1cm^2$. The electric-field enhancing capability of the bowtie antenna is investigated by numerical simulations. Its geometry-dependent resonant frequency is simulated, and then it is experimentally verified on a group of fabricated bowtie antennas on silica substrate. The radiation pattern of this bowtie antenna is also measured.

6.2 DESIGN OF A BOWTIE ANTENNA WITH BROADBAND FIELD ENHANCEMENT

A schematic of the modified bowtie antenna on silica substrate is shown in Fig. 6.1, consisting of a conventional bowtie antenna with capacitive extension bars attached to the apex points of the bowtie [21]. The extension bars have a length, b=300μm, a width, w=10μm and a feed gap, g=10μm. The thickness of the gold film is chosen to be t=5μm, which is far beyond the skin depth of gold at the RF frequency of operation. The thickness of silica

substrate is 1mm, which is not thick enough to adversely affect the broadside radiation of the X-band antenna. Under RF illumination, highly enhanced local electric field is generated inside the feed gap of this bowtie antenna. The current on the bowtie antenna surface, induced by incident RF field, charges the feed gap and subsequently establishes this strong electric field in the feed gap [34]. Generally, the antenna system can be considered as a typical LC circuit, which is mainly composed of the inductive bowtie metallic arms and the capacitive bars, giving rise to an LC resonance determined by the antenna geometry. In this work, this resonance effect is characterized by field enhancement factor, defined as the resonant electric field amplitude at a specific observation point [red dot in Figs. 6.1 (b) and (c)] divided by the incident electric field amplitude. With the feed gap (g=10μm) and capacitive bars (b=300μm, and w=10μm) fixed, the resonant frequency of a bowtie antenna is mainly determined by the length of each bow arm and the flare angle [l and α in Fig. 6.1 (b)] [35].

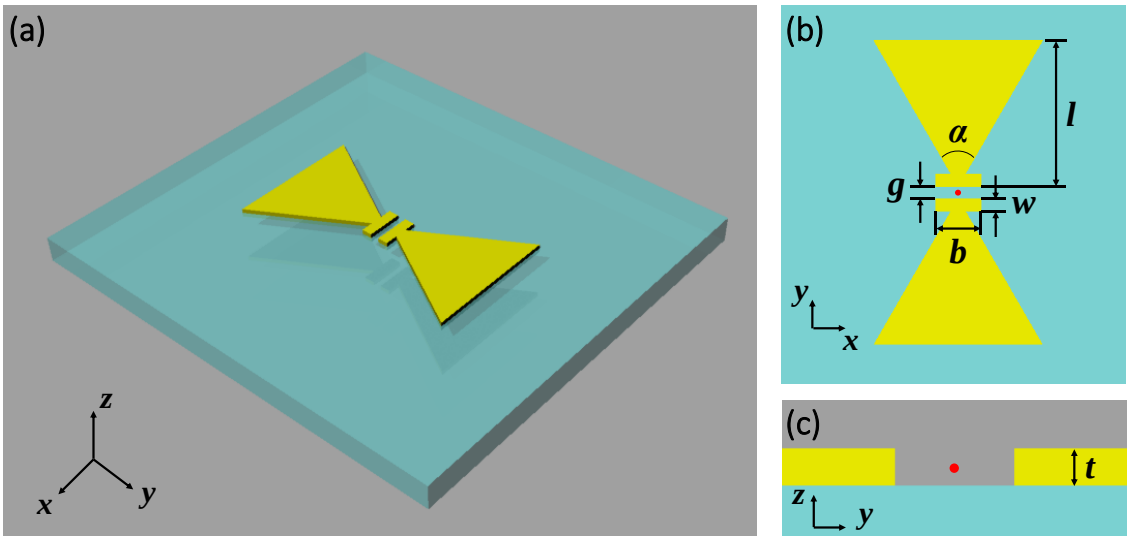

Figure 6.1: continued next page.

Figure 6.1: (a) 3D perspective of our modified gold bowtie antenna on a transparent silica substrate. (b) Top view of the bowtie antenna. *l*: arm length; α: flare angle; *g*: feed gap; *w*: bar width; *b*: bar length. (c) Cross-sectional view of the bowtie antenna. *t*: antenna thickness. The red dot in the center of the feed gap at middle height indicates the observation point for the simulation of electric field enhancement.

COMSOL Multiphysics is used to simulate this bowtie antenna model. The incident electric field is a normalized continuous plane wave linearly polarized along the antenna axis (y-direction) and impinges upon the antenna from the top. Simulation results show that, with the bow arm length l=5.5mm and the flare angle α =60^o, the bowtie antenna has a maximum field enhancement around a resonant frequency of 10.5GHz, and a uniform broadband electric field enhancement over the entire feed gap is created. Fig. 6.2 (a) shows the simulated field enhancement of this bowtie (l=5.5mm, α =60^o) as a function of frequency, indicating that the electric field radiation compressed inside the feed gap is enhanced by a maximum factor of ~688 at 10.5GHz, with a 1-dB RF bandwidth over 9GHz. Figs. 6.2 (b) and (c) show both the top view and the side view of the simulated normalized local electric field amplitude at the resonant frequency. The polarization of the electric field is along the x direction in Figs. 6.2 (b) and (c). The electric field is mainly confined in the feed gap region, and the peak resonant frequency can be tuned by adjusting the arm length and the flare angle of the bowtie antenna. The simulated resonant frequencies at different arm lengths and flare angles are shown in Figs. 6.6 (b) and (d), respectively, and will be correlated with experimental results in Section IV. More detailed theoretical analysis of the geometry-dependent performance of bowtie antennas can be found in Refs. [9, 17, 36].

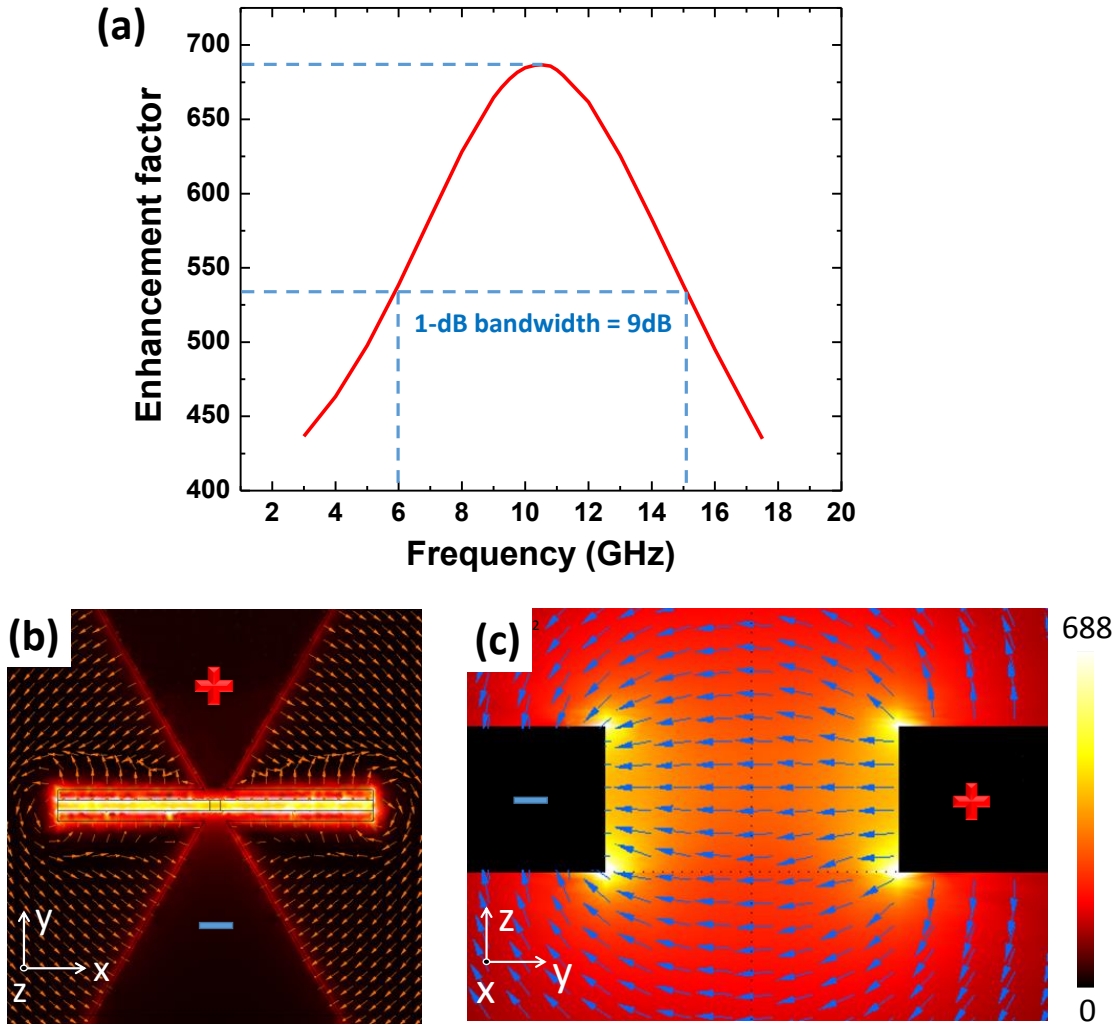

Figure 6.2: (a) The simulated field enhancement spectrum for a bowtie antenna with the arm length of 5.5mm and the flare angle of 60°, indicating a field enhancement factor of ~688 at 10.5GHz and a 1-dB RF bandwidth over 9GHz. (b) Top view of the simulated normalized electric field enhancement distribution at the resonant frequency. (c) Cross-sectional view of the simulated electric field enhancement distribution at the resonant frequency.

6.3 ANTENNA FABRICATION

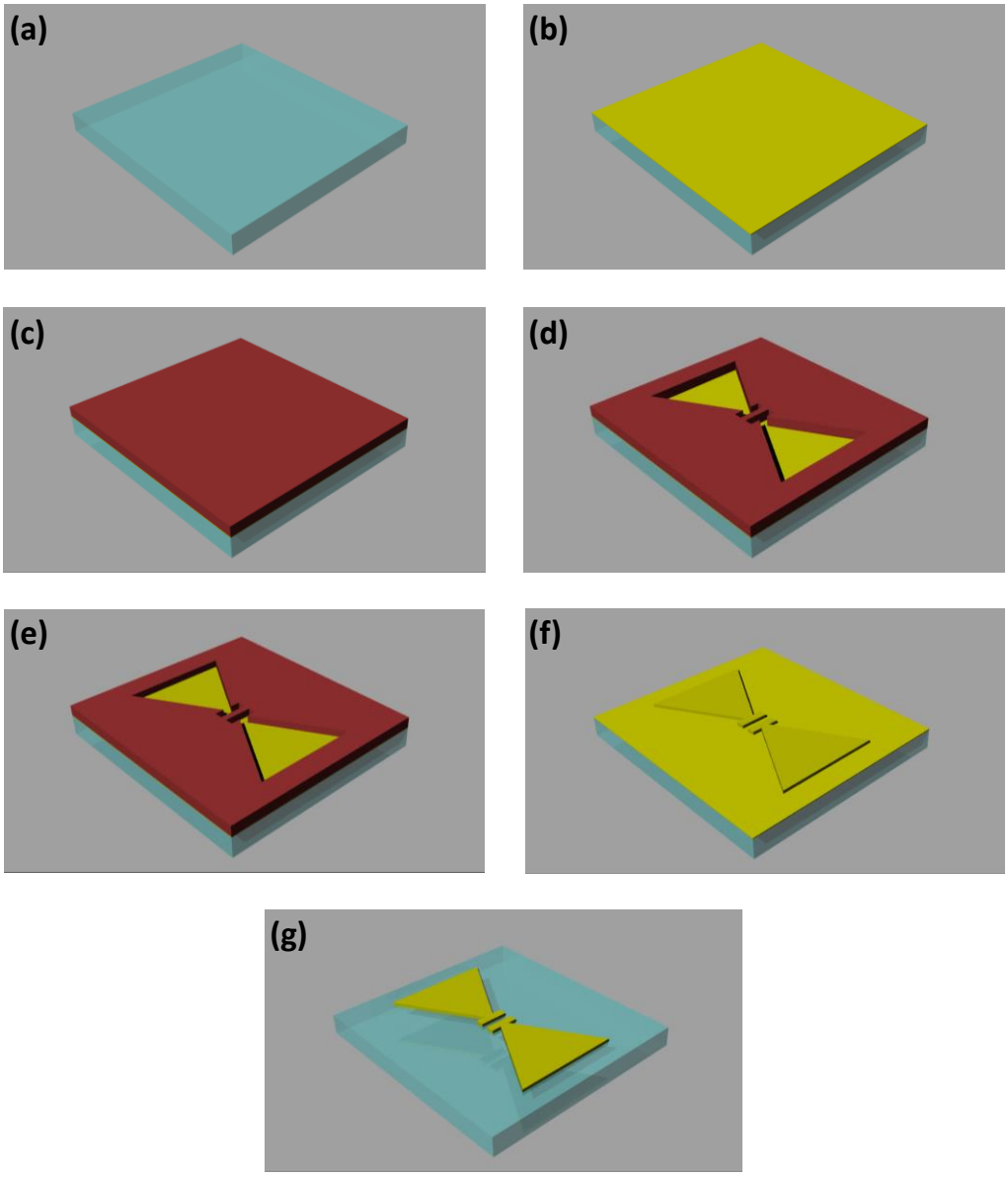

Figure 6.3: Fabrication process. (a) A silica substrate. (b) Seed layer deposition. (c) Photo resist spincoating. (d) Photolithogprahy. (e) Electroplating. (f) Photo resist removal. (g) Seed layer removal.

Two groups of bowtie antennas are fabricated on 1mm-thick silica substrates (Fisher Scientific 12-550C, ε_r=3.9) through standard CMOS manufacturing process. The first group of five bowtie antennas is fabricated with a fixed flare angle of 60 degrees, but arm lengths varying from 3.5mm to 5.5mm in steps of 0.5mm. The second group of three bowtie antennas has a fixed arm length of 4.5mm, but flare angles of 30 degrees, 60 degrees and 90 degrees, respectively. A schematic process flow of fabrication is shown in Fig. 6.3. A 50nm-thick gold seed layer with a 5nm-thick chromium adhesion buffer is deposited on the silica substrate by electron-beam evaporation. A 10μm-thick AZ-9260 photoresist is spincoated on the seed layer and baked at 90°C for 2 min and then at 110°C for 2min. A buffer mask for the bowtie structure is patterned by photolithography (dose: 260mJ/cm^2) and AZ400K developer (diluted 1:4). Next, a 5μm-thick gold film is electroplated by through-mask plating method in a neutral noncyanide electrolyte (Techni-Gold 25ES) under a constant current of 8mA at the temperature around 50°C. A platinum plated titanium mesh serves as the anode and sample is connected to the cathode. The solution is stirred by a magnetic stirrer to keep the concentration of the solution uniform. The resulting electroplating speed is 40~50nm/min depending on the feature size of the buffer mask. After electroplating, the buffer mask is removed using Acetone and then the gold seed layer is removed using wet etchant, leaving the electroplated gold bowtie structure on top of the transparent silica substrate. The conductivity of the electroplated gold film is measured to be 2.2×10^7S/m. Microscope images of a few fabricated devices are shown in Fig. 6.4.

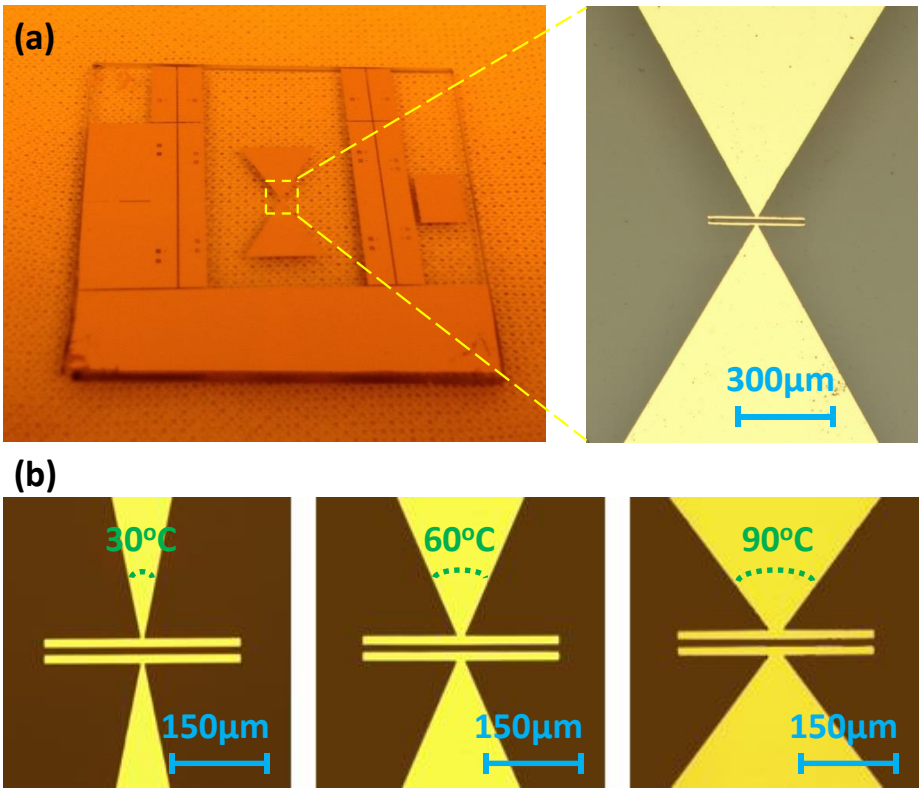

Figure 6.4: (a) A fabricated bowtie antenna on silica substrate. (b) Three bowtie antenna with flare angles of 30 degrees, 60 degrees and 90 degrees, respectively. For all these three bowtie antennas, the arm length *l*=4.5mm, the extended bar length b=300µm, extended bar width w=10µm, and the feed gap g=10µm.

6.4 DEMONSTRATION OF GEOMETRY DEPENDENT RESONANCE FREQUENCY

First, a fabricated bowtie antenna with arm length of 5.5mm and flare angle of 60° is tested as a receiving antenna. RF signal at 10.5GHz from a vector network analyzer (HP 8510C) is applied to an X-band horn antenna which is mounted on top of the fabricated bowtie antenna. The horn antenna is placed sufficiently away in its far-field for

the assumption of quasi-plane wave to hold. The electromagnetic power that the bowtie antenna receives is measured by a microwave spectrum analyzer (HP 8560E) via a ground-signal (GS) microprobe (Cascade Microtech ACP40GS500) which contacts the bow arms of the bowtie. Figure. 6.5 shows the received power of the bowtie antenna. The power response is about 30dB above the noise floor at 10.5GHz. This simple test demonstrates the functionality of the fabricated bowtie antenna. Due to the reciprocity, the bowtie antenna should also work well as a transmitting antenna, which will be demonstrated in the next test.

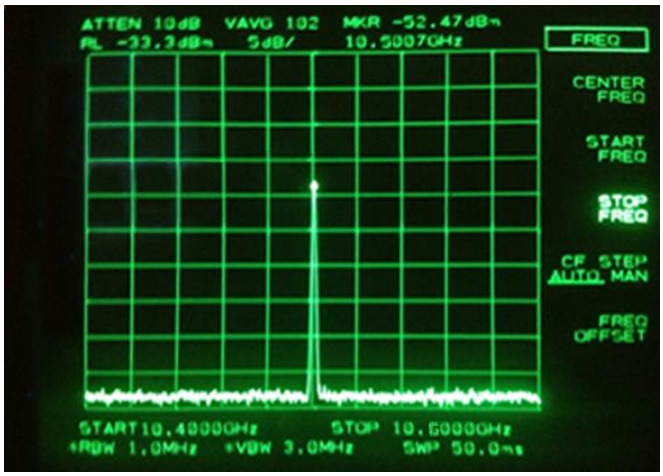

Figure 6.5: Measured response power of the bowtie antenna as a receiving antenna at 10.5GHz.

Next, in order to demonstrate the broadband characteristics of the fabricated bowtie antenna and to investigate the dependence of resonant frequency on the bowtie

geometry, the two groups of bowtie antennas are tested as transmitting antennas. The vector network analyzer is used to measure the S_{11} parameter (reflection signal) of these antennas over a broad frequency range of 1-20GHz via the GS microprobe. Assuming negligible loss, the normalized transmission signal can be inferred from the S_{11} measurements, as shown in Figs. 6.6 (b) and (d), from which a broadband response can be clearly seen. The measured transmission signals of the first group of bowtie antennas are shown in Fig. 6.6 (a). The measured resonant frequency as a function of arm lengths is extracted from the figure, and then correlated with the simulated resonant frequency, as shown in Fig. 6.6 (b). Similarly, the measured resonant frequency as a function of flare angles is extracted from the measured transmission signals of the second group of bowtie antennas in Fig. 6.6 (c), and then correlated with simulated resonant frequency in Fig. 6.6 (d). For longer bowtie arm or larger flare angle, the current flows through longer path to the gap, so the effective antenna size is increased, leading to longer resonant RF wavelength, which corresponds to lower resonant frequency. The trend in measurement results agree with the simulations. It can be seen that there are still some deviations between the measured and simulated resonant frequencies. This could be due to several reasons, such as the difference of the dielectric constant of an actual silica substrate and that assumed in simulations, and slight variations of size and shape of fabricated bowtie antenna from idealized model due to fabrication error.

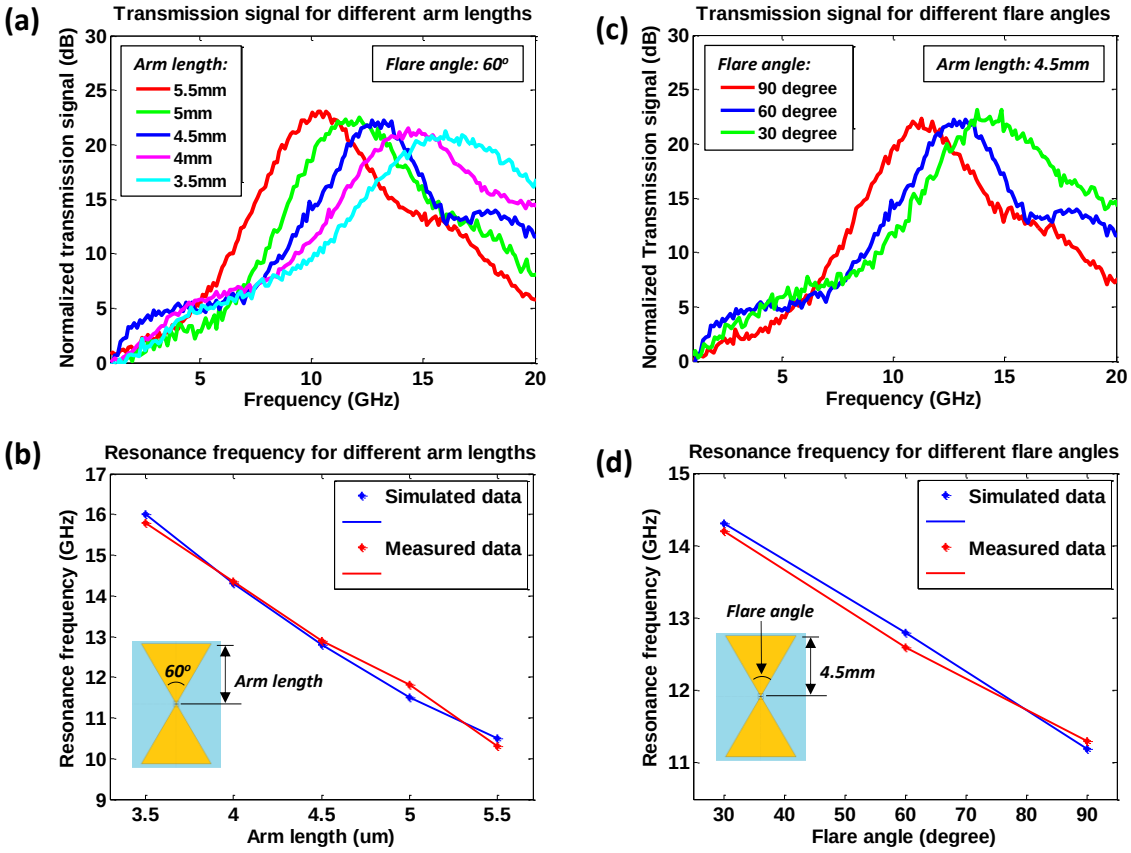

Figure 6.6: (a) Measured normalized transmission spectrum of bowtie antennas with different arm lengths. (b) Correlation of measured resonant frequency with simulated resonant frequency at different arm lengths. In (a) and (b), flare angles are fixed at 60 degrees. (c) Measured normalized transmission spectrum of bowtie antennas with different flare angles. (d) Correlation of measured resonant frequency with simulated resonant frequency at different flare angles. In (a) and (b), arm lengths are fixed at 4.5mm.

6.5 MEASUREMENT OF FAR-FIELD RADIATION PATTERN

In addition, the far field radiation pattern is measured. The bowtie antenna with arm length of 5.5mm and flare angle of 60 degrees is used in this test. The bowtie

antenna is mounted on a rotational stage and is rotated along the x axis in Fig. 6.1. RF signal from the vector network analyzer is coupled into the bowtie antenna through a GS microprobe. The frequency of this RF signal is set to 10.5GHz which is the resonant frequency of the bowtie antenna. A horn antenna is placed 2m away as a receiving antenna in the far field region. The received power is amplified by an RF amplifier and then measured by a microwave spectrum analyzer. The normalized measured power as a function of rotation angle is shown as a blue curve in Fig. 6.7. Simulated radiation pattern (red curve) is also overlaid in the figure, showing a good match between simulation and experimental results. This measured radiation pattern indicates dipole-type characteristics of our bowtie antenna. The half power beam width is measured to be about 90 degrees. This wide beam width is good for the antenna to detect electromagnetic waves coming from a large range of incident angles.

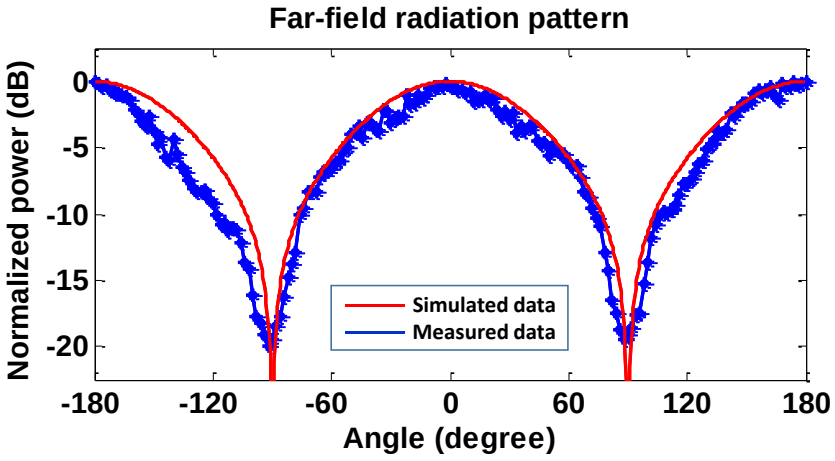

Figure 6.7: Measured far field radiation pattern (blue) of the bowtie antenna at a frequency of 10.5GHz. Simulated radiation pattern is also overlaid (red).

6.6 SUMMARY

In summary, we design, fabricate and experimentally demonstrate an integrated broadband bowtie antenna on transparent silica substrate. The bowtie antenna is optimized to cover a broad frequency bandwidth. Numerical simulation shows that, with the arm length of 5.5mm and the flare angle of 60^{o}, the electric field inside the bowtie feed gap can be enhanced by as high as 688 times at 10.5GHz compared to the incident electric field, with a 1-dB RF bandwidth over 9GHz. The dependency of resonant frequency on bowtie geometry, such as arm length and flare angle is numerically computed and experimentally verified. In addition, the radiation pattern of the bowtie antenna is measured, showing a large angular beam width similar to a typical dipole antenna. The bowtie antenna has compact size smaller than $1cm^2$. This bowtie antenna has potential applications in photonic detection of free-space electromagnetic waves [37-39], RF photonic links and devices [40] complex electromagnetic structures [41], ground penetrating radar [5], THz wave detection [42], plasmonic sensing [43], nano-antenna arrays [8], quantum emitter [44], optical antennas [45], and even light trapping for photovoltaics [46-48]. In addition, from fabrication point of view, solid bowtie antennas [49] or contour bowtie antennas [7] can be fabricated by inkjet printing techniques, which is compatible with roll-to-roll manufacturing processes [50]. These bowtie antennas can also be fabricated on flexible substrates [7, 51-53]. In addition, the gold material can be replaced by ITO or graphene, together with the transparent feature of silica substrate, to potentially enable some 'invisible' integrated electronic and photonic devices [27].

Furthermore, some bowtie antenna integrated devices previously demonstrated on SOI substrates [22] can be transferred as silicon nanomembranes onto silica substrates [54] or directly fabricated on silicon-on-glass substrates [55] to avoid impacts from backside silicon handles and to enhance their device performance.

6.7 REFERENCES

[1] S. Kim, J. Jin, Y.-J. Kim, I.-Y. Park, Y. Kim, and S.-W. Kim, "High-harmonic generation by resonant plasmon field enhancement," *Nature,* vol. 453, pp. 757-760, 2008.

[2] Z. Pan and J. Guo, "Enhanced optical absorption and electric field resonance in diabolo metal bar optical antennas," *Optics Express,* vol. 21, pp. 32491-32500, 2013.

[3] K. Ishihara, K. Ohashi, T. Ikari, H. Minamide, H. Yokoyama, J.-i. Shikata, and H. Ito, "Terahertz-wave near-field imaging with subwavelength resolution using surface-wave-assisted bow-tie aperture," *Applied Physics Letters,* vol. 89, p. 201120, 2006.

[4] S. Sederberg and A. Elezzabi, "Nanoscale plasmonic contour bowtie antenna operating in the mid-infrared," *Optics Express,* vol. 19, pp. 15532-15537, 2011.

[5] M. Roslee, K. S. Subari, and I. S. Shahdan, "Design of bow tie antenna in CST studio suite below 2GHz for ground penetrating radar applications," in *RF and Microwave Conference (RFM), 2011 IEEE International*, 2011, pp. 430-433.

[6] B. Madhav, V. Pisipati, H. Khan, V. Prasad, K. P. Kumar, K. Bhavani, and M. R. Kumar, "Liquid Crystal Bow-Tie Microstrip antenna for Wireless Communication Applications," *Journal of Engineering Science and Technology Review,* vol. 4, pp. 131-134, 2011.

[7] A. C. Durgun, C. A. Balanis, C. R. Birtcher, and D. R. Allee, "Design, simulation, fabrication and testing of flexible bow-tie antennas," *Antennas and Propagation, IEEE Transactions on,* vol. 59, pp. 4425-4435, 2011.

[8] K. D. Ko, A. Kumar, K. H. Fung, R. Ambekar, G. L. Liu, N. X. Fang, and K. C. Toussaint Jr, "Nonlinear optical response from arrays of Au bowtie nanoantennas," *Nano letters,* vol. 11, pp. 61-65, 2010.

[9] M. Rahim, M. Abdul Aziz, and C. Goh, "Bow-tie microstrip antenna design," in *13th IEEE International Conference*, 2005.

[10] W. Yeoh, K. Wong, and W. Rowe, "Wideband miniaturized half bowtie printed dipole antenna with integrated balun for wireless applications," *Antennas and Propagation, IEEE Transactions on,* vol. 59, pp. 339-342, 2011.

[11] K. R. Mahmoud, "Design optimization of a bow-tie antenna for 2.45 GHz RFID readers using a hybrid BSO-NM algorithm," *Progress In Electromagnetics Research,* vol. 100, pp. 105-117, 2010.

[12] J. H. Yoon and Y. C. Lee, "Modified bow‐tie slot antenna for the 2.4/5.2/5.8 GHz WLAN bands with a rectangular tuning stub," *Microwave and optical technology letters,* vol. 53, pp. 126-130, 2011.

[13] A. C. Durgun, M. S. Reese, C. A. Balanis, C. R. Birtcher, D. R. Allee, and S. Venugopal, "Flexible bow-tie antennas with reduced metallization," in *Radio and Wireless Symposium (RWS), 2011 IEEE*, 2011, pp. 50-53.

[14] C. A. Balanis, *Antenna theory: analysis and design*: John Wiley & Sons, 2012.

[15] F. I. Rial, H. Lorenzo, M. Pereira, and J. Armesto, "Analysis of the emitted wavelet of high-resolution bowtie GPR Antennas," *Sensors,* vol. 9, pp. 4230-4246, 2009.

[16] P. Mühlschlegel, H.-J. Eisler, O. Martin, B. Hecht, and D. Pohl, "Resonant optical antennas," *Science,* vol. 308, pp. 1607-1609, 2005.

[17] H. Fischer and O. J. Martin, "Engineering the optical response of plasmonic nanoantennas," *Optics Express,* vol. 16, pp. 9144-9154, 2008.

[18] M. Mivelle, T. S. van Zanten, L. Neumann, N. F. van Hulst, and M. F. Garcia-Parajo, "Ultrabright bowtie nanoaperture antenna probes studied by single molecule fluorescence," *Nano letters,* vol. 12, pp. 5972-5978, 2012.

[19] J. Y. Suh, M. D. Huntington, C. H. Kim, W. Zhou, M. R. Wasielewski, and T. W. Odom, "Extraordinary nonlinear absorption in 3D bowtie nanoantennas," *Nano letters,* vol. 12, pp. 269-274, 2011.

[20] F. M. Congedo, G. Tarricone, and M. L Cannarile, "Broadband bowtie antenna for RF energy scavenging applications," *Antennas and Propagation (EUCAP),* 2011.

[21] S. Wang and Q. Zhan, "Modified bow-tie antenna with strong broadband field enhancement for RF photonic applications," in *SPIE NanoScience+ Engineering*, 2013, pp. 88061V-88061V-6.

[22] X. Zhang, A. Hosseini, H. Subbaraman, S. Wang, Q. Zhan, J. Luo, A. K. Jen, and R. T. Chen, "Integrated Photonic Electromagnetic Field Sensor Based on Broadband Bowtie Antenna Coupled Silicon Organic Hybrid Modulator," *Lightwave Technology, Journal of,* vol. 32, pp. 3774-3784, 2014.

[23] O. D. Herrera, K.-J. Kim, R. Voorakaranam, R. Himmelhuber, S. Wang, V. Demir, Q. Zhan, L. Li, R. A. Norwood, R. L. Nelson, J. Luo, A. K. Y. Jen, and N. Peyghambarian, "Silica/Electro-Optic Polymer Optical Modulator With Integrated

Antenna for Microwave Receiving," *Journal of Lightwave Technology,* vol. 32, pp. 3861-3867, 2014/10/15 2014.

[24] L. Chen and R. M. Reano, "Compact electric field sensors based on indirect bonding of lithium niobate to silicon microrings," *Optics Express,* vol. 20, pp. 4032-4038, 2012.

[25] R. A. Synowicki, "Suppression of backside reflections from transparent substrates," *physica status solidi (c),* vol. 5, pp. 1085-1088, 2008.

[26] D. B. Rutledge, D. P. Neikirk, and D. P. Kasilingam, "Integrated circuit antennas," *Infrared and millimeter waves,* vol. 10, pp. 1-90, 1983.

[27] A. Facchetti and T. J. Marks, "Transparent electronics," *From Synthesis to Applications, Wiley, Chichester, UK,* 2010.

[28] S. Kim, S. Kim, J. Park, S. Ju, and S. Mohammadi, "Fully transparent pixel circuits driven by random network carbon nanotube transistor circuitry," *Acs Nano,* vol. 4, pp. 2994-2998, 2010.

[29] S. Nedic, Y. T. Chun, W.-K. Hong, D. Chu, and M. Welland, "High performance non-volatile ferroelectric copolymer memory based on a ZnO nanowire transistor fabricated on a transparent substrate," *Applied Physics Letters,* vol. 104, p. 033101, 2014.

[30] I. Lahiri, V. P. Verma, and W. Choi, "An all-graphene based transparent and flexible field emission device," *Carbon,* vol. 49, pp. 1614-1619, 2011.

[31] S. C. Lai, K. Yao, Y. F. Chen, L. Zhang, and Y.-F. Lim, "A Photovoltaic UV Sensor With a Ferroelectric Thin Film on Transparent Substrate," 2013.

[32] J. Wang, W. Li, and C. Wang, "Improving light outcoupling efficiency for OLEDs with microlens array fabricated on transparent substrate," *Journal of Nanomaterials,* vol. 2014, 2014.

[33] N. Nath and A. Chilkoti, "A colorimetric gold nanoparticle sensor to interrogate biomolecular interactions in real time on a surface," *Analytical Chemistry,* vol. 74, pp. 504-509, 2002.

[34] Q.-H. Park, "Optical antennas and plasmonics," *Contemporary Physics,* vol. 50, pp. 407-423, 2009.

[35] T. Søndergaard and S. Bozhevolnyi, "Slow-plasmon resonant nanostructures: Scattering and field enhancements," *Physical Review B,* vol. 75, p. 073402, 2007.

[36] J. George, M. Deepukumar, C. Aanandan, P. Mohanan, and K. Nair, "New compact microstrip antenna," *Electronics Letters,* vol. 32, pp. 508-509, 1996.

[37] A. Savchenkov, W. Liang, V. Ilchenko, E. Dale, E. Savchenkova, A. Matsko, D. Seidel, and L. Maleki, "Photonic E-field sensor," *AIP Advances,* vol. 4, p. 122901, 2014.

[38] C.-Y. Lin, A. X. Wang, B. S. Lee, X. Zhang, and R. T. Chen, "High dynamic range electric field sensor for electromagnetic pulse detection," *Optics Express,* vol. 19, pp. 17372-17377, 2011.

[39] Y. N. Wijayanto, H. Murata, and Y. Okamura, "Electrooptic Millimeter-Wave–Lightwave Signal Converters Suspended to Gap-Embedded Patch Antennas on Low-Dielectric Materials," *Selected Topics in Quantum Electronics, IEEE Journal of,* vol. 19, pp. 3400709-3400709, 2013.

[40] X. Zhang, B. Lee, C.-y. Lin, A. X. Wang, A. Hosseini, and R. T. Chen, "Highly Linear Broadband Optical Modulator Based on Electro-Optic Polymer," *Photonics Journal, IEEE,* vol. 4, pp. 2214-2228, 2012.

[41] R. Chang, S. Li, M. Lubarda, B. Livshitz, and V. Lomakin, "FastMag: Fast micromagnetic simulator for complex magnetic structures," *Journal of Applied Physics,* vol. 109, p. 07D358, 2011.

[42] S.-L. Chen, Y.-C. Chang, C. Zhang, J. G. Ok, T. Ling, M. T. Mihnev, T. B. Norris, and L. J. Guo, "Efficient real-time detection of terahertz pulse radiation based on photoacoustic conversion by carbon nanotube nanocomposite," *Nature Photonics,* 2014.

[43] W. Zhang, L. Huang, C. Santschi, and O. J. Martin, "Trapping and sensing 10 nm metal nanoparticles using plasmonic dipole antennas," *Nano letters,* vol. 10, pp. 1006-1011, 2010.

[44] J. N. Farahani, D. W. Pohl, H.-J. Eisler, and B. Hecht, "Single quantum dot coupled to a scanning optical antenna: a tunable superemitter," *Physical review letters,* vol. 95, p. 017402, 2005.

[45] L. Novotny and N. Van Hulst, "Antennas for light," *Nature Photonics,* vol. 5, pp. 83-90, 2011.

[46] X. Li, P. C. Li, L. Ji, C. Stender, C. McPheeters, S. R. Tatavarti, K. Sablon, and E. T. Yu, "Subwavelength nanostructures integrated with polymer‐packaged iii‐v solar cells for omnidirectional, broad‐spectrum improvement of photovoltaic performance," *Progress in Photovoltaics: Research and Applications,* 2014.

[47] C. Zhang, D. Zhao, D. Gu, H. Kim, T. Ling, Y. K. R. Wu, and L. J. Guo, "An Ultrathin, Smooth, and Low‐Loss Al‐Doped Ag Film and Its Application as a Transparent Electrode in Organic Photovoltaics," *Advanced Materials,* vol. 26, pp. 5696-5701, 2014.

[48] X. Li, V. D. Dasika, P.-C. Li, L. Ji, S. R. Bank, and T. Y. Edward, "Minimized open-circuit voltage reduction in GaAs/InGaAs quantum well solar cells with bandgap-engineered graded quantum well depths," *Applied Physics Letters,* vol. 105, p. 123906, 2014.

[49] A. A. Eldek, A. Z. Elsherbeni, and C. E. Smith, "Wideband microstrip‐fed printed bow‐tie antenna for phased‐array systems," *Microwave and optical technology letters,* vol. 43, pp. 123-126, 2004.

[50] X. Lin, T. Ling, H. Subbaraman, X. Zhang, K. Byun, L. J. Guo, and R. T. Chen, "Ultraviolet imprinting and aligned ink-jet printing for multilayer patterning of electro-optic polymer modulators," *Optics letters,* vol. 38, pp. 1597-1599, 2013.

[51] X. Lin, H. Subbaraman, Z. Pan, A. Hosseini, C. Longe, K. Kubena, P. Schleicher, P. Foster, S. Brickey, and R. T. Chen, "Towards Realizing High-Throughput, Roll-to-Roll Manufacturing of Flexible Electronic Systems," *Electronics,* vol. 3, pp. 624-635, 2014.

[52] H. Subbaraman, D. T. Pham, X. C. Xu, M. Y. H. Chen, A. Hosseini, X. Lu, and R. T. Chen, "Inkjet-Printed Two-Dimensional Phased-Array Antenna on a Flexible Substrate," *IEEE Antennas and Wireless Propagation Letters,* vol. 12, pp. 170-173, 2013.

[53] R. T. Chen and X. Zhang, "Silicon nanomembrane based Devices for Optical Sensing and On-chip Interconnects," in *Frontiers in Optics*, 2014, p. FW1B. 2.

[54] O. Nast, T. Puzzer, L. M. Koschier, A. B. Sproul, and S. R. Wenham, "Aluminum-induced crystallization of amorphous silicon on glass substrates above and below the eutectic temperature," *Applied Physics Letters,* vol. 73, pp. 3214-3216, 1998.

[55] J. Rogers, M. Lagally, and R. Nuzzo, "Synthesis, assembly and applications of semiconductor nanomembranes," *Nature,* vol. 477, pp. 45-53, 2011.

Chapter 7: Improved performance of linearized traveling wave directional coupler polymer modulator *

7.1 INTRODUCTION

Analog optical links [1] have been used or have the potential to be used in many fields, due to the intrinsically large bandwidth of optics and the low loss in optical fibers. One of the widespread commercial applications of analog optical links is the distribution of cable television (CATV) signals [2]. Other useful applications of analog optical links include optical true-time delay modules in phased array antennas [3], analog signal generating and processing [4], RF photonics sensors [5], etc. The optical modulator employed in intensity-modulation/direct-detection (IMDD) optical link applications is an intensity modulator with high-speed capability. These optical modulators in analog optical links are required to have high modulation efficiency, good linearity and large bandwidth. Existing commercial $LiNbO_3$ MZI modulators have intrinsic drawbacks in linearity to support high fidelity communication. When multiple tones of signals (f_1 and f_2) are simultaneously carried over a link, nonlinear intermodulation distortion signals are generated. The third-order intermodulation distortions (IMD3), which are the byproducts of the interaction between fundamental frequencies and harmonics and occur at ($2f_1 - f_2$) and ($2f_2 - f_1$), are considered as the most troublesome among all the nonlinear distortions because they usually fall within the usable bandwidth of the system. The

---

* Citation: X. Zhang, B. Lee, C.-y. Lin, A. X. Wang, A. Hosseini, and R. T. Chen, "Highly Linear Broadband Optical Modulator Based on Electro-Optic Polymer," Photonics Journal, IEEE, vol. 4, pp. 2214-2228, 2012.

X. Zhang mainly worked on the simulation, fabrication and characterization, and serves as the first author of the paper. Other coauthors also contributed to the work from simulation, material processing, characterization, discussion, or paper preparation.

spurious free dynamic range (SFDR) is defined as the dynamic range between the smallest signal that can be detected in a system and the largest signal that can be introduced into the system without creating detectable distortions in the bandwidth of concern [6]. The SFDR of high frequency analog optical links is limited by the system noise and the nonlinearity of modulation process. Bias-free Y-fed directional coupler (YFDC) modulators have been shown to provide better linear transfer functions compared to the sine-squared transfer curve of conventional MZI modulators [7, 8]. The device linearity can be further enhanced when the YFDC modulators are incorporated with the Δβ-reversal technique to suppress IMD3s [7, 9-12]. We previously demonstrated a polymer based 2-domain YFDC modulator with Δβ-reversal at low modulation frequencies as a proof of concept [as shown in Fig. 26 (a), using a lumped element electrode], where we achieved an SFDR of 119dB/Hz$^{2/3}$ with 11dB enhancement over the conventional MZI modulator [11].

In addition to the requirement of high linearity, the bandwidth is another important factor in evaluating the performance of a modulator. The first demonstration of optical modulation at GHz frequencies was done on a traveling wave electro-optic (EO) $LiNibO_3$ modulator in 1970s [13, 14]**.** A traveling wave modulator based on an EO polymer operating in the GHz frequency regime was demonstrated in 1992 [15]. Later on, a polymeric modulator operating over 100GHz was verified by groups at UCLA and USC [16]. Up until today the highest frequency that the polymer modulator can work at was demonstrated to be as high as 200GHz by Bell Laboratories [17]. Polymer EO modulators can offer several advantages over the mature $LiNibO_3$ modulators due to the special properties of polymer materials as below [18-20]. Excellent velocity matching

between microwaves and optical waves can be achieved due to a close match between the refractive index of polymers at microwave and optical frequencies, enabling ultra-broad bandwidth operation. The intrinsic relatively low dielectric constant of polymers (2.5-4) also enables 50-ohm driving electrodes to be easily achieved. Polymers also have very large EO coefficients, γ_{33}, which is advantageous for sub-volt half-wave switching voltage (V_π) [21-23]. For example, CDL1/PMMA, an EO polymer with γ_{33}=60pm/V, was used to achieve V_π=0.8V [21]. Another EO polymer with a very large γ_{33}=306pm/V was developed through controlled molecular self-assembly and lattice hardening [24]. In comparison, the EO coefficient of $LiNibO_3$ is only about 30pm/V. In addition, the refractive index of polymers (1.6-1.7) is nearly matched to that of glass optical fibers (1.5-1.6), enabling small Fresnel reflection loss at interfaces in butt-coupling. Polymers can be highly transparent, and the absorption loss can be below 0.1dB/cm at all key communication wavelengths [19]. And also, polymers are spin-on films so they can be easily spincoated onto any substrate. Recently, EO modulations on extremely small geometrical footprints have been demonstrated by infiltrating EO polymer into slot waveguides [25] or slotted photonic crystal waveguides [26]. So far, the largest effective in-device γ_{33}=735pm/V and the smallest $V_\pi L$=0.44V•mm have been demonstrated by our group using EO polymer infiltrated silicon slotted photonic crystal waveguides [27]. Furthermore, compared to the difficult implementation of the domain inversion technique on $LiNibO_3$ [28], Δβ-reversal can be easily achieved by domain-inversion poling on EO polymers. Based on the above advantages of polymer materials, EO polymer modulators

have shown great potentials for a variety of applications, such as telecommunication, analog-to-digital conversion, phased-array radar, and electrical-to-optical signal transduction. Now polymer based modulators with high reliability have been commercially available [29].

In this chapter, we demonstrate an EO polymer based traveling wave directional coupler modulator with $\Delta\beta$-reversal to extend the high linearity performance to the GHz frequency regime. A traveling wave electrode with a unique design for RF microprobe coupling is fabricated with low microwave loss, characteristic impedance matching with 50Ω, and velocity matching between microwaves and optical waves, as well as smooth electric field profile transformation. The bandwidth-length product of 302GHz·cm and the 3-dB bandwidth of 10GHz are achieved. The SFDR of $110 \pm 3 dB/Hz^{2/3}$ is measured over the modulation frequency of 2-8GHz. In addition, a 1×2 multi-mode interference (MMI) 3dB-splitter, a photobeached refractive index taper and a quasi-vertical taper, as well as a smooth silver ground electrode, are used to reduce the optical insertion loss of the device.

7.2 DESIGN OF POLYMERIC OPTICAL WAVEGUIDE DESIGN

Fig. 7.1 (a) shows the schematic top view of our traveling wave MMI-fed directional coupler modulator. The cross section of the optical waveguides consisting of three layers of fluorinated polymers (bottom cladding: UV-15LV, core: AJ-CKL1/APC with γ_{33}=80pm/V, and top cladding: UFC-170A) is shown in Figs. 7.1 (b) and (c). Unlike the sine-squared transfer curve of the conventional MZ structure, a proper design of

coupling length of directional coupler can provide a linear transfer function [30-34]. The linearity of the directional coupler can be further improved by applying $\Delta\beta$-reversal technique to suppress IMD3s [7, 9-11]. Multiple-domain-inversion, which helps increase the linearity of directional coupler modulator, has been demonstrated by our group [12]. Considering the fabrication and poling complexity, in this paper we use a 2-domain-inversion directional coupler for demonstration. The directional coupler is divided into two domains, where EO polymer in the first domain is poled in the opposite direction with respect to that in the second domain. The push-pull configuration is also applied, in which the two arms of the directional coupler in each domain are poled in opposite directions, to double the EO effect. Finally, a single uniform modulation electric field applied by a traveling wave electrode can create $\Delta\beta$-reversal which is indicated by the dashed lines in Fig. 7.1 (a).

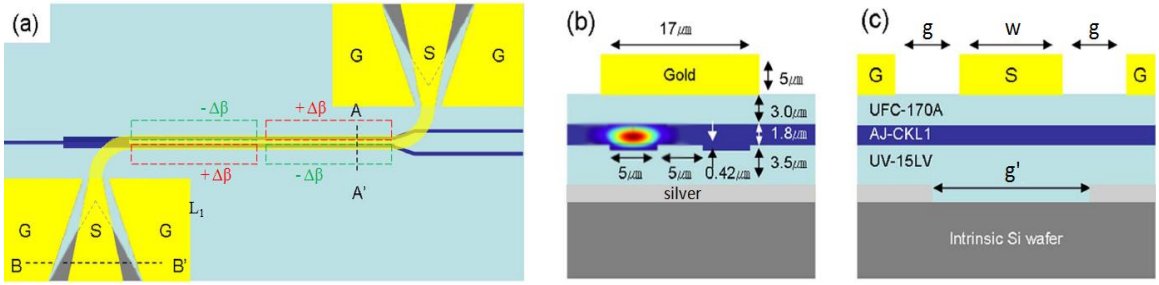

Figure 7.1: (a) The schematic top view of the traveling wave MMI-fed directional coupler modulator with 2-domain-inversion. The red and green dashed lines indicate the area of EO polymer poled in opposite directions. (b) Cross section corresponding to A-A′ in (a), overlaid the optical mode profile in one arm. (c) Cross section corresponding to B-B′ in (a). (S: signal electrode, G: ground electrode).

The IMD3 suppression of a directional coupler modulator is a sensitive function of the normalized interaction length (S_i), defined as the ratio of the interaction length (L_i) of ith section to the coupling length (l_c). Relative IMD3 suppression of a 2-domain directional coupler modulator can be graphically represented by plotting the calculated IMD3 suppressions on (S_1, S_2) plane [35]. $S_1 = S_2$=2.86 provides excellent linearity as well as very high modulation depth [12] and is chosen for demonstration in this paper. For a directional coupler with the total interaction length ($L_1 + L_2$) of 2cm, its coupling length for TM mode should be 3496μm. This coupling length is matched by tuning the parameters of the trench waveguide, such as the core thickness and trench depth, using numerical methods [36]. The thickness of cladding is chosen to be 3.5μm and 3μm at the bottom and top, respectively, considering both the requirement of low driving and poling voltage and the prevention of optical absorption by metallic electrodes. The final cross section dimensions are shown in Fig. 7.1 (b). Based on fabrication experiences and actual measurements, the actual bottom width of a 420nm-deep trench fabricated by reactive ion etching (RIE) is about 4μm while the top width is still 5μm as designed. However, the calculation results show that the resulting coupling length deviation is only 0.55%, which can be explained by the fact that most of the optical power is distributed in the core layer, as shown in Fig. 7.1 (b), and that the field profile interaction happens at the top side of the two trenches which is un-affected.

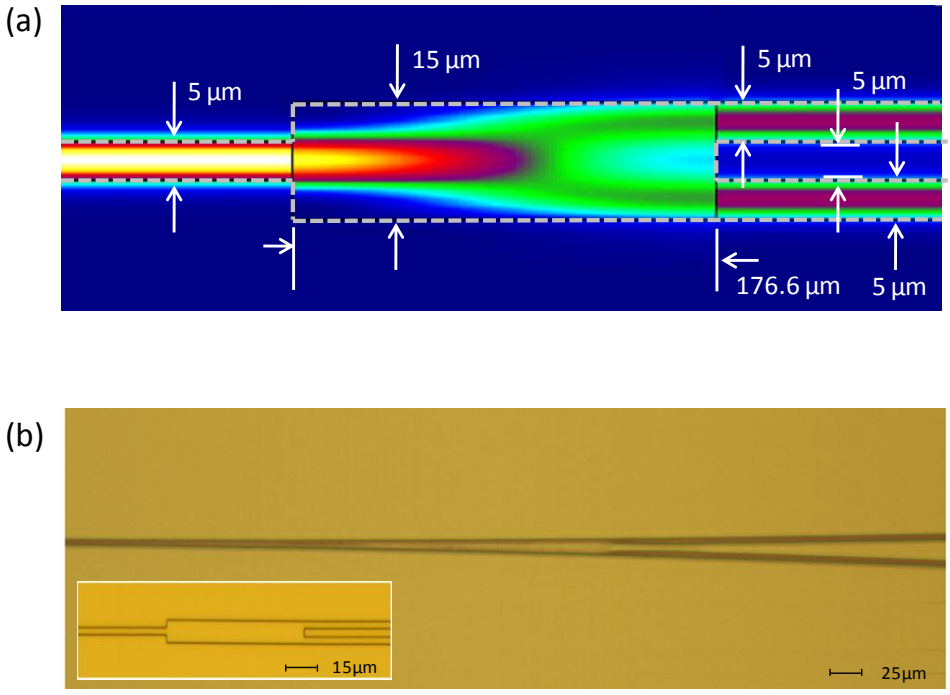

Figure 7.2: (a) The top view of a 1×2 MMI 3-dB coupler, and the optical power distribution in this MMI coupler. (b) A blunt tip of a fabricated Y-junction due to fabrication limitations, compared to a fabricated MMI coupler shown in the inset.

A 1×2 MMI 3-dB coupler is designed to equally split the input optical power among two waveguides of a directional coupler as shown in Fig. 7.2 (a). The symmetric waveguide structure of the MMI-fed directional coupler is intrinsically bias-free; and the modulation is automatically set at 3-dB operation point regardless of the ambient temperature. The dimensions of MMI coupler and the optical power distribution in it are shown in Figs. 7.2 (a) and (b). The total power transmission of this MMI coupler is numerically calculated using eigenmode expansion method [37] to be as high as 94%.

This MMI coupler has a large fabrication tolerance and is insensitive to the photolithography resolution. In comparison, as for previously used Y-junction [7], in practice the fabrication limitations in photolithography and etch resolutions usually lead to a blunt tip under a certain distance between the two waveguides (Fig. 7.2 (b)) and violates the adiabatic requirement, resulting in extra optical loss [38]. In addition, compared with the previous 1000μm-long Y-junction [11], the MMI coupler is only 176.6μm-long and is beneficial to decrease the device length. The inset of Fig. 7.2 (b) shows a microscope image of a fabricated MMI coupler compared with a traditionally used Y-junction.

A polymer trench waveguide is designed to support only a single mode. As shown in Fig. 7.3 (a), the TM mode profile of the designed polymer waveguide is calculated using finite element method [39], with the corresponding optical effective index of 1.599 at 1550nm. Figure. 7.3 (a) also shows the mode profiles of three single mode fibers with different mode field diameters (MFD). It can be seen that the mode profile of the polymer waveguide is in an elliptical geometry, with its major axis of about 7μm and minor axis of about 2.5μm, but that the mode profile of the normally used single mode fibers (e.g. SM980-5.8-125, Thorlabs) is in a circular geometry with MFD of 10.4μm. This mode size mismatch can lead to large optical loss in butt-couplings. To reduce such coupling loss, single mode fibers with MFD of 6.4μm (e.g. SM1500G80, Thorlabs) or lens fibers with MFD of 2.5μm (e.g. TSMJ-3U-1550-9/125-0.25-7-2.5-14-2, OZ Optics) can be used as replacements at the input/output (I/O) sides. The power-coupling loss using these three

fibers are calculated by considering the overlap integral of mode profiles as well as Fresnel reflection loss at interfaces [40, 41]. Figure. 7.3 (b) shows the three-dimensional perspective of the coupling loss as a function of the spatial misalignment in x and y directions for these three fibers. To see a clear comparison of these three fibers, a two-dimensional plot of the same data is shown in Fig. 7.3 (c). It can be seen that the lowest coupling loss, 1.7dB/facet, can be achieved using lens fibers but that there are very large variations versus misalignment along both x and y directions. It can be noticed that, using lens fibers, the coupling efficiency is more sensitive to the misalignment in y direction than that in x direction. Using single mode fibers with MFD of 6.4μm, a larger alignment tolerance can be achieved, while the peak coupling loss is 2.0dB/facet which is just a little higher than that of the lens fibers. Normally used single mode fibers with MFD of 10.5μm can provide the lowest misalignment sensitivity but the highest coupling loss which is up to 4.1dB/fact. Therefore, considering both coupling loss and misalignment tolerance, a single mode fiber with MFD of 6.4μm is finally chosen for our experiment.

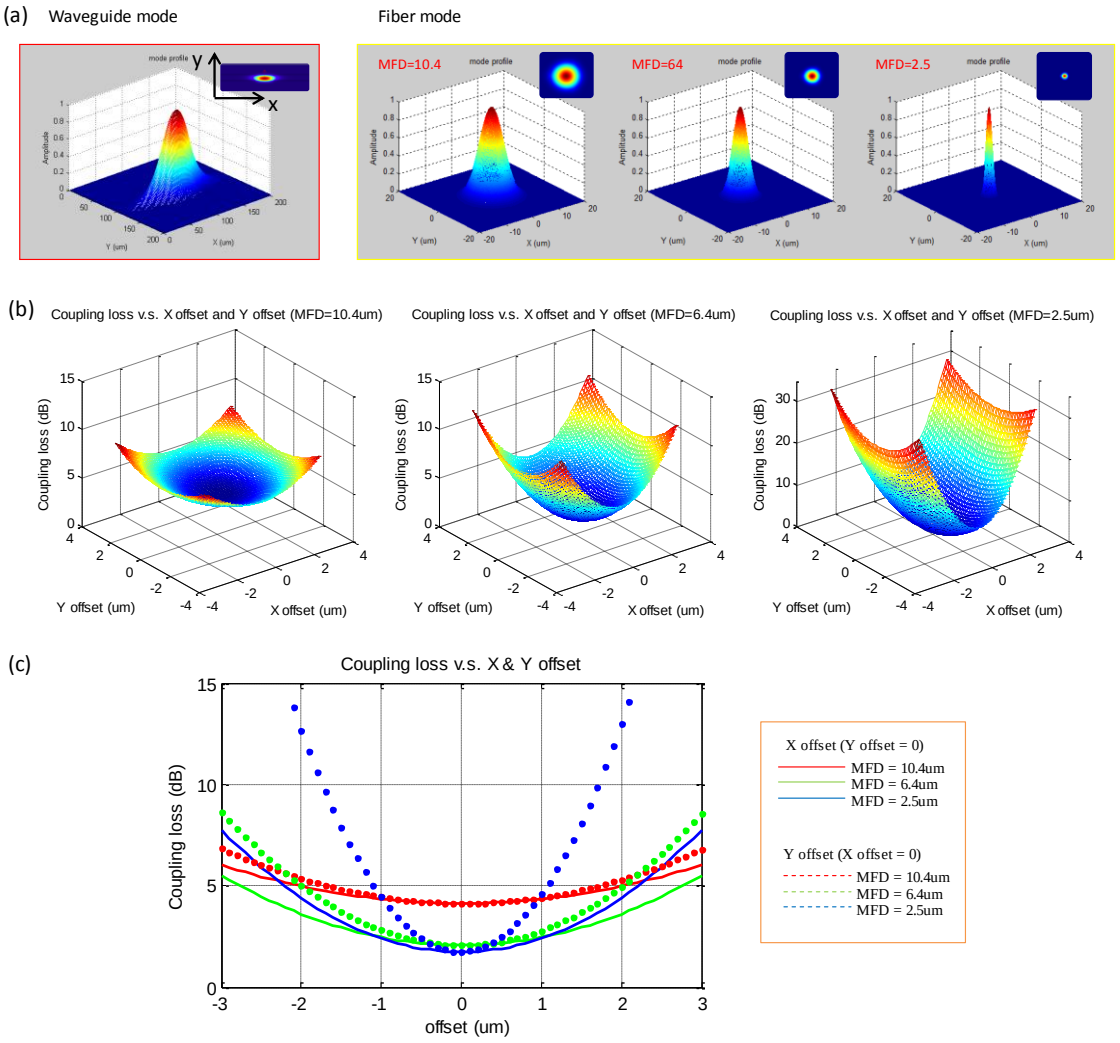

Figure 7.3: (a) Optical mode profile in a polymer waveguide, compared with the optical mode profiles in I/O fibers with MFD of 10.4μm, 6.4μm and 2.5μm. (b) The 3D perspective of the calculated coupling loss versus the misalignment in x and y direction, for using three different I/O fibers. (c) The 2D plot of the calculated coupling loss versus the misalignment in x and y direction. Red curves, green curves and blue curves represent the coupling loss using a fiber with MFD of 10.4μm, 6.4μm and 2.5μm, respectively, and solid curves and dashed curves represent the coupling loss versus the misalignment in x and y directions, respectively.

Another way to reduce the optical coupling loss due to mode size mismatch is to design a taper structure. Here, refractive index tapers are designed at the passive regions of the waveguides so that the optical mode profile at the I/O ends of the polymer waveguide can better match that of the I/O optical fibers. The working mechanism is shown in Fig. 7.4 (a). Refractive index variation of EO polymer core at the passive regions of the waveguide is created by UV photobleaching method, using a gray-scale photomask or discrete step mask-shifting scheme [42]. This refractive index variation leads to the gradual change of optical mode size along the taper, so that the waveguide modes at the facets are large enough to match that of I/O fibers. In addition, to minimize the severe mode size mismatch in vertical direction that can be seen in Fig. 7.3 (a), a quasi-vertical taper structure [43] is designed as shown in Fig. 7.4 (b). It can be fabricated by standard photolithography and RIE twice. After a trench is etched on the bottom cladding polymer, a V-shape groove is etched again into the trench near the I/O facets. This structure works as an optical mode transformer. Because the trenches are deeper at the facets than in the active regions of waveguide, the waveguide mode size in vertical direction becomes larger at the facets and can better match the I/O fiber mode. Numerical calculations using beam propagation method [44] show that the combination of these two tapers can significantly reduce the optical coupling loss by 3dB/facet.

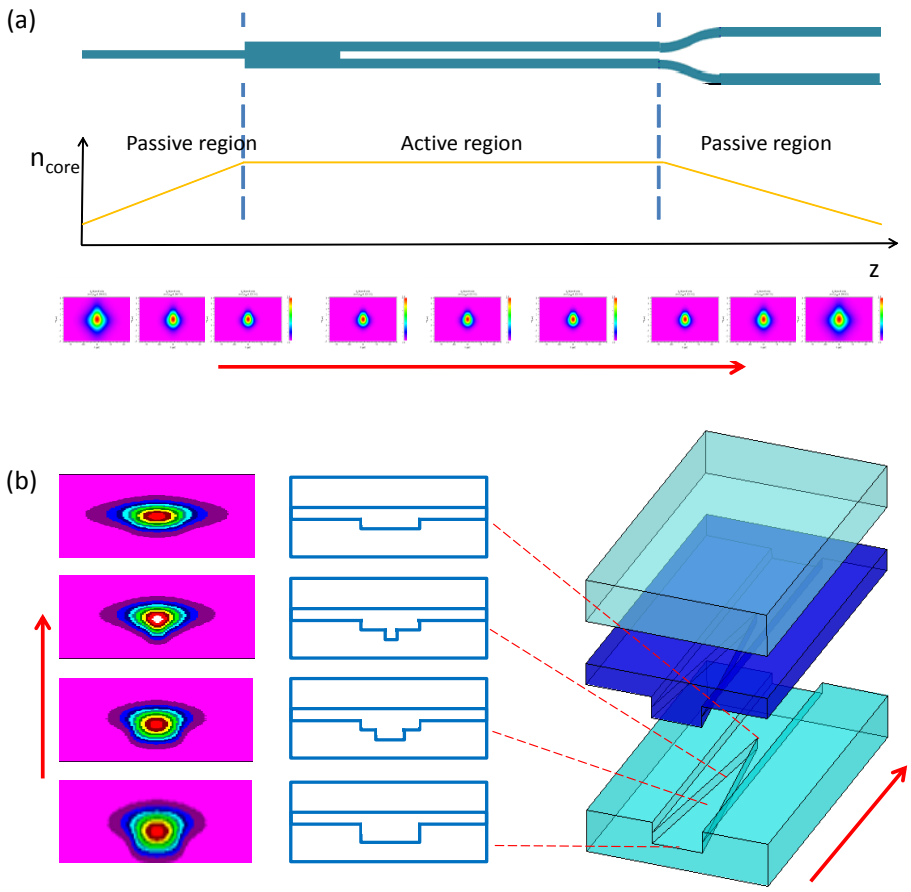

Figure 7.4: (a) Refractive index tapers at the passive regions of the MMI-fed directional coupler. The index variation of the photobleached EO polymer in the core layer leads to the gradual change of optical mode size along the taper. (b) A quasi-vertical taper at one facet of polymer waveguide used for mode profile transformation in vertical direction. The red arrows indicate the beam propagation direction.

Other than the coupling loss, the roughness of polymer waveguide sidewalls usually causes large scattering loss when light propagates in the waveguide. Thus, silver is selected as the ground electrode material and its smooth surface helps reduce waveguide sidewall roughness originating from the scattering of UV light in

photolithography. Compared to other metals, silver is also beneficial to suppress the microwave conductor loss owing to its very low resistivity.

7.3 TRAVELING WAVE ELECTRODE DESIGN

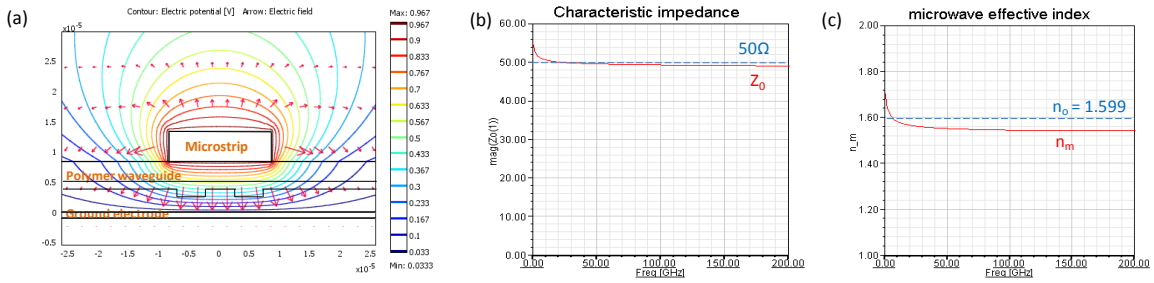

Figure 7.5: (a) The schematic cross section of a microstrip line overlaid the contour of the normalized electric potential. The red arrows indicate the direction of electric field. (b) The characteristic impedance of the microstrip line over the frequency range 1-200GHz. The solid red curve indicates the characteristic impedance and the dashed blue line indicates the 50Ω. (c) The microwave effective index of the microstrip line over the frequency range 1-200GHz. The solid red curve indicates the microwave effective index and the dashed blue line indicates the optical effective index of 1.599.

To extend the highly linear modulation to GHz frequency regime, a traveling wave electrode is necessary. Some basic requirements for the design of a high-speed traveling wave electrode are [45]: (i) impedance matching between the microwave guides and external electrical connectors, (ii) velocity matching between the microwave and optical signals, and (iii) low electrical loss in the microwave guides. In addition to the above requirements, when designing a transition between different types of microwave guides, electric field matching [46, 47] should also be a concern in order to reduce the

microwave coupling loss [47]. In our device structure, polymer is considering the alignment of modulation field with the direction of the γ_{33} in the poled EO polymer film, which is in vertical direction in our device configuration; therefore, a microstrip line is a natural choice for the best alignment. Figure. 7.5 (a) shows the schematic cross section of the designed gold microstrip line overlaid the contour of the normalized electric potential calculated by finite element method [33]. It can be seen that both arms of the directional coupler waveguide are under the effect of a uniform modulation field between the microstrip line and the ground electrode and hence the overlap integral between the optical mode and the RF modulation field can be maximized. In quasi-static analysis, the characteristic impedance Z_0 and the microwave effective index n_m of a transmission line can be expressed as [45, 48]

$$Z_0 = \frac{1}{c\,(C\,C_a)} \tag{7.1}$$

$$n_m = \left(\frac{C}{C_a}\right)^{1/2} \tag{7.2}$$

where C_a is the capacitance per unit length of the electrode structure with the dielectrics replaced by air, C is the capacitance per unit length with the dielectrics present, and c is the speed of light in vacuum. The frequency-dependent characteristic impedance and microwave effective index can be numerically calculated using finite element method [49] to match 50Ω and optical effective index of 1.599, respectively. Conductor loss and

dielectric loss are considered in the calculation so that the results are accurate enough and close to the real case. Given the relative dielectric constant ε_r=3.2, the gap between top and bottom electrodes h=8.3μm and the microstrip thickness t=5μm from the waveguide dimensions and the fabrication conditions, the characteristic impedance of 50Ω can be matched when the microstrip width w=17μm. As shown in Fig. 7.5 (b) and (c), over the frequency range 1-200GHz, the characteristic impedance varies within 49-54.5Ω and the microwave effective index varies within 1.54-1.7. It can be noticed from Fig. 7.5 (b) that the characteristic impedance at low frequencies is relatively higher than that at high frequencies. This is because the internal inductance of the microstrip line decreases with frequency and becomes negligible when skin effect kicks in. Based on fabrication experience and actual measurements, the electroplated gold microstirp line does not have a perfect vertical sidewall but a wall angle of 84°; however, the variation of Z_0 and n_m due to this wall angle are calculated to be within 1Ω and 0.005, respectively, which can be negligible. The bandwidth-length product due to the velocity mismatch can be calculated as [13, 45, 50, 51]

$$f \cdot L \cong \frac{1.8}{\pi |n_m - n_o|} \tag{7.3}$$

where f is the modulation frequency, L is the interaction length, c is the speed of light in vacuum, n_m is the microwave effective index of the microstrip line, and n_o is the

optical effective refractive index of polymer waveguide. Using Equation 3, the bandwidth-length product can be theoretically calculated to be up to 306GHz·cm, corresponding to a modulation frequency limit of 153GHz for a 2cm-long microstrip line.

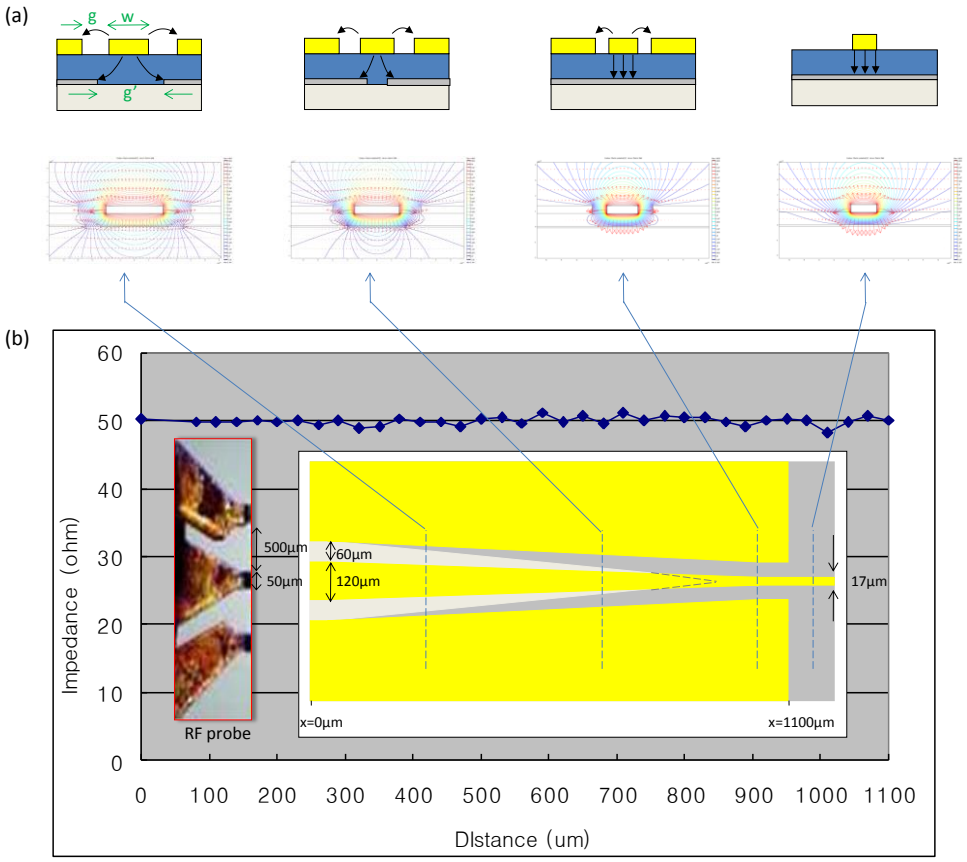

Figure 7.6: (a) The schematic of a smooth transformation of electric field profile in the CPW-to-microstrip transition at the input end of traveling wave electrode. The corresponding distribution of electric field and electric potential along this transition taper is calculated with finite element method. (b) The top view of the quasi-CPW taper, matching the size of a microprobe. The characteristic impedance (at 10GHz) is matched with 50Ω along the transition direction.

To couple the RF power from a GSG microprobe (e.g. ACP40-GSG-250, Cascade Microtech, probe tip width: 50μm, pitch: 500μm, as shown in Fig. 7.6 (b)) into the 17μm-wide microstrip line with minimum coupling loss, a 1.1mm-long quasi-coplanar waveguide (CPW) taper is designed at input end, as shown in Fig. 7.6 (b) . The top width and gap of the coplanar waveguide (w and g in Fig. 7.6 (a)) are gradually changed along the taper to match the dimension of a RF microprobe. In the transition between the CPW and the microstrip line, the electric field profiles of these two microwave guides should be matched to reduce microwave coupling loss. Therefore, unlike the conventional CPW, the ground electrode under the taper is partially removed and the bottom gap [g´in Fig. 7.6 (a)] is gradually tuned along the taper based on ground shaping technique [46, 47], so that there is a smooth transformation of electric field profile in the CPW-to-microstrip transition [33] while the 50Ω is matched at all points along the transition direction [43], as shown in Fig. 7.6. At the output end, a similar microstrip-to-CPW transition taper is designed to couple the RF power from the microstrip line to another GSG microprobe [Fig. 7.1 (a)]. What is more, for the design to be valid, the resistivity of silicon substrate should be sufficiently high (typical l kΩ cm or higher). Otherwise, the finite conductivity of silicon substrate allows the formation of microstrip mode between the signal electrode and silicon substrate, and this microstrip mode would become dominant at wide part of the taper and hinder 50Ω matching. Therefore, an intrinsic silicon wafer with ultra-high resistivity (6-10kΩ•cm) should be used as the substrate of our device.

7.4 DEVICE FABRICATION

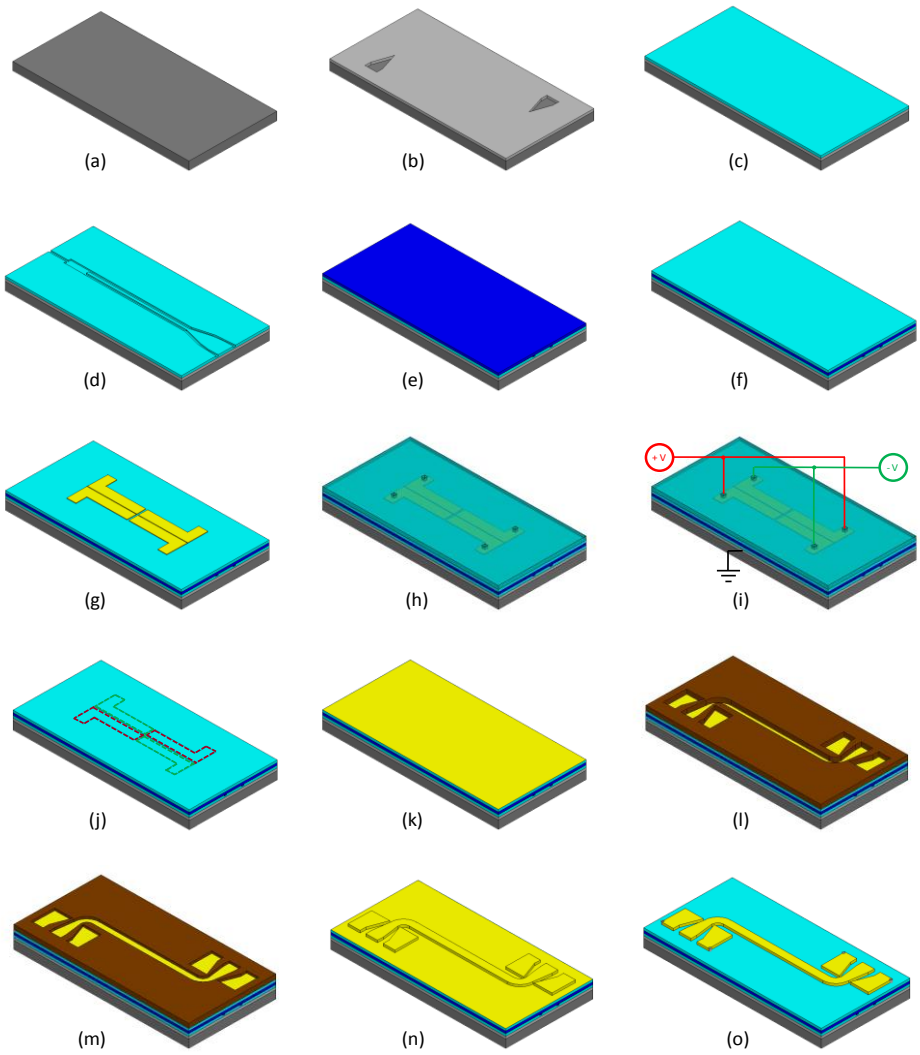

Figure 7.7: Fabrication process flow. (a) An ultra-high resistivity silicon wafer. (b) Ground electrode deposition and patterning. (c) Bottom cladding deposition. (d) Waveguide patterning. (e) EO polymer deposition. (f) Top cladding deposition. (g) Poling electrode deposition and patterning. (h) Protection layer deposition and patterning. (i) Poling. (j) Removal of protection layer and poling electrode. (k) Seed layer deposition. (l) Buffer mask deposition and patterning. (m) Traveling wave electrode electroplating. (n) Buffer mask removal. (o) Seed layer removal and vias drilling.

Figure. 7.7 illustrates the fabrication process flow. The device is fabricated on an ultra-high resistivity silicon wafer. A 1μm-thick silver film is deposited by electron-beam evaporation and then patterned using lift-off process, to serve as the ground electrode for poling process as well as for RF transmission. A polymer trench waveguide is fabricated by spincoating, photolithography and RIE, in which the EO polymer is formulated by doping 25wt% of AJ-CKL1chromophore into amorphous polycarbonate (APC). 150nm-thick gold poling electrodes are deposited by electron-beam evaporation and patterned by lift-off process. 300nm-thick silicon dioxide is deposited by electron-beam evaporation to cover the entire surface of the device as a protection layer. Then contact windows are opened on the silicon dioxide using photolithography and wet etching method, so that the electrodes can be exposed to the probe needles in the following poling process.

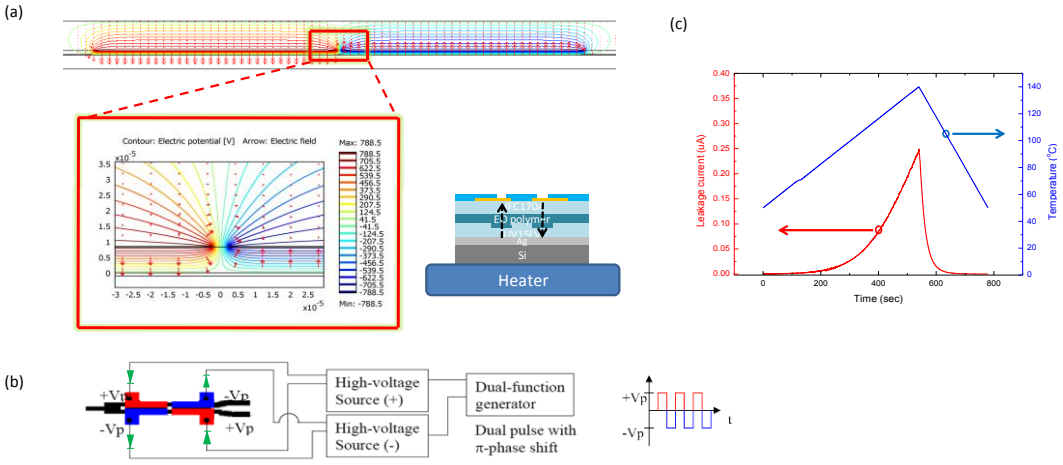

Figure 7.8: (a) The cross section of poling electrodes above the polymer waveguide overlaid the electric potential distribution in push-pull poling configuration. (b) The schematic of push-pull, 2-domain-inversion, alternating-pulse poling. (c) The temperature dependence of leakage current during poling.

Poling is the most important step throughout the entire process since the EO coefficient of a device is determined by poling efficiency [52, 53]. Among several developed poling techniques [54-58], we employ thermally-assisted electric-field contact-poling [59] in this work. In the push-pull configuration, two adjacent poling electrodes above the two arms of directional coupler have opposite polarities and thus the electric field formed between electrodes is very strong, as shown in Fig. 7.8 (a). Given the electrode separation of 5 μm, the polymer waveguide thickness of 8.3 μm and the poling electric field of typically ±100V/μm applied vertically across the polymer waveguide, the maximum electric field between two adjacent electrodes is calculated to be over 300V/μm [33]. This increases the probability of dielectric breakdown which can easily damage the device. To prevent this, the deposited thick silicon dioxide serves as a protection layer, as shown in Fig. 7.8 (a), due to its good insolating property and high dielectric strength (up to 1000V/μm). Experimental tests show that the poling electric field up to 150V/μm can be applied on our device structure at the glass transition temperature (T_g=140^{o}C) of EO polymer without dielectric breakdown. This can significantly increase the poling efficiency. In addition, alternating-pulse poling technique [60, 61] is used to further prevent dielectric breakdown. As shown in Fig. 7.8 (b), the positive and negative voltage sources are controlled by dual pulse with π-phase shift from a dual-function generator, so that two opposite polarities are not applied at the same time. Four diodes are used as clampers. Based on testing experience, the frequency of the alternating pulses should be set to be 1-10Hz to avoid dielectric breakdown.

During the poling process, the temperature is controlled to increase from room temperature to T_g and then quickly decrease back to room temperature. Throughout the entire poling process, leakage current is monitored by a picoammeter. A current-limiting resistor and two back-to-back diodes are used in the circuit connection to protect the picoammeter from being damaged by any unexpected breakdown-induced high current. Figure. 7.8 (c) shows a leakage current curve depending on the controlled temperature during the poling time.

After poling is done, the silicon dioxide layer and the poling electrodes are removed by wet etching method. A 50nm-thick gold seed layer with 5nm-thick chromium adhesion buffer is then deposited above the polymer waveguide by electron-beam evaporation. The buffer mask for the traveling wave electrode is patterned on 10μm-thick AZ-9260 photoresist by photolithography. A 5μm-thick gold film is electroplated using Techni-Gold 25ES electrolyte. A constant current of 8mA is used in the entire gold electroplating process. For the electroplating area of about $11cm^2$, the corresponding current density is as low as $0.73mA/cm^2$ which enables a uniform gold thickness. The conductivity of the electroplated gold film is measured to be $2.2\times10^7 S/m$. The coplanar and ground electrodes are then connected with silver epoxy through via-holes. Finally, the device is diced and the waveguide facets are polished.

7.5 MEASUREMENT OF BROAD BANDWIDTH

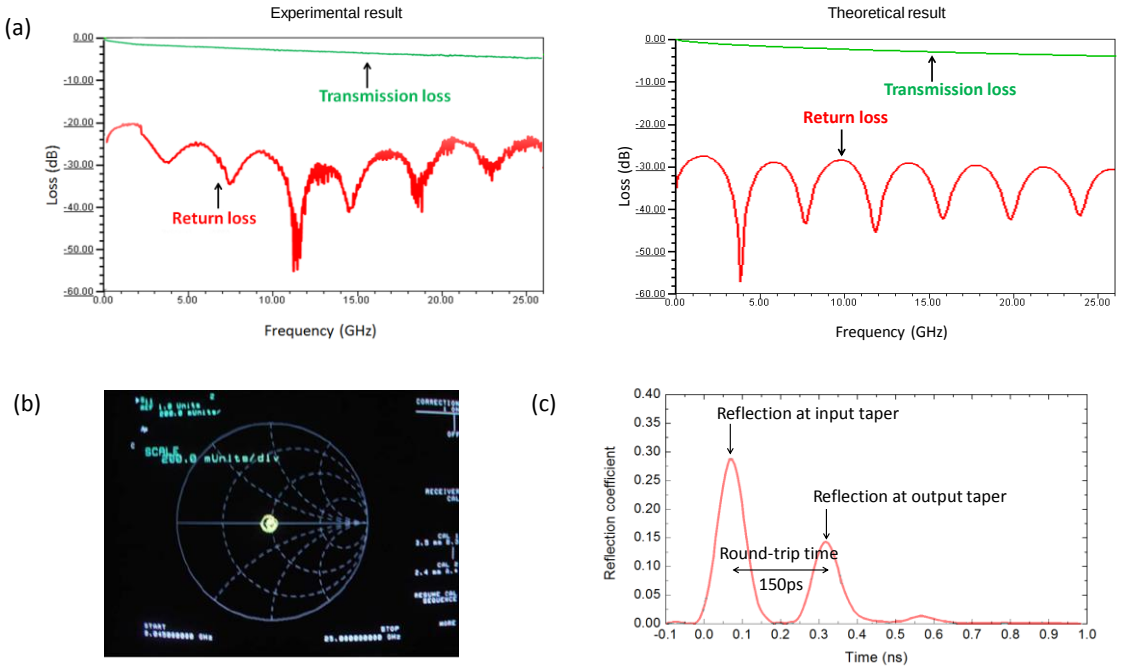

Figure 7.9: (a) The measured transmission loss and return loss of the fabricated traveling wave electrode over the frequency range 1-26GHz (left side), almost matching the theoretical calculations (right side). (b) The measured characteristic impedance of the fabricated traveling wave electrode is well centered at 50Ω on Smith Chart, indicating impedance matching. (c) The time domain measurement of the reflection loss, for the demonstration of velocity matching.

The performance of the fabricated traveling wave electrode is characterized by a vector network analyzer (HP 8510C). Two air coplanar probes (ACP40-GSG-250, Cascade Microtech) are used to couple RF power into and out of the tapered quasi-coplanar waveguides. The measured microwave loss of the traveling wave electrode over the frequency range 1-26GHz (upper frequency limited by equipment) is presented on the left side in Fig. 7.9 (a). For reference, the theoretically calculated electrode loss using

finite element method [43] is shown on the right side in Fig. 7.9 (a). It can be seen that the measured transmission loss is proportional to the square root of frequency, implying that the microwave loss is dominated by the conductor loss (skin effect loss) of the electrode [62, 63] which is measured to be 0.65 ± 0.05dB/cm/GHz$^{1/2}$. The 3-dB electrical bandwidth measured from transmission loss curve is 10GHz, nearly the same value as that from the theoretical calculation in which the actual conductor loss of the electroplated gold electrode has been considered. This bandwidth is limited by the relatively low conductivity of the poorly electroplated gold electrode and can be enhanced by improving the electroplating quality. The measured return loss is well below -20dB. This low return loss is mainly due to the excellent impedance matching as well as the smooth electric field transformation in the CPW-microstrip-CPW transition. It can be noticed that this value is still higher than the theoretical result (<-27dB), probably due to the fabrication imperfection. The periodic ripples in the return loss curve are attributed to the RF Fabry-Perot effect. It is shown in Fig. 7.9 (b) that the characteristic impedance is well centered at 50Ω on Smith chart, indicating impedance matching. The velocity matching between microwaves and optical waves is evaluated by the time domain measurement of the return loss, as shown in Fig. 7.9 (c). The effective relative dielectric constant of the microstrip line is measured to be 2.76 and the resulting index mismatch between microwave sand optical waves is 0.06. Then the bandwidth-length product due to this velocity mismatch can be calculated by Equation (3) to be 302GHz·cm, so the

modulation frequency limit corresponding to 2cm interaction length would be 151GHz, which matches the theoretical calculation result [153GHz from Fig. 7.5 (c)] pretty well.

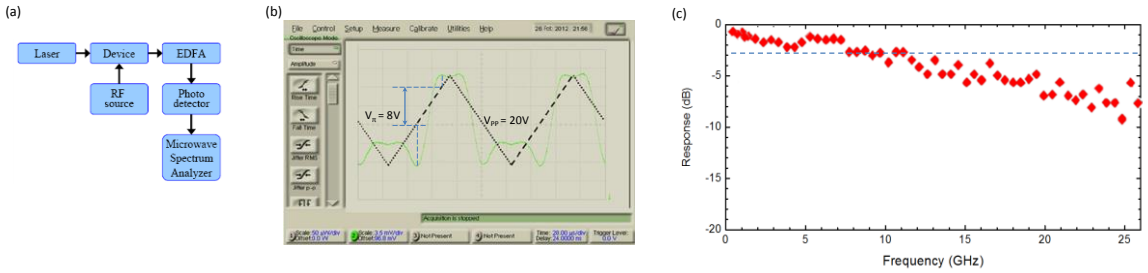

Figure 7.10: (a) The schematic of testing system for small signal optical modulation measurement. (b) Transfer function of over-modulation with V_{pp}=40V at 10kHz (wavelength=1550nm). The switching voltage is measured to be 16.5V. (c) The frequency response of the small signal modulation measured at 4% modulation depth. The 3-dB bandwidth is measured to be 10GHz.

The frequency response of the device is evaluated by the small signal optical modulation measured at 4% modulation depth. The testing system is shown in Fig. 7.10 (a). TM-polarized light with 1550nm wavelength from a tunable laser (Santec ML-200, Santec Corp.) is butt-coupled into the waveguide through a single mode fiber. The measured optical insertion loss is 16 dB, which includes propagation loss of 9dB (absorption loss of 2dB/cm for AJ-CKL1 times the total device length of 3cm, scattering loss of 1dB/cm times 3cm), coupling loss of 6dB (3dB/fact times 2 facets), and 1 dB loss from the MMI splitter. This relatively high loss is attributed to the roughness of the 3-cm long waveguide sidewalls generated in RIE process and the roughness of input and output waveguide facets. To measure the switching voltage (V_π), a testing RF signal with

V_{pp}=20V at 10kHz is used. The transfer function of an over-modulation test is shown in Fig. 7.10 (b). The switching voltage is measured to be 8V at 10kHz, which is a little high probably due to the low poling efficiency of EO polymer and electrode loss. For the small signal optical modulation, RF signal from HP 83651B is fed into the traveling wave electrode through a GSG microprobe. The modulated optical signal is boosted by an erbium doped fiber amplifier (Intelligain, Bay Spec Inc.), converted to electrical signal by a photodiode (DSC-R409, Discovery Semiconductors Inc.), and then measured by a microwave spectrum analyzer (HP 8560E). The frequency response measured at 4% modulation depth is presented in Fig. 7.10 (c), from which the 3-dB bandwidth of the device can be found to be 10GHz. This bandwidth is mainly limited by conductor loss of the traveling wave electrode.

7.6 MEASUREMENT OF HIGH LINEARITY

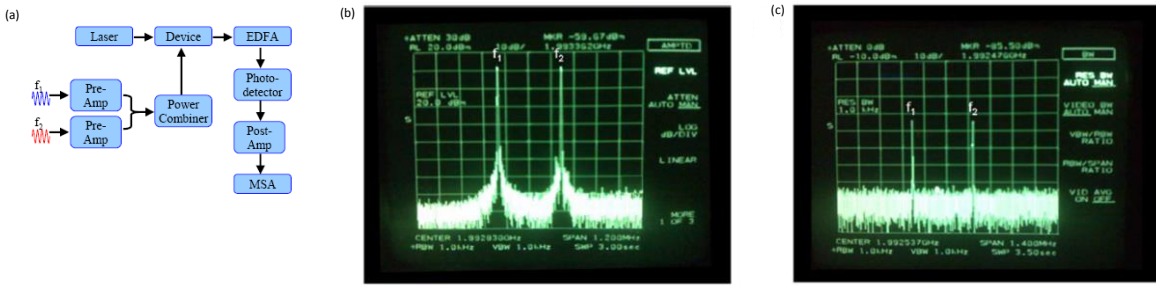

Figure 7.11: (a) The schematic of system for two-tone test. (b) Input two-tone signals ($f_1$and f_2) centered at 1.9928 GHz with 330 kHz tone-interval. (c) Measured output fundamental signals.

A two-tone test is performed to evaluate the linearity of the device. The testing system is illustrated in Fig. 7.11 (a). HP 8620C sweep oscillator is used as the second RF source for the two-tone input signals. Agilent 83020A and HP8449B are used as pre- and post-RF amplifiers, respectively. The two input RF signals are combined by a coaxial two-way RF power combiner (RFLT2W1G04G, RF-Lambda). New Focus model-1014 is used for optical-to-electrical conversion of the modulated signal. The two-tone input signals and the resulting output signals are shown in Figs. 7.11 (b) and (c), respectively. IMD3 signals, which are supposed to appear at one tone-interval away from the fundamental signals if present, are not observed in Fig. 7.11 (c). A possible reason is that the IMD3 signals are well suppressed and buried under the noise floor at this modulation depth. The power level of the two-tone input signals is 12dBm as shown in Fig. 7.11 (b), which is the maximum level available in our two-tone test setup, and this power level translates into the modulation depth of 15%. The simulation result in [12] predicts the IMD3 suppression at 15% modulation depth to be 74dB and the corresponding experimental result in [11] is 69dB, which is a reasonable value considering the fabrication and measurement errors. Neglecting the performance degradation due to microwave loss and velocity mismatch, IMD3 signals would be 30dB below the noise floor in Fig. 7.11 (b) at 1kHz bandwidth resolution.

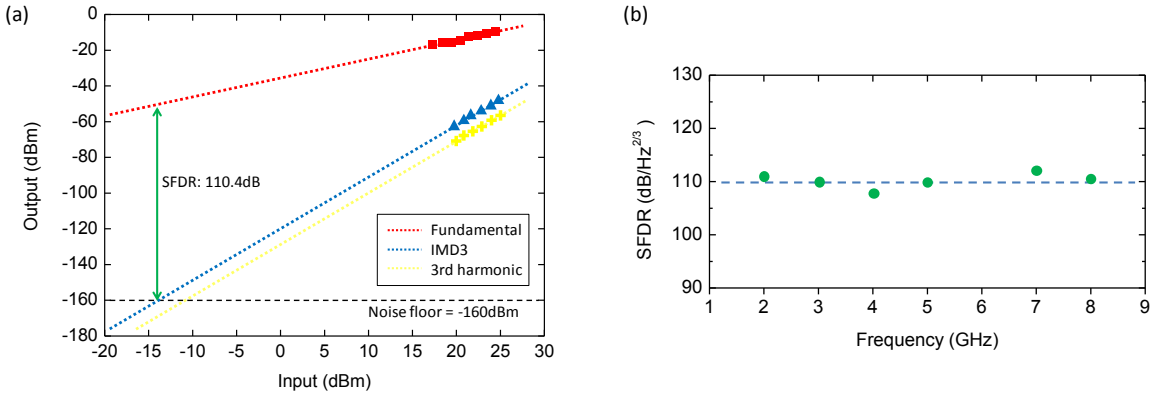

Figure 7.12: (a) The plot of fundamental and third-order intermodulation distortion signals measured at 8GHz. (b) Spurious free dynamic range measured at 2-8GHz.

Since the IMD3 suppression of the fabricated device is out of the measurable range in our two-tone test setup, SFDR is evaluated through an indirect method. It is known that, with the same modulation depth for both tones, IMD3 is three times or 9.54dB higher than the third harmonic distortion [64]. A mono-tone test is done under the same conditions as the two-tone test. The power level of mono-tone input signal is extended up to 29dBm by combining the RF source (HP 83651B) with the pre-amplifier (Agilent 83020A). It is found that the third harmonic distortion of our device comes in the detectable range at the mono-tone input signal level above 20dBm. The IMD3 signals are obtained by adding 9.54dB to the measured third harmonic distortion signals. The SFDR is measured by extrapolating the IMD3 plot to find an intercept point with the noise floor and then measuring the difference with the extrapolated fundamental signal as illustrated in Fig. 7.12 (a). Considering the relative intensity noise (RIN) of the

distributed feedback (DFB) laser and the shot noise of the photodiode, it is very difficult to achieve a noise floor below -145dBm in real analog optical links [12]. However, laboratory test results in most literatures are frequently presented assuming the noise floor at -160dBm considering the typical fiber-optic link parameters [30, 65, 66]. Using -160dBm as noise floor, our measured SFDR is within $110 \pm 3 dB/Hz^{2/3}$ over the modulation frequency range 2-8GHz as shown in Fig. 7.12 (b). The low end frequency is determined by the operation range (2-26.5GHz) of the pre-amplifier (Agilent 83020A) and the high end is limited to 8GHz because the third harmonic of the modulation frequency above 8GHz goes beyond the scope (~26.5GHz) of the microwave spectrum analyzer. The SFDR at 6GHz is missing due to the irregular gain of the post-amplifier at 18GHz. As a comparison, Schaffner et al. reported the SFDR of $109.6 dB/Hz^{2/3}$ at 1 GHz with a $LiNibO_3$ directional coupler modulator which is linearized by adding passive bias sections [6]. In their measurement, however, the noise floor was set at -171dBm, which offers 7.3dB extra dynamic range compared with the noise floor at -160dBm. Hung et al. achieved even higher SFDR of $115.5 dB/Hz^{2/3}$ at 3GHz with a linearized polymeric directional coupler modulator by subtracting the distortions of the measurement system [66]. Here our SFDR of $110 \pm 3 dB/Hz^{2/3}$ includes the distortions from the entire measurement system as well as the device. To the best of our knowledge, such high linearity is first measured at a frequency up to 8GHz.

7.7 SUMMARY

We have demonstrated a linearized traveling wave MMI-fed directional coupler modulator based on EO polymer. Domain-inversion poling is applied to implement the Δβ-reversal technique. The traveling wave electrode is evaluated to be functional up to 151GHz for our device design due to the excellent velocity matching between microwaves and optical waves. The SFDR of $110 \pm 3 dB/Hz^{2/3}$ is achieved over the modulation frequency of 2-8GHz. The measured 3-dB bandwidth of the device is 10GHz, which is mainly limited by conductor loss and needs further improvement for practical applications. The optical loss still needs to be further suppressed for application, and this will be improved in our future work by choosing low loss sol-gel passive materials and by using wet etching method for waveguide fabrication [67].

7.8 REFERENCES

[1] E. I. Ackerman and C. H. Cox, "RF fiber-optic link performance," *Microwave Magazine, IEEE,* vol. 2, pp. 50-58, 2001.

[2] T. E. Darcie and G. E. Bodeep, "Lightwave subcarrier CATV transmission systems," *Microwave Theory and Techniques, IEEE Transactions on,* vol. 38, pp. 524-533, 1990.

[3] G. Lenz, B. Eggleton, C. K. Madsen, and R. Slusher, "Optical delay lines based on optical filters," *Quantum Electronics, IEEE Journal of,* vol. 37, pp. 525-532, 2001.

[4] K. P. Jackson, S. A. Newton, B. Moslehi, M. Tur, C. C. Cutler, J. W. Goodman, and H. Shaw, "Optical fiber delay-line signal processing," *Microwave Theory and Techniques, IEEE Transactions on,* vol. 33, pp. 193-210, 1985.

[5] C.-Y. Lin, A. X. Wang, B. S. Lee, X. Zhang, and R. T. Chen, "High dynamic range electric field sensor for electromagnetic pulse detection," *Optics Express,* vol. 19, pp. 17372-17377, 2011.

[6] J. H. Schaffner, J. F. Lam, C. J. Gaeta, G. L. Tangonan, R. L. Joyce, M. L. Farwell, and W. S. C. Chang, "Spur-free dynamic range measurements of a fiber optic link with traveling wave linearized directional coupler modulators," *Photonics Technology Letters, IEEE,* vol. 6, pp. 273-275, 1994.

[7] S. Thaniyavarn, "Modified 1×2 directional coupler waveguide modulator," *Electronics Letters,* vol. 22, pp. 941-942, 1986.
[8] S. Dubovitsky, W. Steier, S. Yegnanarayanan, and B. Jalali, "Analysis and improvement of Mach-Zehnder modulator linearity performance for chirped and tunable optical carriers," *Lightwave Technology, Journal of,* vol. 20, pp. 886-891, 2002.
[9] H. Kogelnik and R. V. Schmidt, "Switched directional couplers with alternating Δβ," *Quantum Electronics, IEEE Journal of,* vol. 12, pp. 396-401, 1976.
[10] R. F. Tavlykaev and R. V. Ramaswamy, "Highly linear Y-fed directional coupler modulator with low intermodulation distortion," *Lightwave Technology, Journal of,* vol. 17, pp. 282-291, 1999.
[11] B. Lee, C. Y. Lin, A. X. Wang, R. Dinu, and R. T. Chen, "Linearized electro-optic modulators based on a two-section Y-fed directional coupler," *Applied optics,* vol. 49, pp. 6485-6488, 2010.
[12] X. Wang, B. S. Lee, C. Y. Lin, D. An, and R. T. Chen, "Electroptic polymer linear modulators based on multiple-domain Y-fed directional coupler," *Journal of Lightwave Technology,* vol. 28, pp. 1670-1676, 2010.
[13] M. Izutsu, Y. Yamane, and T. Sueta, "Broad-band traveling-wave modulator using a LiNbO3optical waveguide," *Quantum Electronics, IEEE Journal of,* vol. 13, pp. 287-290, 1977.
[14] M. Izutsu, T. Itoh, and T. Sueta, "10 GHz bandwidth traveling-wave LiNbO3optical waveguide modulator," *Quantum Electronics, IEEE Journal of,* vol. 14, pp. 394-395, 1978.
[15] C. Teng, "Traveling‐wave polymeric optical intensity modulator with more than 40 GHz of 3‐dB electrical bandwidth," *Applied Physics Letters,* vol. 60, pp. 1538-1540, 1992.
[16] D. Chen, H. R. Fetterman, A. Chen, W. H. Steier, L. R. Dalton, W. Wang, and Y. Shi, "Demonstration of 110 GHz electro-optic polymer modulators," *Applied Physics Letters,* vol. 70, p. 3335, 1997.
[17] M. Lee, H. E. Katz, C. Erben, D. M. Gill, P. Gopalan, J. D. Heber, and D. J. McGee, "Broadband modulation of light by using an electro-optic polymer," *Science,* vol. 298, pp. 1401-1403, 2002.
[18] L. R. Dalton, A. W. Harper, B. Wu, R. Ghosn, J. Laquindanum, Z. Liang, A. Hubbel, and C. Xu, "Polymeric Electro‐Optic Modulators: Matereials synthesis and processing," *Advanced Materials,* vol. 7, pp. 519-540, 1995.
[19] J. D. Kraus and R. J. Marhefka, *Antenna for all applications*, 3rd ed.: McGraw-Hill 2002.
[20] M. C. Oh, H. Zhang, C. Zhang, H. Erlig, Y. Chang, B. Tsap, D. Chang, A. Szep, W. H. Steier, and H. R. Fetterman, "Recent advances in electrooptic polymer modulators incorporating highly nonlinear chromophore," *Selected Topics in Quantum Electronics, IEEE Journal of,* vol. 7, pp. 826-835, 2001.

[21] Y. Shi, C. Zhang, H. Zhang, J. H. Bechtel, L. R. Dalton, B. H. Robinson, and W. H. Steier, "Low (sub-1-volt) halfwave voltage polymeric electro-optic modulators achieved by controlling chromophore shape," *Science,* vol. 288, pp. 119-122, 2000.

[22] Y. Enami, C. Derose, D. Mathine, C. Loychik, C. Greenlee, R. Norwood, T. Kim, J. Luo, Y. Tian, and A. K. Y. Jen, "Hybrid polymer/sol–gel waveguide modulators with exceptionally large electro–optic coefficients," *Nature Photonics,* vol. 1, pp. 180-185, 2007.

[23] Y. Enami, D. Mathine, C. DeRose, R. Norwood, J. Luo, A. K. Y. Jen, and N. Peyghambarian, "Hybrid cross-linkable polymer/sol-gel waveguide modulators with 0.65 V half wave voltage at 1550 nm," *Applied Physics Letters,* vol. 91, p. 093505, 2007.

[24] J. Luo, S. Huang, Y. J. Cheng, T. D. Kim, Z. Shi, X. H. Zhou, and K. Y. J. Alex, "Phenyltetraene-based nonlinear optical chromophores with enhanced chemical stability and electrooptic activity," *Organic letters,* vol. 9, pp. 4471-4474, 2007.

[25] T. Baehr-Jones, M. Hochberg, G. Wang, R. Lawson, Y. Liao, P. Sullivan, L. Dalton, A. K. Y. Jen, and A. Scherer, "Optical modulation and detection in slotted silicon waveguides," *Optics Express,* vol. 13, pp. 5216-5226, 2005.

[26] J. H. Wülbern, J. Hampe, A. Petrov, M. Eich, J. Luo, A. K. Y. Jen, A. Di Falco, T. F. Krauss, and J. Bruns, "Electro-optic modulation in slotted resonant photonic crystal heterostructures," *Applied Physics Letters,* vol. 94, p. 241107, 2009.

[27] X. Wang, C. Y. Lin, S. Chakravarty, J. Luo, A. K. Y. Jen, and R. T. Chen, "Effective in-device r< sub> 33</sub> of 735 pm/V on electro-optic polymer infiltrated silicon photonic crystal slot waveguides," *Optics letters,* vol. 36, pp. 882-884, 2011.

[28] A. C. G. Nutt, V. Gopalan, and M. C. Gupta, "Domain inversion in LiNbO3 using direct electron - beam writing," *Applied Physics Letters,* vol. 60, pp. 2828-2830, 1992.

[29] D. Jin, H. Chen, A. Barklund, J. Mallari, G. Yu, E. Miller, and R. Dinu, "EO polymer modulators reliability study," in *Proc. SPIE 7599*, 2010, pp. 75990H-8.

[30] R. B. Childs and V. A. O'Byrne, "Predistortion linearization of directly modulated DFB lasers and external modulators for AM video transmission," in *Proc. Tech. Dig. Opt. Fiber Commun. Conf.,*, San Francisco, CA, 1990.

[31] R. M. D. E. Ridder and S. Korotky, "Feedforward compensation of integrated optic modulator distortion," in *Proc. Tech. Dig. Opt. Fiber Commun. Conf.*, San Francisco, CA, 1990.

[32] L. M. Johnson and H. Roussell, "Reduction intermodulation distortion in interferometric optical modulators," *Optics letters,* vol. 13, pp. 928-930, 1988.

[33] S. K. Korotky and R. De Ridder, "Dual parallel modulation schemes for low-distortion analog optical transmission," *Selected Areas in Communications, IEEE Journal on,* vol. 8, pp. 1377-1381, 1990.

[34] M. L. Farwell, Z. Q. Lin, E. Wooten, and W. Chang, "An electrooptic intensity modulator with improved linearity," *Photonics Technology Letters, IEEE,* vol. 3, pp. 792-795, 1991.
[35] B. Lee, C. Lin, X. Wang, R. T. Chen, J. Luo, and A. K. Y. Jen, "Bias-free electro-optic polymer-based two-section Y-branch waveguide modulator with 22 dB linearity enhancement," *Optics letters,* vol. 34, pp. 3277-3279, 2009.
[36] FIMMWAVE simulation software, http://www.photond.com/products/fimmwave.htm
[37] FIMMPROP simulation software, http://www.photond.com/products/fimmprop.htm
[38] G. T. Reed, *Silicon Photonics: the state of the art*. UK: Wiley-Interscience, 2008.
[39] COMSOL Multiphysics Simulation Software, http://www.comsol.com.
[40] R. G. Hunsperger, A. Yariv, and A. Lee, "Parallel end-butt coupling for optical integrated circuits," *Applied optics,* vol. 16, pp. 1026-1032, 1977.
[41] M. Sanghadasa, P. R. Ashley, E. L. Webster, C. Cocke, G. A. Lindsay, and A. J. Guenthner, "A simplified technique for efficient fiber-polymer-waveguide power coupling using a customized cladding with tunable index of refraction," *Lightwave Technology, Journal of,* vol. 24, pp. 3816-3823, 2006.
[42] K. Geary, S. K. Kim, B. J. Seo, Y. C. Hung, W. Yuan, and H. R. Fetterman, "Photobleached refractive index tapers in electrooptic polymer rib waveguides," *Photonics Technology Letters, IEEE,* vol. 18, pp. 64-66, 2006.
[43] I. E. Day, I. Evans, A. Knights, F. Hopper, S. Roberts, J. Johnston, S. Day, J. Luff, H. K. Tsang, and M. Asghari, "Tapered silicon waveguides for low insertion loss highly-efficient high-speed electronic variable optical attenuators," in *Optical Fiber Communications Conference*, 2003, pp. 249 - 251
[44] Rsoft simulation software, http://www.rsoftdesign.com/
[45] W. S. Chang, *RF photonic technology in optical fiber links*: Cambridge Univ Pr, 2002.
[46] D. Chen, Q. Wang, and Z. Shen, "A broadband microstrip-to-CPW transition," in *Microwave Conference Proceedings, 2005. APMC 2005. Asia-Pacific Conference Proceedings*, 2005, p. 4.
[47] T.-D. Kim, J. Luo, Y.-J. Cheng, Z. Shi, S. Hau, S.-H. Jang, X.-H. Zhou, Y. Tian, B. Polishak, S. Huang, Ma.Hong, L. R. Dalton, and A. K.-Y. Jen, "Binary Chromophore Systems in Nonlinear Optical Dendrimers and Polymers for Large Electrooptic Activities†," *The Journal of Physical Chemistry C,* vol. 112, pp. 8091-8098, 2008.
[48] E. Yamashita, "Variational method for the analysis of microstrip-like transmission lines," *Microwave Theory and Techniques, IEEE Transactions on,* vol. 16, pp. 529-535, 1968.
[49] ANSYS HFSS simulation software, http://www.ansys.com/
[50] A. Chen and E. Murphy, *Broadband Optical Modulators: Science, Technology, and Applications*: CRC Press, 2011.

[51] R. C. Alferness, "Waveguide electrooptic modulators," *IEEE Transactions on Microwave Theory Techniques,* vol. 30, pp. 1121-1137, 1982.
[52] D. M. Burland, R. D. Miller, and C. A. Walsh, "Second-order nonlinearity in poled-polymer systems," *Chemical Reviews,* vol. 94, pp. 31-75, 1994.
[53] L. R. Dalton, P. A. Sullivan, and D. H. Bale, "Electric field poled organic electro-optic materials: state of the art and future prospects," *Chemical Reviews,* vol. 110, pp. 25-55, 2009.
[54] M. A. Mortazavi, A. Knoesen, S. T. Kowel, B. G. Higgins, and A. Dienes, "Second-harmonic generation and absorption studies of polymer—dye films oriented by corona-onset poling at elevated temperatures," *JOSA B,* vol. 6, pp. 733-741, 1989.
[55] H. Tang, J. M. Taboada, G. Cao, L. Li, and R. T. Chen, "Enhanced electro-optic coefficient of nonlinear optical polymer using liquid contact poling," *Applied Physics Letters,* vol. 70, p. 538, 1997.
[56] Z. Z. Yue, D. An, R. T. Chen, and S. Tang, "1000 V/μm pulsed poling technique for photolime-gel electro-optic polymer with room-temperature repoling feature," *Applied Physics Letters,* vol. 72, p. 3420, 1998.
[57] S. Huang, T. D. Kim, J. Luo, S. K. Hau, Z. Shi, X. H. Zhou, H. L. Yip, and A. K. Y. Jen, "Highly efficient electro-optic polymers through improved poling using a thin TiO-modified transparent electrode," *Applied Physics Letters,* vol. 96, p. 243311, 2010.
[58] S. Huang, J. Luo, H. L. Yip, A. Ayazi, X. H. Zhou, M. Gould, A. Chen, T. Baehr‐Jones, M. Hochberg, and A. K. Y. Jen, "Electro‐optical Materials: Efficient Poling of Electro‐Optic Polymers in Thin Films and Silicon Slot Waveguides by Detachable Pyroelectric Crystals (Adv. Mater. 10/2012)," *Advanced Materials,* vol. 24, pp. OP1-OP1, 2012.
[59] R. Blum, M. Sprave, J. Sablotny, and M. Eich, "High-electric-field poling of nonlinear optical polymers," *JOSA B,* vol. 15, pp. 318-328, 1998.
[60] T. A. Tumolillo Jr and P. R. Ashley, "A novel pulse-poling technique for EO polymer waveguide devices using device electrode poling," *Photonics Technology Letters, IEEE,* vol. 4, pp. 142-145, 1992.
[61] V. Taggi, F. Michelotti, M. Bertolotti, G. Petrocco, V. Foglietti, A. Donval, E. Toussaere, and J. Zyss, "Domain inversion by pulse poling in polymer films," *Applied Physics Letters,* vol. 72, p. 2794, 1998.
[62] J. Baker-Jarvis, M. D. Janezic, B. Riddle, C. L. Holloway, and N. Paulter, "Dielectric and conductor-loss characterization and measurements on electronic packaging materials," *2001.,* 2001.
[63] G. K. Gopalakrishnan, W. K. Burns, R. W. McElhanon, C. H. Bulmer, and A. S. Greenblatt, "Performance and modeling of broadband LiNbO3 traveling wave optical intensity modulators," *Lightwave Technology, Journal of,* vol. 12, pp. 1807-1819, 1994.

[64] P. L. Liu, B. Li, and Y. Trisno, "In search of a linear electrooptic amplitude modulator," *Photonics Technology Letters, IEEE,* vol. 3, pp. 144-146, 1991.
[65] W. B. Bridges and J. H. Schaffner, "Distortion in linearized electrooptic modulators," *Microwave Theory and Techniques, IEEE Transactions on,* vol. 43, pp. 2184-2197, 1995.
[66] Y. C. Hung, S. K. Kim, H. Fetterman, J. Luo, and A. K. Y. Jen, "Experimental demonstration of a linearized polymeric directional coupler modulator," *Photonics Technology Letters, IEEE,* vol. 19, pp. 1762-1764, 2007.
[67] C. T. DeRose, R. Himmelhuber, D. Mathine, R. Norwood, J. Luo, A. K. Y. Jen, and N. Peyghambarian, "High Δn strip-loaded electro-optic polymer waveguide modulator with low insertion loss," *Optics Express,* vol. 17, pp. 3316-3321, 2009.

Chapter 8: Thermo-optic Switch Based on Silicon Coupled Photonic Crystal Microcavities

8.1 INTRODUCTION

Integrated optical switches are important building blocks in silicon photonics [1-3] and have many potential applications including optical interconnects, optical routing, protecting switching, and reconfigurable optical add-drop multiplexing (ROADM) [4]. Silicon optical switches based on Thermo-optic (TO) effect [5] are very attractive due to their small size, large scalability, and potential for integration with wavelength-division-multiplexing (WDM) multiplexers. The speed of TO switches is adequate for all routing applications [6]. Since silicon's TO effect is significantly larger than its electro-optic (EO) effect [7], silicon TO switches promises efficient and low-power optical switching. Conventional Mach–Zehnder interferometer switches or directional coupler switches [8, 9] have large size and require relatively high switching power compared to other structures, which limits the integration density and energy conservation. Another type of widely-used compact and efficient structures for optical switching is microring resonators [10]. So far, the smallest ring diameter reported is 3μm [11]; however, one drawback of microring switches is the very narrow operational optical bandwidth (<1nm) and the requirements of resonance tuning techniques. To address this issue, cascaded microrings along one waveguide have been developed to broaden the overall optical bandwidth [12-14]; however, the total size of the device has to increase

accordingly. Furthermore, although all these microrings are designed to be ideal, the randomness in fabrication may make them slightly off-resonance among each other and with different extinction ratios; therefore, resonance tuning on each individual microring is required and thus makes the whole device and tuning system more complex [15]. In recent years, some photonic crystal (PC)-based devices have been proposed as compact and low-power switches [16, 17], but many of them rely on a membrane geometry that is susceptible to damage and difficult to integrate with heaters and electrical contacts. PC designs based on silicon-on-insulator (SOI) substrates are more robust [18, 19]. For example, a PC directional coupler switch was demonstrated with a length of 4.9μm and insertion loss of 1-2dB [20]; however, the dispersion diagram needs to be carefully engineered to maximize the change of wave vector for minimum change in frequency or refractive index (to maximize the extinction ratio), and also its operational optical bandwidth is limited due to the high dispersion of PCs. Another type of switch is based on band-edge shifted photonic crystal waveguides (PCWs) [21, 22]. However, this device needs to be operated very close to its photonic band edge where the large group index causes high optical loss, and its high dispersion feature near the band edge limits the operational optical bandwidth. The band edge shifted PCW also requires larger heating and temperature shifts for switching and therefore does not present a significant advantage in terms of speed and power consumption [17]. Therefore, a TO switch with compact size, wide optical bandwidth, low loss and low switching power, as well as ease of design and fabrication, is highly required.

In this chapter, we design, fabricate and characterize a compact and high-performance TO switch based on two coupled L0 type PC microcavities integrated with a micro-heater on a SOI substrate. Various coupled PC microcavities have been theoretically studied and experimentally demonstrated previously for switching in the context of gap solitons [23] and optical analogs to electromagnetically induced transparency [24]. However, this structure has rarely been explored as an optical switch. In this work, simulations are performed to design coupled PC microcavities with 6nm-wide resonance dip in the transmission spectrum. Measurement results on the fabricated coupled PC microcavities verifies this 6nm-wide resonance dip and also shows an optical extinction ratio of ~20dB. This relatively wide resonance dip enables significantly broader operational optical bandwidth with only two coupled PC resonators compared to widely-used multi-cascaded ring resonators and have potential for applications such as coarse WDM in cable television networks [25]. A microheater is designed to efficiently drive the device. The resonance shifts are measured under different DC driving power, and a constant switching power for this 6nm-wide operational spectrum is measured to be 18.2mW. The TO tuning efficiency is measured to be 0.63nm/mW. On-off switching is performed, and a rise time of 14.8μsec and a fall time of 18.5μsec are measured. The on-chip optical loss is measured to be about 1dB. While TO tuning is used here to demonstrate the functional switching on the coupled PC microcavities, higher switching speed could be achieved by free carrier modulation in the future, enabling more potential

applications including high-speed photonic interconnects and broadband optical communication systems.

8.2 DESIGN OF SILICON PHOTONIC CRYSTAL NANO-CAVITY

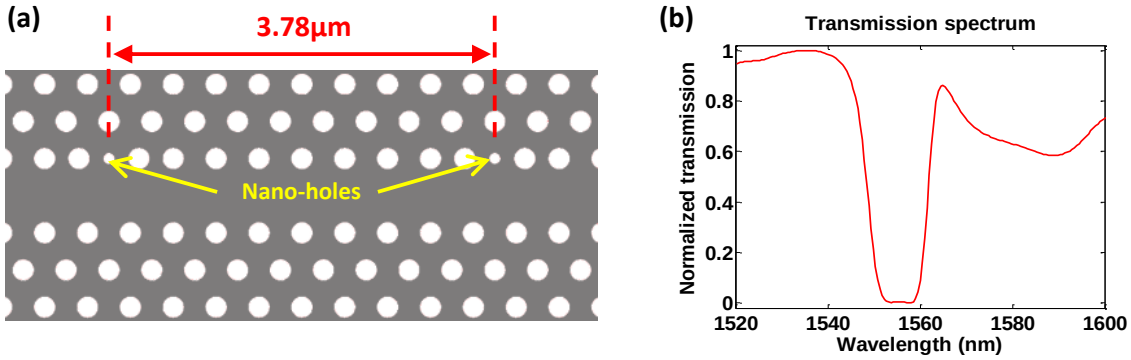

Figure 8.1: (a) Top view of the W1 PCW with a coupled PC microcavity. (b) Simulated transmission spectrum of the coupled PC microcavity, showing a 6nm-wide resonance dip in the transmission band.

Figs. 8.1 (a) and (b) show a simple schematic of the TO switch on an SOI substrate (Si thickness=250nm, buried oxide thickness=3µm). A 35µm-long W1 PCW is designed with a lattice constant of 420nm, hole diameter of 201nm, and with 7 rows of holes on each side. Two nanoholes with diameter d_{NH}=100.5nm are separated by 9 periods of holes. The nanoholes are in the center of the individual L0 PC microcavities formed by shifting two adjacent air holes by 84nm from their lattice positions, away from each other, forming a 3.78µm-long cavity, as shown in Fig. 8.1 (a). Coupling of the two resonators leads to an 6nm-wide resonance dip [24], as shown by the FDTD simulation

result in Fig. 8.1 (b). This resonance is located ~70nm far away from the band edge (at ~1620nm). The group index in this low-dispersion region is ~6, which is relatively lower compared to band-edge shifting switches [21] and promises low optical loss. The input and output strip waveguides are connected to the PCW using low-loss group index tapers.

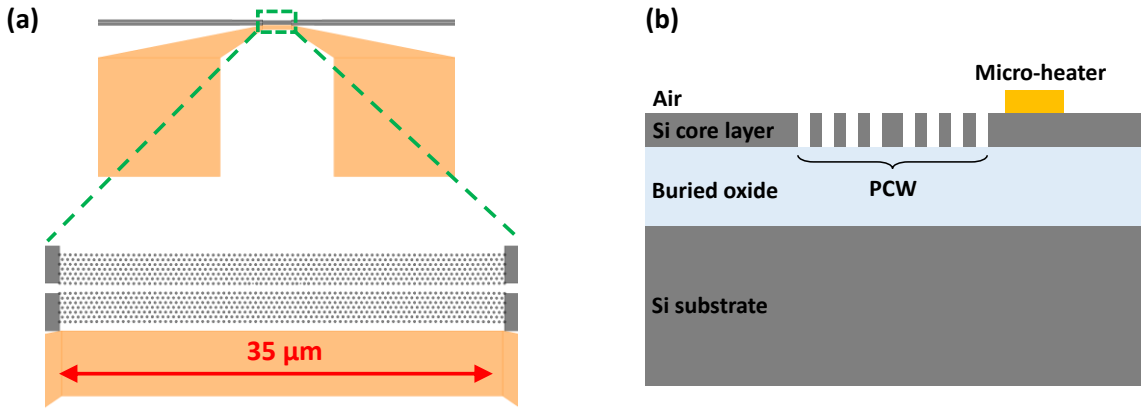

Figure 8.2: (a) Top view of the micro-heater integrated with W1 PCW. (b) Cross section of the micro-heater integrated on an SOI substrate.

A gold strip micro-heater electrode [26] is used to efficiently drive the device through TO effect, as shown in Figs. 8.2 (a) and (b). This resistive micro-heater is 35 µm long, 5 µm wide, and 150nm thick, and is placed sideways the PCW with a separation of 3 µm from the PCW center, far enough to avoid extra optical loss. The current flow results in Joule heating on silicon. The direct contact between the micro-heater and the silicon core layer allows an efficient heat transfer owing to the high thermal conductivity of silicon (k=149 W $\cdot$m^{-1} $\cdot$K^{-1}). In addition, the buried oxide layer of SOI wafer functions

as a vertical thermal barrier, which further facilitates lateral heat exchange between the heater and the waveguide region [26]. This efficient micro-heater, together with the large TO coefficient of silicon ($dn/dT=1.86\times10^{-4}K^{-1}$ at room temperature), is beneficial for high-speed and low-power operation. Air serves as top cladding, and no passivation layer is required, which simplifies the fabrication steps.

8.3 DEVICE FABRICATION

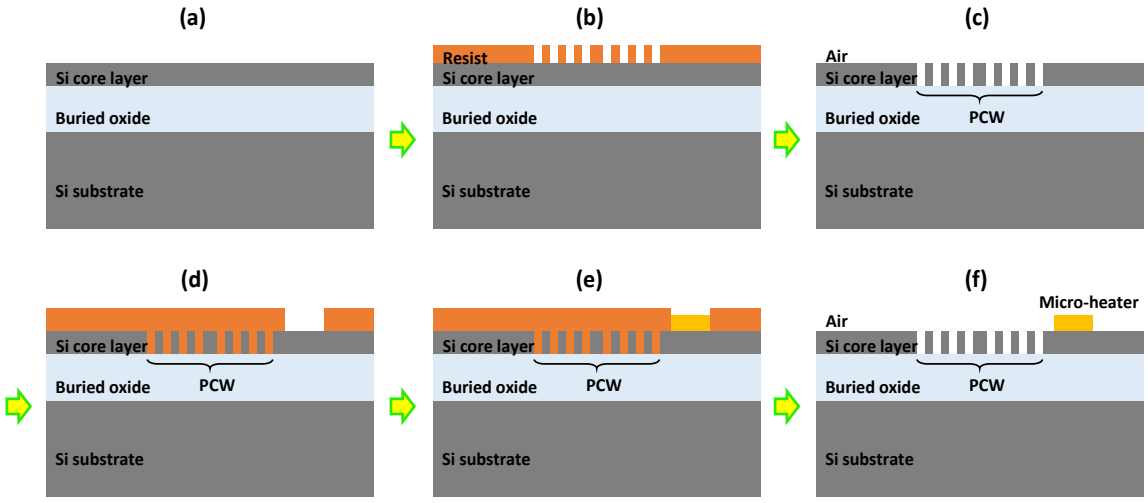

Figure 8.3: Fabrication process flow. (a) SOI wafer. (b) E-beam lithography. (c) RIE. (d) Photolithography alignment. (e) E-beam evaporation. (f) Lift-off.

The silicon PCW with cavities is fabricated using e-beam lithography and RIE in a single patterning/etching step, while gold micro-heater is patterned by photolithography, e-beam evaporation and lift-off process, as shown in the fabrication flow in Fig. 8.3. 2D PC structures with similar geometries have been recently fabricated by our group by

photolithography using commercial foundry resources. A microscope image of the fabricated TO switch is shown in Figs. 8.4 (a) and (b). SEM images of the fabricated photonic crystal waveguide with nanoholes are shown in Figs 8.4 (c) and (d).

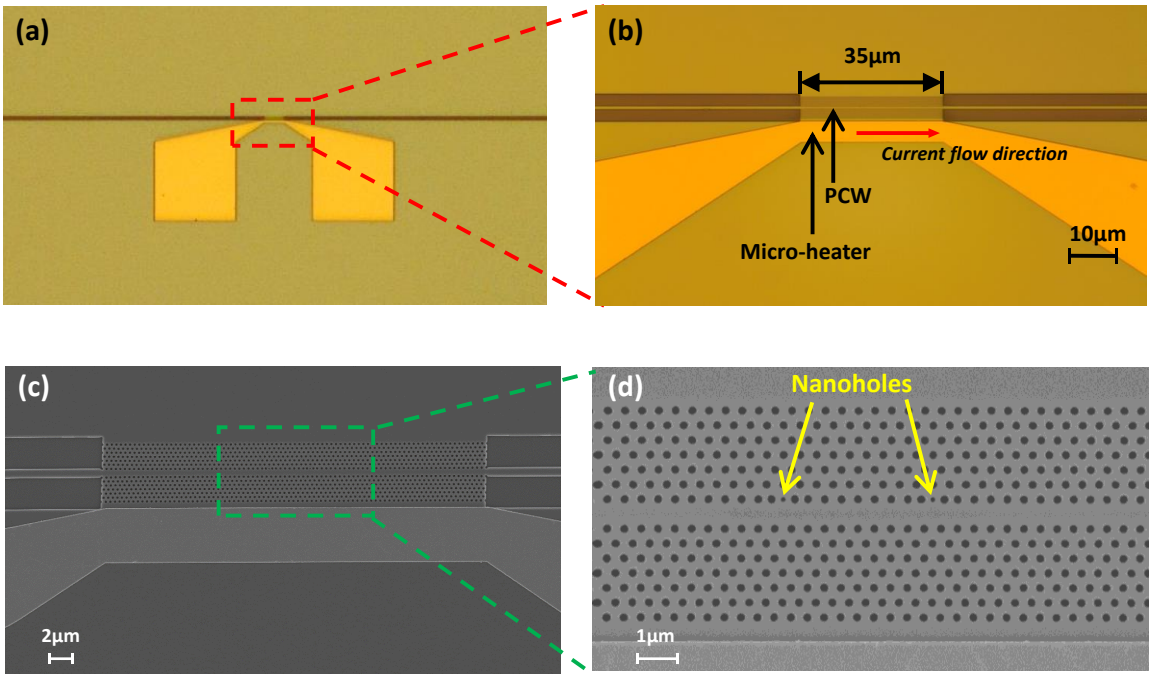

Figure 8.4: Fabrication devices. (a) and (b) Microscope images of the fabricated device (top view). (c) and (d) SEM imges of the fabrication devices.

8.4 MEASUREMENT OF RESONANCE SHIFTING UNDER DC POWER

To characterize the coupled PC microcavity TO switch, light from a broadband amplified spontaneous emission (ASE) source is amplified by an Erbium-doped fiber amplifier (EDFA) and coupled into and out of the device via grating couplers, and then the optical output is sent to an optical spectrum analyzer. The measured normalized

transmission spectrum of the device is shown by the dark blue curve in Fig. 8.5 (a). A resonance with an almost flat dip is observed from 1552nm to 1558nm. The measured loss on the PCW is about 1dB at the left transmission band. Next, constant voltage is applied onto the micro-heater, and the voltage (V_1-V_5) is tuned from 0V to 0.8V in step of 0.2V, corresponding to the power (P_1-P_5) of 0mW, 1.2mW, 4.7mW, 10.4mW and 18.2mW (calculated from the measured current and voltage). As a result, the measured transmission spectrum is red-shifted as the power increases, as shown by the overlaid spectra in Fig. 8.5 (a). This is because the increases of temperature leads to the increase of refractive index of silicon PCW and thus moves the dielectric band farther away from the air band in the photonic band diagram. Alternatively, this can be explained by the increased effective total optical round trip length of the cavity due to the increase of silicon index. Based on Fig. 8.5 (a), if a laser wavelength is fixed at 1552nm which is the left edge of the resonance dip, then the required power to switch the optical output power from minimum to maximum is 4.7mW. If a laser wavelength is fixed at the right boundary of the resonance dip, 1560nm, then the required switching power 18.2mW. This 18.2mW is the constant power for switching from off-state to on-state for all 6nm-wide wavelength range. The optical extinction ratio measured from Fig. 8.5 (a) is 20dB. By extracting the measured data of resonance shifts as a function of thermal power applied on the microheater, a TO tuning efficiency of 0.63nm/mW is obtained.

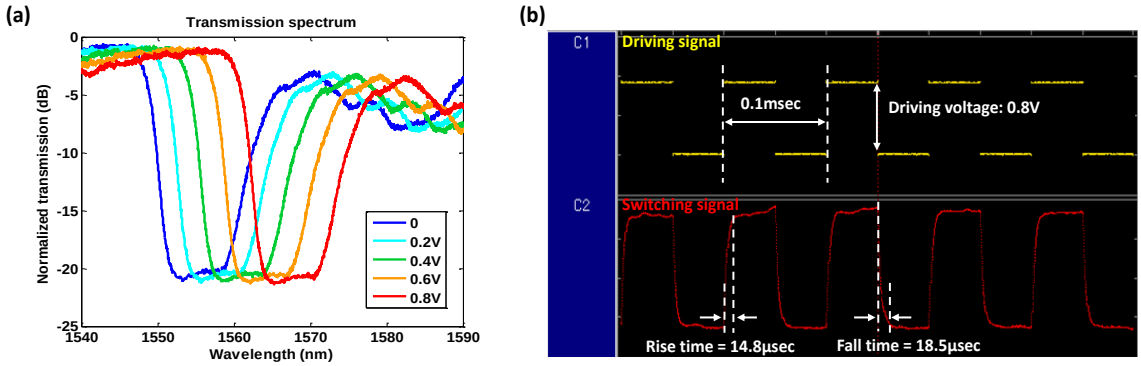

Figure 8.5: (a) Measured normalized transmission spectra of the PCW TO switch under different driving voltage. (b) Measured on-off switching characteristics at 10KHz.

8.5 MEASUREMENT OF THERMAL-OPTIC SWITCHING TRANSFER FUNCTION

Furthermore, an on-off switching test is performed. A tunable laser passing a polarization controller is used to provide TE-polarized optical input, and its wavelength is tuned to 1555 nm which is within the resonance dip in the spectrum. Square wave RF signal with V_{pp}=0.8V at 10KHz is applied on the micro-heater. The switching optical signal is sent to a photodetector and displayed on an oscilloscope, as shown in Fig. 8.5 (b). The switching rise time (from 10% to 90% transmission) and fall time (from 90% to 10% transmission) are measured to be 14.8 µsec and 18.5 µsec, respectively. We also observe the switching characteristic when the laser is tuned from 1552nm to 1558nm, indicating the 6nm-wide operational optical bandwidth, which is much better than ring resonator switches whose operation optical bandwidth is smaller than 1nm. This

relatively wide resonance dip enables broader operational optical bandwidth than widely-used ring resonators and are potential for applications such as coarse WDM in cable television networks [25].

8.6 SUMMARY

In conclusion, we demonstrate a compact and high-performance TO switch based on two coupled L0 type cavities integrated with a micro-heater. The L0 PC microcavity is formed by simply shifting two PC air holes adjacent to the W1 PCW by 0.2a, and is further modified by inserting a nanohole with radius d_{NH}=0.5d, where a is the lattice constant and d is the diameter of the air holes in the bulk PC lattice. Two nanoholes are separated by 9 periods of holes, forming a 3.78μm-long cavity. The measured transmission spectrum shows a ~6nm-wide resonance dip with an optical extinction ratio of ~20dB. This relatively wide resonance dip enables broader operational optical bandwidth than widely-used ring resonators and is thus useful for improving traffic management in coarse WDM in cable television networks [25] . The resonance shifts are measured under different DC driving power with a measured TO tuning efficiency of 0.63nm/mW, and a constant switching power for this 6nm-wide operational spectrum is measured to be 18.2mW. A rise time of 14.8μsec and a fall time of 18.5μsec are measured in an on-off switching test. There is enough room for further optimization of switching speed and power efficiency. In the future, to improve the switching speed, the L0 PC microcavity can be appropriately doped to form a p-n or p-i-n structure and be operated as a fast electro-optic switch via free carrier modulation [27, 28]. The coupled

PC microcavities can be modified with different resonance dip width (e.g. 1nm, 2nm, etc.) by proper design of microcavity structures and active control of resonant mode-splitting [29]. And also, the device can be cascaded [30] to enable multiple resonances for more potential applications such as wavelength selective switches [31] and tunable multichannel optical filters [32]. Some other potential applications of this very compact TO device can be generalized and extended, such as a thermal (or temperature) sensor on photonic integrated circuits. Since the device is fabricated without top surface cladding, it can also be used for biochemical sensing applications that simultaneously required local heating [33].

8.7 REFERENCES

[1] R. Soref, "The past, present, and future of silicon photonics," *Selected Topics in Quantum Electronics, IEEE Journal of,* vol. 12, pp. 1678-1687, 2006.

[2] B. Jalali and S. Fathpour, "Silicon photonics," *Lightwave Technology, Journal of,* vol. 24, pp. 4600-4615, 2006.

[3] H. Subbaraman, X. Xu, A. Hosseini, X. Zhang, Y. Zhang, D. Kwong, and R. T. Chen, "Recent advances in silicon-based passive and active optical interconnects," *Optics Express,* vol. 23, pp. 2487-2511, 2015.

[4] S. Yao, B. Mukherjee, and S. Dixit, "Advances in photonic packet switching: an overview," *Communications Magazine, IEEE,* vol. 38, pp. 84-94, 2000.

[5] G. Cocorullo and I. Rendina, "Thermo-optical modulation at 1.5 μm in silicon etalon," *Electronics Letters,* vol. 28, pp. 83-85, 1992.

[6] G. Coppola, L. Sirleto, I. Rendina, and M. Iodice, "Advance in thermo-optical switches: principles, materials, design, and device structure," *Optical Engineering,* vol. 50, pp. 071112-071112-14, 2011.

[7] R. A. Soref and B. R. Bennett, "Electrooptical effects in silicon," *Quantum Electronics, IEEE Journal of,* vol. 23, pp. 123-129, 1987.

[8] M. W. Geis, S. J. Spector, R. Williamson, and T. Lyszczarz, "Submicrosecond submilliwatt silicon-on-insulator thermooptic switch," *Photonics Technology Letters, IEEE,* vol. 16, pp. 2514-2516, 2004.

[9] S. Nakamura, Y. Ueno, and K. Tajima, "168-Gb/s all-optical wavelength conversion with a symmetric-Mach-Zehnder-type switch," *Photonics Technology Letters, IEEE,* vol. 13, pp. 1091-1093, 2001.

[10] Y. Vlasov, W. M. Green, and F. Xia, "High-throughput silicon nanophotonic wavelength-insensitive switch for on-chip optical networks," *Nature Photonics,* vol. 2, pp. 242-246, 2008.

[11] Q. Xu, D. Fattal, and R. G. Beausoleil, "Silicon microring resonators with 1.5-μm radius," *Optics Express,* vol. 16, pp. 4309-4315, 2008.

[12] Q. Xu, B. Schmidt, J. Shakya, and M. Lipson, "Cascaded silicon micro-ring modulators for WDM optical interconnection," *Optics Express,* vol. 14, pp. 9431-9435, 2006.

[13] A. W. Poon, X. Luo, F. Xu, and H. Chen, "Cascaded microresonator-based matrix switch for silicon on-chip optical interconnection," *Proceedings of the IEEE,* vol. 97, pp. 1216-1238, 2009.

[14] W. S. Fegadolli, V. R. Almeida, and J. E. B. Oliveira, "Reconfigurable silicon thermo-optical device based on spectral tuning of ring resonators," *Optics Express,* vol. 19, pp. 12727-12739, 2011.

[15] W. S. Fegadolli, L. Feng, M. M.-U. Rahman, J. E. Oliveira, V. R. Almeida, and A. Scherer, "Experimental demonstration of a reconfigurable silicon thermo-optical device based on spectral tuning of ring resonators for optical signal processing," *Optics Express,* vol. 22, pp. 3425-3431, 2014.

[16] Y. A. Vlasov, M. O'Boyle, H. F. Hamann, and S. J. McNab, "Active control of slow light on a chip with photonic crystal waveguides," *Nature,* vol. 438, pp. 65-69, 2005.

[17] M. Tinker and J. Lee, "Thermal and optical simulation of a photonic crystal light modulator based on the thermo-optic shift of the cut-off frequency," *Optics Express,* vol. 13, pp. 7174-7188, 2005.

[18] E. A. Camargo, H. M. Chong, and R. M. De La Rue, "Highly compact asymmetric Mach-Zehnder device based on channel guides in a two-dimensional photonic crystal," *Applied optics,* vol. 45, pp. 6507-6510, 2006.

[19] N. Yamamoto, T. Ogawa, and K. Komori, "Photonic crystal directional coupler switch with small switching length and wide bandwidth," *Optics Express,* vol. 14, pp. 1223-1229, 2006.

[20] D. M. Beggs, T. P. White, L. Cairns, L. O'Faolain, and T. F. Kraus, "Ultrashort photonic crystal optical switch actuated by a microheater," *Photonics Technology Letters, IEEE,* vol. 21, pp. 24-26, 2009.

[21] S. Leonard, H. Van Driel, J. Schilling, and R. Wehrspohn, "Ultrafast band-edge tuning of a two-dimensional silicon photonic crystal via free-carrier injection," *Physical Review B,* vol. 66, p. 161102, 2002.

[22] X. Wang, S. Chakravarty, B. S. Lee, C. Lin, and R. T. Chen, "Ultraefficient control of light transmission through photonic potential barrier modulation," *Optics letters,* vol. 34, pp. 3202-3204, 2009.

[23] B. Maes, P. Bienstman, and R. Baets, "Switching in coupled nonlinear photonic-crystal resonators," *JOSA B,* vol. 22, pp. 1778-1784, 2005.
[24] X. Yang, M. Yu, D.-L. Kwong, and C. W. Wong, "All-optical analog to electromagnetically induced transparency in multiple coupled photonic crystal cavities," *Physical review letters,* vol. 102, p. 173902, 2009.
[25] H. Ishio, J. Minowa, and K. Nosu, "Review and status of wavelength-division-multiplexing technology and its application," *Journal of Lightwave Technology,* vol. 2, pp. 448-463, 1984.
[26] L. Gu, W. Jiang, X. Chen, and R. T. Chen, "Thermooptically tuned photonic crystal waveguide silicon-on-insulator Mach–Zehnder interferometers," *Photonics Technology Letters, IEEE,* vol. 19, pp. 342-344, 2007.
[27] A. Liu, L. Liao, D. Rubin, H. Nguyen, B. Ciftcioglu, Y. Chetrit, N. Izhaky, and M. Paniccia, "High-speed optical modulation based on carrier depletion in a silicon waveguide," *Optics Express,* vol. 15, pp. 660-668, 2007.
[28] W. M. Green, M. J. Rooks, L. Sekaric, and Y. A. Vlasov, "Ultra-compact, low RF power, 10 Gb/s silicon Mach-Zehnder modulator," *Optics Express,* vol. 15, pp. 17106-17113, 2007.
[29] M. C. Souza, L. A. Barea, G. Wiederhecker, A. A. von Zuben, and N. C. Frateschi, "Tunable Spectral Engineering of Coupled Silicon Microcavities," in *CLEO: QELS_Fundamental Science*, 2015, p. JTu5A. 49.
[30] D. O'Brien, M. Settle, T. Karle, A. Michaeli, M. Salib, and T. Krauss, "Coupled photonic crystal heterostructure nanocavities," *Optics Express,* vol. 15, pp. 1228-1233, 2007.
[31] J. Wu, P. Cao, T. Pan, Y. Yang, C. Qiu, C. Tremblay, and Y. Su, "Compact on-chip 1× 2 wavelength selective switch based on silicon microring resonator with nested pairs of subrings," *Photonics Research,* vol. 3, pp. 9-14, 2015.
[32] Y. Yi, P. Bermel, K. Wada, X. Duan, J. Joannopoulos, and L. Kimerling, "Tunable multichannel optical filter based on silicon photonic band gap materials actuation," *Applied Physics Letters,* vol. 81, pp. 4112-4114, 2002.
[33] W. S. Fegadolli, N. Pavarelli, P. O'Brien, S. Njoroge, V. R. Almeida, and A. Scherer, "Thermally controllable silicon photonic crystal nanobeam cavity without surface cladding for sensing applications," *ACS Photonics,* vol. 2, pp. 470-474, 2015.

Chapter 9: Suggested future work

9.1 IN-DEVICE PYROELECTRIC POLING OF EO POLYMER

9.1.1 Introduction of pyroelectric poling

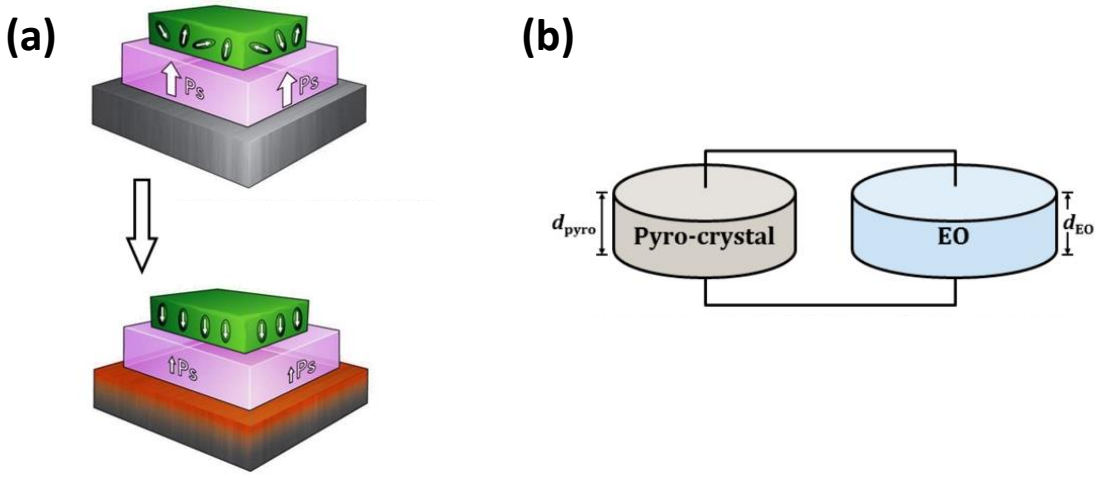

Figure 9.1: Schematic of pyroelectric poling of EO polymer. (a) The pyroelectric crystal is in contact with the EO polymer film to be poled. (b) The pyroelectric crystal is connected with the EO polymer film by external electrical wires.

In this section, we report our recent progress and proposed future work on an advanced in-device EO polymer poling approach called pyroelectric poling [1]. Pyroelectric crystals, such as lithium niobate (LN), lithium tantalite (LT), and lead zirconate titanate (PZT) crystals, can develop surface charges and generate high electric

fields on insulators through modest change of temperatures. Under the equilibrium condition, the spontaneous polarization of pyroelectric crystals is completely balanced by the surface screening charges. Heating or cooling of these crystals develop equal but opposite charges on both polar surfaces due to the change of polarization as a function of temperature, as shown in Fig. 9.1. Due to very high resistivity (10^{15} ohm·m) of pyroelectric crystals, the leakage current could be very small. The electric field directly generated by these pyroelectric crystals is expected to be higher than that in conventional contact poling.

The EO polymer used for this pyroelectric poling research is SEO300 which is provided by Soluxra, LLC. It has a refractive index, n=1.63 at 1550nm, and an exceptional combination of large EO coefficient (r_{33} of ~80pm/V at 1330nm, and ~70pm/V at 1550nm), low optical loss, synthetic scalability, as well as excellent photochemical stability. Its relatively high glass transition temperature of 150℃ provides good temporal stability, and the EO coefficients of poled SEO125 are essentially unchanged under ambient conditions. Some detailed studies of EO polymer thermal stability indicate that operation up to 150℃ results in a change of EO coefficients < 10% [2, 3]. The SEO300 chromophores and the host matrix polymer (Amorphous Polycarbonate, APC) are weighed in a proper ratio (1:3), and then mixed in solvent (Dibromomethane) with a concentration of 5.6wt% in a clean vial. Next, this formulated solution is placed on an automatic roller overnight to form a very viscous and dark solution. The homogeneous solution is then filtered into a new clean vial through a 0.2μm

poly(tetrafluoroethylene) (PTFE) filter before spincoating. Next, the EO polymer is spincoated into thin films or onto a fabricated silicon photonic devices such as slot photonic crystal waveguides (PCWs), slot ring resonators, etc., and infiltrate into the slot and hole patterns. The total thickness of the EO polymer cladding is around 2μm by using the spin speed of 2000rpm for 40 sec. After spin coating, the EO polymer devices are cured in a vacuum oven at 80℃ overnight.

The achieved in-device r_{33} value depends on the strength of poling electric field applied across the EO polymer. There are several ways to generate this poling electric field, such as contact poling, corona poling and pyroelectric poling. The contact poling and corona poling rely on external voltage sources to provide maximum electric field strengths of 1-2MV/cm and 2-5MV/cm, respectively, and higher electric field will lead to dielectric breakdown due to the infinite number of charges that the external voltage sources keep providing. Differently, in pyroelectric poling, the source of poling electric field does not reply on any external voltage source but originates from the generation of uncompensated charges through the pyroelectric effect in a pyro crystal. As a result, the poling electric field can be as large as 50-350MV/cm (by electrostatics analysis), and the probability of breakdown is low due to the finite number of charges provided by pyro crystals [1].

In our pyroelectric poling test, we use PZT pyro crystal. The pyro crystal plays an important role in the pyroelectric poling process. We need to consider some important parameters which determine the pyroelectric poling efficiency. Some parameters related

to pyro crystal material itself include pyroelectric coefficient, Curie temperature, resistivity, dielectric constant, thermal conductivity, heat capacity, and surface area. Some parameters relevant to the EO polymer material include the cross-sectional area, dielectric constant, and resistivity. Some parameters related external environmental conditions include change of temperature, ramping rate of temperature change, poling temperature.

During this pyroelectric poling process, the leakage current is monitored. The smaller leakage current indicates higher poling field across the EO polymer, that is, higher poling efficiency. For reference, the typical leakage current density can be 1-10A/m^2 based on the measured results both in a thin film configuration and in-device poled EO polymer [4]. In pyroelectric poling process, the leakage current is expected to be low, and the achieved r_{33} efficiency is supposed to be high. Just for reference, based on the thin-film pyroelectric poling results from Prof. Alex Jen's group at the University of Washington group, 40% r_{33} efficiency achieved under contact poling using the highest current of 40nA achieved in pyroelectric poling, and the peak leakage current density in contact poling (400nA) is 10 times higher than that in pyroelectric poling (40nA). The motivation of this work is to demonstrate the in-device pyroelectric poling on slot PCW structures.

9.1.2 Pyroelectric poling test pattern

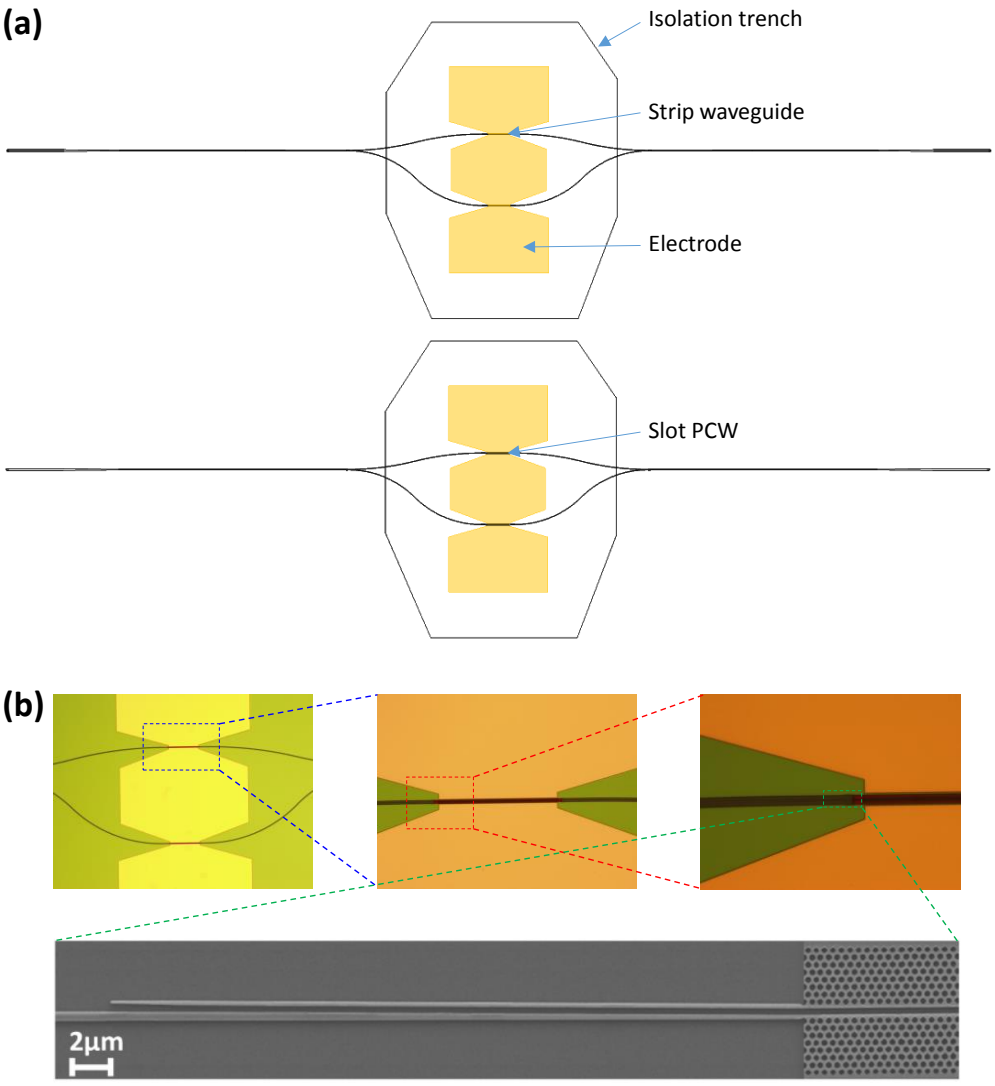

Figure 9.2: (a) The layout of the two asymmetric MZIs for testing. Upper: no PCWs on both arms. Lower: PCWs on both arms. (b) Fabricated device.

The testing devices used in this work are asymmetric Mach–Zehnder interferometer (MZI). The layout of the devices is shown in Fig. 9.2 (a). The first MZI device does not have slot photonic crystal waveguide (PCW), and the second MZI has

200μm-long slot filled with EO polymer on both arms. The slot width is 320nm. The fabrication process of the testing devices starts with an SOI wafer. The silicon slot PCW MZI is fabricated by electron beam lithography and then reactive ion etching in a single pattering/etching step. And then gold electrodes are patterned by using electron beam lithography aligner, followed by electron beam evaporation and a lift-off process. The EO polymer is filled into the slot PCW by spin coating. The silicon PCW regions including holes and the slot are fully covered by the EO polymer. The optical microscope images and an SEM image of a fabricated device are shown in Fig. 9.2 (b).

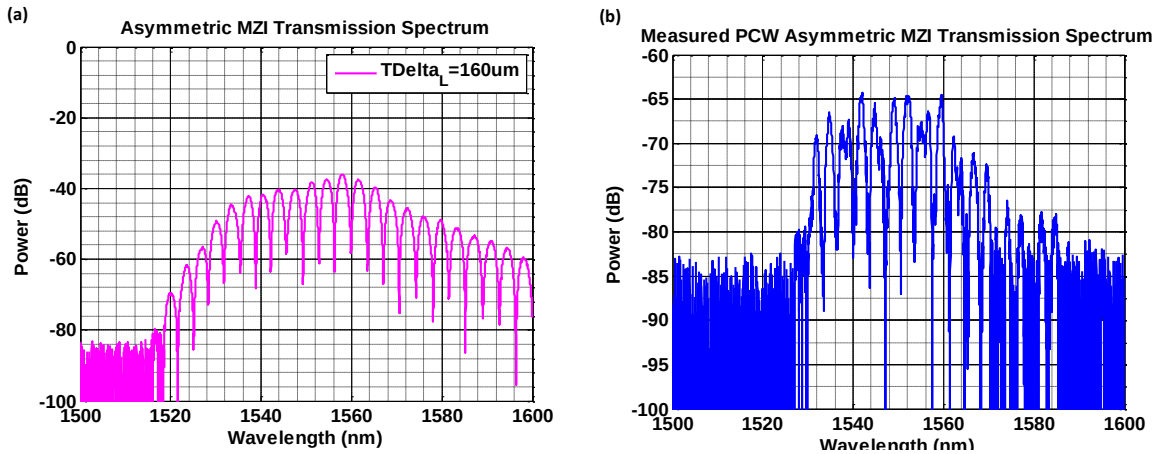

Figure 9.3: (a) Measured transmission spectrum of strip waveguide asymmetric MZI. (b) Measured transmission spectrum of asymmetric MZI with PCWs on both arms.

Optical passive tests are then performed to characterize the fabricated asymmetric MZIs with and without PCWs, and the measured transmission spectra of the devices are

shown in Fig. 9.3. The method for measuring the in-device r_{33} is proposed as below. The in-device electro-optic coefficient (r_{33}) after poling is determined by measuring the optical transmission as a function of wavelength with one arm of the asymmetric MZI biased at several DC voltages, using an external DC signal source. For PCW MZI, the optical wavelength is tuned to the 8nm-wide low-dispersion slow-light wavelength range of the slot PCW, so that the change of refractive index of EO polymer is very weakly dependent on the wavelength in this wavelength range. The voltage-induced wavelength shift ($\Delta\lambda$) in the MZI output spectrum can be used to extract the voltage-induced phase shift ($\Delta\varphi$) using the relationship $\Delta\varphi = 2\pi\Delta\lambda/FSR$, where FSR is the free spectral range of the asymmetric MZI. Then, considering the slow-light enhancement, the in-device r_{33} can be obtained by using the relationship $L = \frac{\lambda}{2\sigma n_g}(\frac{n}{\Delta n})$ and $\Delta n = \sigma n^3 r_{33} V/(2d)$, where L is the interaction length, σ is the confinement factor, n_g is the group index, n is the EO polymer index, V is the applied DC voltage, d is the electrode separation (slot width for slot PCW structure). Under different DC voltage, the transmissions spectra of the MZIs will shift accordingly, which can give us the information about the modulation-induced phase shift.

9.1.3 In-device pyroelectric poling setup

A schematic setup for the detached pyroelectric poling is proposed as shown in Fig. 9.4 (a). One hot plate is used to heat up the device to the T_g of the EO polymer, and another hot plate precisely controlled by a microprocessor is used to heat up the pyro

crystal from room temperature by 60°C under a fixed ramping rate. The top and bottom surface of the pyro crystal is connected by electrically conductive wires to the electrode pads across one arm (or two arms) of the MZI device. A picoammeter (Keithley 6485) is used to measure the leakage current, and a voltage meter (Keithley 237) is used to in-situ monitor the induced voltage drop across the 320nm-wide slot in the device. Some pictures of real pyroelectric poling setup are shown in Fig. 9.4 (b).

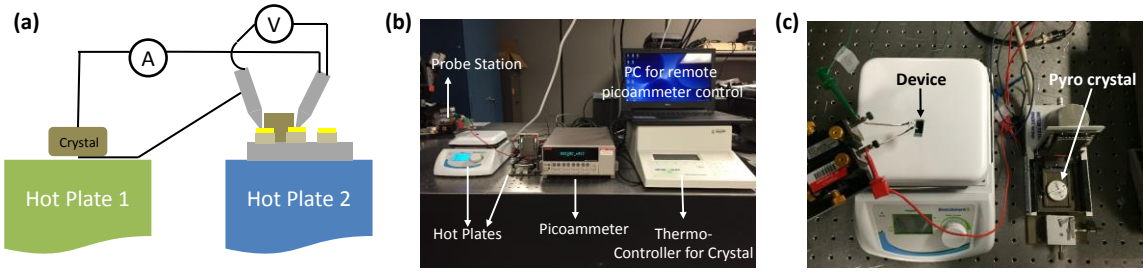

Figure 9.4: (a) A schematic of pyroelectric poling setup. (b) A picture of real pyroelectric poling setup. (c) Two hot plates heating up EO polymer device and pyro crystal.

In order to accurately measure the voltage drop and leakage current across the EO polymer, several specification requirements of the voltage meter must be met. The poling setup can simply be treated as two capacitor charging and discharging problem. If we add a voltage meter and a picoammeter into the circuit, the equivalent circuit is shown in Fig. 9.5 (a). The resistance of the EO polymer is usually larger than $10^{11}\,\Omega$, we need a voltage meter whose resistance is even higher than this value. Conventional multi-meter functioned as voltage meter has resistance $10^{7}\,\Omega$. Using conventional multi-meter will not

measure the correct value of the EO polymer; instead, it will act as a leakage current pathway. Therefore, an ultra-high impedance voltage meter, Keithley 237, whose resistance is over 10^{14} Ω, is used to correctly measure in-situ voltage (electric field) generated by the pyro crystal. The resistance and capacitances of EO polymer, voltage meter and picoammeter are shown in Fig. 9.5 (b).

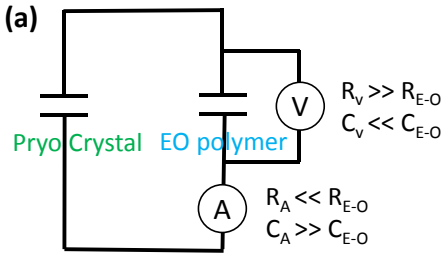

(b)

	EO polymer*	Voltage meter (Keithley 237)	Picoammeter (Keithley 6485)
Resistance	10^{11} Ω	**$>10^{14}$ Ω**	≈ 0
Capacitance	0.4 nF	20 pF	10 nF – 1 μF

Figure 9.5: (a) Equivalent circuit connection. (b) The parameters of components in the equivalent circuit.

In this two-hotplate setup, operative temperature range of the lead zirconium titanate (PZT) crystal is only limited to the curie temperature of itself. The PZT crystal is 3cm in diameter, and its thickness is 1mm. The temperature changing sequence is arranged as followed: (1) Heat up the sample to EO polymer glass transition temperature (150℃) and hold at this temperature. (2) Heat up the PZT crystal from 30 to 90℃, with a constant ramp rate (e.g.20℃/min). (3) Hold for 1 min. (4) Cool down the EO polymer to room temperature. (5) Cool the PZT crystal to room temperature and disconnect the PZT

crystal and sample. Figure 9.6 illustrates the controlled temperature for both EO polymer and pyro crystal in this process.

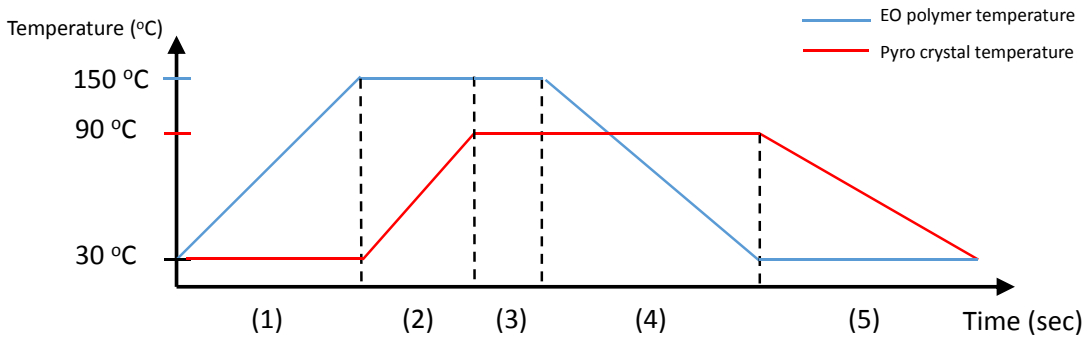

Figure 9.6: Temperature change on two hot plates in the whole pyroelectric poling process.

9.1.4 Preliminary electrical test of in-device pyroelectric poling

First, one arm of the EO polymer refilled slot PCW MZI is poled under different pyroelectric poling conditions. The change of temperature on the pyro crystal PZT and the ramping rate of temperature are varied, and the corresponding peak leakage current and maximum induced voltage across the slot in the pyroelectric poling process are recorded in Table 9.1. The peak leakage current density and maximum electric field are calculated based on the measured data. As a comparison reference, the measured peak leakage current and applied voltage in a contact poling on the same device are also listed in the table. Figure 9.7 (a) shows the maximum electric field as a function of temperature

variation (ΔT) for both pyroelectric poling and contact poling, and Fig. 9.7 (b) shows the maximum electric field as a function of ramping rate also for both poling approaches. It can be seen that increasing the ΔT and ramping rate can lead to higher electric field induced across the slot. The maximum ramping rate here is limited by processor-controlled hot plate, and this can be improved by using a better equipment in the future. The maximum ΔT is limited by the Curie temperature of the pyro crystal. The maximum induced electric field can be 141.25V/μm is achieved in Test No. 3 when ΔT=100°C and ramping rate=20°C/min. Figure 9.7 (c) shows the measured leakage current and induced voltage as a function of time in the Test No. 3. As a comparison, the leakage current and induced voltage measured in a contact poling process (Test No. 6) are shown in Fig. 9.7 (d). It can be seen that pyroelectric poling can generate higher electric field and lower leakage current than conventional contact poling.

Table 9.1 Measured leakage current, current density, voltage and electric field under different temperature variations and ramping rates

Test No.	Setup	ΔT for Crystal	Ramp rate	Peak leakage Current	Peak leakage Current density	Max. Voltage	Corresponding Electrical Field
1	Pryo	60 °C	20 °C/min	114.3 nA	0.152 A/cm^2	36.7 V	114.69 V/μm
2	Pryo	80 °C	20 °C/min	119.9nA	0.160 A/cm^2	39.2 V	122.5 V/μm
3	**Pryo**	**100°C**	**20 °C/min**	**129.8 nA**	**0.173 A/cm^2**	**45.2 V**	**141.25 V/μm**
4	Pryo	60°C	10 °C/min	59.0nA	0.078 A/cm^2	24.0 V	75 V/μm
5	Pryo	60°C	15 °C/min	84.4 nA	0.112 A/cm^2	29.8 V	93.13 V/μm
6	**Contact**	**-**	**-**	**363.9 nA**	**0.484 A/cm^2**	**32V**	**100 V/μm**

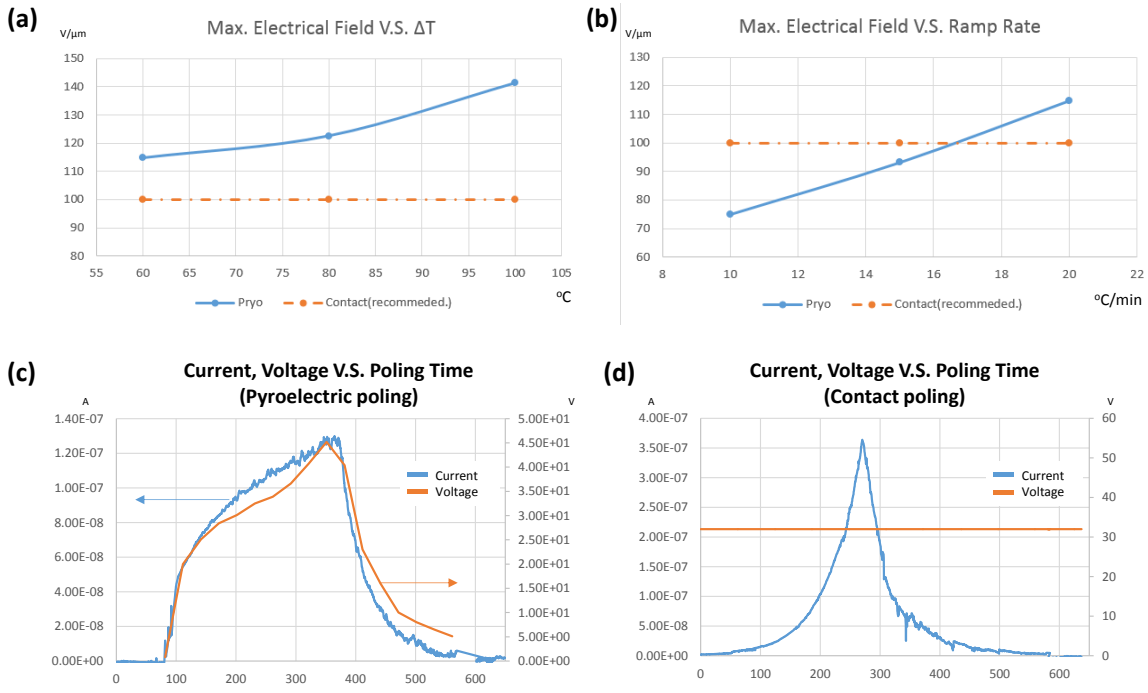

Figure 9.7: (a) Measured electric field and leakage current as a function of temperature variation for both pyroelectric poling and contact poling. (b) Measured electric field and leakage current as a function of ramping rate for both poling approaches. (c) Measured time-dependent leakage current and induced voltage in the pyroelectric poling process. (d) Measured time-dependent leakage current and induced voltage in the contact poling process.

More pyroelectric poling is to be performed to provide a systematic analysis. We are still working on the complete study of leakage current and induced voltage under different pyroelectric poling condition, such as using different pyro crystals, using different EO polymers, and using different slot widths.

9.1.5 Preliminary optical test of devices poled by pyroelectric poling

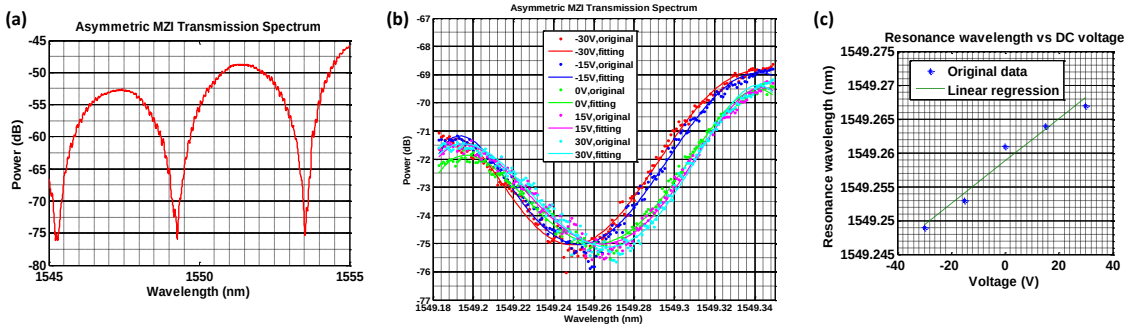

Figure 9.8: (a) Measured transmission spectrum of asymmetric MZI with arm length difference of 140nm. The measured FSR is about 3.97nm. (b) The spectrum shift under different DC voltages. The solid curve is the polynomial fitting of measured data points. (c) Extracted data of measured resonance wavelength as a function of applied DC voltage.

Next, an asymmetric MZI with arm length difference of 140nm is used for optical test, and then the in-device r_{33} of EO polymer after in-device pyroelectric poling will be estimated. Note that no silicon slot PCWs are used in this test structure, and the EO polymer serves as claddings of silicon strip waveguides. Based on the simulations, the percentage of power in the EO polymer cladding is 16%. The separation of the electrodes aside the waveguide are 6μm. The EO polymer is poled on both arms. The transmission spectrum is shown in Fig. 9.8 (a), and the free spectrum range (FSR) is measured to be about 4nm. Then DC voltages of -30V, -15V, 0V, 15V, and 30V are applied across both arms of the asymmetric MZI in the same direction as the EO polymer poling direction (no push-pull configuration), and the corresponding transmission spectra are recorded. From the overlay of transmission spectra in Fig. 9.8 (b), the local minimum power of transmission (resonance) of the asymmetric MZI is shifted to longer wavelength with the

increase of voltage. The extracted resonance as a function of applied voltage is shown in Fig. 9.8 (c), and a linear regression is performed based on the data points. The slope of the linear curve can be used for the estimation of in-device poling efficiency. Based on the estimation methods in Section 9.1.2, as well as the simulated percentage of power in the EO polymer cladding (16%), the in-device r_{33} is measured to be approximately 15.4pm/V at around 1550nm. Considering the thin-film r_{33} of EO polymer of ~70pm/V at 1550nm, the in-device poling efficiency can be estimated to be 22%. The device structure and measurements can be further optimized in our future work, so that higher poling efficiency can be achieved.

In the future, more work will be done on EO polymer filled slot PCW asymmetric MZI to estimate the in-device poling efficiency and will be compared with contact poling efficiency on the same device, in order to demonstrate that higher in-device r_{33} could be archived using pyroelectric poling than contact poling.

9.2 MILLIMETER- OR TERAHERTZ-WAVE SENSOR BASED ON ELECTRO-OPTIC POLYMER FILLED PLASMONIC SLOT WAVEGUIDE

9.2.1 Proposal of device schematic

In Chapter 5, we have designed, fabricated and experimentally demonstrated a compact, broadband and highly sensitive integrated photonic electromagnetic field sensor to cover the X band of the electromagnetic spectrum (8-12GHz). The key parts of our photonic electromagnetic field sensor are shown schematically in Figs. 9.9 (a) and (b), including an EO polymer refilled silicon slot PCW phase modulator and a gold bowtie

antenna [5]. The frequency was targeted around 10GHz which is the central frequency of X band. In our next stage of research, we are trying to develop an advanced version of this sensor to cover wide electromagnetic spectrum up to 10THz, including the range of microwave, millimeter wave and even terahertz wave.

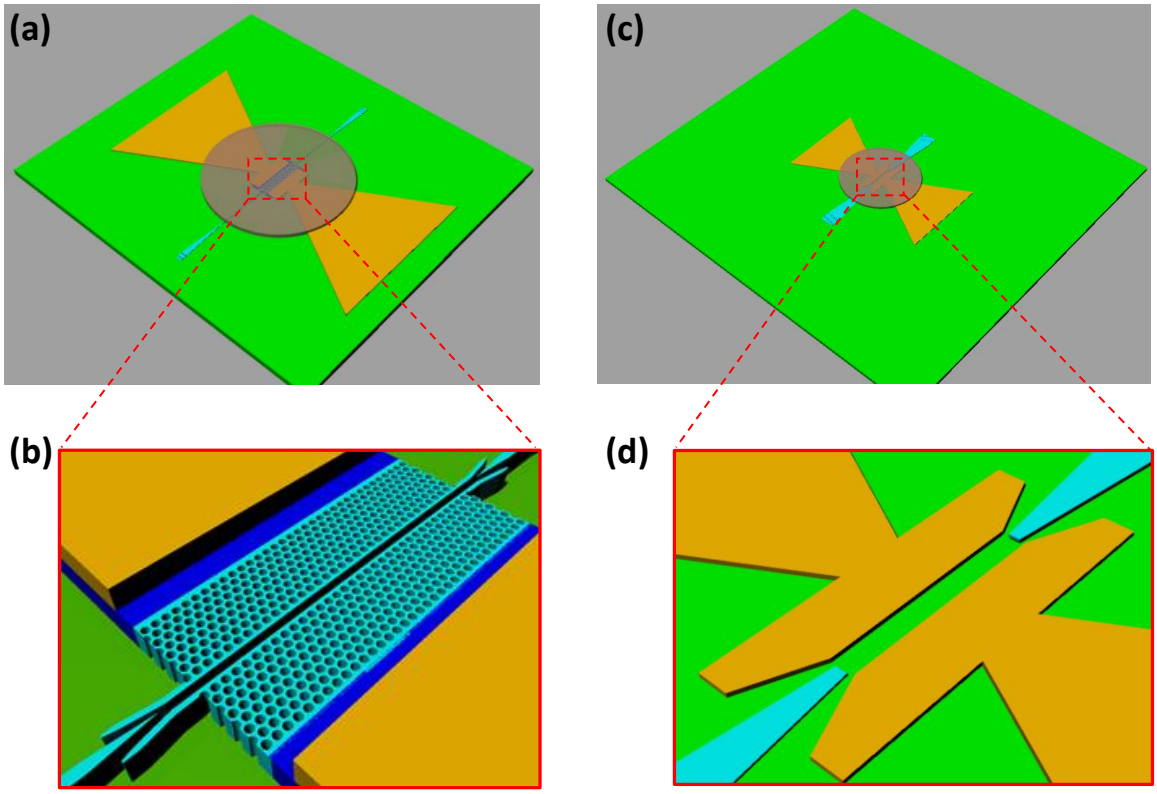

Figure 9.9: (a) A schematic view of theelectromagnetic field sensor consisting of an EO polymer refilled silicon slot PCW phase modulator and a bowtie antenna. (b) Magnified image of slot PCW. (c) A schematic view of the electromagnetic field sensor consisting of an EO polymer refilled plasmonic slot waveguide phase modulator and a bowtie antenna. (d) Magnified image of plasmonic slot waveguide. Note: the EO polymer layer covered on top of the device is not shown in (b) and (d) for better visualization.

To make our sensor to cover a large range up to THz frequency regime, the device is modified, as shown in Figs. 9.9 (c) and (d). First, the arm length of the bowtie antenna is scaled to provide a broad bandwidth with central resonance frequency in Terahertz range. Second, the silicon slot PCW is removed and the gap between the two extended bars are narrowed down to 250nm to form a plasmonic slot waveguide. The light is coupled from an input optical fiber into a silicon strip waveguide via a grating coupler, and then coupled into a plasmonic slot waveguide through a strip-to-plasmonic mode converter [6], as shown in Fig. 9.9 (d). Optical modulations can be achieved in this plasmonic slot waveguide as demonstrated recently in Ref. [7]. Third, we need to note that the EO polymer filled inside the metal slot has an ultrafast response time in the sale of femtosecond, corresponding to an upper frequency limit in THz range. Therefore, the response time of the EO polymer material does not limit the frequency bandwidth of this device.

The working principle is as follows. A continuous wave (CW) laser input is coupled into and out of the device. The bowtie antenna harvests incident electromagnetic waves, transforms it into high-power-density time-varying electric field within the feed gap, which directly interacts with the light propagating along the EO polymer refilled plasmonic slot waveguide. The refractive index of the EO polymer is controlled by the applied electric field via the EO effect, which modulates the phase of the surface plasmonic waves. Finally, by measuring the modulated optical signal, an incident

microwaves, millimeter waves or terahertz waves from free space can be detected through optical means.

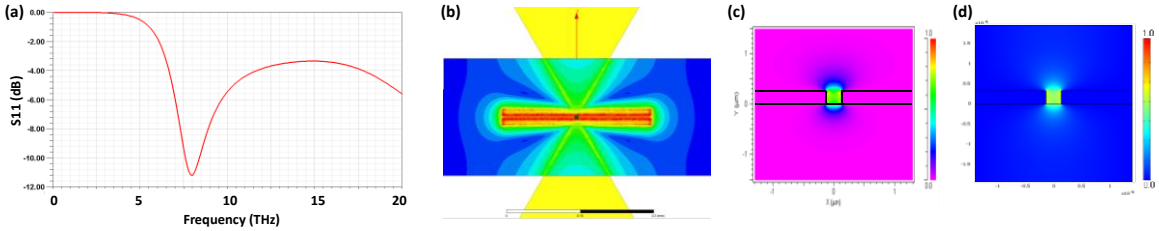

Figure 9.10: (a) Simulated S11 parameter over a frequency range 1-20THz. (b) Simulated normalized electric field distribution on bowtie antenna at 8THz. (c) Simulated plasmonic slot waveguide mode profile. (d) Simulated RF electric field profile on the plasmonic slot waveguide.

Figure 9.10 (a) shows the simulated S11 parameter of the bowtie antenna, with a resonance frequency around 8THz, and Fig. 9.10 (b) shows the simulated normalized electric field distribution on bowtie antenna at the resonance frequency (8THz) with a strong near-field enhancement inside the feed gap. Figure 9.10 (c) shows the simulated mode profile of the plasmonic slot waveguide, from which it can be seen that most of optical power is confined inside the slot. The modulation electric field is also concentrated in the slot, as shown by the simulation results in Fig. 9.10 (d), leading to a very large overlap between optical mode and modulation field and thus a very high modulation efficiency.

9.2.2 Discussion

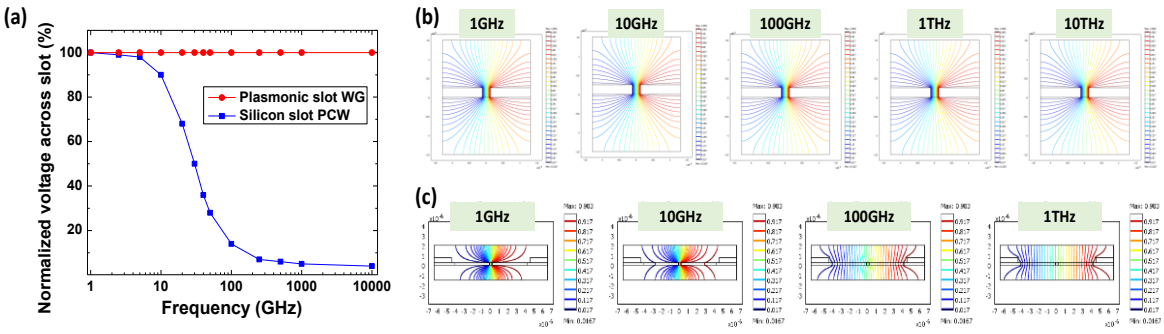

Figure 9.11: (a) Simulated normalized voltage drop across the silicon slot PCW and the plasmonic slot waveguide. (b) Simulated electric potential distribution on the plasmonic slot waveguide, at 1GHz, 10GHz, 100GHz, and 1THz, respectively. (c) Simulated electric potential distribution on the silicon slot PCW, at 1GHz, 10GHz, 100GHz, respectively.

There are several important benefits of this plasmonic-based Millimeter-/Terahertz-wave sensor. (1) Due to the removal of silicon PCW and the high conductivity of metals, the RC time delay is significantly reduced, enabling a very broad frequency bandwidth. The resonance of the bowtie antenna can be engineered to cover a frequency range from 1GHz to 10THz. Based on simulation results as shown in Fig. 9.11 (a), the normalized electric field dropped across the metal slot is almost constant from the frequency of 1GHz to 10THz. As a comparison, for silicon PCW slot, the normalized electric field across the decreases as the frequency increases due to the finite conductivity of the silicon. Its 3-dB bandwidth is about 30GHz, which limits the detectable frequency band of the sensor. Figures 9.11 (b) and (c) show the electric field potential distribution on the plasmonic slot waveguide and the silicon slot PCW at frequencies up to 10THz. It

can be seen that the most of the modulation field is still efficiently dropped across the plasmonic slot where EO polymer is filled.

(2) The electric field enhancement factor is increased when the bowtie feed gap is reduced, so the 250nm-wide metal slot can provide higher local electric field enhancement which improve the sensitivity of this sensor. A 2X improvement in sensitivity is expected compared to 320nm-wide silicon slot PCW. Since the 250nm-wide metal gap is not optimized yet, the sensitivity can be further improved by reducing the metal slot width.

(3) The large overlap between the modulation electric field and the surface plasmonic mode enables more efficient modulation, which can reduce the required interaction length. The interaction length can be further reduced by using new EO polymers with larger r_{33} values. Although plasmonic waveguides have higher propagation loss per unit length compared to regular waveguides, the short device length is helpful in reducing the total propagation loss. In Ref. [7], an interaction length of only 29μm and a total insertion loss of 12dB are demonstrated. Based on the simulated complex effective index achieved in Fig. 9.10 (c), the propagation loss of our un-optimized plasmonic slot waveguide is 0.320dB/μm. we expect the total insertion loss of our device can be controlled below 10dB, with the optimization of the plasmonic slot waveguide, the selection of metal with lower propagation loss (i.e. copper to replace gold), as well as improved fabrication quality provided by CMOS foundry.

(4) By properly designing the plasmonic slot waveguide and engineering its dispersion diagram, a large group index can be achieved in the surface plasmonic mode and this slow-light effect can be used to enhance the modulation efficiency and the detection sensitivity.

(5) Some existing electronic-based THz detector requires low temperature to reduce electron noise, so it required a cooling process such as liquid Nitrogen flow; on the contrary, our photonic (plasmonic) detection approach has good noise immunity. Our device can also reduce the impact of perturbing fields, since it is based on an optical modulation technique.

To the best of our knowledge, this will be the first electromagnetic wave sensor based on electro-plasmonic modulation. The working bandwidth of this sensor can be tuned by modifying the bowtie antenna geometry, in order to enable potential applications in other frequency ranges such as microwave detection, millimeter wave imaging, and even light trapping for photovoltaics.

9.3 LOW-LOSS SILICON-POLYMER HYBRID PHOTONIC CRYSTAL WAVEGUIDE FABRICATED BY CMOS FOUNDRY

In our next stage of research, we plan to improve the optical loss and fabrication yield by using a mature commercial CMOS foundry to fabricate our PCW devices [8]. Our design patterns are sent to IMEC for fabrication. Figure 9.12 shows the SEM image of the fabricated slotted silicon photonic crystal waveguide with a mode converter and a group index taper. EO polymer is then spincoated onto the device to cover the slot and

PCW holes. More work will be done to investigate the fabrication tolerance and yield. 2D PC structures with similar geometries have been characterized with improved optical loss. To the best of our knowledge, this will be the first demonstration of a silicon-polymer hybrid slotted PCW device.

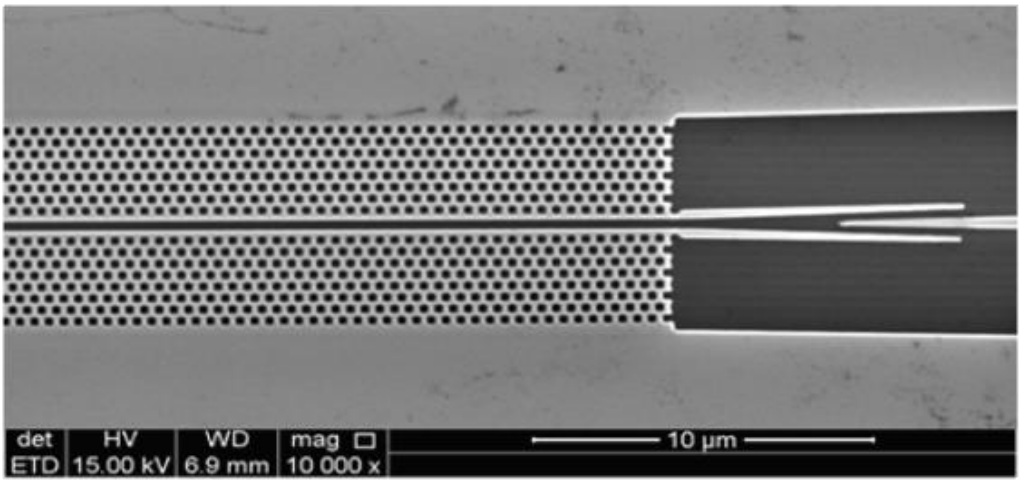

Figure 9.12: An SEM image of a silicon slotted photonic crystal waveguide fabricated by external CMOS foundry.

The fiber-to-fiber total insertion loss of the device has several contributions listed in the Table 9.2. For overall reduction of the device insertion loss, the efforts will be done on these components, as shown in Table 9.2. The total insertion loss is finally expected to be controlled below 9dB, if grating couplers are used for fiber-to-chip coupling. If inverse tapers are used to replace grating couplers, the total insertion loss is expected to be below 6dB.

Table 9.2 Expected final total insertion loss (fiber-to-fiber)

	Target Loss	**Comments**
Propagation Loss in PCWs	<1.5dB	An external CMOS foundry will be used to improve the quality of fabricated PCWs. New EO polymer with larger r_{33} will be used to shorten the PCW length. New pyroelectric poling technique [1] will be used to improve the in-device r_{33} and also reduce leakage current induced optical loss. The band engineered PCW design will be optimized for lower loss. And post-fabrication roughness reduction will be carried out.
Propagation Loss in ridge waveguides	<0.5dB	We will use multimode waveguides [9] and shorten the length of the input/output silicon ridge waveguides.
PCW group index tapers	<0.5dB	Extending our past work [10-12], we will engineer a short and efficient PCW group index taper.
Mode converters	~0.08dB	We have recently demonstrated a low-loss adiabatic mode converter for 320nm-wide slot PCW [13].
MMI couplers	~0.4dB	We have previously demonstrated an efficient MMI couplers [11].
Option (a): Grating couplers	~2.3dB	We have previously demonstrated a low loss subwavelength grating couplers [14]. In addition, the grating coupler will be optimized for coupling through angle-polished fibers [15].
Option (b): Inverse tapers	<1dB	An efficient inverse taper has been demonstrated by NTT with loss of 0.8dB [16].
Total insertion loss Option (a)	<9dB	
Total insertion loss Option (B)	<6dB	

To improve the quality of fabricated PCWs and reduce optical loss, an external CMOS foundry will be used. New EO polymer with larger r_{33} will be used to shorten the

required PCW length. New pyroelectric poling technique [1] will be used to improve the in-device r_{33} (to reduce required PCW length) and also reduce leakage current induced optical loss. A low-loss PCW will be designed and the band engineering can be further optimized for loss reduction. And post-fabrication roughness reduction will be carried out.

In our previous designs, the input/output (I/O) grating couplers are 9mm apart. Since the active portion of the on-chip waveguide length is only 300μm the grating couplers can be easily placed less than 2mm apart taking advantage of the surface normal coupling scheme provided by the grating couplers. Shortening of the waveguiding structure and the use of low loss multimode waveguides [9] outside of the active region are expected to lower the loss in the passive waveguides to less than 0.5dB. Propagation loss as low as 0.026dB/cm in 3μm wide multimode silicon waveguides has been recently reported [9].

A group index tapers is required for coupling into the high group index (n_g) PCW [10-12], since it can provide a transition of group index over the wavelength range of interest. This transition can be engineered to improve the performance of the group index taper. In addition, We have recently demonstrated a low-loss adiabatic mode converter for 320nm-wide slot PCW [13], and the loss of 0.08dB per mode converter is measured. What is more, our group have previously demonstrated an efficient MMI couplers [11] to split/combine optical beams in MZIs.

To coupling light between I/O optical fibers and our device, our group have previously demonstrated an efficient subwavelength grating couplers [14]. In addition, the grating coupler will be optimized for coupling through angle-polished fibers [15]. Another option for fiber-to-chip coupling is using inverse tapers. Inversed tapers with overlaid polymer waveguide has been demonstrated by NTT with optical loss of 0.8dB [16].

9.4 OPTIMIZATION OF PHOTONIC CRYSTAL WAVEGUIDE BY INVESTIGATION OF SLOT WIDTH

To the best of our knowledge, all of the slot waveguides and slot PCWs demonstrated by other research groups have slot widths less than 220nm [17-19]. As demonstrated in Chapters 1-5, wide slots (320nm) are very effective in reducing the leakage current during the poling process and achieving high poling efficiencies. However, the 320nm wide slots, presented first by Omega Optics, Inc. [20], have not been yet optimized. Despite higher poling efficiency, wider slots result in less confinement (σ=33%) of the photons in the slot region. Unfortunately, the understanding of nature of the current injection through the interface between silicon and EO polymer in silicon slot waveguides is still limited. A series of design and experiments are necessary to quantify the effects of the slot width on the leakage current and propagation loss. These findings will be helpful for us to model leakage current and modify the EO polymer to reduce the leakage current. This will also make possible maximizing the poling efficiency and field confinement in the slot, which ultimately leads to higher

performance in terms of higher $V_\pi \times L$ for modulation applications and higher sensitivity for electric field sensing applications. The optical propagation loss per unit length may also be improved.

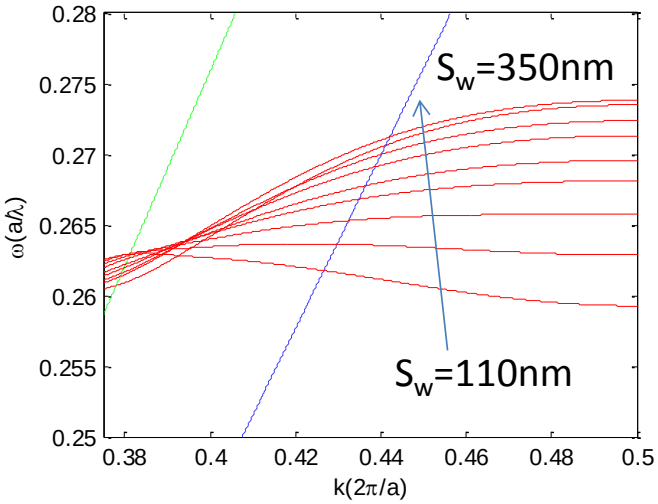

Figure 9.13: Band Structure (Normalized Frequency Vs. Normalized Propagation Constant, the Fundamental Guided Defect Mode) for Varying Slot Width (S_w). No Band Engineering is done. The Distance Between the Two Innermost Rows is Increases with the Slot Width.

There is also a need to understand the behavior of the fundamental defect mode at wide slow width, where the band gap is located at shorter wavelength relative to the band edge (see Fig. 9.13). In our previous designs, the EO polymer SEO125 used in a slot resulted in 1006pm/V effective in-device r_{33} with a group index of 20.4. We estimated that the in-device actual r_{33} without the slow light effect was 74pm/V. We expect that an improvement of 25% in the r_{33} of the EO polymer and an increase of 25% in the group

index will lead to over 1500pm/V effective r_{33} in our next stage of research. Any improvement in the confinement of photons in the slot will further improve the device performance.

In addition, the modification of the slot width will also affect the capacitance of the slot, so the RC time constant will be changed, leading to a change of RF bandwidth [~1/(2RC)] and power consumption (~$2\pi fCV^2$). Therefore, a new figure of merit will need to be defined to evaluate the device performance.

9.5 TRAVELING WAVE SILICON-POLYMER HYBRID SLOT PHOTONIC CRYSTAL WAVEGUIDE MODULATOR

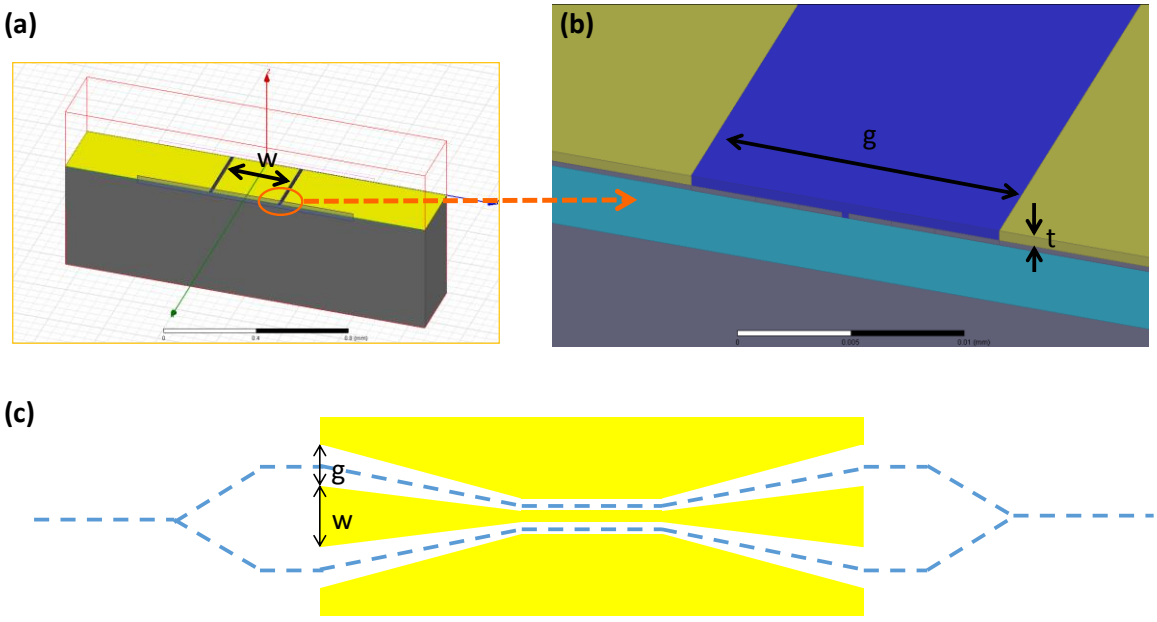

Figure 9.14: (a) A coplanar waveguide model on doped silicon slot photonic crystal waveguide MZI filled with EO polymer. (b) A magnified image one one arm of the MZI. (c) A schematic of the top view of the traveling wave silicon-polymer hybrid slot PCW MZI modulator.

In the future, a traveling wave electrode on doped silicon photonic crystal waveguide can be designed to further improve the modulation speed of our silicon-polymer hybrid slot PCW modulator. A schematic of this modulator is shown in Fig. 9.14. A coplanar waveguide structure is a good choice for our MZI modulator. The coplanar waveguide needs to be tapered to couple a RF probe, as shown in Fig. 9.14 (c), and the optical waveguides need to be routed accordingly. Since our PCW interaction length is very shorter (300μm long), and even smaller than the RF wavelength, the velocity mismatch between the RF wave and the slow optical wave in the PCW is not a dominating factor for high-speed modulation. ANSYS HFSS is used for the simulation. Effective medium approximation method used in Chapter 5 will be applied in this simulation. The simulated characteristic impedance and the microwave effective index up to 50GHz are shown in Figs. 9.15 (a) and (b). It can be seen that the impedance mismatching (50ohm) is achieved. The simulated microwave effective index above 10GHz is about 2; therefore, by using Eq. 7.4, the 3-dB bandwidth limited by velocity mismatch only is estimated to be 33GHz. Figures 9.15 (c) an (d) shows the simulated S parameters. The simulated S11 parameter shows the return loss is well below -24dB up to 50GHz, and the simulated S21 shows that the insertion loss is also very small and mainly limited by conductor loss. In addition, the impedance matching is also met along the taper region by tuning the geometry parameters of the coplanar waveguide. For different doping-levels [21] on our device, the geometry can be also be tuned to achieve impedance matching.

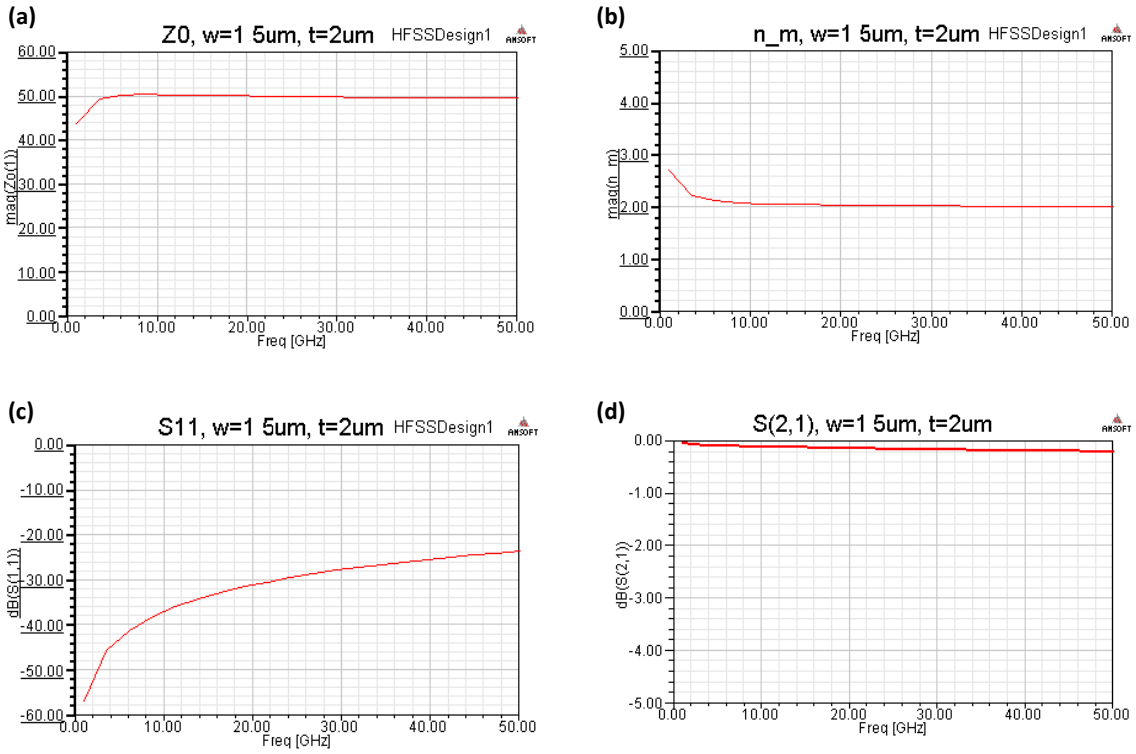

Figure 9.15: (a) Simulated characteristic impedance. (b) Simulated microwave effective index. (c) Simulated S11 parameter. (d) Simulated S21 parameter.

Furthermore, we will also get involved in coherent modulation schemes and advanced modulation formats in the future.

9.6 DEVELOPMENT OF EFFICIENT TAILGATED DEVICE AND PACKAGING

In the future, we will deliver a pigtailed electromagnetic wave sensor. In order to prepare a robust package for the device, we have decided to test the technique proposed in [15] [Fig. 9.16 (a)]. In this technique, the fiber is placed horizontally and fixed onto the surface of chip using a UV curable epoxy. The epoxy is dropped away from the grating and the polished surface. We are in the process of characterizing angle-polished fibers

from OE Land Inc. (www.o-eland.com) [Fig. 9.16 (b)]. A polished facet at $\theta_f=41.6^o$ provides a final $\theta_{out}=10^o$ out-going beam, while the beam hits the polished fact at an angle larger than the total-internal-reflection angle and is thoroughly reflected. A SWG will be designed for optimum coupling with angle-polished fibers. We will also investigate if the reflectivity can be enhanced by coating the angled-polished facet by a metal. Holding horizontal fibers in place by epoxy will let us avoid the grating coupling testing setup and it will be significantly easier to bring the horizontal fibers close to each other in order to decrease the length of the passive waveguides.

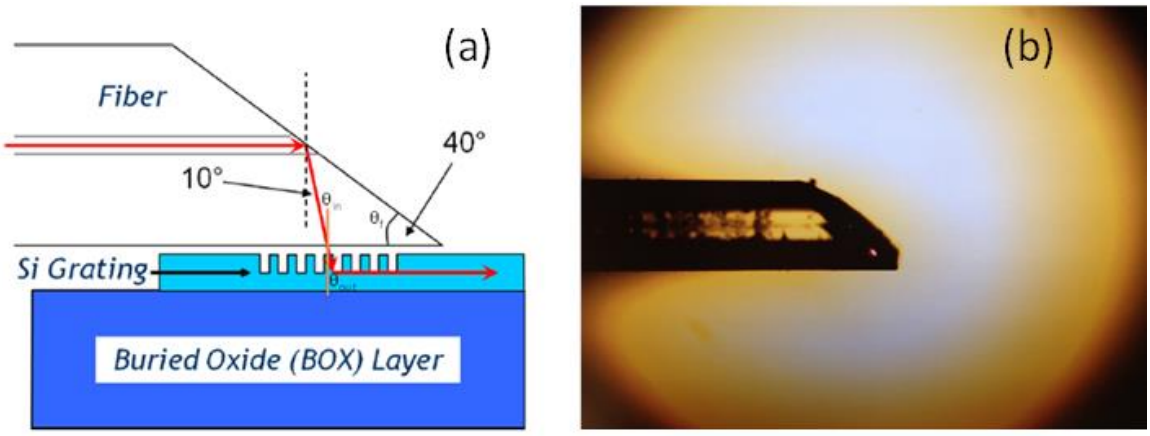

Figure 9.16: (a) A schematic of Angle-Polished Fiber-Grating Coupler (Figure From [15]). $\theta_{in}=90^o-2\times\theta_f$, $\theta_{out}=\sin^{-1}(\sin(\theta_{in})\times n_{fiber})$, $n_{fiber}=1.4682$, For $\theta_{out}=10^o$ => $\theta_f=41.6^o$, Angle_TIR = $\sin^{-1}(1/n_{fiber})=42.93^o$. (b) A Microscope Image of an Angle-Polished Fiber Acquired from OE Land Inc.

We envision that the fully packaged device will look like the schematic shown in Fig. 9.17. The Angled Polished Fiber – Grating Coupler scheme will make possible a tailgated device to be delivered. In addition, we will also examine the packaging and

reliability issues, such as the tolerance to the fiber tip displacement and rotation, effects of the packaging on the sensor and modulator applications, and the mechanical durability of the couplers.

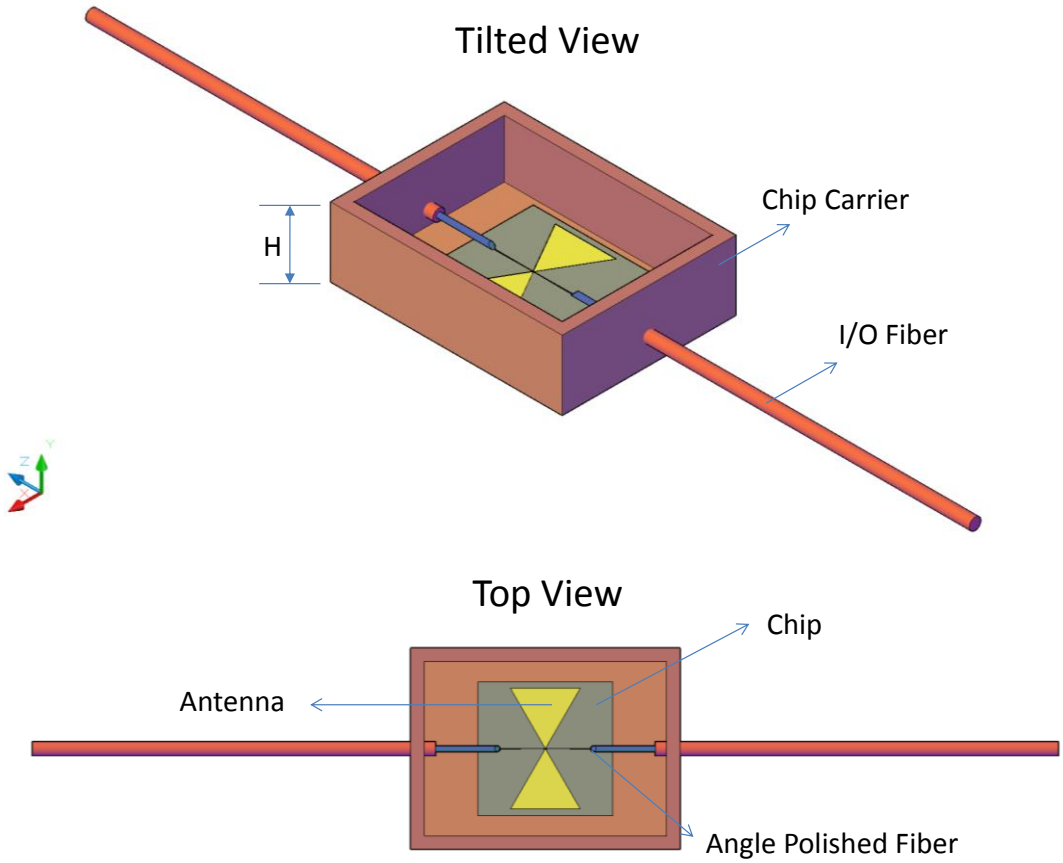

Figure 9.17: Schematics of the fully packaged and tailgated electromagnetic wave sensor. The height of the chip carrier (H) will be adjusted for the testing setup.

9.7 LOGIC DEVICES BASED ON ELECTRO-OPTIC POLYMER MICRORING RESONATORS FABRICATED BY UV IMPRINTING AND INK-JET PRINTING

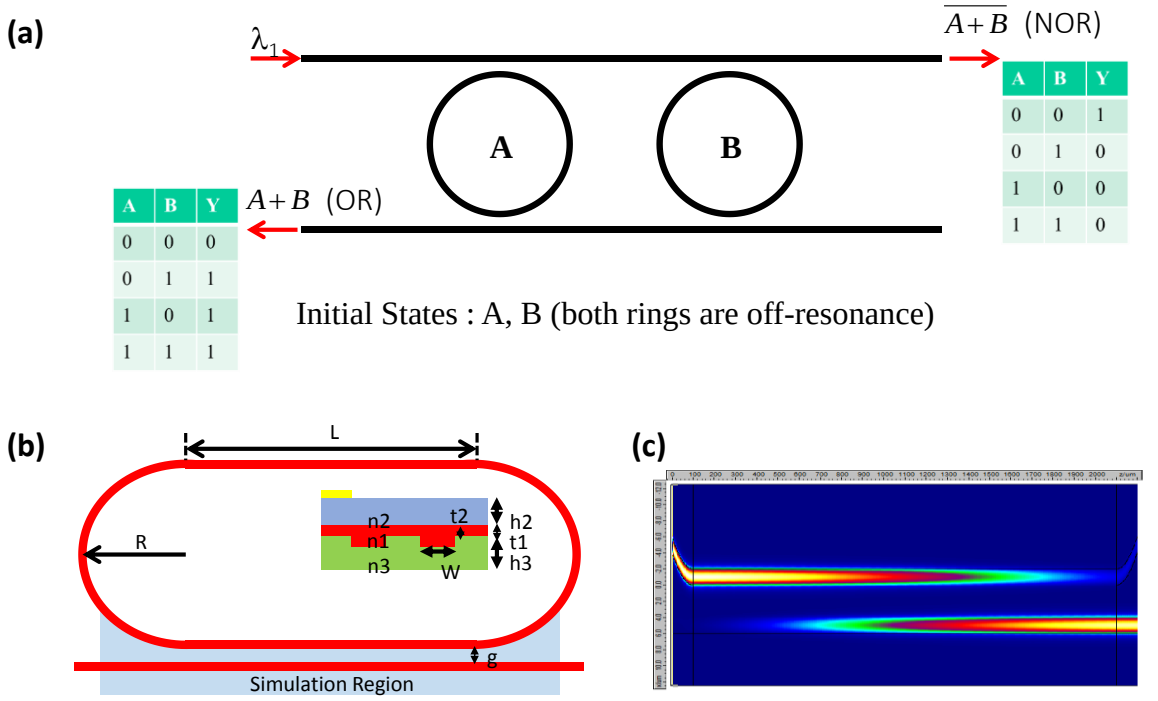

Figure 9.18: (a) A schematic of the EO polymer ring resonator. (b) Optical simulation about the coupling between ring and bus waveguide. (c) A example of the logic device based on EO polymer ring.

Another work we are currently working on is the design, fabrication and testing of an electro-optic (EO) polymer OR/NOR logic gate based on microring resonators and bus waveguides, each of which implements a switching operation [22]. An conventional optical waveguide made by UV15LV, EO polymer and UFC170A is designed, similar to the one in Chapter 7. The index of the EO polymer core can be changed by applying electric field across it, so the resonance of the ring resonator can be shifted. Simulation results show that the OR/NOR directed logic gate could be achieved. Direct logic structures utilize microring resonators and bus waveguides as switching elements to

control the propagation direction of light going through them. Each microring resonator is driven by an electrical pulse signal, which is regarded as the operand. The high and low levels of the electrical pulse signal represent logic 1 and 0, respectively, while the larger and smaller optical output powers at the output ports represent logic 1 and 0, respectively. Figure 9.18 (a) shows an example of the logic device. In the design and modeling, the dimension parameters of this device, as shown in Fig. 9.18 (b), are designed to achieve the best coupling within a reasonable coupling length. A simulation result made in FIMMWAVE is shown in Fig. 9.18 (c). A group of ring resonators with radius varied from 400 μm to 600 μm are designed.

The whole device is fabricated by imprinting method. Frist, a silicon hard mold is made by ebeam lithography and RIE. A thin layer of silver film is ink-jet printed on the silicon substrate to serve as the ground electrode for both switching and poling. Then, UV15LV is deposited to a form bottom cladding layer, and the silicon mold containing the ring structure is brought into conformal contact with the bottom cladding layer, followed by the UV imprinting and de-molding process. The EO polymer is then coated, followed by top cladding UFC-170A deposition, to form a trench waveguide structure. Finally, a top silver electrode is ink-jet printed on top of the top cladding layer, and aligned to the ring as shown in Fig. 9.18 (b). The key advantage of this fabrication technique is the utilization of an ink-jet printing method for patterning both bottom/ground and top/driving electrode layers without the need for evaporation or lift-off processes. Figures 9.19 (a)-(d) show the optical microscope pictures of a fabricated

devices. The EO effect of EO polymer is created by contact poling process or pyroelectric poling process.

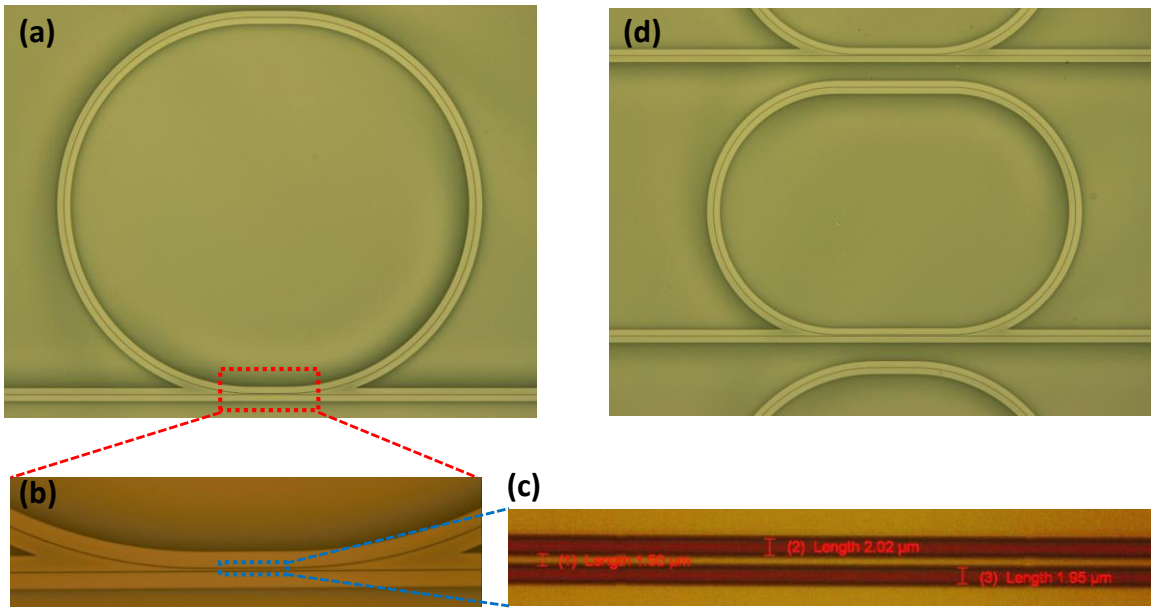

Figure 9.19: (a) One of the fabricated EO polymer ring. (b) and (c) Magnified images. (d) Another fabricated EO polymer ring with different coupling length.

The characterization work is then performed. Resonances with Q factor of about 68,000 are measured from the transmission spectrum. Some more active test will be performed on this device to demonstrate logic switching. To the best of our knowledge, this will be the first imprinted EO polymer ring logic device.

9.8 REFERENCES

[1] S. Huang, J. Luo, H. L. Yip, A. Ayazi, X. H. Zhou, M. Gould, A. Chen, T. Baehr‐Jones, M. Hochberg, and A. K. Y. Jen, "Efficient Poling of Electro‐Optic Polymers in Thin Films and Silicon Slot Waveguides by Detachable Pyroelectric Crystals," *Advanced Materials,* vol. 24, pp. OP42-OP47, 2012.

[2] S. Huang, J. Luo, Z. Jin, X.-H. Zhou, Z. Shi, and A. K.-Y. Jen, "Enhanced temporal stability of a highly efficient guest–host electro-optic polymer through a barrier layer assisted poling process," *Journal of Materials Chemistry,* vol. 22, pp. 20353-20357, 2012.

[3] Z. Shi, J. Luo, S. Huang, B. M. Polishak, X.-H. Zhou, S. Liff, T. R. Younkin, B. A. Block, and A. K.-Y. Jen, "Achieving excellent electro-optic activity and thermal stability in poled polymers through an expeditious crosslinking process," *Journal of Materials Chemistry,* vol. 22, pp. 951-959, 2012.

[4] X. Zhang, A. Hosseini, S. Chakravarty, J. Luo, A. K.-Y. Jen, and R. T. Chen, "Wide optical spectrum range, subvolt, compact modulator based on an electro-optic polymer refilled silicon slot photonic crystal waveguide," *Optics letters,* vol. 38, pp. 4931-4934, 2013.

[5] X. Zhang, A. Hosseini, H. Subbaraman, S. Wang, Q. Zhan, J. Luo, A. K. Jen, and R. T. Chen, "Integrated Photonic Electromagnetic Field Sensor Based on Broadband Bowtie Antenna Coupled Silicon Organic Hybrid Modulator," *Lightwave Technology, Journal of,* vol. 32, pp. 3774-3784, 2014.

[6] C. T. Chen, X. Xu, A. Hosseini, Z. Pan, H. Subbaraman, X. Zhang, Ray T. Chen, "Design of Highly Efficient Hybrid Si-Au Taper for Dielectric Strip Waveguide to Plasmonic Slot Waveguide Mode Converter," IEEE Journal of Lightwave Technology (To appear).

[7] A. Melikyan, L. Alloatti, A. Muslija, D. Hillerkuss, P. Schindler, J. Li, R. Palmer, D. Korn, S. Muehlbrandt, D. Van Thourhout, B. Chen, R. Dinu, M. Sommer, C. Koos, M. Kohl, W. Freude, and J. Leuthold, "High-speed plasmonic phase modulators," *Nature Photonics,* vol. 8, pp. 229-233, 2014.

[8] E. Schelew, G. W. Rieger, and J. F. Young, "Characterization of integrated planar photonic crystal circuits fabricated by a CMOS foundry," *Lightwave Technology, Journal of,* vol. 31, pp. 239-248, 2013.

[9] G. Li, J. Yao, H. Thacker, A. Mekis, X. Zheng, I. Shubin, Y. Luo, J. Lee, K. Raj, and J. E. Cunningham, "Ultralow-loss, high-density SOI optical waveguide routing for macrochip interconnects," *Optics Express,* vol. 20, pp. 12035-12039, 2012.

[10] S. Rahimi, A. Hosseini, X. Xu, H. Subbaraman, and R. T. Chen, "Group-index independent coupling to band engineered SOI photonic crystal waveguide with large slow-down factor," *Optics Express,* vol. 19, pp. 21832-21841, 2011.

[11] A. Hosseini, X. Xu, D. N. Kwong, H. Subbaraman, W. Jiang, and R. T. Chen, "On the role of evanescent modes and group index tapering in slow light photonic crystal waveguide coupling efficiency," *Applied Physics Letters,* vol. 98, pp. 031107-031107-3, 2011.

[12] C. Y. Lin, A. X. Wang, W. C. Lai, J. L. Covey, S. Chakravarty, and R. T. Chen, "Coupling loss minimization of slow light slotted photonic crystal waveguides using mode matching with continuous group index perturbation," *Optics letters,* vol. 37, pp. 232-234, 2012.

[13] X. Zhang, H. Subbaraman, A. Hosseini, and R. T. Chen, "Highly efficient mode converter for coupling light into wide slot photonic crystal waveguide," *Optics Express,* vol. 22, pp. 20678-20690, 2014.

[14] X. Xu, H. Subbaraman, J. Covey, D. Kwong, A. Hosseini, and R. T. Chen, "Complementary metal–oxide–semiconductor compatible high efficiency subwavelength grating couplers for silicon integrated photonics," *Applied Physics Letters,* vol. 101, p. 031109, 2012.

[15] B. Snyder and P. O'Brien, "Planar fiber packaging method for silicon photonic integrated circuits," 2012.

[16] T. Shoji, T. Tsuchizawa, T. Watanabe, K. Yamada, and H. Morita, "Low loss mode size converter from 0.3 μm square Si wire waveguides to singlemode fibres," *Electronics Letters,* vol. 38, pp. 1669-1670, 2002.

[17] A. Säynätjoki, L. Karvonen, T. Alasaarela, X. Tu, T. Liow, M. Hiltunen, A. Tervonen, G. Lo, and S. Honkanen, "Low-loss silicon slot waveguides and couplers fabricated with optical lithography and atomic layer deposition," *Optics Express,* vol. 19, pp. 26275-26282, 2011.

[18] R. Palmer, L. Alloatti, D. Korn, W. Heni, P. Schindler, J. Bolten, M. Karl, M. Waldow, T. Wahlbrink, and W. Freude, "Highly Efficient Strip-to-Slot Mode Converters," in *CLEO: Science and Innovations*, 2012.

[19] A. Di Falco, M. Massari, M. Scullion, S. Schulz, F. Romanato, and T. Krauss, "Propagation Losses of Slotted Photonic Crystal Waveguides," *Photonics Journal, IEEE,* vol. 4, pp. 1536-1541, 2012.

[20] X. Wang, C. Y. Lin, S. Chakravarty, J. Luo, A. K. Y. Jen, and R. T. Chen, "Effective in-device r< sub> 33</sub> of 735 pm/V on electro-optic polymer infiltrated silicon photonic crystal slot waveguides," *Optics letters,* vol. 36, pp. 882-884, 2011.

[21] X. Zhang, A. Hosseini, X. Xu, S. Wang, Q. Zhan, Y. Zou, S. Chakravarty, and R. T. Chen, "Electric field sensor based on electro-optic polymer refilled silicon slot photonic crystal waveguide coupled with bowtie antenna," in *SPIE OPTO*, 2013, pp. 862418-862418-8.

[22] P. Zhou, L. Zhang, Y. Tian, and L. Yang, "GHz electro-optical OR/NOR directed logic device based on silicon micro-ring resonators," *Optics letters,* vol. 39, pp. 1937-1940, 2014/04/01 2014.

Appendix

PUBLICATIONS

1. **(Invited Paper) X. Zhang**, A. Hosseini, X. Lin, H. Subbaraman, and R. T. Chen, "Polymer-based Hybrid Integrated Photonic Devices for Silicon On-chip Modulation and Board-level Optical Interconnects," IEEE Journal of Selected Topics in Quantum Electronics 16, 3401115-3401115 (2013)
2. **(Invited Paper)** H. Subbaraman, X., Xu, A. Hosseini, **X. Zhang**, Y. Zhang, D. Kwong, R. T. Chen, et al, "Recent Advances in Silicon-based Passive and Active Optical Interconnects," Optics Express, Vol. 23, Issue 3, pp. 2487-2511 (2015)
3. **(Invited Paper) X. Zhang**, C. Chung, A. Hosseini, H. Subbaraman, J. Luo, A. Jen, R. L. Nelson, C. Lee, and Ray T. Chen "High performance Optical Modulator Based on Electro-optic Polymer Infiltrated Silicon Slot Photonic Crystal Waveguide," Journal of Lightwave Technology (To Appear)
4. **(Invited Talk) X. Zhang,** C.-J. Chung, H. Subbaraman, H. Yan, X. Chen, R. T. Chen, "Wideband Integrated Photonic Electromagnetic Field Sensor Based on Electro-optic Polymer Filled Slot Photonic Crystal Waveguide," International Microwave Symposium (IMS) 2015, Phoenix, Arizona, USA, May 17-22, 2015, WSP-3
5. **(Invited Talk)** R. T. Chen, **X. Zhang**, "Silicon Nanomembrane Based Devices for Optical Sensing and On-chip Interconnects," Frontiers in Optics 2014, Tucson, Arizona, USA, October 19-23, 2014, Abstract ID: FW1B.2
6. **(Invited Talk)** C.-Y. Lin, A. X. Wang, **X. Zhang**, B. S. Lee, and R. T. Chen, "EO-polymer waveguide based high dynamic range EM wave sensors," SPIE Photonics West 2012, Paper No. 82580Y-1
7. **(Best Paper Award) X. Zhang**, A. Hosseini, H. Subbaraman, S. Wang, Q. Zhan, J. Luo, A. Jen, C. Chung, H. Yan, Z. Pan, R. Nelson, C. Lee, R. T. Chen, "Antenna-coupled silicon-organic hybrid integrated photonic crystal modulator for broadband electromagnetic wave detection," SPIE Photonics West 2015, Paper No. OE106-9

8. **(Best Paper Award) X. Zhang**, A. Hosseini, J. Luo, A. Jen, R. T. Chen, "Miniaturized low-power electro-optic modulator based on silicon integrated nanophotonics and organic polymers," SPIE Opitcs and Photonics Conference 2014, 9181-40
9. **X. Zhang**, H. Subbaraman, A. Hosseini, and R. T. Chen, "Highly Efficient Mode Converter for Coupling Light into Wide Slot Photonic Crystal Waveguide," Optics Express, Vol. 22, Issue 17, pp. 20678-20690 (2014)
10. **X. Zhang**, A. Hosseini, H. Subbaraman, S. Wang, Q. Zhan, J. Luo, A. K.-Y. Jen, and R. T. Chen, "Integrated Photonic Electromagnetic Field Sensor Based on Broadband Bowtie Antenna Coupled Silicon Organic Hybrid Modulator," Journal of Lightwave Technology, vol. 32, pp. 3774 - 3784 (2014).
11. **X. Zhang**, A. Hosseini, J. Luo, A. K.-Y. Jen, and R. T. Chen, "Wide Optical Spectrum Range, Sub-volt, Compact Modulator Based on Electro-optic Polymer Refilled Silicon Slot Photonic Crystal Waveguide," Optics Letters, 38, 4931-4934 (2013)
12. **X. Zhang**, B. Lee, C.-Y. Lin, A. X. Wang, A. Hosseini, R. T. Chen, "Highly Linear, Broadband Optical Modulator Based on Electro-optic Polymer," IEEE Photonics Journal, vol. 4, pp. 2214-2228 (2012)
13. **X. Zhang**, M. Tomes, T. Carmon, "Precession Optomechanics," Optics Express, Vol. 19, pp. 9066-9073 (2011)
14. C.-T. Chen, X. Xu, A. Hosseini, Z. Pan, H. Subbaraman, **X. Zhang**, and R. T. Chen, "Design of Highly Efficient Hybrid Si-Au Taper for Dielectric Strip Waveguide to Plasmonic Slot Waveguide Mode Converter", Journal of Lightwave Technology, 33(2), 535 - 540 (2015)
15. X. Lin, T. Ling, H. Subbaraman, **X. Zhang**, K. Byun, L. J. Guo and R. T. Chen, "Ultraviolet Imprinting and Aligned Ink-jet Printing for Multi-layer Patterning of Electro-Optic Polymer Modulator," Optics Letters, 38, 1597-1599 (2013)
16. C.-Y. Lin, A. X. Wang, B. Lee, **X. Zhang**, and R. T. Chen, "High Dynamic Range Electric Field Sensor for Electromagnetic Pulse Detection," Optics Express, Vol. 19,

Issue 18, pp. 17372-17377 (2011)

17. **X. Zhang**, S. Wang, H. Subbaraman, A. Hosseini, and R. T. Chen, "Integrated broadband bowtie antennas on transparent glass substrate," IEEE Antennas and Wireless Propagation Letters (Under Review)
18. **X. Zhang**, S. Chakravarty, C.-J. Chung, Z. Pan, H. Yan, and R. T. Chen, "Wide-spectrum-range Power-efficient Compact Thermo-optic Switch Based on Coupled Photonic Crystal Microcavities," Applied Physics Letters (In Preparation)
19. Z. Pan, H. Subbaraman, Y. Zou, X. Xu, **X. Zhang**, C. Zhang, Q. Li, J. Guo, and R. T. Chen, "Quasi-Vertical Tapers for Polymer Waveguide Based Inter-Board Optical Interconnects," Photonics Research (Under Review)
20. C.-J. Chung, **X. Zhang**, H. Subbaraman, J. Luo, A. Jen, and R. T. Chen, "In-device pyroelectric poling on EO polymer filled slot photonic crystal waveguides," (In Preparation)
21. **X. Zhang**, S. Chakravarty, C.-J. Chung, Z. Pan, and R. T. Chen, "Microheater-integrated silicon coupled photonic crystal microcavities for low-power thermo-optic switching over a wide spectrum," SPIE Photonics West 2016 (Submitted)
22. **X. Zhang**, C.-J. Chung, Z. Pan, H. Subbaraman, and R. T. Chen, "Design of a plasmonic-organic hybrid slot waveguide integrated with a bowtie-antenna for terahertz wave detection," SPIE Photonics West 2016 (Submitted)
23. H. Subbaraman, Z. Pan, **X. Zhang**, C.-J. Chung, C. Zhang, Q. Li, J. Guo, and R. T. Chen, "Printed electro-optic polymer based reconfigurable logic devices for optical interconnects," SPIE Photonics West 2016 (Submitted)
24. **X. Zhang**, A. Hosseini, H. Subbaraman, and R. T. Chen, "An RF Wave Sensor Based on Hybrid Integration of Silicon Photonic Crystal and Organic Electro-optic Polymer," IEDM 2015 (Submitted)
25. **X. Zhang**, A. Hosseini, H. Subbaraman, J. Luo, A. Jen, R. Nelson, and R. T. Chen, "High-speed Energy-efficient Silicon-polymer Hybrid Integrated Slot Photonic Crystal Waveguide Modulator," CLEO 2015, Abstract ID: 2185966

26. **X. Zhang**, H. Subbaraman, Z. Pan, C.-J. Chung, A. Hosseini, and R. T. Chen, "Low-loss Mode Converter for Silicon-Polymer Hybrid Slot Photonic Crystal Waveguide," CLEO 2015, Abstract ID: 2186479
27. **X. Zhang**, S. Chakravarty, C.-J. Chung, Z. Pan, and R. T. Chen, "Wide-spectrum-range Power-efficient Compact Thermo-optic Switch Based on Coupled Photonic Crystal Microcavities," CLEO 2015, Abstract ID: 2186491
28. **X. Zhang**, S. Chakravarty, C.-J. Chung, Z. Pan, and R. T. Chen, "Coupled Photonic Crystal Microcavities for Optical Switching over Wide Spectral Range," IEEE Optical Interconnects Conference 2015, WC6
29. **X. Zhang**, A. Hosseini, H. Subbaraman, J. Luo, A. Jen, R. Nelson, and R. T. Chen, "Backside-gate-assisted Broadband Modulation on Silicon-polymer Hybrid Photonic Crystal Waveguide," IEEE Optical Interconnects Conference 2015, WC7
30. **X. Zhang**, A. Hosseini, H. Subbaraman, J. Luo, A. Jen, C. Chung, H. Yan, Z. Pan, R. T. Chen, "Broadband energy-efficient optical modulation by hybrid integration of silicon nanophotonics and organic electro-optic polymer," SPIE Photonics West 2015, Paper No. OE112-30
31. **X. Zhang**, H. Subbaraman, A. Hosseini, Z. Pan, H. Yan, C. Chung, and R. T. Chen, "Low-loss mode converter for coupling light into slotted photonic crystal waveguide," SPIE Photonics West 2015, Paper No. OE112-5
32. **X. Zhang**, S. Wang, H. Subbaraman, A. Hosseini, Q. Zhan, Z. Pan, C. Chung, H. Yan, and R. T. Chen, "Integrated broadband bowtie antenna on transparent substrate," SPIE Photonics West 2015, Paper No. OE106-10
33. Z. Pan, H. Subbaraman, C. Zhang, A. Panday, Q. Li, **X. Zhang**, Y. Zou, X. Xu, J. Guo, and R. T. Chen, "Reconfigurable Thermo-Optic polymer switch based True-Time-Delay network utilizing imprinting and inkjet printing," SPIE Photonics West 2015, Paper No. 936214
34. Z. Pan, H. Subbaraman, **X. Zhang**, Q. Li, C. Zhang, J. Guo, and R. T. Chen, "High optical coupling efficient quasi-vertical tapers for polymer waveguide," SPIE

Photonics West 2015, Paper No. 936808

35. **X. Zhang**, A. Hosseini, H. Subbaraman, J. Luo, A. Jen, R. Nelson, and R. T. Chen, "Broadband Low-power Optical Modulator Based on Electro-optic Polymer Infiltrated Silicon Slot Photonic Crystal Waveguide," Frontiers in Optics 2014 (Optical Society of America), FTu1D
36. **X. Zhang**, A. Hosseini, H. Subbaraman, S. Wang, Q. Zhan, J. Luo, A. Jen, and R. T. Chen, "Electric Field Detection Using an Electro-optic Polymer Refilled Silicon Slot Photonic Crystal Waveguide," Frontiers in Optics 2014 (Optical Society of America), FW5B.4
37. **X. Zhang**, A. Hosseini, H. Subbaraman, S. Wang, Q. Zhan, J. Luo, A. Jen, and R. T. Chen, "High-performance Optical Modulator Based on Electro-optic Polymer Infiltrated Silicon Slot Photonic Crystal Waveguide," Advanced Photonics for Communications 2014 (Optical Society of America), IW2A.2
38. **X. Zhang**, A. Hosseini, J. Luo, A. Jen, and R. T. Chen, "Electro-optic Polymer Infiltrated Silicon Slot Photonic Crystal Waveguide for Broadband Electromagnetic Field Sensing," Advanced Photonics for Communications 2014 (Optical Society of America), IW2A.3
39. **X. Zhang**, A. Hosseini, J. Luo, A. Jen, and R. T. Chen, "Ultralow Power Consumption of 1.5nW Over Wide Optical Spectrum Range in Silicon Organic Hybrid Modulator," CLEO: 2014, Abstract ID SM2G.4
40. **X. Zhang**, A. Hosseini, H. Subbaraman, S. Wang, Q. Zhan, J. Luo, A. Jen, and R. T. Chen, "Wideband Electromagnetic Wave Sensing Using Electro-optic Polymer Infiltrated Silicon Slot Photonic Crystal Waveguide," in CLEO: 2014, Abstract ID SM2M.5
41. **X. Zhang**, H. Subbaraman, A. Hosseini, and R. T. Chen, "Optimization of Highly Efficient Mode Converter for Coupling Light into Large-slot Photonic Crystal Waveguide," IEEE Optical Interconnects Conference 2014, PTu9.
42. **X. Zhang**, A. Hosseini, J. Luo, A. Jen, and R. T. Chen, "Ultraperformance

Nanophotonic Modulator Based On Silicon Organic Hybrid Technology," in IEEE Optical Interconnects Conference 2014, MD2

43. **X. Zhang**, A. Hosseini, J. Luo, A. Jen, and R. T. Chen, "Hybrid silicon-electro-optic-polymer integrated high-performance optical modulator," Proc. SPIE 8991, Optical Interconnects XIV, 89910O, 2014
44. **X. Zhang**, A. Hosseini, C.-Y. Lin, J. Luo, A. K.-Y. Jen, and R. T. Chen, "Demonstration of Effective In-device r_{33} over 1000pm/V in Electro-optic Polymer Refilled Silicon Slot Photonic Crystal Waveguide Modulator," CLEO 2013, CTu2F.6
45. H. Subbaraman, X. Lin, T. Ling, **X. Zhang**, L. J. Guo, and R. T. Chen, "Printable EO Polymer Modulators," CLEO: Science and Innovations, 2013, p. CW1O. 2.
46. **X. Zhang**, A. Hosseini, X. Xu, S. Wang, Q. Zhan, and R. T. Chen, "Electric field sensor based on electro-optic polymer refilled silicon slot photonic crystal waveguide coupled with bowtie antenna," Proc. SPIE 8624, 862418, 2013
47. **X. Zhang**, B. Lee, C.-Y. Lin, A. Wang, A. Hosseini, and R. T. Chen, "Highly Linear Electro-optic Polymer Based Traveling Wave MMI-fed Directional Coupler Modulator," CLEO: Science and Innovations, 2012, CF1A.6
48. **X. Zhang**, B. Lee, C.-Y. Lin, A. X. Wang, A. Hosseini, X. Lin, and R. T. Chen, "Improved performance of traveling wave directional coupler modulator based on electro-optic polymer," SPIE Photonics West 2012, Proc., 82671B
49. **X. Zhang**, M. Tomes, T. Carmon, "Gyroscopic Optomechanics," Frontiers in Optics Conference 2010, Rochester, USA, FTuZ2
50. **X. Zhang**, M. Tomes, T. Carmon, "Gyroscopic Optomechanics," Optical MEMS and Nanophotonics Conference 2010, Sapporo, Japan, p. 159-160

Bibliography

Chapter 1

[1] S. Huang, J. Luo, H. L. Yip, A. Ayazi, X. H. Zhou, M. Gould, A. Chen, T. Baehr‐Jones, M. Hochberg, and A. K. Y. Jen, "Efficient Poling of Electro‐Optic Polymers in Thin Films and Silicon Slot Waveguides by Detachable Pyroelectric Crystals," *Advanced Materials,* vol. 24, pp. OP42-OP47, 2012.

[2] S. Huang, J. Luo, Z. Jin, X.-H. Zhou, Z. Shi, and A. K.-Y. Jen, "Enhanced temporal stability of a highly efficient guest–host electro-optic polymer through a barrier layer assisted poling process," *Journal of Materials Chemistry,* vol. 22, pp. 20353-20357, 2012.

[3] Z. Shi, J. Luo, S. Huang, B. M. Polishak, X.-H. Zhou, S. Liff, T. R. Younkin, B. A. Block, and A. K.-Y. Jen, "Achieving excellent electro-optic activity and thermal stability in poled polymers through an expeditious crosslinking process," *Journal of Materials Chemistry,* vol. 22, pp. 951-959, 2012.

[4] X. Zhang, A. Hosseini, S. Chakravarty, J. Luo, A. K.-Y. Jen, and R. T. Chen, "Wide optical spectrum range, subvolt, compact modulator based on an electro-optic polymer refilled silicon slot photonic crystal waveguide," *Optics letters,* vol. 38, pp. 4931-4934, 2013.

[5] X. Zhang, A. Hosseini, H. Subbaraman, S. Wang, Q. Zhan, J. Luo, A. K. Jen, and R. T. Chen, "Integrated Photonic Electromagnetic Field Sensor Based on Broadband Bowtie Antenna Coupled Silicon Organic Hybrid Modulator," *Lightwave Technology, Journal of,* vol. 32, pp. 3774-3784, 2014.

[6] C. T. Chen, X. Xu, A. Hosseini, Z. Pan, H. Subbaraman, X. Zhang, Ray T. Chen, "Design of Highly Efficient Hybrid Si-Au Taper for Dielectric Strip Waveguide to Plasmonic Slot Waveguide Mode Converter," IEEE Journal of Lightwave Technology (To appear).

[7] A. Melikyan, L. Alloatti, A. Muslija, D. Hillerkuss, P. Schindler, J. Li, R. Palmer, D. Korn, S. Muehlbrandt, D. Van Thourhout, B. Chen, R. Dinu, M. Sommer, C. Koos, M. Kohl, W. Freude, and J. Leuthold, "High-speed plasmonic phase modulators," *Nature Photonics,* vol. 8, pp. 229-233, 2014.

[8] E. Schelew, G. W. Rieger, and J. F. Young, "Characterization of integrated planar photonic crystal circuits fabricated by a CMOS foundry," *Lightwave Technology, Journal of,* vol. 31, pp. 239-248, 2013.

[9] G. Li, J. Yao, H. Thacker, A. Mekis, X. Zheng, I. Shubin, Y. Luo, J. Lee, K. Raj, and J. E. Cunningham, "Ultralow-loss, high-density SOI optical waveguide routing for macrochip interconnects," *Optics Express,* vol. 20, pp. 12035-12039, 2012.

[10] S. Rahimi, A. Hosseini, X. Xu, H. Subbaraman, and R. T. Chen, "Group-index independent coupling to band engineered SOI photonic crystal waveguide with large slow-down factor," *Optics Express,* vol. 19, pp. 21832-21841, 2011.

[11] A. Hosseini, X. Xu, D. N. Kwong, H. Subbaraman, W. Jiang, and R. T. Chen, "On the role of evanescent modes and group index tapering in slow light photonic crystal waveguide coupling efficiency," *Applied Physics Letters,* vol. 98, pp. 031107-031107-3, 2011.

[12] C. Y. Lin, A. X. Wang, W. C. Lai, J. L. Covey, S. Chakravarty, and R. T. Chen, "Coupling loss minimization of slow light slotted photonic crystal waveguides using mode matching with continuous group index perturbation," *Optics letters,* vol. 37, pp. 232-234, 2012.

[13] X. Zhang, H. Subbaraman, A. Hosseini, and R. T. Chen, "Highly efficient mode converter for coupling light into wide slot photonic crystal waveguide," *Optics Express,* vol. 22, pp. 20678-20690, 2014.

[14] X. Xu, H. Subbaraman, J. Covey, D. Kwong, A. Hosseini, and R. T. Chen, "Complementary metal–oxide–semiconductor compatible high efficiency subwavelength grating couplers for silicon integrated photonics," *Applied Physics Letters,* vol. 101, p. 031109, 2012.

[15] B. Snyder and P. O'Brien, "Planar fiber packaging method for silicon photonic integrated circuits," 2012.

[16] T. Shoji, T. Tsuchizawa, T. Watanabe, K. Yamada, and H. Morita, "Low loss mode size converter from 0.3 μm square Si wire waveguides to singlemode fibres," *Electronics Letters,* vol. 38, pp. 1669-1670, 2002.

[17] A. Säynätjoki, L. Karvonen, T. Alasaarela, X. Tu, T. Liow, M. Hiltunen, A. Tervonen, G. Lo, and S. Honkanen, "Low-loss silicon slot waveguides and couplers fabricated with optical lithography and atomic layer deposition," *Optics Express,* vol. 19, pp. 26275-26282, 2011.

[18] R. Palmer, L. Alloatti, D. Korn, W. Heni, P. Schindler, J. Bolten, M. Karl, M. Waldow, T. Wahlbrink, and W. Freude, "Highly Efficient Strip-to-Slot Mode Converters," in *CLEO: Science and Innovations*, 2012.

[19] A. Di Falco, M. Massari, M. Scullion, S. Schulz, F. Romanato, and T. Krauss, "Propagation Losses of Slotted Photonic Crystal Waveguides," *Photonics Journal, IEEE,* vol. 4, pp. 1536-1541, 2012.

[20] X. Wang, C. Y. Lin, S. Chakravarty, J. Luo, A. K. Y. Jen, and R. T. Chen, "Effective in-device r< sub> 33</sub> of 735 pm/V on electro-optic polymer infiltrated silicon photonic crystal slot waveguides," *Optics letters,* vol. 36, pp. 882-884, 2011.

[21] X. Zhang, A. Hosseini, X. Xu, S. Wang, Q. Zhan, Y. Zou, S. Chakravarty, and R. T. Chen, "Electric field sensor based on electro-optic polymer refilled silicon slot photonic crystal waveguide coupled with bowtie antenna," in *SPIE OPTO*, 2013, pp. 862418-862418-8.

[22] P. Zhou, L. Zhang, Y. Tian, and L. Yang, "GHz electro-optical OR/NOR directed logic device based on silicon micro-ring resonators," *Optics letters,* vol. 39, pp. 1937-1940, 2014/04/01 2014.

Chapter 2

[1] A. Di Falco, L. O'Faolain, and T. Krauss, "Dispersion control and slow light in slotted photonic crystal waveguides," *Applied Physics Letters,* vol. 92, p. 083501, 2008.

[2] Q. Xu, V. R. Almeida, R. R. Panepucci, and M. Lipson, "Experimental demonstration of guiding and confining light in nanometer-size low-refractive-index material," *Optics letters,* vol. 29, pp. 1626-1628, 2004.

[3] V. R. Almeida, Q. Xu, C. A. Barrios, and M. Lipson, "Guiding and confining light in void nanostructure," *Optics letters,* vol. 29, pp. 1209-1211, 2004.

[4] C. Koos, P. Vorreau, T. Vallaitis, P. Dumon, W. Bogaerts, R. Baets, B. Esembeson, I. Biaggio, T. Michinobu, F. Diederich, W. Freude, and J. Leuthold, "All-optical high-speed signal processing with silicon–organic hybrid slot waveguides," *Nature Photonics,* vol. 3, pp. 216-219, 2009.

[5] Y. A. Vlasov, M. O'Boyle, H. F. Hamann, and S. J. McNab, "Active control of slow light on a chip with photonic crystal waveguides," *Nature,* vol. 438, pp. 65-69, 2005.

[6] Y. Jiang, W. Jiang, L. Gu, X. Chen, and R. T. Chen, "80-micron interaction length silicon photonic crystal waveguide modulator," *Applied Physics Letters,* vol. 87, p. 221105, 2005.

[7] J.-M. Brosi, C. Koos, L. C. Andreani, M. Waldow, J. Leuthold, and W. Freude, "High-speed low-voltage electro-optic modulator with a polymer-infiltrated silicon photonic crystal waveguide," *Optics Express,* vol. 16, pp. 4177-4191, 2008.

[8] J. H. Wülbern, J. Hampe, A. Petrov, M. Eich, J. Luo, A. K.-Y. Jen, A. Di Falco, T. F. Krauss, and J. Bruns, "Electro-optic modulation in slotted resonant photonic crystal heterostructures," *Applied Physics Letters,* vol. 94, p. 241107, 2009.

[9] X. Zhang, A. Hosseini, C.-y. Lin, J. Luo, A. K. Jen, and R. T. Chen, "Demonstration of Effective In-device r33 over 1000 pmV in Electro-optic Polymer Refilled Silicon Slot Photonic Crystal Waveguide Modulator," in *CLEO: Science and Innovations*, 2013, p. CTu2F. 6.

[10] X. Zhang, A. Hosseini, X. Lin, H. Subbaraman, and R. T. Chen, "Polymer-based Hybrid Integrated Photonic Devices for Silicon On-chip Modulation and Board-level Optical Interconnects," *IEEE Journal of Selected Topics in Quantum Electronics,* vol. 19, pp. 196-210, 2013.

[11] X. Zhang, A. Hosseini, H. Subbaraman, S. Wang, Q. Zhan, J. Luo, A. Jen, and R. Chen, "Integrated Photonic Electromagnetic Field Sensor Based on Broadband

Bowtie Antenna Coupled Silicon Organic Hybrid Modulator," *Lightwave Technology, Journal of,* vol. PP, pp. 1-1, 2014.

[12] X. Zhang, A. Hosseini, X. Xu, S. Wang, Q. Zhan, Y. Zou, S. Chakravarty, and R. T. Chen, "Electric field sensor based on electro-optic polymer refilled silicon slot photonic crystal waveguide coupled with bowtie antenna," in *SPIE Photonic West 2013: Terahertz, RF, Millimeter, and Submillimeter-Wave Technology and Applications VI*, 2013, p. 862418.

[13] S. Lin, J. Hu, L. Kimerling, and K. Crozier, "Design of nanoslotted photonic crystal waveguide cavities for single nanoparticle trapping and detection," *Optics letters,* vol. 34, pp. 3451-3453, 2009.

[14] X. Zhang, A. Hosseini, H. Subbaraman, J. Luo, A. K.-Y. Jen, R. L. Nelson, and R. T. Chen, "Ultra-performance Optical Modulator Based on Electro-optic Polymer Infiltrated Silicon Slot Photonic Crystal Waveguide" (Under review)

[15] R. Palmer, A. Luca, D. Korn, P. Schindler, M. Baier, J. Bolten, T. Wahlbrink, M. Waldow, R. Dinu, W. Freude, C. Koos, and J. Leuthold, "Low power mach-zehnder modulator in silicon-organic hybrid technology," *Photonics Technology Letters, IEEE,* vol. 25, 2013.

[16] R. Blum, M. Sprave, J. Sablotny, and M. Eich, "High-electric-field poling of nonlinear optical polymers," *JOSA B,* vol. 15, pp. 318-328, 1998.

[17] X. Zhang, B. Lee, C.-y. Lin, A. X. Wang, A. Hosseini, and R. T. Chen, "Highly Linear Broadband Optical Modulator Based on Electro-Optic Polymer," *Photonics Journal, IEEE,* vol. 4, pp. 2214-2228, 2012.

[18] X. Lin, T. Ling, H. Subbaraman, X. Zhang, K. Byun, L. J. Guo, and R. T. Chen, "Ultraviolet imprinting and aligned ink-jet printing for multilayer patterning of electro-optic polymer modulators," *Optics letters,* vol. 38, pp. 1597-1599, 2013.

[19] C.-Y. Lin, A. X. Wang, X. Zhang, B. S. Lee, and R. T. Chen, "EO-polymer waveguide based high dynamic range EM wave sensors," in *SPIE OPTO*, 2012, pp. 82580Y-82580Y-7.

[20] H. Subbaraman, X. Lin, T. Ling, X. Zhang, L. J. Guo, and R. T. Chen, "Printable EO Polymer Modulators," in *CLEO: Science and Innovations*, 2013, p. CW1O. 2.

[21] S. Huang, T.-D. Kim, J. Luo, S. K. Hau, Z. Shi, X.-H. Zhou, H.-L. Yip, and A. K.-Y. Jen, "Highly efficient electro-optic polymers through improved poling using a thin TiO 2-modified transparent electrode," *Applied Physics Letters,* vol. 96, pp. 243311-243311-3, 2010.

[22] X. Wang, C.-Y. Lin, S. Chakravarty, J. Luo, A. K.-Y. Jen, and R. T. Chen, "Effective in-device r33 of 735 pm/V on electro-optic polymer infiltrated silicon photonic crystal slot waveguides," *Optics letters,* vol. 36, pp. 882-884, 2011.

[23] X. Zhang, A. Hosseini, S. Chakravarty, J. Luo, A. K.-Y. Jen, and R. T. Chen, "Wide optical spectrum range, subvolt, compact modulator based on an electro-optic polymer refilled silicon slot photonic crystal waveguide," *Optics letters,* vol. 38, pp. 4931-4934, 2013.

[24] H. Chen, B. Chen, D. Huang, D. Jin, J. Luo, A.-Y. Jen, and R. Dinu, "Broadband electro-optic polymer modulators with high electro-optic activity and low poling induced optical loss," *Applied Physics Letters,* vol. 93, p. 043507, 2008.

[25] T. Baehr-Jones, B. Penkov, J. Huang, P. Sullivan, J. Davies, J. Takayesu, J. Luo, T.-D. Kim, L. Dalton, and A. Jen, "Nonlinear polymer-clad silicon slot waveguide modulator with a half wave voltage of 0.25 V," *Applied Physics Letters,* vol. 92, p. 163303, 2008.

[26] X. Zhang, A. Hosseini, H. Subbaraman, J. Luo, A. Jen, R. Chen, "Broadband Low-power Optical Modulator Based on Electro-optic Polymer Infiltrated Silicon Slot Photonic Crystal Waveguide," Frontiers in Optics/Laser Science Conference, Optical Society of America, 2014), p. FTu1D.4.

[27] X. Zhang, A. Hosseini, J. Luo, A. Jen, and R. Chen, "Ultralow Power Consumption of 1.5 nW Over Wide Optical Spectrum Range in Silicon Organic Hybrid Modulator," in *CLEO: Science and Innovations*, 2014, p. SM2G. 4.

[28] Z. Wang, N. Zhu, Y. Tang, L. Wosinski, D. Dai, and S. He, "Ultracompact low-loss coupler between strip and slot waveguides," *Optics letters,* vol. 34, pp. 1498-1500, 2009.

[29] C.-Y. Lin, X. Wang, S. Chakravarty, B. S. Lee, W. Lai, J. Luo, A. K.-Y. Jen, and R. T. Chen, "Electro-optic polymer infiltrated silicon photonic crystal slot waveguide modulator with 23 dB slow light enhancement," *Applied Physics Letters,* vol. 97, p. 093304, 2010.

[30] J. Blasco and C. Barrios, "Compact slot-waveguide/channel-waveguide mode-converter," in *Lasers and Electro-Optics Europe, 2005. CLEO/Europe. 2005 Conference on*, 2005, pp. 607-607.

[31] Y. Liu, T. Baehr-Jones, J. Li, A. Pomerene, and M. Hochberg, "Efficient Strip to Strip-Loaded Slot Mode Converter in Silicon-on-Insulator," *Photonics Technology Letters, IEEE,* vol. 23, pp. 1496-1498, 2011.

[32] R. Palmer, A. Luca, D. Korn, W. Heni, P. Schindler, J. Bolten, M. Karl, M. Waldow, T. Wahlbrink, W. Freude, K. C, and L. J, "Low-loss silicon strip-to-slot mode converters," *IEEE Photonics Journal,* 2013.

[33] W.-C. Lai, S. Chakravarty, X. Wang, C. Lin, and R. T. Chen, "On-chip methane sensing by near-IR absorption signatures in a photonic crystal slot waveguide," *Optics letters,* vol. 36, pp. 984-986, 2011.

[34] H. C. Nguyen, Y. Sakai, M. Shinkawa, N. Ishikura, and T. Baba, "10 Gb/s operation of photonic crystal silicon optical modulators," *Optics Express,* vol. 19, pp. 13000-13007, 2011.

[35] C. Caer, X. Le Roux, J. Oden, L. Vivien, N. Dubreuil, and E. Cassan, "Design and fabrication of hollow core slow light slot photonic crystal waveguides for nonlinear optics," in *Asia Communications and Photonics Conference*, 2013, p. AW4B. 1.

[36] A. Hosseini, X. Xu, D. N. Kwong, H. Subbaraman, W. Jiang, and R. T. Chen, "On the role of evanescent modes and group index tapering in slow light photonic

crystal waveguide coupling efficiency," *Applied Physics Letters,* vol. 98, pp. 031107-031107-3, 2011.

[37] A. Hosseini, X. Xu, H. Subbaraman, C.-Y. Lin, S. Rahimi, and R. T. Chen, "Large optical spectral range dispersion engineered silicon-based photonic crystal waveguide modulator," *Opt. Express,* vol. 20, pp. 12318-12325, 2012.

[38] S. Schulz, L. O'Faolain, D. Beggs, T. White, A. Melloni, and T. Krauss, "Dispersion engineered slow light in photonic crystals: a comparison," *Journal of Optics,* vol. 12, p. 104004, 2010.

[39] A. Hosseini, X. Xu, H. Subbaraman, C.-Y. Lin, S. Rahimi, and R. T. Chen, "Large optical spectral range dispersion engineered silicon-based photonic crystal waveguide modulator," *Opt. Express,* vol. 20, pp. 12318-12325, 2012.

[40] H. Subbaraman, X. Xu, J. Covey, and R. T. Chen, "Efficient light coupling into in-plane semiconductor nanomembrane photonic devices utilizing a sub-wavelength grating coupler," *Optics Express,* vol. 20, pp. 20659-20665, 2012.

[41] X. Xu, H. Subbaraman, J. Covey, D. Kwong, A. Hosseini, and R. T. Chen, "Complementary metal–oxide–semiconductor compatible high efficiency subwavelength grating couplers for silicon integrated photonics," *Applied Physics Letters,* vol. 101, pp. 031109-031109-4, 2012.

[42] J. Witzens, T. Baehr-Jones, and M. Hochberg, "Design of transmission line driven slot waveguide Mach-Zehnder interferometers and application to analog optical links," *Optics Express,* vol. 18, pp. 16902-16928, 2010.

[43] R. Palmer, S. Koeber, D. L. Elder, M. Woessner, W. Heni, D. Korn, M. Lauermann, W. Bogaerts, L. Dalton, W. Freude, J. Leuthold, and C. Koos, "High-Speed, Low Drive-Voltage Silicon-Organic Hybrid Modulator Based on a Binary-Chromophore Electro-Optic Material," *Journal of Lightwave Technology,* vol. 32, pp. 2726-2734, 2014.

[44] X. Zhang, A. Hosseini, J. Luo, A. K.-Y. Jen, and R. T. Chen, "Hybrid silicon-electro-optic-polymer integrated high-performance optical modulator," in *SPIE Photonic West, OPTO*, 2014, pp. 89910O-89910O-6.

[45] X. Zhang, A. Hosseini, J. Luo, A. K.-Y. Jen, and R. T. Chen, "Ultraperformance Nanophotonic Modulator Based On Silicon Organic Hybrid Technology," presented at the Optical Interconnects Conference, 2014.

[46] R. Ding, T. Baehr-Jones, W.-J. Kim, B. Boyko, R. Bojko, A. Spott, A. Pomerene, C. Hill, W. Reinhardt, and M. Hochberg, "Low-loss asymmetric strip-loaded slot waveguides in silicon-on-insulator," *Applied Physics Letters,* vol. 98, p. 233303, 2011.

[47] A. Spott, T. Baehr-Jones, R. Ding, Y. Liu, R. Bojko, T. O'Malley, A. Pomerene, C. Hill, W. Reinhardt, and M. Hochberg, "Photolithographically fabricated low-loss asymmetric silicon slot waveguides," *Optics Express,* vol. 19, pp. 10950-10958, 2011.

[48] F. Kish, "500Gb/s and Beyond PIC-Module Transmitters and Receivers," in *Optical Fiber Communication Conference*, 2014, p. W3I. 1.

[49] D. Dai, J. Bauters, and J. E. Bowers, "Passive technologies for future large-scale photonic integrated circuits on silicon: polarization handling, light non-reciprocity and loss reduction," *Light: Science & Applications,* vol. 1, p. e1, 2012.

[50] Z. Yuan, A. Anopchenko, N. Daldosso, R. Guider, D. Navarro-Urrios, A. Pitanti, R. Spano, and L. Pavesi, "Silicon nanocrystals as an enabling material for silicon photonics," *Proceedings of the IEEE,* vol. 97, pp. 1250-1268, 2009.

[51] B. G. Lee, A. V. Rylyakov, W. M. Green, S. Assefa, C. W. Baks, R. Rimolo-Donadio, D. M. Kuchta, M. H. Khater, T. Barwicz, and C. Reinholm, "Monolithic Silicon Integration of Scaled Photonic Switch Fabrics, CMOS Logic, and Device Driver Circuits," *Journal of Lightwave Technology,* vol. 32, pp. 743-751, 2014.

[52] X. Zheng and A. V. Krishnamoorthy, "Si photonics technology for future optical interconnection," in *SPIE/OSA/IEEE Asia Communications and Photonics*, 2011, pp. 83091V-83091V-11.

[53] A. V. Krishnamoorthy, K. W. Goossen, W. Jan, X. Zheng, R. Ho, G. Li, R. Rozier, F. Liu, D. Patil, and J. Lexau, "Progress in low-power switched optical interconnects," *Selected Topics in Quantum Electronics, IEEE Journal of,* vol. 17, pp. 357-376, 2011.

[54] F. E. Doany, C. L. Schow, C. W. Baks, D. M. Kuchta, P. Pepeljugoski, L. Schares, R. Budd, F. Libsch, R. Dangel, and F. Horst, "160 Gb/s bidirectional polymer-waveguide board-level optical interconnects using CMOS-based transceivers," *Advanced Packaging, IEEE Transactions on,* vol. 32, pp. 345-359, 2009.

[55] C.-H. Chen, C. Li, A. Shafik, M. Fiorentino, P. Chiang, S. Palermo, and R. Beausoleil, "A WDM Silicon Photonic Transmitter Based on Carrier-Injection Microring Modulators," 2014.

[56] R. Ryf, S. Randel, N. K. Fontaine, M. Montoliu, E. Burrows, S. Chandrasekhar, A. H. Gnauck, C. Xie, R.-J. Essiambre, and P. Winzer, "32-bit/s/Hz spectral efficiency WDM transmission over 177-km few-mode fiber," in *Optical Fiber Communication Conference*, 2013, p. PDP5A. 1.

[57] W. M. Green, M. J. Rooks, L. Sekaric, and Y. A. Vlasov, "Ultra-compact, low RF power, 10 Gb/s silicon Mach-Zehnder modulator," *Optics Express,* vol. 15, pp. 17106-17113, 2007.

[58] J. Ding, R. Ji, L. Zhang, and L. Yang, "Electro-optical response analysis of a 40 Gb/s silicon Mach-Zehnder optical modulator," *Journal of Lightwave Technology,* vol. 31, pp. 2434-2440, 2013.

[59] D. M. Gill, J. E. Proesel, C. Xiong, J. Rosenberg, M. Khater, T. Barwicz, S. Assefa, S. M. Shank, C. Reinholm, and E. Kiewra, "Monolithic Travelling-Wave Mach-Zehnder Transmitter with High-Swing Stacked CMOS Driver," in *CLEO: Science and Innovations*, 2014, p. SM2G. 3.

[60] C. DeRose, "Integrated RF Silicon Photonics from High Power Photodiodes to Linear Modulators," in *Integrated Photonics Research, Silicon and Nanophotonics*, 2014, p. IW2A. 1.

[61] D. Mahgerefteh, "Transmission system comprising a semiconductor laser and a fiber grating discriminator," ed: Google Patents, 2000.
[62] X. Zheng, E. Chang, P. Amberg, I. Shubin, J. Lexau, F. Liu, H. Thacker, S. S. Djordjevic, S. Lin, and Y. Luo, "A high-speed, tunable silicon photonic ring modulator integrated with ultra-efficient active wavelength control," *Optics Express,* vol. 22, pp. 12628-12633, 2014.
[63] C.-Y. Lin, A. X. Wang, B. S. Lee, X. Zhang, and R. T. Chen, "High dynamic range electric field sensor for electromagnetic pulse detection," *Optics Express,* vol. 19, pp. 17372-17377, 2011.
[64] A. B. Matsko, A. A. Savchenkov, V. S. Ilchenko, D. Seidel, and L. Maleki, "On the sensitivity of all-dielectric microwave photonic receivers," *Journal of Lightwave Technology,* vol. 28, pp. 3427-3438, 2010.
[65] R. Chang, V. Lomakin, and E. Michielssen, "Coupling electromagnetics with micromagnetics," in *Antennas and Propagation Society International Symposium (APSURSI), 2012 IEEE*, 2012, pp. 1-2.
[66] X. Zhang, A. Hosseini, H. Subbaraman, S. Wang, Q. Zhan, J. Luo, A. K. Jen, and R. Chen, "Wideband Electromagnetic Wave Sensing Using Electro-optic Polymer Infiltrated Silicon Slot Photonic Crystal Waveguide," in *CLEO: Science and Innovations*, 2014, p. SM2M. 5.

Chapter 3

[1] Y. Shi, C. Zhang, H. Zhang, J. H. Bechtel, L. R. Dalton, B. H. Robinson, and W. H. Steier, "Low (sub-1-volt) halfwave voltage polymeric electro-optic modulators achieved by controlling chromophore shape," *Science,* vol. 288, pp. 119-122, 2000.
[2] D. Chen, H. R. Fetterman, A. Chen, W. H. Steier, L. R. Dalton, W. Wang, and Y. Shi, "Demonstration of 110 GHz electro-optic polymer modulators," *Applied Physics Letters,* vol. 70, pp. 3335-3337, 1997.
[3] X. Zhang, A. Hosseini, X. Lin, H. Subbaraman, and R. T. Chen, "Polymer-based Hybrid Integrated Photonic Devices for Silicon On-chip Modulation and Board-level Optical Interconnects," *IEEE Journal of Selected Topics in Quantum Electronics,* vol. 16, pp. 3401115-3401115, 2013.
[4] R. Ding, T. Baehr-Jones, W.-J. Kim, A. Spott, M. Fournier, J.-M. Fedeli, S. Huang, J. Luo, A. K.-Y. Jen, and L. Dalton, "Sub-volt silicon-organic electro-optic modulator with 500 MHz bandwidth," *Journal of Lightwave Technology,* vol. 29, pp. 1112-1117, 2011.
[5] M. Gould, T. Baehr-Jones, R. Ding, S. Huang, J. Luo, A. K.-Y. Jen, J.-M. Fedeli, M. Fournier, and M. Hochberg, "Silicon-polymer hybrid slot waveguide ring-resonator modulator," *Optics Express,* vol. 19, pp. 3952-3961, 2011.

[6] J. H. Wülbern, S. Prorok, J. Hampe, A. Petrov, M. Eich, J. Luo, A. K.-Y. Jen, M. Jenett, and A. Jacob, "40 GHz electro-optic modulation in hybrid silicon–organic slotted photonic crystal waveguides," *Optics letters,* vol. 35, pp. 2753-2755, 2010.

[7] X. Wang, C.-Y. Lin, S. Chakravarty, J. Luo, A. K.-Y. Jen, and R. T. Chen, "Effective in-device r< sub> 33</sub> of 735 pm/V on electro-optic polymer infiltrated silicon photonic crystal slot waveguides," *Optics letters,* vol. 36, pp. 882-884, 2011.

[8] H. C. Nguyen, Y. Sakai, M. Shinkawa, N. Ishikura, and T. Baba, "10 Gb/s operation of photonic crystal silicon optical modulators," *Optics Express,* vol. 19, pp. 13000-13007, 2011.

[9] J. H. Wülbern, J. Hampe, A. Petrov, M. Eich, J. Luo, A. K.-Y. Jen, A. Di Falco, T. F. Krauss, and J. Bruns, "Electro-optic modulation in slotted resonant photonic crystal heterostructures," *Applied Physics Letters,* vol. 94, p. 241107, 2009.

[10] H. C. Nguyen, Y. Sakai, M. Shinkawa, N. Ishikura, and T. Baba, "Photonic crystal silicon optical modulators: carrier-injection and depletion at 10 Gb/s," *Quantum Electronics, IEEE Journal of,* vol. 48, pp. 210-220, 2012.

[11] A. Hosseini, X. Xu, H. Subbaraman, C.-Y. Lin, S. Rahimi, and R. T. Chen, "Large optical spectral range dispersion engineered silicon-based photonic crystal waveguide modulator," *Opt. Express20 (11),* pp. 12318-12325, 2012.

[12] S. Rahimi, A. Hosseini, X. Xu, H. Subbaraman, and R. T. Chen, "Group-index independent coupling to band engineered SOI photonic crystal waveguide with large slow-down factor," *Opt. Express19 (22),* pp. 21832-21841, 2011.

[13] Y. Hamachi, S. Kubo, and T. Baba, "Slow light with low dispersion and nonlinear enhancement in a lattice-shifted photonic crystal waveguide," *Optics letters,* vol. 34, pp. 1072-1074, 2009.

[14] S. Schulz, L. O'Faolain, D. Beggs, T. White, A. Melloni, and T. Krauss, "Dispersion engineered slow light in photonic crystals: a comparison," *Journal of Optics,* vol. 12, p. 104004, 2010.

[15] A. Y. Petrov and M. Eich, "Zero dispersion at small group velocities in photonic crystal waveguides," *Applied Physics Letters,* vol. 85, pp. 4866-4868, 2004.

[16] J. Luo, X.-H. Zhou, and A. K.-Y. Jen, "Rational molecular design and supramolecular assembly of highly efficient organic electro-optic materials," *Journal of Materials Chemistry,* vol. 19, pp. 7410-7424, 2009.

[17] A. Hosseini, X. Xu, D. N. Kwong, H. Subbaraman, W. Jiang, and R. T. Chen, "On the role of evanescent modes and group index tapering in slow light photonic crystal waveguide coupling efficiency," *Applied Physics Letters,* vol. 98, pp. 031107-031107-3, 2011.

[18] A. Hosseini, D. Kwong, C.-Y. Lin, B. S. Lee, and R. T. Chen, "Output Formulation for Symmetrically Excited One-to-< formula formulatype=," *Selected Topics in Quantum Electronics, IEEE Journal of,* vol. 16, pp. 61-69, 2010.

[19] X. Xu, H. Subbaraman, J. Covey, D. Kwong, A. Hosseini, and R. T. Chen, "Complementary metal–oxide–semiconductor compatible high efficiency subwavelength grating couplers for silicon integrated photonics," *Applied Physics Letters,* vol. 101, pp. 031109-031109-4, 2012.

[20] A. Hosseini, D. Kwong, C. Y. Lin, B. S. Lee, and R. T. Chen, "Output Formulation for Symmetrically Excited One-to-< formula formulatype=," *Selected Topics in Quantum Electronics, IEEE Journal of,* vol. 16, pp. 61-69, 2010.

[21] X. Zhang, B. Lee, C.-y. Lin, A. X. Wang, A. Hosseini, and R. T. Chen, "Highly Linear Broadband Optical Modulator Based on Electro-Optic Polymer," *Photonics Journal, IEEE,* vol. 4, pp. 2214-2228, 2012.

[22] C.-Y. Lin, X. Wang, S. Chakravarty, B. S. Lee, W. Lai, J. Luo, A. K.-Y. Jen, and R. T. Chen, "Electro-optic polymer infiltrated silicon photonic crystal slot waveguide modulator with 23 dB slow light enhancement," *Applied Physics Letters,* vol. 97, p. 093304, 2010.

[23] C. Greenlee, A. Guilmo, A. Opadeyi, R. Himmelhuber, R. A. Norwood, M. Fallahi, J. Luo, S. Huang, X.-H. Zhou, and A. K.-Y. Jen, "Mach–Zehnder interferometry method for decoupling electro-optic and piezoelectric effects in poled polymer films," *Applied Physics Letters,* vol. 97, pp. 041109-041109-3, 2010.

[24] T. Baehr-Jones, B. Penkov, J. Huang, P. Sullivan, J. Davies, J. Takayesu, J. Luo, T.-D. Kim, L. Dalton, and A. Jen, "Nonlinear polymer-clad silicon slot waveguide modulator with a half wave voltage of< equation> 0.25< span style=," *Applied Physics Letters,* vol. 92, pp. 163303-163303-3, 2008.

[25] R. Ding, T. Baehr-Jones, Y. Liu, R. Bojko, J. Witzens, S. Huang, J. Luo, S. Benight, P. Sullivan, and J. Fedeli, "Demonstration of a low V< sub> π</sub> L modulator with GHz bandwidth based on electro-optic polymer-clad silicon slot waveguides," *Optics Express,* vol. 18, pp. 15618-15623, 2010.

[26] C.-Y. Lin, X. Wang, S. Chakravarty, B. S. Lee, W. Lai, J. Luo, A. K.-Y. Jen, and R. T. Chen, "Electro-optic polymer infiltrated silicon photonic crystal slot waveguide modulator with 23 dB slow light enhancement," *Applied Physics Letters,* vol. 97, p. 093304, 2010.

[27] R. Palmer, L. Alloatti, D. Korn, W. Heni, P. C. Schindler, J. Bolten, M. Karl, M. Waldow, T. Wahlbrink, W. Freude, C. Koos, and J. Leuthold, "Low-Loss Silicon Strip-to-Slot Mode Converters," *Ieee Photonics Journal,* vol. 5, Feb 2013.

[28] B. Snyder and P. O'Brien, "Planar fiber packaging method for silicon photonic integrated circuits," in *Optical Fiber Communication Conference and Exposition (OFC/NFOEC), 2012 and the National Fiber Optic Engineers Conference*, 2012, pp. 1-3.

[29] R. Dinu, D. Jin, G. M. Yu, B. Q. Chen, D. Y. Huang, H. Chen, A. Barklund, E. Miller, C. L. Wei, and J. Vemagiri, "Environmental Stress Testing of Electro-

Optic Polymer Modulators," *Journal of Lightwave Technology,* vol. 27, pp. 1527-1532, Jun 1 2009.

[30] D. Jin, H. Chen, A. Barklund, J. Mallari, G. Yu, E. Miller, and R. Dinu, "EO polymer modulators reliability study," in *Proceeding of SPIE*, 2010, pp. 75990H-1-75990H-8.

[31] S. Takahashi, B. Bhola, A. Yick, W. H. Steier, J. Luo, A. K.-Y. Jen, D. Jin, and R. Dinu, "Photo-Stability Measurement of Electro-Optic Polymer Waveguides With High Intensity at 1550-nm Wavelength," *Journal of Lightwave Technology,* vol. 27, pp. 1045-1050, 2009.

Chapter 4

[1] V. R. Almeida, Q. Xu, C. A. Barrios, and M. Lipson, "Guiding and confining light in void nanostructure," *Optics letters,* vol. 29, pp. 1209-1211, 2004.

[2] C. Koos, P. Vorreau, T. Vallaitis, P. Dumon, W. Bogaerts, R. Baets, B. Esembeson, I. Biaggio, T. Michinobu, F. Diederich, W. Freude, and J. Leuthold, "All-optical high-speed signal processing with silicon–organic hybrid slot waveguides," *Nature Photonics,* vol. 3, pp. 216-219, 2009.

[3] J. Leuthold, C. Koos, W. Freude, L. Alloatti, R. Palmer, D. Korn, J. Pfeifle, M. Lauermann, R. Dinu, S. Wehrli, M. Jazbinsek, P. Gunter, M. Waldow, T. Wahlbrink, J. Bolten, H. Kurz, M. Fournier, J.-M. Fedeli, H. Yu, and W. Bogaerts, "Silicon-organic hybrid electro-optical devices," *Selected Topics in Quantum Electronics, IEEE Journal of,* vol. 19, pp. 3401413-3401413, 2013.

[4] J. H. Wülbern, J. Hampe, A. Petrov, M. Eich, J. Luo, A. K.-Y. Jen, A. Di Falco, T. F. Krauss, and J. Bruns, "Electro-optic modulation in slotted resonant photonic crystal heterostructures," *Applied Physics Letters,* vol. 94, p. 241107, 2009.

[5] J.-M. Brosi, C. Koos, L. C. Andreani, M. Waldow, J. Leuthold, and W. Freude, "High-speed low-voltage electro-optic modulator with a polymer-infiltrated silicon photonic crystal waveguide," *Optics Express,* vol. 16, pp. 4177-4191, 2008.

[6] J. Takayesu, M. Hochberg, T. Baehr-Jones, E. Chan, G. Wang, P. Sullivan, Y. Liao, J. Davies, L. Dalton, A. Scherer, and W. Krug, "A Hybrid Electrooptic Microring Resonator-Based 1×4×1 ROADM for Wafer Scale Optical Interconnects," *Journal of Lightwave Technology,* vol. 27, pp. 440-448, 2009.

[7] X. Zhang, A. Hosseini, X. Lin, H. Subbaraman, and R. T. Chen, "Polymer-based Hybrid Integrated Photonic Devices for Silicon On-chip Modulation and Board-level Optical Interconnects," *IEEE Journal of Selected Topics in Quantum Electronics,* vol. 19, pp. 196-210, 2013.

[8] X. Zhang, A. Hosseini, H. Subbaraman, S. Wang, Q. Zhan, J. Luo, A. K. Jen, and R. T. Chen, "Integrated Photonic Electromagnetic Field Sensor Based on

Broadband Bowtie Antenna Coupled Silicon Organic Hybrid Modulator," *Lightwave Technology, Journal of,* vol. 32, pp. 3774-3784, 2014.

[9] D. Chen, H. R. Fetterman, A. Chen, W. H. Steier, L. R. Dalton, W. Wang, and Y. Shi, "Demonstration of 110 GHz electro-optic polymer modulators," *Applied Physics Letters,* vol. 70, pp. 3335-3337, 1997.

[10] Y. Shi, C. Zhang, H. Zhang, J. H. Bechtel, L. R. Dalton, B. H. Robinson, and W. H. Steier, "Low (sub-1-volt) halfwave voltage polymeric electro-optic modulators achieved by controlling chromophore shape," *Science,* vol. 288, pp. 119-122, 2000.

[11] R. T. Chen, L. Lin, C. Choi, Y. J. Liu, B. Bihari, L. Wu, S. Tang, R. Wickman, B. Picor, M. Hibb-Brenner, J. Bristow, and Y. S. Liu, "Fully embedded board-level guided-wave optoelectronic interconnects," *Proceedings of the IEEE,* vol. 88, pp. 780-793, 2000.

[12] X. Lin, T. Ling, H. Subbaraman, X. Zhang, K. Byun, L. J. Guo, and R. T. Chen, "Ultraviolet imprinting and aligned ink-jet printing for multilayer patterning of electro-optic polymer modulators," *Optics letters,* vol. 38, pp. 1597-1599, 2013.

[13] G. T. Reed, G. Mashanovich, F. Gardes, and D. Thomson, "Silicon optical modulators," *Nature Photonics,* vol. 4, pp. 518-526, 2010.

[14] R. Soref, "The past, present, and future of silicon photonics," *Selected Topics in Quantum Electronics, IEEE Journal of,* vol. 12, pp. 1678-1687, 2006.

[15] T. Baba, "Slow light in photonic crystals," *Nature Photonics,* vol. 2, pp. 465-473, 2008.

[16] Y. A. Vlasov, M. O'Boyle, H. F. Hamann, and S. J. McNab, "Active control of slow light on a chip with photonic crystal waveguides," *Nature,* vol. 438, pp. 65-69, 2005.

[17] Y. Jiang, W. Jiang, L. Gu, X. Chen, and R. T. Chen, "80-micron interaction length silicon photonic crystal waveguide modulator," *Applied Physics Letters,* vol. 87, p. 221105, 2005.

[18] H. C. Nguyen, S. Hashimoto, M. Shinkawa, and T. Baba, "Compact and fast photonic crystal silicon optical modulators," *Optics Express,* vol. 20, pp. 22465-22474, 2012.

[19] C.-Y. Lin, X. Wang, S. Chakravarty, B. S. Lee, W. Lai, J. Luo, A. K.-Y. Jen, and R. T. Chen, "Electro-optic polymer infiltrated silicon photonic crystal slot waveguide modulator with 23 dB slow light enhancement," *Applied Physics Letters,* vol. 97, p. 093304, 2010.

[20] X. Wang, C.-Y. Lin, S. Chakravarty, J. Luo, A. K.-Y. Jen, and R. T. Chen, "Effective in-device r33 of 735 pm/V on electro-optic polymer infiltrated silicon photonic crystal slot waveguides," *Optics letters,* vol. 36, pp. 882-884, 2011.

[21] X. Zhang, A. Hosseini, S. Chakravarty, J. Luo, A. K.-Y. Jen, and R. T. Chen, "Wide optical spectrum range, subvolt, compact modulator based on an electro-optic polymer refilled silicon slot photonic crystal waveguide," *Optics letters,* vol. 38, pp. 4931-4934, 2013.

[22] S. Huang, T.-D. Kim, J. Luo, S. K. Hau, Z. Shi, X.-H. Zhou, H.-L. Yip, and A. K.-Y. Jen, "Highly efficient electro-optic polymers through improved poling using a thin TiO 2-modified transparent electrode," *Applied Physics Letters,* vol. 96, pp. 243311-243311-3, 2010.

[23] H. Chen, B. Chen, D. Huang, D. Jin, J. Luo, A.-Y. Jen, and R. Dinu, "Broadband electro-optic polymer modulators with high electro-optic activity and low poling induced optical loss," *Applied Physics Letters,* vol. 93, p. 043507, 2008.

[24] T. Baehr-Jones, B. Penkov, J. Huang, P. Sullivan, J. Davies, J. Takayesu, J. Luo, T.-D. Kim, L. Dalton, and A. Jen, "Nonlinear polymer-clad silicon slot waveguide modulator with a half wave voltage of 0.25 V," *Applied Physics Letters,* vol. 92, p. 163303, 2008.

[25] H. C. Nguyen, Y. Sakai, M. Shinkawa, N. Ishikura, and T. Baba, "10 Gb/s operation of photonic crystal silicon optical modulators," *Optics Express,* vol. 19, pp. 13000-13007, 2011.

[26] J. Blasco and C. Barrios, "Compact slot-waveguide/channel-waveguide mode-converter," in *Lasers and Electro-Optics Europe, 2005. CLEO/Europe. 2005 Conference on*, 2005, pp. 607-607.

[27] R. Palmer, A. Luca, D. Korn, W. Heni, P. Schindler, J. Bolten, M. Karl, M. Waldow, T. Wahlbrink, W. Freude, K. C, and L. J, "Low-loss silicon strip-to-slot mode converters," *IEEE Photonics Journal,* 2013.

[28] X. Zhang, H. Subbaraman, A. Hosseini, and R. T. Chen, "Highly efficient mode converter for coupling light into wide slot photonic crystal waveguide," *Optics Express,* vol. 22, pp. 20678-20690, 2014.

[29] A. Hosseini, X. Xu, D. N. Kwong, H. Subbaraman, W. Jiang, and R. T. Chen, "On the role of evanescent modes and group index tapering in slow light photonic crystal waveguide coupling efficiency," *Applied Physics Letters,* vol. 98, pp. 031107-031107-3, 2011.

[30] X. Xu, H. Subbaraman, J. Covey, D. Kwong, A. Hosseini, and R. T. Chen, "Complementary metal–oxide–semiconductor compatible high efficiency subwavelength grating couplers for silicon integrated photonics," *Applied Physics Letters,* vol. 101, pp. 031109-031109-4, 2012.

[31] M. Soljačić, S. G. Johnson, S. Fan, M. Ibanescu, E. Ippen, and J. Joannopoulos, "Photonic-crystal slow-light enhancement of nonlinear phase sensitivity," *JOSA B,* vol. 19, pp. 2052-2059, 2002.

[32] J. Witzens, T. Baehr-Jones, and M. Hochberg, "Design of transmission line driven slot waveguide Mach-Zehnder interferometers and application to analog optical links," *Optics Express,* vol. 18, pp. 16902-16928, 2010.

[33] J. H. WŘlbern, A. Petrov, and M. Eich, "Electro-optical modulator in a polymerinfiltrated silicon slotted photonic crystal waveguide heterostructure resonator," *Optics Express,* vol. 17, pp. 304-313, 2009.

[34] S. K. Ghandhi, *VLSI fabrication principles: silicon and gallium arsenide*: John Wiley & Sons, 2008.

[35] J. Doylend, P. Jessop, and A. Knights, "Optical attenuation in ion-implanted silicon waveguide racetrack resonators," *Opt. Express19 (16),* pp. 14913-14918, 2011.
[36] A. Chen, H. Sun, A. Szep, S. Shi, D. Prather, Z. Lin, R. S. Kim, and D. Abeysinghe, "Achieving higher modulation efficiency in electrooptic polymer modulator with slotted silicon waveguide," *Lightwave Technology, Journal of,* vol. 29, pp. 3310-3318, 2011.
[37] S. Ristić, A. Prijić, and Z. Prijić, "Dependence of static dielectric constant of silicon on resistivity at room temperature," *Serbian Journal of Electrical Engineering,* vol. 1, pp. 237-247, 2004.
[38] W. Perrins, D. McKenzie, and R. McPhedran, "Transport properties of regular arrays of cylinders," *Proceedings of the Royal Society of London. A. Mathematical and Physical Sciences,* vol. 369, pp. 207-225, 1979.
[39] T. C. Choy, *Effective medium theory: principles and applications*: Oxford University Press, 1999.
[40] L. Alloatti, D. Korn, R. Palmer, D. Hillerkuss, J. Li, A. Barklund, R. Dinu, J. Wieland, M. Fournier, J. Fedeli, H. Yu, W. Bogaerts, P. Dumon, R. Baets, C. Koos, W. Freude, and J. Leuthold, "42.7 Gbit/s electro-optic modulator in silicon technology," *Optics Express,* vol. 19, pp. 11841-11851, 2011.
[41] R. Palmer, A. Luca, D. Korn, P. Schindler, M. Baier, J. Bolten, T. Wahlbrink, M. Waldow, R. Dinu, W. Freude, C. Koos, and J. Leuthold, "Low power mach-zehnder modulator in silicon-organic hybrid technology," *Photonics Technology Letters, IEEE,* vol. 25, 2013.
[42] L. Alloatti, M. Lauermann, C. Sürgers, C. Koos, W. Freude, and J. Leuthold, "Optical absorption in silicon layers in the presence of charge inversion/accumulation or ion implantation," *Applied Physics Letters,* vol. 103, p. 051104 2013.
[43] C.-Y. Lin, A. X. Wang, B. S. Lee, X. Zhang, and R. T. Chen, "High dynamic range electric field sensor for electromagnetic pulse detection," *Optics Express,* vol. 19, pp. 17372-17377, 2011.
[44] X. Zhang, B. Lee, C.-y. Lin, A. X. Wang, A. Hosseini, and R. T. Chen, "Highly Linear Broadband Optical Modulator Based on Electro-Optic Polymer," *Photonics Journal, IEEE,* vol. 4, pp. 2214-2228, 2012.
[45] X. Zhang, A. Hosseini, J. Luo, A. K.-Y. Jen, and R. T. Chen, "Hybrid silicon-electro-optic-polymer integrated high-performance optical modulator," in *SPIE Photonic West, OPTO*, 2014, pp. 89910O-89910O-6.
[46] A. Hosseini, X. Xu, H. Subbaraman, C.-Y. Lin, S. Rahimi, and R. T. Chen, "Large optical spectral range dispersion engineered silicon-based photonic crystal waveguide modulator," *Opt. Express20 (11),* pp. 12318-12325, 2012.
[47] T. F. Krauss, "Slow light in photonic crystal waveguides," *Journal of Physics D: Applied Physics,* vol. 40, p. 2666, 2007.

[48] S.-i. Inoue and A. Otomo, "Electro-optic polymer/silicon hybrid slow light modulator based on one-dimensional photonic crystal waveguides," *Applied Physics Letters,* vol. 103, p. 171101, 2013.
[49] J. H. Wülbern, S. Prorok, J. Hampe, A. Petrov, M. Eich, J. Luo, A. K.-Y. Jen, M. Jenett, and A. Jacob, "40 GHz electro-optic modulation in hybrid silicon–organic slotted photonic crystal waveguides," *Optics letters,* vol. 35, pp. 2753-2755, 2010.
[50] L. D. Tzuang, M. Soltani, Y. H. D. Lee, and M. Lipson, "High RF carrier frequency modulation in silicon resonators by coupling adjacent free-spectral-range modes," *Optics letters,* vol. 39, pp. 1799-1802, 2014.
[51] Y. N. Wijayanto, H. Murata, and Y. Okamura, "Electro-optic microwave-lightwave converters utilizing patch antennas with orthogonal gaps," *Journal of Nonlinear Optical Physics & Materials,* vol. 21, 2012.
[52] A. Melikyan, L. Alloatti, A. Muslija, D. Hillerkuss, P. Schindler, J. Li, R. Palmer, D. Korn, S. Muehlbrandt, D. Van Thourhout, B. Chen, R. Dinu, M. Sommer, C. Koos, M. Kohl, W. Freude, and J. Leuthold, "High-speed plasmonic phase modulators," *Nature Photonics,* vol. 8, pp. 229-233, 2014.
[53] O. Herrera, K. Kim, R. Voorakaranam, R. Himmelhuber, S. Wang, Q. Zhan, L. Li, R. Norwood, R. Neilson, and J. Luo, "Silica/Electro-optic Polymer Optical Modulator with Integrated Antenna for Microwave Receiving."
[54] H. Bartzsch, D. Glöß, P. Frach, M. Gittner, E. Schultheiß, W. Brode, and J. Hartung, "Electrical insulation properties of sputter‐deposited SiO2, Si3N4 and Al2O3 films at room temperature and 400° C," *Physica Status Solidi (A),* vol. 206, pp. 514-519, 2009.
[55] S. M. Sze and K. K. Ng, *Physics of semiconductor devices*: John Wiley & Sons, 2006.
[56] D. A. Miller, "Energy consumption in optical modulators for interconnects," *Optics Express,* vol. 20, pp. A293-A308, 2012.
[57] J. Leuthold, C. Koos, W. Freude, L. Alloatti, R. Palmer, D. Korn, J. Pfeifle, M. Lauermann, R. Dinu, S. Wehrli, M. Jazbinsek, P. Gunter, M. Waldow, T. Wahlbrink, J. Bolten, M. Fournier, J. M. Fedeli, W. Bogaerts, and H. Yu, "High-speed, low-power optical modulators in silicon," in *Transparent Optical Networks (ICTON), 2013 15th International Conference on*, 2013, pp. 1-4.
[58] R. Palmer, S. Koeber, W. Heni, D. Elder, D. Korn, H. Yu, L. Alloatti, S. Koenig, P. Schindler, W. Bogaerts, L. Dalton, W. Freude, J. Leuthold, and C. Koos, "High-speed silicon-organic hybrid (SOH) modulator with 1, 6 fJ/bit and 180 pm/V in-device nonlinearity," in *39th European Conference and Exhibition on Optical Communication (ECOC-2013)*, 2013.
[59] H. C. Nguyen, Y. Sakai, M. Shinkawa, N. Ishikura, and T. Baba, "Photonic crystal silicon optical modulators: carrier-injection and depletion at 10 Gb/s," *Quantum Electronics, IEEE Journal of,* vol. 48, pp. 210-220, 2012.

[60] A. Hosseini, X. Xu, H. Subbaraman, C.-Y. Lin, S. Rahimi, and R. T. Chen, "Large optical spectral range dispersion engineered silicon-based photonic crystal waveguide modulator," *Opt. Express,* vol. 20, pp. 12318-12325, 2012.

[61] M. Gould, T. Baehr-Jones, R. Ding, S. Huang, J. Luo, A. K.-Y. Jen, J.-M. Fedeli, M. Fournier, and M. Hochberg, "Silicon-polymer hybrid slot waveguide ring-resonator modulator," *Optics Express,* vol. 19, pp. 3952-3961, 2011.

[62] C. Zhang, T. Ling, S.-L. Chen, and L. J. Guo, "Ultrabroad Bandwidth and Highly Sensitive Optical Ultrasonic Detector for Photoacoustic Imaging," *ACS Photonics,* 2014.

[63] L. Chen, Q. Xu, M. G. Wood, and R. M. Reano, "Hybrid silicon and lithium niobate electro-optical ring modulator," *Optica,* vol. 1, pp. 112-118, 2014.

[64] C. Xiong, W. H. Pernice, J. H. Ngai, J. W. Reiner, D. Kumah, F. J. Walker, C. H. Ahn, and H. X. Tang, "Active silicon integrated nanophotonics: ferroelectric BaTiO3 devices," *Nano letters,* vol. 14, pp. 1419-1425, 2014.

[65] Y. Terada and T. Baba, "Low-Voltage 25 Gbps Modulators Based On Si Photonic Crystal Slow Light Waveguides," in *CLEO: Science and Innovations*, 2014, p. SM2G. 2.

[66] L. Alloatti, R. Palmer, S. Diebold, K. P. Pahl, B. Q. Chen, R. Dinu, M. Fournier, J. M. Fedeli, T. Zwick, W. Freude, C. Koos, and J. Leuthold, "100 GHz silicon-organic hybrid modulator," *Light-Science & Applications,* vol. 3, May 2014.

[67] E. Schelew, G. W. Rieger, and J. F. Young, "Characterization of integrated planar photonic crystal circuits fabricated by a CMOS foundry," *Lightwave Technology, Journal of,* vol. 31, pp. 239-248, 2013.

[68] B. Snyder and P. O'Brien, "Planar fiber packaging method for silicon photonic integrated circuits," in *Optical Fiber Communication Conference and Exposition (OFC/NFOEC) 2012*, 2012, pp. 1-3.

[69] R. Palmer, S. Koeber, D. L. Elder, M. Woessner, W. Heni, D. Korn, M. Lauermann, W. Bogaerts, L. Dalton, W. Freude, J. Leuthold, and C. Koos, "High-Speed, Low Drive-Voltage Silicon-Organic Hybrid Modulator Based on a Binary-Chromophore Electro-Optic Material," *Journal of Lightwave Technology,* vol. 32, pp. 2726-2734, 2014.

[70] M. Li, S. Huang, X.-H. Zhou, Y. Zang, J. Wu, Z. Cui, J. Luo, and A. K. Jen, "Poling Efficiency Enhancement of Tethered Binary Nonlinear Optical Chromophores for Achieving Ultrahigh n3r33 Figure-of-Merit of 2601 pm/V," *Journal of Materials Chemistry C,* 2015.

[71] D. Korn, R. Palmer, H. Yu, P. C. Schindler, L. Alloatti, M. Baier, R. Schmogrow, W. Bogaerts, S. K. Selvaraja, G. Lepage, M. Pantouvaki, J. Wouters, P. Verheyen, J. V. Campenhout, B. Chen, R. Baets, P. Absil, R. Dinu, C. Koos, W. Freude, and J. Leuthold, "Silicon-organic hybrid (SOH) IQ modulator using the linear electro-optic effect for transmitting 16QAM at 112 Gbit/s," *Optics Express,* vol. 21, pp. 13219-13227, 2013.

[72] C. Weimann, P. Schindler, R. Palmer, S. Wolf, D. Bekele, D. Korn, J. Pfeifle, S. Koeber, R. Schmogrow, L. Alloatti, D. Elder, H. Yu, W. Bogaerts, L. R. Dalton, W. Freude, J. Leuthold, and C. Koos, "Silicon-organic hybrid (SOH) frequency comb sources for terabit/s data transmission," *Optics Express,* vol. 22, pp. 3629-3637, 2014.

[73] M. Lauermann, R. Palmer, S. Koeber, P. C. Schindler, D. Korn, T. Wahlbrink, J. Bolten, M. Waldow, D. L. Elder, L. R. Dalton, J. Leuthold, W. Freude, and C. Koos, "Low-power silicon-organic hybrid (SOH) modulators for advanced modulation formats," *Optics Express,* vol. 22, pp. 29927-29936, 2014/12/01 2014.

[74] G. Li, X. Zheng, J. Yao, H. Thacker, I. Shubin, Y. Luo, K. Raj, J. E. Cunningham, and A. V. Krishnamoorthy, "25Gb/s 1V-driving CMOS ring modulator with integrated thermal tuning," *Optics Express,* vol. 19, pp. 20435-20443, 2011.

[75] S. Koeber, R. Palmer, M. Lauermann, W. Heni, D. L. Elder, D. Korn, M. Woessner, L. Alloatti, S. Koenig, and P. C. Schindler, "Femtojoule electro-optic modulation using a silicon-organic hybrid device," *Light Sci. Appl.(to be published),* 2014.

[76] S. Takahashi, B. Bhola, A. Yick, W. Steier, J. Luo, A. Y. Jen, D. Jin, and R. Dinu, "Photo-Stability Measurement of Electro-Optic Polymer Waveguides With High Intensity at 1550-nm Wavelength," *Journal of Lightwave Technology,* vol. 27, pp. 1045-1050, 2009/04/15 2009.

[77] S. Huang, J. Luo, Z. Jin, X.-H. Zhou, Z. Shi, and A. K.-Y. Jen, "Enhanced temporal stability of a highly efficient guest–host electro-optic polymer through a barrier layer assisted poling process," *Journal of Materials Chemistry,* vol. 22, pp. 20353-20357, 2012.

[78] Z. Shi, J. Luo, S. Huang, B. M. Polishak, X.-H. Zhou, S. Liff, T. R. Younkin, B. A. Block, and A. K.-Y. Jen, "Achieving excellent electro-optic activity and thermal stability in poled polymers through an expeditious crosslinking process," *Journal of Materials Chemistry,* vol. 22, pp. 951-959, 2012.

Chapter 5

[1] P. Drexler and P. Fiala, "Methods for high-power EM pulse measurement," *Sensors Journal, IEEE,* vol. 7, pp. 1006-1011, 2007.

[2] Q. Wu and X. C. Zhang, "Ultrafast electro‐optic field sensors," *Applied Physics Letters,* vol. 68, pp. 1604-1606, 1996.

[3] H. Bassen and G. Smith, "Electric field probes--A review," *Antennas and Propagation, IEEE Transactions on,* vol. 31, pp. 710-718, 1983.

[4] A. Pedersen, C. Cattell, C.-G. Fälthammar, V. Formisano, P.-A. Lindqvist, F. Mozer, and R. Torbert, "Quasistatic electric field measurements with spherical double probes on the GEOS and ISEE satellites," *Space science reviews,* vol. 37, pp. 269-312, 1984.

[5] G. Gustafsson, R. Boström, B. Holback, G. Holmgren, A. Lundgren, K. Stasiewicz, L. Åhlén, F. Mozer, D. Pankow, and P. Harvey, "The electric field and wave experiment for the Cluster mission," in *The Cluster and Phoenix Missions*, ed: Springer, 1997, pp. 137-156.

[6] H. Bassen, C. Bulmer, and W. Burns, "An RF Field Strength Measurement System Using unintegrated Optical Linear Modulator," in *Microwave symposium Digest, 1980 IEEE MTT-S International*, 1980, pp. 317-318.

[7] N. A. Jaeger and L. Young, "High-voltage sensor employing an integrated optics Mach-Zehnder interferometer in conjunction with a capacitive divider," *Lightwave Technology, Journal of,* vol. 7, pp. 229-235, 1989.

[8] W. B. Bridges, F. T. Sheehy, and J. H. Schaffner, "Wave-coupled LiNbO/sub 3/electrooptic modulator for microwave and millimeter-wave modulation," *Photonics Technology Letters, IEEE,* vol. 3, pp. 133-135, 1991.

[9] F. T. Sheehy, W. B. Bridges, and J. H. Schaffner, "60 GHz and 94 GHz antenna-coupled LiNbO3 electrooptic modulators," *IEEE photonics technology letters,* vol. 5, pp. 307-310, 1993.

[10] Y. Wijayanto, H. Murata, and Y. Okamura, "Electro-optic wireless millimeter-wave-lightwave signal converters using planar Yagi-Uda array antennas coupled to resonant electrodes," in *Opto-Electronics and Communications Conference (OECC), 2012 17th*, 2012, pp. 543-544.

[11] Y. N. Wijayanto, H. Murata, and Y. Okamura, "Electrooptic Millimeter-Wave–Lightwave Signal Converters Suspended to Gap-Embedded Patch Antennas on Low-Dielectric Materials," *Selected Topics in Quantum Electronics, IEEE Journal of,* vol. 19, pp. 3400709-3400709, 2013.

[12] A. B. Matsko, A. A. Savchenkov, V. S. Ilchenko, D. Seidel, and L. Maleki, "On the sensitivity of all-dielectric microwave photonic receivers," *Journal of Lightwave Technology,* vol. 28, pp. 3427-3438, 2010.

[13] N. Kuwabara, K. Tajima, R. Kobayashi, and F. Amemiya, "Development and analysis of electric field sensor using LiNbO< sub> 3</sub> optical modulator," *Electromagnetic Compatibility, IEEE Transactions on,* vol. 34, pp. 391-396, 1992.

[14] K. Tajima, R. Kobayashi, N. Kuwabara, and M. Tokuda, "Development of optical isotropic E-field sensor operating more than 10 GHz using mach-zehnder interferometers," *IEICE Transactions on Electronics,* vol. 85 pp. 961-968, 2002.

[15] V. Passaro, F. Dell'Olio, and F. De Leonardis, "Electromagnetic field photonic sensors," *Progress in quantum electronics,* vol. 30, pp. 45-73, 2006.

[16] J. Leuthold, W. Freude, J.-M. Brosi, R. Baets, P. Dumon, I. Biaggio, M. L. Scimeca, F. Diederich, B. Frank, and C. Koos, "Silicon organic hybrid technology—A platform for practical nonlinear optics," *Proceedings of the IEEE,* vol. 97, pp. 1304-1316, 2009.

[17] X. Zhang, B. Lee, C.-y. Lin, A. X. Wang, A. Hosseini, and R. T. Chen, "Highly Linear Broadband Optical Modulator Based on Electro-Optic Polymer," *Photonics Journal, IEEE,* vol. 4, pp. 2214-2228, 2012.

[18] X. Zhang, A. Hosseini, C.-y. Lin, J. Luo, A. K. Jen, and R. T. Chen, "Demonstration of Effective In-device r33 over 1000 pmV in Electro-optic Polymer Refilled Silicon Slot Photonic Crystal Waveguide Modulator," in *CLEO: Science and Innovations*, 2013, p. CTu2F. 6.

[19] F. E. Doany, C. L. Schow, B. G. Lee, R. Budd, C. Baks, R. Dangel, R. John, F. Libsch, J. A. Kash, and B. Chan, "Terabit/sec-class board-level optical interconnects through polymer waveguides using 24-channel bidirectional transceiver modules," in *Electronic Components and Technology Conference (ECTC), 2011 IEEE 61st*, 2011, pp. 790-797.

[20] X. Zhang, A. Hosseini, X. Lin, H. Subbaraman, and R. T. Chen, "Polymer-based Hybrid Integrated Photonic Devices for Silicon On-chip Modulation and Board-level Optical Interconnects," *IEEE Journal of Selected Topics in Quantum Electronics,* vol. 19, pp. 196-210, 2013.

[21] C.-Y. Lin, A. X. Wang, B. S. Lee, X. Zhang, and R. T. Chen, "High dynamic range electric field sensor for electromagnetic pulse detection," *Optics Express,* vol. 19, pp. 17372-17377, 2011.

[22] L. Jingdong and A. K. Y. Jen, "Highly Efficient Organic Electrooptic Materials and Their Hybrid Systems for Advanced Photonic Devices," *Selected Topics in Quantum Electronics, IEEE Journal of,* vol. 19, pp. 42-53, 2013.

[23] T.-D. Kim, J. Luo, Y.-J. Cheng, Z. Shi, S. Hau, S.-H. Jang, X.-H. Zhou, Y. Tian, B. Polishak, S. Huang, Ma.Hong, L. R. Dalton, and A. K.-Y. Jen, "Binary Chromophore Systems in Nonlinear Optical Dendrimers and Polymers for Large Electrooptic Activities†," *The Journal of Physical Chemistry C,* vol. 112, pp. 8091-8098, 2008.

[24] R. Soref, "The past, present, and future of silicon photonics," *Selected Topics in Quantum Electronics, IEEE Journal of,* vol. 12, pp. 1678-1687, 2006.

[25] B. Jalali and S. Fathpour, "Silicon photonics," *Lightwave Technology, Journal of,* vol. 24, pp. 4600-4615, 2006.

[26] T. Baba, "Slow light in photonic crystals," *Nature Photonics,* vol. 2, pp. 465-473, 2008.

[27] Y. A. Vlasov, M. O'Boyle, H. F. Hamann, and S. J. McNab, "Active control of slow light on a chip with photonic crystal waveguides," *Nature,* vol. 438, pp. 65-69, 2005.

[28] X. Zhang, A. Hosseini, J. Luo, A. K.-Y. Jen, and R. T. Chen, "Hybrid silicon-electro-optic-polymer integrated high-performance optical modulator," in *SPIE Photonic West, OPTO*, 2014, pp. 89910O-89910O-6.

[29] Y. Jiang, W. Jiang, L. Gu, X. Chen, and R. T. Chen, "80-micron interaction length silicon photonic crystal waveguide modulator," *Applied Physics Letters,* vol. 87, p. 221105, 2005.

[30] X. Zhang, A. Hosseini, H. Subbaraman, S. Wang, Q. Zhan, J. Luo, A. K. Jen, and R. Chen, "Wideband electromagnetic wave sensing using electro-optic polymer infiltrated silicon slot photonic crystal waveguide," in *CLEO: Science and Innovations*, 2014, p. SM2M. 5.

[31] X. Zhang, A. Hosseini, H. Subbaraman, J. Luo, A. Jen, R. Nelson, and R. T. Chen, "Broadband low-power optical modulator based on electro-optic polymer Infiltrated Silicon Slot Photonic Crystal Waveguide," in *Frontiers in Optics*, 2014, p. FTu1D. 4.

[32] J. H. Wülbern, S. Prorok, J. Hampe, A. Petrov, M. Eich, J. Luo, A. K.-Y. Jen, M. Jenett, and A. Jacob, "40 GHz electro-optic modulation in hybrid silicon–organic slotted photonic crystal waveguides," *Optics letters,* vol. 35, pp. 2753-2755, 2010.

[33] L. Alloatti, D. Korn, R. Palmer, D. Hillerkuss, J. Li, A. Barklund, R. Dinu, J. Wieland, M. Fournier, J. Fedeli, H. Yu, W. Bogaerts, P. Dumon, R. Baets, C. Koos, W. Freude, and J. Leuthold, "42.7 Gbit/s electro-optic modulator in silicon technology," *Optics Express,* vol. 19, pp. 11841-11851, 2011.

[34] S. Wang and Q. Zhan, "Modified bow-tie antenna with strong broadband field enhancement for RF photonic applications," in *SPIE NanoScience+ Engineering*, 2013, pp. 88061V-88061V-6.

[35] X. Zhang, S. Wang, H. Subbaraman, Q. Zhan, Z. Pan, C.-j. Chung, H. Yan, and R. T. Chen, "Integrated broadband bowtie antenna on transparent substrate," in *SPIE OPTO*, 2015, pp. 93620P-93620P-8.

[36] D. Marpaung, C. Roeloffzen, R. Heideman, A. Leinse, S. Sales, and J. Capmany, "Integrated microwave photonics," *Laser & Photonics Reviews,* vol. 7, pp. 506-538, 2013.

[37] X. Zhang, A. Hosseini, S. Chakravarty, J. Luo, A. K. Y. Jen, and R. T. Chen, "Wide optical spectrum range, subvolt, compact modulator based on an electro-optic polymer refilled silicon slot photonic crystal waveguide," *Optics letters,* vol. 38, pp. 4931-4934, 2013.

[38] X. Zhang, A. Hosseini, X. Xu, S. Wang, Q. Zhan, Y. Zou, S. Chakravarty, and R. T. Chen, "Electric field sensor based on electro-optic polymer refilled silicon slot photonic crystal waveguide coupled with bowtie antenna," in *SPIE Photonic West 2013: Terahertz, RF, Millimeter, and Submillimeter-Wave Technology and Applications VI*, 2013, p. 862418.

[39] A. Hosseini, X. Xu, H. Subbaraman, C.-Y. Lin, S. Rahimi, and R. T. Chen, "Large optical spectral range dispersion engineered silicon-based photonic crystal waveguide modulator," *Opt. Express,* vol. 20, pp. 12318-12325, 2012.

[40] H. C. Nguyen, Y. Sakai, M. Shinkawa, N. Ishikura, and T. Baba, "10 Gb/s operation of photonic crystal silicon optical modulators," *Optics Express,* vol. 19, pp. 13000-13007, 2011/07/04 2011.

[41] X. Wang, C.-Y. Lin, S. Chakravarty, J. Luo, A. K.-Y. Jen, and R. T. Chen, "Effective in-device r33 of 735 pm/V on electro-optic polymer infiltrated silicon photonic crystal slot waveguides," *Optics letters,* vol. 36, pp. 882-884, 2011.

[42] X. Zhang, H. Subbaraman, A. Hosseini, and R. T. Chen, "Highly efficient mode converter for coupling light into wide slot photonic crystal waveguide," *Optics Express,* vol. 22, pp. 20678-20690, 2014.
[43] Z. Wang, N. Zhu, Y. Tang, L. Wosinski, D. Dai, and S. He, "Ultracompact low-loss coupler between strip and slot waveguides," *Optics letters,* vol. 34, pp. 1498-1500, 2009.
[44] X. Xu, H. Subbaraman, J. Covey, D. Kwong, A. Hosseini, and R. T. Chen, "Complementary metal–oxide–semiconductor compatible high efficiency subwavelength grating couplers for silicon integrated photonics," *Applied Physics Letters,* vol. 101, pp. 031109-031109-4, 2012.
[45] H. Subbaraman, X. Xu, J. Covey, and R. T. Chen, "Efficient light coupling into in-plane semiconductor nanomembrane photonic devices utilizing a sub-wavelength grating coupler," *Optics Express,* vol. 20, pp. 20659-20665, 2012.
[46] A. Yariv and P. Yeh, *Optical waves in crystal propagation and control of laser radiation*: Wiley-Interscience, 1983.
[47] S. K. Ghandhi, *VLSI fabrication principles: silicon and gallium arsenide*: John Wiley & Sons, 2008.
[48] J. Doylend, P. Jessop, and A. Knights, "Optical attenuation in ion-implanted silicon waveguide racetrack resonators," *Opt. Express19 (16),* pp. 14913-14918, 2011.
[49] X. Lin, T. Ling, H. Subbaraman, X. Zhang, K. Byun, L. J. Guo, and R. T. Chen, "Ultraviolet imprinting and aligned ink-jet printing for multilayer patterning of electro-optic polymer modulators," *Optics letters,* vol. 38, pp. 1597-1599, 2013.
[50] H. Subbaraman, X. Lin, T. Ling, X. Zhang, L. J. Guo, and R. T. Chen, "Printable EO Polymer Modulators," in *CLEO: Science and Innovations*, 2013, p. CW1O. 2.
[51] S. Ristić, A. Prijić, and Z. Prijić, "Dependence of static dielectric constant of silicon on resistivity at room temperature," *Serbian Journal of Electrical Engineering,* vol. 1, pp. 237-247, 2004.
[52] T. C. Choy, *Effective medium theory: principles and applications*: Oxford University Press, 1999.
[53] D. Gao and Z. Zhou, "Nonlinear equation method for band structure calculations of photonic crystal slabs," *Applied Physics Letters,* vol. 88, p. 163105, 2006.
[54] W. Perrins, D. McKenzie, and R. McPhedran, "Transport properties of regular arrays of cylinders," *Proceedings of the Royal Society of London. A. Mathematical and Physical Sciences,* vol. 369, pp. 207-225, 1979.
[55] C. A. Balanis, *Antenna theory: analysis and design*: John Wiley & Sons, 2012.
[56] J. D. Kraus and R. J. Marhefka, *Antenna for all applications*, 3rd ed.: McGraw-Hill 2002.
[57] H. Duan, A. I. Fernández-Domínguez, M. Bosman, S. A. Maier, and J. K. Yang, "Nanoplasmonics: classical down to the nanometer scale," *Nano letters,* vol. 12, pp. 1683-1689, 2012.

[58] O. Peña-Rodríguez, J. Olivares, M. Carrascosa, Á. García-Cabañes, A. Rivera, and F. Agulló-López, "Optical Waveguides Fabricated by Ion Implantation/Irradiation: A Review," *Ion Implantation, Prof. Mark Goorsky (Ed.), ISBN,* pp. 978-953, 2012.
[59] D. M. Pozar, *Microwave engineering*, 4th ed.: Wiley, 2011.
[60] A. Chen and E. J. Murphy, *Broadband optical modulators: science, technology, and applications*: CRC Press, 2011.
[61] D. Perry, S. Chadderdon, R. Gibson, B. Shreeve, R. H. Selfridge, S. M. Schultz, W. C. Wang, R. Forber, and J. Luo, "Electro-optic polymer electric field sensor," in *SPIE Smart Structures and Materials+ Nondestructive Evaluation and Health Monitoring*, 2011, pp. 79820Q-79820Q-8.
[62] W. C. Wang, H. Lotem, R. Forber, and K. Bui, "Optical electric-field sensors," *Optical Engineering,* vol. 45, pp. 124402-124402-8, 2006.

Chapter 6

[1] S. Kim, J. Jin, Y.-J. Kim, I.-Y. Park, Y. Kim, and S.-W. Kim, "High-harmonic generation by resonant plasmon field enhancement," *Nature,* vol. 453, pp. 757-760, 2008.
[2] Z. Pan and J. Guo, "Enhanced optical absorption and electric field resonance in diabolo metal bar optical antennas," *Optics Express,* vol. 21, pp. 32491-32500, 2013.
[3] K. Ishihara, K. Ohashi, T. Ikari, H. Minamide, H. Yokoyama, J.-i. Shikata, and H. Ito, "Terahertz-wave near-field imaging with subwavelength resolution using surface-wave-assisted bow-tie aperture," *Applied Physics Letters,* vol. 89, p. 201120, 2006.
[4] S. Sederberg and A. Elezzabi, "Nanoscale plasmonic contour bowtie antenna operating in the mid-infrared," *Optics Express,* vol. 19, pp. 15532-15537, 2011.
[5] M. Roslee, K. S. Subari, and I. S. Shahdan, "Design of bow tie antenna in CST studio suite below 2GHz for ground penetrating radar applications," in *RF and Microwave Conference (RFM), 2011 IEEE International*, 2011, pp. 430-433.
[6] B. Madhav, V. Pisipati, H. Khan, V. Prasad, K. P. Kumar, K. Bhavani, and M. R. Kumar, "Liquid Crystal Bow-Tie Microstrip antenna for Wireless Communication Applications," *Journal of Engineering Science and Technology Review,* vol. 4, pp. 131-134, 2011.
[7] A. C. Durgun, C. A. Balanis, C. R. Birtcher, and D. R. Allee, "Design, simulation, fabrication and testing of flexible bow-tie antennas," *Antennas and Propagation, IEEE Transactions on,* vol. 59, pp. 4425-4435, 2011.

[8] K. D. Ko, A. Kumar, K. H. Fung, R. Ambekar, G. L. Liu, N. X. Fang, and K. C. Toussaint Jr, "Nonlinear optical response from arrays of Au bowtie nanoantennas," *Nano letters,* vol. 11, pp. 61-65, 2010.

[9] M. Rahim, M. Abdul Aziz, and C. Goh, "Bow-tie microstrip antenna design," in *13th IEEE International Conference*, 2005.

[10] W. Yeoh, K. Wong, and W. Rowe, "Wideband miniaturized half bowtie printed dipole antenna with integrated balun for wireless applications," *Antennas and Propagation, IEEE Transactions on,* vol. 59, pp. 339-342, 2011.

[11] K. R. Mahmoud, "Design optimization of a bow-tie antenna for 2.45 GHz RFID readers using a hybrid BSO-NM algorithm," *Progress In Electromagnetics Research,* vol. 100, pp. 105-117, 2010.

[12] J. H. Yoon and Y. C. Lee, "Modified bow‐tie slot antenna for the 2.4/5.2/5.8 GHz WLAN bands with a rectangular tuning stub," *Microwave and optical technology letters,* vol. 53, pp. 126-130, 2011.

[13] A. C. Durgun, M. S. Reese, C. A. Balanis, C. R. Birtcher, D. R. Allee, and S. Venugopal, "Flexible bow-tie antennas with reduced metallization," in *Radio and Wireless Symposium (RWS), 2011 IEEE*, 2011, pp. 50-53.

[14] C. A. Balanis, *Antenna theory: analysis and design*: John Wiley & Sons, 2012.

[15] F. I. Rial, H. Lorenzo, M. Pereira, and J. Armesto, "Analysis of the emitted wavelet of high-resolution bowtie GPR Antennas," *Sensors,* vol. 9, pp. 4230-4246, 2009.

[16] P. Mühlschlegel, H.-J. Eisler, O. Martin, B. Hecht, and D. Pohl, "Resonant optical antennas," *Science,* vol. 308, pp. 1607-1609, 2005.

[17] H. Fischer and O. J. Martin, "Engineering the optical response of plasmonic nanoantennas," *Optics Express,* vol. 16, pp. 9144-9154, 2008.

[18] M. Mivelle, T. S. van Zanten, L. Neumann, N. F. van Hulst, and M. F. Garcia-Parajo, "Ultrabright bowtie nanoaperture antenna probes studied by single molecule fluorescence," *Nano letters,* vol. 12, pp. 5972-5978, 2012.

[19] J. Y. Suh, M. D. Huntington, C. H. Kim, W. Zhou, M. R. Wasielewski, and T. W. Odom, "Extraordinary nonlinear absorption in 3D bowtie nanoantennas," *Nano letters,* vol. 12, pp. 269-274, 2011.

[20] F. M. Congedo, G. Tarricone, and M. L Cannarile, "Broadband bowtie antenna for RF energy scavenging applications," *Antennas and Propagation (EUCAP),* 2011.

[21] S. Wang and Q. Zhan, "Modified bow-tie antenna with strong broadband field enhancement for RF photonic applications," in *SPIE NanoScience+ Engineering*, 2013, pp. 88061V-88061V-6.

[22] X. Zhang, A. Hosseini, H. Subbaraman, S. Wang, Q. Zhan, J. Luo, A. K. Jen, and R. T. Chen, "Integrated Photonic Electromagnetic Field Sensor Based on

Broadband Bowtie Antenna Coupled Silicon Organic Hybrid Modulator," *Lightwave Technology, Journal of,* vol. 32, pp. 3774-3784, 2014.

[23] O. D. Herrera, K.-J. Kim, R. Voorakaranam, R. Himmelhuber, S. Wang, V. Demir, Q. Zhan, L. Li, R. A. Norwood, R. L. Nelson, J. Luo, A. K. Y. Jen, and N. Peyghambarian, "Silica/Electro-Optic Polymer Optical Modulator With Integrated Antenna for Microwave Receiving," *Journal of Lightwave Technology,* vol. 32, pp. 3861-3867, 2014/10/15 2014.

[24] L. Chen and R. M. Reano, "Compact electric field sensors based on indirect bonding of lithium niobate to silicon microrings," *Optics Express,* vol. 20, pp. 4032-4038, 2012.

[25] R. A. Synowicki, "Suppression of backside reflections from transparent substrates," *physica status solidi (c),* vol. 5, pp. 1085-1088, 2008.

[26] D. B. Rutledge, D. P. Neikirk, and D. P. Kasilingam, "Integrated circuit antennas," *Infrared and millimeter waves,* vol. 10, pp. 1-90, 1983.

[27] A. Facchetti and T. J. Marks, "Transparent electronics," *From Synthesis to Applications, Wiley, Chichester, UK,* 2010.

[28] S. Kim, S. Kim, J. Park, S. Ju, and S. Mohammadi, "Fully transparent pixel circuits driven by random network carbon nanotube transistor circuitry," *Acs Nano,* vol. 4, pp. 2994-2998, 2010.

[29] S. Nedic, Y. T. Chun, W.-K. Hong, D. Chu, and M. Welland, "High performance non-volatile ferroelectric copolymer memory based on a ZnO nanowire transistor fabricated on a transparent substrate," *Applied Physics Letters,* vol. 104, p. 033101, 2014.

[30] I. Lahiri, V. P. Verma, and W. Choi, "An all-graphene based transparent and flexible field emission device," *Carbon,* vol. 49, pp. 1614-1619, 2011.

[31] S. C. Lai, K. Yao, Y. F. Chen, L. Zhang, and Y.-F. Lim, "A Photovoltaic UV Sensor With a Ferroelectric Thin Film on Transparent Substrate," 2013.

[32] J. Wang, W. Li, and C. Wang, "Improving light outcoupling efficiency for OLEDs with microlens array fabricated on transparent substrate," *Journal of Nanomaterials,* vol. 2014, 2014.

[33] N. Nath and A. Chilkoti, "A colorimetric gold nanoparticle sensor to interrogate biomolecular interactions in real time on a surface," *Analytical Chemistry,* vol. 74, pp. 504-509, 2002.

[34] Q.-H. Park, "Optical antennas and plasmonics," *Contemporary Physics,* vol. 50, pp. 407-423, 2009.

[35] T. Søndergaard and S. Bozhevolnyi, "Slow-plasmon resonant nanostructures: Scattering and field enhancements," *Physical Review B,* vol. 75, p. 073402, 2007.

[36] J. George, M. Deepukumar, C. Aanandan, P. Mohanan, and K. Nair, "New compact microstrip antenna," *Electronics Letters,* vol. 32, pp. 508-509, 1996.

[37] A. Savchenkov, W. Liang, V. Ilchenko, E. Dale, E. Savchenkova, A. Matsko, D. Seidel, and L. Maleki, "Photonic E-field sensor," *AIP Advances,* vol. 4, p. 122901, 2014.

[38] C.-Y. Lin, A. X. Wang, B. S. Lee, X. Zhang, and R. T. Chen, "High dynamic range electric field sensor for electromagnetic pulse detection," *Optics Express,* vol. 19, pp. 17372-17377, 2011.

[39] Y. N. Wijayanto, H. Murata, and Y. Okamura, "Electrooptic Millimeter-Wave–Lightwave Signal Converters Suspended to Gap-Embedded Patch Antennas on Low-Dielectric Materials," *Selected Topics in Quantum Electronics, IEEE Journal of,* vol. 19, pp. 3400709-3400709, 2013.

[40] X. Zhang, B. Lee, C.-y. Lin, A. X. Wang, A. Hosseini, and R. T. Chen, "Highly Linear Broadband Optical Modulator Based on Electro-Optic Polymer," *Photonics Journal, IEEE,* vol. 4, pp. 2214-2228, 2012.

[41] R. Chang, S. Li, M. Lubarda, B. Livshitz, and V. Lomakin, "FastMag: Fast micromagnetic simulator for complex magnetic structures," *Journal of Applied Physics,* vol. 109, p. 07D358, 2011.

[42] S.-L. Chen, Y.-C. Chang, C. Zhang, J. G. Ok, T. Ling, M. T. Mihnev, T. B. Norris, and L. J. Guo, "Efficient real-time detection of terahertz pulse radiation based on photoacoustic conversion by carbon nanotube nanocomposite," *Nature Photonics,* 2014.

[43] W. Zhang, L. Huang, C. Santschi, and O. J. Martin, "Trapping and sensing 10 nm metal nanoparticles using plasmonic dipole antennas," *Nano letters,* vol. 10, pp. 1006-1011, 2010.

[44] J. N. Farahani, D. W. Pohl, H.-J. Eisler, and B. Hecht, "Single quantum dot coupled to a scanning optical antenna: a tunable superemitter," *Physical review letters,* vol. 95, p. 017402, 2005.

[45] L. Novotny and N. Van Hulst, "Antennas for light," *Nature Photonics,* vol. 5, pp. 83-90, 2011.

[46] X. Li, P. C. Li, L. Ji, C. Stender, C. McPheeters, S. R. Tatavarti, K. Sablon, and E. T. Yu, "Subwavelength nanostructures integrated with polymer‐packaged iii‐v solar cells for omnidirectional, broad‐spectrum improvement of photovoltaic performance," *Progress in Photovoltaics: Research and Applications,* 2014.

[47] C. Zhang, D. Zhao, D. Gu, H. Kim, T. Ling, Y. K. R. Wu, and L. J. Guo, "An Ultrathin, Smooth, and Low‐Loss Al‐Doped Ag Film and Its Application as a Transparent Electrode in Organic Photovoltaics," *Advanced Materials,* vol. 26, pp. 5696-5701, 2014.

[48] X. Li, V. D. Dasika, P.-C. Li, L. Ji, S. R. Bank, and T. Y. Edward, "Minimized open-circuit voltage reduction in GaAs/InGaAs quantum well solar cells with

bandgap-engineered graded quantum well depths," *Applied Physics Letters,* vol. 105, p. 123906, 2014.
[49] A. A. Eldek, A. Z. Elsherbeni, and C. E. Smith, "Wideband microstrip‐fed printed bow‐tie antenna for phased‐array systems," *Microwave and optical technology letters,* vol. 43, pp. 123-126, 2004.
[50] X. Lin, T. Ling, H. Subbaraman, X. Zhang, K. Byun, L. J. Guo, and R. T. Chen, "Ultraviolet imprinting and aligned ink-jet printing for multilayer patterning of electro-optic polymer modulators," *Optics letters,* vol. 38, pp. 1597-1599, 2013.
[51] X. Lin, H. Subbaraman, Z. Pan, A. Hosseini, C. Longe, K. Kubena, P. Schleicher, P. Foster, S. Brickey, and R. T. Chen, "Towards Realizing High-Throughput, Roll-to-Roll Manufacturing of Flexible Electronic Systems," *Electronics,* vol. 3, pp. 624-635, 2014.
[52] H. Subbaraman, D. T. Pham, X. C. Xu, M. Y. H. Chen, A. Hosseini, X. Lu, and R. T. Chen, "Inkjet-Printed Two-Dimensional Phased-Array Antenna on a Flexible Substrate," *IEEE Antennas and Wireless Propagation Letters,* vol. 12, pp. 170-173, 2013.
[53] R. T. Chen and X. Zhang, "Silicon nanomembrane based Devices for Optical Sensing and On-chip Interconnects," in *Frontiers in Optics*, 2014, p. FW1B. 2.
[54] O. Nast, T. Puzzer, L. M. Koschier, A. B. Sproul, and S. R. Wenham, "Aluminum-induced crystallization of amorphous silicon on glass substrates above and below the eutectic temperature," *Applied Physics Letters,* vol. 73, pp. 3214-3216, 1998.
[55] J. Rogers, M. Lagally, and R. Nuzzo, "Synthesis, assembly and applications of semiconductor nanomembranes," *Nature,* vol. 477, pp. 45-53, 2011.

Chapter 7

[1] E. I. Ackerman and C. H. Cox, "RF fiber-optic link performance," *Microwave Magazine, IEEE,* vol. 2, pp. 50-58, 2001.
[2] T. E. Darcie and G. E. Bodeep, "Lightwave subcarrier CATV transmission systems," *Microwave Theory and Techniques, IEEE Transactions on,* vol. 38, pp. 524-533, 1990.
[3] G. Lenz, B. Eggleton, C. K. Madsen, and R. Slusher, "Optical delay lines based on optical filters," *Quantum Electronics, IEEE Journal of,* vol. 37, pp. 525-532, 2001.
[4] K. P. Jackson, S. A. Newton, B. Moslehi, M. Tur, C. C. Cutler, J. W. Goodman, and H. Shaw, "Optical fiber delay-line signal processing," *Microwave Theory and Techniques, IEEE Transactions on,* vol. 33, pp. 193-210, 1985.

[5] C.-Y. Lin, A. X. Wang, B. S. Lee, X. Zhang, and R. T. Chen, "High dynamic range electric field sensor for electromagnetic pulse detection," *Optics Express,* vol. 19, pp. 17372-17377, 2011.

[6] J. H. Schaffner, J. F. Lam, C. J. Gaeta, G. L. Tangonan, R. L. Joyce, M. L. Farwell, and W. S. C. Chang, "Spur-free dynamic range measurements of a fiber optic link with traveling wave linearized directional coupler modulators," *Photonics Technology Letters, IEEE,* vol. 6, pp. 273-275, 1994.

[7] S. Thaniyavarn, "Modified 1×2 directional coupler waveguide modulator," *Electronics Letters,* vol. 22, pp. 941-942, 1986.

[8] S. Dubovitsky, W. Steier, S. Yegnanarayanan, and B. Jalali, "Analysis and improvement of Mach-Zehnder modulator linearity performance for chirped and tunable optical carriers," *Lightwave Technology, Journal of,* vol. 20, pp. 886-891, 2002.

[9] H. Kogelnik and R. V. Schmidt, "Switched directional couplers with alternating Δβ," *Quantum Electronics, IEEE Journal of,* vol. 12, pp. 396-401, 1976.

[10] R. F. Tavlykaev and R. V. Ramaswamy, "Highly linear Y-fed directional coupler modulator with low intermodulation distortion," *Lightwave Technology, Journal of,* vol. 17, pp. 282-291, 1999.

[11] B. Lee, C. Y. Lin, A. X. Wang, R. Dinu, and R. T. Chen, "Linearized electro-optic modulators based on a two-section Y-fed directional coupler," *Applied optics,* vol. 49, pp. 6485-6488, 2010.

[12] X. Wang, B. S. Lee, C. Y. Lin, D. An, and R. T. Chen, "Electroptic polymer linear modulators based on multiple-domain Y-fed directional coupler," *Journal of Lightwave Technology,* vol. 28, pp. 1670-1676, 2010.

[13] M. Izutsu, Y. Yamane, and T. Sueta, "Broad-band traveling-wave modulator using a LiNbO3optical waveguide," *Quantum Electronics, IEEE Journal of,* vol. 13, pp. 287-290, 1977.

[14] M. Izutsu, T. Itoh, and T. Sueta, "10 GHz bandwidth traveling-wave LiNbO3optical waveguide modulator," *Quantum Electronics, IEEE Journal of,* vol. 14, pp. 394-395, 1978.

[15] C. Teng, "Traveling‐wave polymeric optical intensity modulator with more than 40 GHz of 3‐dB electrical bandwidth," *Applied Physics Letters,* vol. 60, pp. 1538-1540, 1992.

[16] D. Chen, H. R. Fetterman, A. Chen, W. H. Steier, L. R. Dalton, W. Wang, and Y. Shi, "Demonstration of 110 GHz electro-optic polymer modulators," *Applied Physics Letters,* vol. 70, p. 3335, 1997.

[17] M. Lee, H. E. Katz, C. Erben, D. M. Gill, P. Gopalan, J. D. Heber, and D. J. McGee, "Broadband modulation of light by using an electro-optic polymer," *Science,* vol. 298, pp. 1401-1403, 2002.

[18] L. R. Dalton, A. W. Harper, B. Wu, R. Ghosn, J. Laquindanum, Z. Liang, A. Hubbel, and C. Xu, "Polymeric Electro‐Optic Modulators: Matereials synthesis and processing," *Advanced Materials,* vol. 7, pp. 519-540, 1995.

[19] J. D. Kraus and R. J. Marhefka, *Antenna for all applications*, 3rd ed.: McGraw-Hill 2002.
[20] M. C. Oh, H. Zhang, C. Zhang, H. Erlig, Y. Chang, B. Tsap, D. Chang, A. Szep, W. H. Steier, and H. R. Fetterman, "Recent advances in electrooptic polymer modulators incorporating highly nonlinear chromophore," *Selected Topics in Quantum Electronics, IEEE Journal of,* vol. 7, pp. 826-835, 2001.
[21] Y. Shi, C. Zhang, H. Zhang, J. H. Bechtel, L. R. Dalton, B. H. Robinson, and W. H. Steier, "Low (sub-1-volt) halfwave voltage polymeric electro-optic modulators achieved by controlling chromophore shape," *Science,* vol. 288, pp. 119-122, 2000.
[22] Y. Enami, C. Derose, D. Mathine, C. Loychik, C. Greenlee, R. Norwood, T. Kim, J. Luo, Y. Tian, and A. K. Y. Jen, "Hybrid polymer/sol–gel waveguide modulators with exceptionally large electro–optic coefficients," *Nature Photonics,* vol. 1, pp. 180-185, 2007.
[23] Y. Enami, D. Mathine, C. DeRose, R. Norwood, J. Luo, A. K. Y. Jen, and N. Peyghambarian, "Hybrid cross-linkable polymer/sol-gel waveguide modulators with 0.65 V half wave voltage at 1550 nm," *Applied Physics Letters,* vol. 91, p. 093505, 2007.
[24] J. Luo, S. Huang, Y. J. Cheng, T. D. Kim, Z. Shi, X. H. Zhou, and K. Y. J. Alex, "Phenyltetraene-based nonlinear optical chromophores with enhanced chemical stability and electrooptic activity," *Organic letters,* vol. 9, pp. 4471-4474, 2007.
[25] T. Baehr-Jones, M. Hochberg, G. Wang, R. Lawson, Y. Liao, P. Sullivan, L. Dalton, A. K. Y. Jen, and A. Scherer, "Optical modulation and detection in slotted silicon waveguides," *Optics Express,* vol. 13, pp. 5216-5226, 2005.
[26] J. H. Wülbern, J. Hampe, A. Petrov, M. Eich, J. Luo, A. K. Y. Jen, A. Di Falco, T. F. Krauss, and J. Bruns, "Electro-optic modulation in slotted resonant photonic crystal heterostructures," *Applied Physics Letters,* vol. 94, p. 241107, 2009.
[27] X. Wang, C. Y. Lin, S. Chakravarty, J. Luo, A. K. Y. Jen, and R. T. Chen, "Effective in-device r< sub> 33</sub> of 735 pm/V on electro-optic polymer infiltrated silicon photonic crystal slot waveguides," *Optics letters,* vol. 36, pp. 882-884, 2011.
[28] A. C. G. Nutt, V. Gopalan, and M. C. Gupta, "Domain inversion in LiNbO3 using direct electron - beam writing," *Applied Physics Letters,* vol. 60, pp. 2828-2830, 1992.
[29] D. Jin, H. Chen, A. Barklund, J. Mallari, G. Yu, E. Miller, and R. Dinu, "EO polymer modulators reliability study," in *Proc. SPIE 7599*, 2010, pp. 75990H-8.
[30] R. B. Childs and V. A. O'Byrne, "Predistortion linearization of directly modulated DFB lasers and external modulators for AM video transmission," in *Proc. Tech. Dig. Opt. Fiber Commun. Conf.,*, San Francisco, CA, 1990.
[31] R. M. D. E. Ridder and S. Korotky, "Feedforward compensation of integrated optic modulator distortion," in *Proc. Tech. Dig. Opt. Fiber Commun. Conf.*, San Francisco, CA, 1990.

[32] L. M. Johnson and H. Roussell, "Reduction intermodulation distortion in interferometric optical modulators," *Optics letters,* vol. 13, pp. 928-930, 1988.
[33] S. K. Korotky and R. De Ridder, "Dual parallel modulation schemes for low-distortion analog optical transmission," *Selected Areas in Communications, IEEE Journal on,* vol. 8, pp. 1377-1381, 1990.
[34] M. L. Farwell, Z. Q. Lin, E. Wooten, and W. Chang, "An electrooptic intensity modulator with improved linearity," *Photonics Technology Letters, IEEE,* vol. 3, pp. 792-795, 1991.
[35] B. Lee, C. Lin, X. Wang, R. T. Chen, J. Luo, and A. K. Y. Jen, "Bias-free electro-optic polymer-based two-section Y-branch waveguide modulator with 22 dB linearity enhancement," *Optics letters,* vol. 34, pp. 3277-3279, 2009.
[36] FIMMWAVE simulation software, http://www.photond.com/products/fimmwave.htm
[37] FIMMPROP simulation software, http://www.photond.com/products/fimmprop.htm
[38] G. T. Reed, *Silicon Photonics: the state of the art*. UK: Wiley-Interscience, 2008.
[39] COMSOL Multiphysics Simulation Software, http://www.comsol.com.
[40] R. G. Hunsperger, A. Yariv, and A. Lee, "Parallel end-butt coupling for optical integrated circuits," *Applied optics,* vol. 16, pp. 1026-1032, 1977.
[41] M. Sanghadasa, P. R. Ashley, E. L. Webster, C. Cocke, G. A. Lindsay, and A. J. Guenthner, "A simplified technique for efficient fiber-polymer-waveguide power coupling using a customized cladding with tunable index of refraction," *Lightwave Technology, Journal of,* vol. 24, pp. 3816-3823, 2006.
[42] K. Geary, S. K. Kim, B. J. Seo, Y. C. Hung, W. Yuan, and H. R. Fetterman, "Photobleached refractive index tapers in electrooptic polymer rib waveguides," *Photonics Technology Letters, IEEE,* vol. 18, pp. 64-66, 2006.
[43] I. E. Day, I. Evans, A. Knights, F. Hopper, S. Roberts, J. Johnston, S. Day, J. Luff, H. K. Tsang, and M. Asghari, "Tapered silicon waveguides for low insertion loss highly-efficient high-speed electronic variable optical attenuators," in *Optical Fiber Communications Conference*, 2003, pp. 249 - 251
[44] Rsoft simulation software, http://www.rsoftdesign.com/
[45] W. S. Chang, *RF photonic technology in optical fiber links*: Cambridge Univ Pr, 2002.
[46] D. Chen, Q. Wang, and Z. Shen, "A broadband microstrip-to-CPW transition," in *Microwave Conference Proceedings, 2005. APMC 2005. Asia-Pacific Conference Proceedings*, 2005, p. 4.
[47] T.-D. Kim, J. Luo, Y.-J. Cheng, Z. Shi, S. Hau, S.-H. Jang, X.-H. Zhou, Y. Tian, B. Polishak, S. Huang, Ma.Hong, L. R. Dalton, and A. K.-Y. Jen, "Binary Chromophore Systems in Nonlinear Optical Dendrimers and Polymers for Large Electrooptic Activities†," *The Journal of Physical Chemistry C,* vol. 112, pp. 8091-8098, 2008.

[48] E. Yamashita, "Variational method for the analysis of microstrip-like transmission lines," *Microwave Theory and Techniques, IEEE Transactions on,* vol. 16, pp. 529-535, 1968.
[49] ANSYS HFSS simulation software, http://www.ansys.com/
[50] A. Chen and E. Murphy, *Broadband Optical Modulators: Science, Technology, and Applications*: CRC Press, 2011.
[51] R. C. Alferness, "Waveguide electrooptic modulators," *IEEE Transactions on Microwave Theory Techniques,* vol. 30, pp. 1121-1137, 1982.
[52] D. M. Burland, R. D. Miller, and C. A. Walsh, "Second-order nonlinearity in poled-polymer systems," *Chemical Reviews,* vol. 94, pp. 31-75, 1994.
[53] L. R. Dalton, P. A. Sullivan, and D. H. Bale, "Electric field poled organic electro-optic materials: state of the art and future prospects," *Chemical Reviews,* vol. 110, pp. 25-55, 2009.
[54] M. A. Mortazavi, A. Knoesen, S. T. Kowel, B. G. Higgins, and A. Dienes, "Second-harmonic generation and absorption studies of polymer—dye films oriented by corona-onset poling at elevated temperatures," *JOSA B,* vol. 6, pp. 733-741, 1989.
[55] H. Tang, J. M. Taboada, G. Cao, L. Li, and R. T. Chen, "Enhanced electro-optic coefficient of nonlinear optical polymer using liquid contact poling," *Applied Physics Letters,* vol. 70, p. 538, 1997.
[56] Z. Z. Yue, D. An, R. T. Chen, and S. Tang, "1000 V/μm pulsed poling technique for photolime-gel electro-optic polymer with room-temperature repoling feature," *Applied Physics Letters,* vol. 72, p. 3420, 1998.
[57] S. Huang, T. D. Kim, J. Luo, S. K. Hau, Z. Shi, X. H. Zhou, H. L. Yip, and A. K. Y. Jen, "Highly efficient electro-optic polymers through improved poling using a thin TiO-modified transparent electrode," *Applied Physics Letters,* vol. 96, p. 243311, 2010.
[58] S. Huang, J. Luo, H. L. Yip, A. Ayazi, X. H. Zhou, M. Gould, A. Chen, T. Baehr‐Jones, M. Hochberg, and A. K. Y. Jen, "Electro‐optical Materials: Efficient Poling of Electro‐Optic Polymers in Thin Films and Silicon Slot Waveguides by Detachable Pyroelectric Crystals (Adv. Mater. 10/2012)," *Advanced Materials,* vol. 24, pp. OP1-OP1, 2012.
[59] R. Blum, M. Sprave, J. Sablotny, and M. Eich, "High-electric-field poling of nonlinear optical polymers," *JOSA B,* vol. 15, pp. 318-328, 1998.
[60] T. A. Tumolillo Jr and P. R. Ashley, "A novel pulse-poling technique for EO polymer waveguide devices using device electrode poling," *Photonics Technology Letters, IEEE,* vol. 4, pp. 142-145, 1992.
[61] V. Taggi, F. Michelotti, M. Bertolotti, G. Petrocco, V. Foglietti, A. Donval, E. Toussaere, and J. Zyss, "Domain inversion by pulse poling in polymer films," *Applied Physics Letters,* vol. 72, p. 2794, 1998.

[62] J. Baker-Jarvis, M. D. Janezic, B. Riddle, C. L. Holloway, and N. Paulter, "Dielectric and conductor-loss characterization and measurements on electronic packaging materials," *2001.,* 2001.
[63] G. K. Gopalakrishnan, W. K. Burns, R. W. McElhanon, C. H. Bulmer, and A. S. Greenblatt, "Performance and modeling of broadband LiNbO3 traveling wave optical intensity modulators," *Lightwave Technology, Journal of,* vol. 12, pp. 1807-1819, 1994.
[64] P. L. Liu, B. Li, and Y. Trisno, "In search of a linear electrooptic amplitude modulator," *Photonics Technology Letters, IEEE,* vol. 3, pp. 144-146, 1991.
[65] W. B. Bridges and J. H. Schaffner, "Distortion in linearized electrooptic modulators," *Microwave Theory and Techniques, IEEE Transactions on,* vol. 43, pp. 2184-2197, 1995.
[66] Y. C. Hung, S. K. Kim, H. Fetterman, J. Luo, and A. K. Y. Jen, "Experimental demonstration of a linearized polymeric directional coupler modulator," *Photonics Technology Letters, IEEE,* vol. 19, pp. 1762-1764, 2007.
[67] C. T. DeRose, R. Himmelhuber, D. Mathine, R. Norwood, J. Luo, A. K. Y. Jen, and N. Peyghambarian, "High Δn strip-loaded electro-optic polymer waveguide modulator with low insertion loss," *Optics Express,* vol. 17, pp. 3316-3321, 2009.

Chapter 8

[1] R. Soref, "The past, present, and future of silicon photonics," *Selected Topics in Quantum Electronics, IEEE Journal of,* vol. 12, pp. 1678-1687, 2006.
[2] B. Jalali and S. Fathpour, "Silicon photonics," *Lightwave Technology, Journal of,* vol. 24, pp. 4600-4615, 2006.
[3] H. Subbaraman, X. Xu, A. Hosseini, X. Zhang, Y. Zhang, D. Kwong, and R. T. Chen, "Recent advances in silicon-based passive and active optical interconnects," *Optics Express,* vol. 23, pp. 2487-2511, 2015.
[4] S. Yao, B. Mukherjee, and S. Dixit, "Advances in photonic packet switching: an overview," *Communications Magazine, IEEE,* vol. 38, pp. 84-94, 2000.
[5] G. Cocorullo and I. Rendina, "Thermo-optical modulation at 1.5 μm in silicon etalon," *Electronics Letters,* vol. 28, pp. 83-85, 1992.
[6] G. Coppola, L. Sirleto, I. Rendina, and M. Iodice, "Advance in thermo-optical switches: principles, materials, design, and device structure," *Optical Engineering,* vol. 50, pp. 071112-071112-14, 2011.
[7] R. A. Soref and B. R. Bennett, "Electrooptical effects in silicon," *Quantum Electronics, IEEE Journal of,* vol. 23, pp. 123-129, 1987.
[8] M. W. Geis, S. J. Spector, R. Williamson, and T. Lyszczarz, "Submicrosecond submilliwatt silicon-on-insulator thermooptic switch," *Photonics Technology Letters, IEEE,* vol. 16, pp. 2514-2516, 2004.

[9] S. Nakamura, Y. Ueno, and K. Tajima, "168-Gb/s all-optical wavelength conversion with a symmetric-Mach-Zehnder-type switch," *Photonics Technology Letters, IEEE,* vol. 13, pp. 1091-1093, 2001.

[10] Y. Vlasov, W. M. Green, and F. Xia, "High-throughput silicon nanophotonic wavelength-insensitive switch for on-chip optical networks," *Nature Photonics,* vol. 2, pp. 242-246, 2008.

[11] Q. Xu, D. Fattal, and R. G. Beausoleil, "Silicon microring resonators with 1.5-μm radius," *Optics Express,* vol. 16, pp. 4309-4315, 2008.

[12] Q. Xu, B. Schmidt, J. Shakya, and M. Lipson, "Cascaded silicon micro-ring modulators for WDM optical interconnection," *Optics Express,* vol. 14, pp. 9431-9435, 2006.

[13] A. W. Poon, X. Luo, F. Xu, and H. Chen, "Cascaded microresonator-based matrix switch for silicon on-chip optical interconnection," *Proceedings of the IEEE,* vol. 97, pp. 1216-1238, 2009.

[14] W. S. Fegadolli, V. R. Almeida, and J. E. B. Oliveira, "Reconfigurable silicon thermo-optical device based on spectral tuning of ring resonators," *Optics Express,* vol. 19, pp. 12727-12739, 2011.

[15] W. S. Fegadolli, L. Feng, M. M.-U. Rahman, J. E. Oliveira, V. R. Almeida, and A. Scherer, "Experimental demonstration of a reconfigurable silicon thermo-optical device based on spectral tuning of ring resonators for optical signal processing," *Optics Express,* vol. 22, pp. 3425-3431, 2014.

[16] Y. A. Vlasov, M. O'Boyle, H. F. Hamann, and S. J. McNab, "Active control of slow light on a chip with photonic crystal waveguides," *Nature,* vol. 438, pp. 65-69, 2005.

[17] M. Tinker and J. Lee, "Thermal and optical simulation of a photonic crystal light modulator based on the thermo-optic shift of the cut-off frequency," *Optics Express,* vol. 13, pp. 7174-7188, 2005.

[18] E. A. Camargo, H. M. Chong, and R. M. De La Rue, "Highly compact asymmetric Mach-Zehnder device based on channel guides in a two-dimensional photonic crystal," *Applied optics,* vol. 45, pp. 6507-6510, 2006.

[19] N. Yamamoto, T. Ogawa, and K. Komori, "Photonic crystal directional coupler switch with small switching length and wide bandwidth," *Optics Express,* vol. 14, pp. 1223-1229, 2006.

[20] D. M. Beggs, T. P. White, L. Cairns, L. O'Faolain, and T. F. Kraus, "Ultrashort photonic crystal optical switch actuated by a microheater," *Photonics Technology Letters, IEEE,* vol. 21, pp. 24-26, 2009.

[21] S. Leonard, H. Van Driel, J. Schilling, and R. Wehrspohn, "Ultrafast band-edge tuning of a two-dimensional silicon photonic crystal via free-carrier injection," *Physical Review B,* vol. 66, p. 161102, 2002.

[22] X. Wang, S. Chakravarty, B. S. Lee, C. Lin, and R. T. Chen, "Ultraefficient control of light transmission through photonic potential barrier modulation," *Optics letters,* vol. 34, pp. 3202-3204, 2009.

[23] B. Maes, P. Bienstman, and R. Baets, "Switching in coupled nonlinear photonic-crystal resonators," *JOSA B,* vol. 22, pp. 1778-1784, 2005.
[24] X. Yang, M. Yu, D.-L. Kwong, and C. W. Wong, "All-optical analog to electromagnetically induced transparency in multiple coupled photonic crystal cavities," *Physical review letters,* vol. 102, p. 173902, 2009.
[25] H. Ishio, J. Minowa, and K. Nosu, "Review and status of wavelength-division-multiplexing technology and its application," *Journal of Lightwave Technology,* vol. 2, pp. 448-463, 1984.
[26] L. Gu, W. Jiang, X. Chen, and R. T. Chen, "Thermooptically tuned photonic crystal waveguide silicon-on-insulator Mach–Zehnder interferometers," *Photonics Technology Letters, IEEE,* vol. 19, pp. 342-344, 2007.
[27] A. Liu, L. Liao, D. Rubin, H. Nguyen, B. Ciftcioglu, Y. Chetrit, N. Izhaky, and M. Paniccia, "High-speed optical modulation based on carrier depletion in a silicon waveguide," *Optics Express,* vol. 15, pp. 660-668, 2007.
[28] W. M. Green, M. J. Rooks, L. Sekaric, and Y. A. Vlasov, "Ultra-compact, low RF power, 10 Gb/s silicon Mach-Zehnder modulator," *Optics Express,* vol. 15, pp. 17106-17113, 2007.
[29] M. C. Souza, L. A. Barea, G. Wiederhecker, A. A. von Zuben, and N. C. Frateschi, "Tunable Spectral Engineering of Coupled Silicon Microcavities," in *CLEO: QELS_Fundamental Science*, 2015, p. JTu5A. 49.
[30] D. O'Brien, M. Settle, T. Karle, A. Michaeli, M. Salib, and T. Krauss, "Coupled photonic crystal heterostructure nanocavities," *Optics Express,* vol. 15, pp. 1228-1233, 2007.
[31] J. Wu, P. Cao, T. Pan, Y. Yang, C. Qiu, C. Tremblay, and Y. Su, "Compact on-chip 1× 2 wavelength selective switch based on silicon microring resonator with nested pairs of subrings," *Photonics Research,* vol. 3, pp. 9-14, 2015.
[32] Y. Yi, P. Bermel, K. Wada, X. Duan, J. Joannopoulos, and L. Kimerling, "Tunable multichannel optical filter based on silicon photonic band gap materials actuation," *Applied Physics Letters,* vol. 81, pp. 4112-4114, 2002.
[33] W. S. Fegadolli, N. Pavarelli, P. O'Brien, S. Njoroge, V. R. Almeida, and A. Scherer, "Thermally controllable silicon photonic crystal nanobeam cavity without surface cladding for sensing applications," *ACS Photonics,* vol. 2, pp. 470-474, 2015.

Chapter 9

[1] S. Huang, J. Luo, H. L. Yip, A. Ayazi, X. H. Zhou, M. Gould, A. Chen, T. Baehr‐Jones, M. Hochberg, and A. K. Y. Jen, "Efficient Poling of Electro‐Optic Polymers in Thin Films and Silicon Slot Waveguides by Detachable Pyroelectric Crystals," *Advanced Materials,* vol. 24, pp. OP42-OP47, 2012.

[2] S. Huang, J. Luo, Z. Jin, X.-H. Zhou, Z. Shi, and A. K.-Y. Jen, "Enhanced temporal stability of a highly efficient guest–host electro-optic polymer through a barrier layer assisted poling process," *Journal of Materials Chemistry,* vol. 22, pp. 20353-20357, 2012.

[3] Z. Shi, J. Luo, S. Huang, B. M. Polishak, X.-H. Zhou, S. Liff, T. R. Younkin, B. A. Block, and A. K.-Y. Jen, "Achieving excellent electro-optic activity and thermal stability in poled polymers through an expeditious crosslinking process," *Journal of Materials Chemistry,* vol. 22, pp. 951-959, 2012.

[4] X. Zhang, A. Hosseini, S. Chakravarty, J. Luo, A. K.-Y. Jen, and R. T. Chen, "Wide optical spectrum range, subvolt, compact modulator based on an electro-optic polymer refilled silicon slot photonic crystal waveguide," *Optics letters,* vol. 38, pp. 4931-4934, 2013.

[5] X. Zhang, A. Hosseini, H. Subbaraman, S. Wang, Q. Zhan, J. Luo, A. K. Jen, and R. T. Chen, "Integrated Photonic Electromagnetic Field Sensor Based on Broadband Bowtie Antenna Coupled Silicon Organic Hybrid Modulator," *Lightwave Technology, Journal of,* vol. 32, pp. 3774-3784, 2014.

[6] C. T. Chen, X. Xu, A. Hosseini, Z. Pan, H. Subbaraman, X. Zhang, Ray T. Chen, "Design of Highly Efficient Hybrid Si-Au Taper for Dielectric Strip Waveguide to Plasmonic Slot Waveguide Mode Converter," IEEE Journal of Lightwave Technology (To appear).

[7] A. Melikyan, L. Alloatti, A. Muslija, D. Hillerkuss, P. Schindler, J. Li, R. Palmer, D. Korn, S. Muehlbrandt, D. Van Thourhout, B. Chen, R. Dinu, M. Sommer, C. Koos, M. Kohl, W. Freude, and J. Leuthold, "High-speed plasmonic phase modulators," *Nature Photonics,* vol. 8, pp. 229-233, 2014.

[8] E. Schelew, G. W. Rieger, and J. F. Young, "Characterization of integrated planar photonic crystal circuits fabricated by a CMOS foundry," *Lightwave Technology, Journal of,* vol. 31, pp. 239-248, 2013.

[9] G. Li, J. Yao, H. Thacker, A. Mekis, X. Zheng, I. Shubin, Y. Luo, J. Lee, K. Raj, and J. E. Cunningham, "Ultralow-loss, high-density SOI optical waveguide routing for macrochip interconnects," *Optics Express,* vol. 20, pp. 12035-12039, 2012.

[10] S. Rahimi, A. Hosseini, X. Xu, H. Subbaraman, and R. T. Chen, "Group-index independent coupling to band engineered SOI photonic crystal waveguide with large slow-down factor," *Optics Express,* vol. 19, pp. 21832-21841, 2011.

[11] A. Hosseini, X. Xu, D. N. Kwong, H. Subbaraman, W. Jiang, and R. T. Chen, "On the role of evanescent modes and group index tapering in slow light photonic crystal waveguide coupling efficiency," *Applied Physics Letters,* vol. 98, pp. 031107-031107-3, 2011.

[12] C. Y. Lin, A. X. Wang, W. C. Lai, J. L. Covey, S. Chakravarty, and R. T. Chen, "Coupling loss minimization of slow light slotted photonic crystal waveguides using mode matching with continuous group index perturbation," *Optics letters,* vol. 37, pp. 232-234, 2012.

[13] X. Zhang, H. Subbaraman, A. Hosseini, and R. T. Chen, "Highly efficient mode converter for coupling light into wide slot photonic crystal waveguide," *Optics Express,* vol. 22, pp. 20678-20690, 2014.
[14] X. Xu, H. Subbaraman, J. Covey, D. Kwong, A. Hosseini, and R. T. Chen, "Complementary metal–oxide–semiconductor compatible high efficiency subwavelength grating couplers for silicon integrated photonics," *Applied Physics Letters,* vol. 101, p. 031109, 2012.
[15] B. Snyder and P. O'Brien, "Planar fiber packaging method for silicon photonic integrated circuits," 2012.
[16] T. Shoji, T. Tsuchizawa, T. Watanabe, K. Yamada, and H. Morita, "Low loss mode size converter from 0.3 μm square Si wire waveguides to singlemode fibres," *Electronics Letters,* vol. 38, pp. 1669-1670, 2002.
[17] A. Säynätjoki, L. Karvonen, T. Alasaarela, X. Tu, T. Liow, M. Hiltunen, A. Tervonen, G. Lo, and S. Honkanen, "Low-loss silicon slot waveguides and couplers fabricated with optical lithography and atomic layer deposition," *Optics Express,* vol. 19, pp. 26275-26282, 2011.
[18] R. Palmer, L. Alloatti, D. Korn, W. Heni, P. Schindler, J. Bolten, M. Karl, M. Waldow, T. Wahlbrink, and W. Freude, "Highly Efficient Strip-to-Slot Mode Converters," in *CLEO: Science and Innovations*, 2012.
[19] A. Di Falco, M. Massari, M. Scullion, S. Schulz, F. Romanato, and T. Krauss, "Propagation Losses of Slotted Photonic Crystal Waveguides," *Photonics Journal, IEEE,* vol. 4, pp. 1536-1541, 2012.
[20] X. Wang, C. Y. Lin, S. Chakravarty, J. Luo, A. K. Y. Jen, and R. T. Chen, "Effective in-device r< sub> 33</sub> of 735 pm/V on electro-optic polymer infiltrated silicon photonic crystal slot waveguides," *Optics letters,* vol. 36, pp. 882-884, 2011.
[21] X. Zhang, A. Hosseini, X. Xu, S. Wang, Q. Zhan, Y. Zou, S. Chakravarty, and R. T. Chen, "Electric field sensor based on electro-optic polymer refilled silicon slot photonic crystal waveguide coupled with bowtie antenna," in SPIE OPTO, 2013, pp. 862418-862418-8.
[22] P. Zhou, L. Zhang, Y. Tian, and L. Yang, "GHz electro-optical OR/NOR directed logic device based on silicon micro-ring resonators," Optics letters, vol. 39, pp. 1937-1940, 2014/04/01 2014.

VITA

Xingyu Zhang was born in Mudanjiang, Heilongjiang, China, in 1986. He received the B.S. degree in electrical engineering from Beijing Institute of Technology, Beijing, China, in 2009, the M.S. degree in electrical engineering from University of Michigan, Ann Arbor, MI, USA, in 2010. He joined the University of Texas, Austin, TX, USA, in 2011, and worked toward his Ph.D degree under the supervision of Prof. Ray T. Chen. His research focuses on the design, fabrication, and characterization of silicon-polymer hybrid integrated microwave photonic devices for optical interconnects, electro-optic modulation, and electromagnetic wave detection. He has published about 50 peer-reviewed papers in journals and conferences during the Ph.D degree, about 35 of which he first authored, including 3 invited papers and 3 invited talks. He is the recipient of SPIE Photonics West 2015 Best Student Paper Award, SPIE Optics and Photonics 2014 Best Student Paper Award, OSA Incubic Milton Chang Student Travel Grant, SPIE Student Travel Grant, Chinese Government Award for Outstanding Self-financed Students Abroad, Engineering Scholarship Award at UT-Austin, Professional Development Award at UT-Austin, Full Fellowship at UM-Ann Arbor, Xu Teli Scholarship at BIT, etc. He has so far served as a reviewer for 21 journals in his research area, such as Scientific Reports, Applied Physics Letters, Optics Letters, Optics Express, Nanoscale, ACS Photonics, etc., and his review work was recognized by 2015 OSA Outstanding Reviewer Award. He is a student member IEEE, SPIE and OSA. Xingyu has internship experience at Oracle and IBM, and he will work at HP Labs as a postdoctoral researcher after obtaining his Ph.D degree.

Permanent email address:

xzhang@utexas.edu

This dissertation was typed by the author.